ulm university universität ulm

Novel peptide nanofibrils as efficient transduction enhancers for *ex vivo* viral gene transfer

Cumulative dissertation submitted in partial fulfilment of the requirements for the degree of „Doctor rerum naturalium" (Dr. rer. nat.) of the International Graduate School in Molecular Medicine Ulm

Institute of Molecular Virology
Ulm University Medical Center
Head: Prof. Dr. Frank Kirchhoff and Prof. Dr. Jan Münch

Author: Lena Rauch-Wirth

Born in Velbert (Germany)

2026

Current dean of the Medical Faculty: Prof. Dr. Thomas Wirth

Current Chairman of the Graduate School: Prof. Dr. Bernd Knöll

Thesis Advisory Committee:
1st supervisor: Prof. Dr. Jan Münch
2nd supervisor: Prof. Dr. Barbara Spellerberg
3rd supervisor: Prof. Dr. Tanja Weil

External reviewer: Prof. Dr. Meytal Landau

Day doctorate awarded: 23.09.26

Results gained in my thesis have previously been published in the following publications:

Rauch-Wirth, L.*, Schütz, D.*, Groß, R., Rode, S., Glocker, B., Müller, J. A., Walther, P., Read, C. & Münch, J. **Transduction enhancing EF-C peptide nanofibrils are endocytosed by macropinocytosis and subsequently degraded.** *Biomaterials* 317, 123044 (2025). * These authors contributed equally.

Reference[1] and Appendix 1.

License: CC By 4.0 (https://creativecommons.org/licenses/by/4.0/)

Rauch-Wirth, L., Renner, A., Kaygisiz, K., Weil, T., Zimmermann, L., Rodriguez-Alfonso, A. A., Schütz, D., Wiese, S., Ständker, L., Weil, T., Schmiedel, D. & Münch, J. **Optimized peptide nanofibrils as efficient transduction enhancers for in vitro and ex vivo gene transfer.** *Front. Immunol.* **14**, 1270243 (2023).

Reference[2] and Appendix 2.

License: CC By 4.0 (https://creativecommons.org/licenses/by/4.0/)

Rauch-Wirth, L.*, La Roche, J.*, Kaygisiz, K., Kuhn, A., Jeon, N., Stifel, U., Zech, F., Fischer-Posovszky, P., Weil, T., Read, C. & Münch, J. **Structural morphology of peptide nanofibrils dictates viral capture and cellular uptake in gene therapy applications.** *Nano Today* 69, 103015 (2026). * These authors contributed equally.

Reference[3] and Appendix 3.

License: CC By 4.0 (https://creativecommons.org/licenses/by/4.0/)

Copies of these articles are attached in the appendix.

Table of contents

Abbreviations vi

1 Introduction 1

1.1 Gene therapy 1

1.1.1 Delivery methods for gene therapy 1

1.2 CAR T cell therapy 2

1.2.1 Mechanism of CAR T cells 4

1.2.2 Manufacturing process 5

1.2.3 Challenges and solutions 6

1.2.4 Lentiviral and γ-retroviral vectors in CAR T cell therapy 7

1.3 Optimization of retroviral transduction 9

1.3.1 Peptide nanofibrils as transduction enhancer 10

1.3.2 Mechanism of transduction enhancing activity of β-sheet PNFs 11

1.4 Scientific aim 14

2 Results and Discussion 15

2.1 Transduction enhancing EF-C peptide nanofibrils are endocytosed by macropinocytosis and subsequently degraded 15

2.2 Optimized peptide nanofibrils as efficient transduction enhancers for *in vitro* and *ex vivo* gene transfer 17

2.3 Structural morphology of peptide nanofibrils dictates viral capture and cellular uptake in gene therapy applications 20

2.3.1 Structural and morphological analysis of D4 and Vectofusin-1 21

2.3.2 Virus-like particle binding induces morphological and kinetic changes in PNFs 22

2.3.3 D4 PNFs are taken up via endocytosis followed by lysosomal degradation 22

3 Summary 26

4 References 28

5 Appendices 46
5.1 Appendix 1 46
5.2 Appendix 2 60
5.3 Appendix 3 77
6 List of publications 98
7 Acknowledgments 100
8 Statutory declaration 101

Abbreviations

AAV	adeno-associated virus
ADCC	antibody-dependent cellular cytotoxicity
AdV5	adenovirus serotype 5
APC	antigen-representing cell
B-ALL	B cell acute lymphoblastic leukemia
BaEV	baboon endogenous virus glycoprotein
BCMA	B-cell maturation antigen
BCL	B cell lymphoma
B-NHL	B cell non-Hodgkin lymphoma
°C	degree Celsius
CAR	chimeric antigen receptor
CD	cluster of differentiation
CLEM	Correlative light and electron microscopy
CLL	chronic lymphocytic leukemia
CR	complete response
CRS	cytokine release syndrome
DEAE	diethylaminoethyl
DMSO	dimethyl sulfoxide
DNA	deoxyribonucleic acid
E. coli	*Escherichia coli*
EDTA	ethylenediaminetetraacetic acid
EF-C	enhancing factor-C
FasL	Fas ligand
FDA	Food and Drug Administration
FL	follicular lymphoma
FRET	Förster resonance energy transfer
GALV	gibbon ape leukemia virus
GMP	good manufacturing practice
gp120	HIV gp120 envelope glycoprotein
GvHD	graft-versus-host-disease
HEK293T	human embryonic kidney 293 large T antigen cells
HIV-1	human immunodeficiency virus 1
HSA	human serum albumin
HSCs	hematopoietic stem cells
HSPG	heparan sulfate proteoglycans
L	liter
IL	interleukin
iPSC	induced pluripotent stem cells
IRF	interferon regulatory factor
LBCL	large B cell lymphoma
LDL-R	low-density lipoprotein receptor
LPS	lipopolysaccharide
LTR	long terminal repeat
LV	lentiviral vector
µ	micro (10^{-6})
m	meter
m	milli (10^{-3})
MCL	mantle cell lymphoma

MD	molecular dynamics
MHC	major histocompatibility complex
MLV	murine leukemia virus
MM	multiple myeloma
mRNA	messenger ribonucleic acid
MSCV	murine stem cell virus
MVBs	multivesicular bodies
NF-κB	nuclear factor- κB
NK	natural killer
NTA	nanoparticle tracking analysis
OS	overall survival
PAP	prostatic acid phosphatase
PAs	peptide amphiphiles
PBS	phosphate buffered saline
pFTAA	pentameric form of formyl thiophene acetic acid
pI	isoelectric point
PNFs	peptide nanofibrils
RD114/TR	chimeric envelope glycoprotein derived from feline leukemia virus with the cytoplasmic tail derived from the murine leukemia virus glycoprotein
REMS	Risk Evaluation and Mitigation Strategies
RNA	ribonucleic acid
RNPs	ribonucleoprotein complexes
RV	γ-retroviral vector
SAR	structure-activity relationship
scFv	single-chain variable fragment
SEM	scanning electron microscopy
SEVI	semen-derived enhancer of viral infection
SIN	self-inactivating
SLL	small lymphocytic lymphoma
STEM	scanning transmission electron microscopy
TCR	T cell receptor
TEM	transmission electron microscopy
UCB	umbilical cord blood
VLP	virus-like particle
VSV-G	vesicular stomatitis virus glycoprotein
YFP	yellow fluorescence protein

Amino acid code:

Ala	Alanine (A)	Ile	Isoleucine (I)	Arg	Arginine (R)
Cys	Cysteine (C)	Lys	Lysine (K)	Ser	Serine (S)
Asp	Aspartic acid (D)	Leu	Leucine (L)	Thr	Threonine (T)
Glu	Glutamic acid (E)	Met	Methionine (M)	Val	Valine (V)
Phe	Phenylalanine (F)	Asn	Asparagine (N)	Trp	Tryptophan (W)
Gly	Glycine (G)	Pro	Proline (P)	Tyr	Tyrosine (Tyr)
His	Histidine (H)	Gln	Glutamine (Q)		

1 Introduction

1.1 Gene therapy

Gene therapy aims to treat or cure human diseases such as cancer, infections, and genetic disorders by modifying the genetic material of patients' cells[4]. This can be achieved through different strategies including gene addition, silencing, editing, or replacement using viral and non-viral delivery systems[4]. Since the first approved human gene transfer study in 1989[5], more than 30 gene therapies have been approved worldwide, predominantly for cancer, a trend also reflected in clinical trials (Fig. 1A)[6].

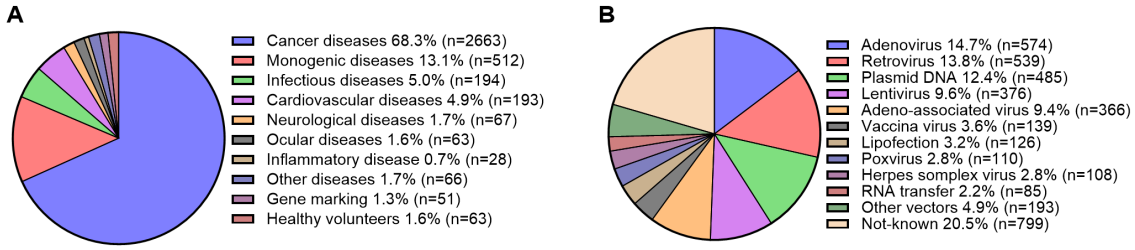

Figure 1. Indications (A) and used vectors for gene transfer (B) in gene therapy clinical trials. As of March 2023, a total of 3,9000 trials across 46 countries were included in this analysis. Adapted and reprinted from Ginn *et al.* 2024 [6] with permission according to the copyright © 2024 by John Wileys & Sons LTD.

Gene therapies can be administered *ex vivo*, in which the patient's cells are collected and genetically modified before being reintroduced into the patient [7], or *in vivo*, in which genetic material is delivered directly to the patient via a vector[8]. In the *ex vivo* approach hematopoietic stem cells (HSCs) and T cells are most frequently modified to treat cancer, blood disorders and infectious diseases[9]. In the *in vivo* approach, genetic material is delivered directly into the target organ or its associated vascular system. This strategy is mainly applied to treat monogenic diseases affecting organs such as lungs, muscles, liver, heart and eyes[9,10].

1.1.1 Delivery methods for gene therapy

Gene delivery methods are classified into viral and non-viral systems. Viral vectors are typically restricted to DNA delivery, while non-viral methods can deliver DNA, mRNA and ribonucleoprotein complexes (RNPs)[9,10]. Naked plasmid DNA remains the most commonly used non-viral method in clinical trials (Fig. 1B)[6], often combined with electroporation to enhance transfection efficiency[11]. However, electroporation can potentially lead to cell damage and a change of cellular homeostasis[10,11]. To protect genetic cargo from degradation by cellular enzymes, engineered carriers such as liposomes are used in

lipofection (3.2% of clinical trials[6], Fig. 1B), where cationic lipid vesicles encapsulate DNA and facilitate membrane fusion[12,13].

However, viral vectors remain the most commonly used tools in gene therapy (around 60 % of clinical trials, Fig. 1B) due to their superior delivery efficiency[6]. The main viral vectors include γ-retroviral (RVs), lentiviral (LVs), and adenovirus vectors, as well as adeno-associated virus (AAV)[6]. Most RVs are based on the γ-retrovirus murine leukemia virus (MLV) or murine stem cell virus (MSCV)[14,15], while LVs are derived from the human immunodeficiency virus 1 (HIV-1)[16]. Both RVs and LVs integrate their genetic cargo into the host cell genome leading to long-term stable expression. RVs can only integrate their genes into dividing cells, whereas LVs can transduce cells independently of the cell cycle[9]. Nevertheless, genomic integration by these vectors can lead to insertional mutagenesis[17,18], which has been associated with leukemia in some cases[19], limiting their use primarily to *ex vivo* delivery[9]. An examination of 784 patients from 38 T cell therapy trials predominantly involving chimeric antigen receptor (CAR) T cell therapy, revealed no indications of LV or RV-mediated insertional mutagenesis, supporting the long-term safety of these vectors for *ex vivo* gene therapy applications[20]. Adenoviral vectors, typically based on human adenovirus serotype 5 (AdV5), do not integrate into the host genome[21]. They exhibit high transduction efficiencies in both dividing and non-dividing cells but often induce strong innate immune responses[22]. AAV vectors are less immunogenic, largely non-integrating, and show expression independent of cell division[10]. However, they are limited by low packing capacity of less than 5 kb[23] and by unstable expression in dividing cells over time[24].

1.2 CAR T cell therapy

CAR T cell therapy is a groundbreaking *ex vivo* gene therapy for the treatment of patients with relapsed or refractory (r/r) hematological malignancies, including different forms of multiple myeloma (MM), B cell acute lymphoblastic leukemia (B-ALL) and B cell lymphoma (BCL) [25–30]. CAR T cells are autologous T cells that are genetically modified, mostly using RVs and LVs, to express the CAR on their surface[31]. After the patient has received lymphodepleting chemotherapy to create an optimal environment for CAR T cells[32–34], the cells are infused back into the patient, where they recognize and eliminate tumor cells expressing the target antigen[35]. Currently, thirteen CAR-T cell therapies are approved worldwide and depending on the product, disease, and time point, an overall survival (OS) rate of 40-73% has been reported (Tab. 1). Among these, nine therapies target

cluster of differentiation (CD)19 for the treatment of BCL and B-ALL, and four target B-cell maturation antigen (BCMA) for MM (Tab. 1). Because both targets are not expressed by HSCs or non-HSCs but are highly expressed by B cell malignancies, they were selected as targets for CAR T cell therapy[36–39].

Table 1. Overview of approved CAR T cell therapies worldwide. B-ALL, B cell acute lymphoblastic leukemia; BCMA, B-cell maturation antigen; B-NHL, B cell non-Hodgkin lymphoma; CLL, chronic lymphocytic leukemia; CR, complete response; CD19, cluster of differentiation 19; FL, follicular lymphoma; LBCL, large B cell lymphoma; LV, lentiviral vector; MCL, mantle cell lymphoma; MM, multiple myeloma; OS, overall survival; r/r, relapsed/refractory; RV, γ-retroviral vector; SLL, small lymphocytic lymphoma. The data presented here were obtained from Yin *et al*. 2025[40] and the references listed in the table.

Commercial name / Generic name	Transgene integration method	CAR target	Indications	OS rate	Year first approved	First approval country
Kymriah®/ Tisagenlecleucel[27,35,41]	LV	CD19	Pediatric and young adults r/r B-Cell precursor ALL, r/r LBCL, r/r FL	55% for r/r B-cell ALL after 5 years[42,43]	2017	USA
Yescarta®/ axicabtagene ciloleucel[25,44,45]	RV	CD19	r/r LBCL, r/r FL	42.6% for r/r LBCL after 4 years[46]	2017	USA
Tecartus®/ brexucabtagene autoleucel[47]	RV	CD19	B-cell precursor ALL, MCL	40% for r/r B-cell ALL after 4 years[48]; 39 % for r/r MCL after 5 years[49]	2020	USA
Breyanzi®/ lisocabtagene maraleucel[50–52]	LV	CD19	LBCL, FL, r/r CLL, r/r SLL, r/r MCL	62.8% for r/r LBCL after 3 years[53]	2021	USA
Abecma™/ Idecabtagene vicleucel[29]	LV	BCMA	MM	73 % for r/r MM after 2 years[54]	2021	USA
Carteyva®/ relmacabtagene autoleucel[55–57]	LV	CD19	r/r LBCL, r/r FL, r/r MCL	66.7 % for r/r LBCL after 4 years[58]	2021	China
Carvykti/® Ciltacabtagene autoleucel[59,60]	LV	BCMA	MM	73 % for r/r MM after 2 years[54]	2022	USA
Fucaso®/ equecabtagene autoleucel[61]	LV	BCMA	r/r MM	-	2023	China
NexCAR19/ actalycabtagene autoleucel[62,63]	LV	CD19	r/r B-cell ALL, r/r B cell lymphoma	-	2023	India
Yuanruida/ inaticabtagene autoleucel[64]	LV	CD19	r/r B-cell ALL	-	2023	China
Zevor-cel/ zevorcabtagene autoleucel[65]	LV	BCMA	r/r MM	-	2024	China
Aucatzyl®/ obecabtagene autoleucel[66,67]	LV	CD19	r/r B-cell precursor ALL	-	2024	USA
Quartemi/ varnimcabtagene autoleucel[68,69]	LV	CD19	r/r B-NHL	-	2025	India, Spain

However, CAR T cell therapy is frequently associated with severe side effects, most notably cytokine release syndrome (CRS) and neurologic toxicities[70,71], as well as less common complications such as B-cell aplasia, tumor lysis syndrome, uncontrolled CAR T cell proliferation, and genotoxicity[72]. Due to these side effects, the Risk Evaluation and Mitigation Strategies (REMS) was applied for the Food and Drug Administration

(FDA)-approved CAR-T cell therapies[73], with the exception of Aucatzyl, which was approved in November 2024 (Tab. 1)[67]. REMS is a safety program for specific medications with serious safety concerns, designed to ensure that the benefits of therapy outweigh the risks[74]. It included certified hospitals and clinics that have on-site access to tocilizumab for the treatment of CRS[75,76], post-treatment monitoring, and driving restrictions[73,77], imposing a substantial financial and logistical burden and limiting access to CAR T cell therapies for many patients[78]. However, in June 2025, the FDA eliminated REMS for autologous CAR T cell therapies due to established treatment guidelines and extensive experience in diagnosing and managing CRS and neurological toxicities, which is expected to significantly improve accessibility to CAR T cell therapy in the future [73,75,79].

1.2.1 Mechanism of CAR T cells

A CAR is a recombinant receptor composed of three major components: (i) an extracellular antigen-binding domain derived from a single-chain variable fragment (scFv) of a monoclonal antibody, (ii) a transmembrane domain for surface anchoring, and (iii) an intracellular signaling domain containing an activation domain (CD3ζ), which initiates signal transduction after antigen binding[31]. CD3ζ is one of the CD3 chains that, together with two T cell receptor (TCR) chains, form the TCR complex[80,81]. The signaling domain also contains co-stimulatory domains (e.g. CD28 or 4-1BB) to amplify signal transduction[31], thereby promoting effector functions, proliferation and survival of CAR T cells[82–87].

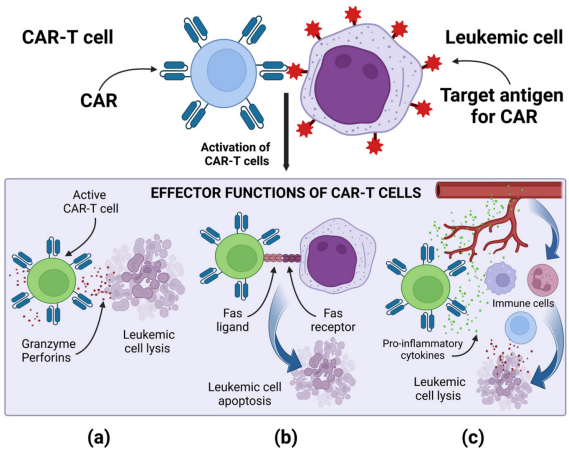

Figure 2. Effector functions of CAR T cells. Upon activation of CAR T cells by binding to leukemic cells three effector functions are induced: (**a**) Secretion of perforins and granzymes leading to leukemic cell lysis. (**b**) Fas ligand expressed by CAR T cells binds to the Fas receptor on leukemic cells leading to cell death. (**c**) Secretion of pro-inflammatory cytokines that recruit other immune cells. Reprinted from Zarychta *et al.* 2023[88], CC BY 4.0, (https://creativecommons.org/licenses/by/4.0/).

In contrast to physiological major histocompatibility complex (MHC)-restricted TCRs, CARs recognize unprocessed, native cell-surface antigens independently of MHC presentation[31], with much higher binding affinity (100-1000×), and can therefore recognize a broader range of targets[87]. Unlike the highly organized TCR immune synapse, the CAR-mediated synapse is disorganized[87] and forms more rapidly, allowing faster recruitment of

lytic granules containing granzyme and perforin (Fig. 2)[89–91]. These findings may explain the superior cytotoxic activity of CAR T cells[92,93]. In addition, full effector function of CAR T cells involves death receptor pathways, such as Fas-Fas ligand (FasL) interactions, in which FasL expressed by CAR T cells binds to Fas on tumor cells, inducing apoptosis[94] and secretion of pro-inflammatory cytokines, thereby enhancing the anti-tumor activity of other immune cells (Fig. 2)[95].

1.2.2 Manufacturing process

The manufacturing process of CAR T cells starts with patient leukapheresis, followed by isolation of CD4+ helper and CD8+ cytotoxic T cells using magnetic or density-based beads (Fig. 3). T cells are then activated using anti-CD3/CD28-coated beads or soluble anti-CD3/CD28 antibodies that mimic antigen-presenting cell (APC) co-stimulation[96–99]. In the next step, cells are transduced with LVs or RVs to express the CAR on their surface[96], whereby LVs are more commonly used, as reflected by the approved CAR T cell products (Tab. 1). Subsequently, CAR T cells are expanded until they reach the desired cell number, followed by formulation and cryopreservation[96]. The manufacturing process from leukapheresis to cryopreservation takes approximately 14 days[100] followed by quality control (7-15 days) and transfer of the final product to the clinical site (Fig. 3)[96].

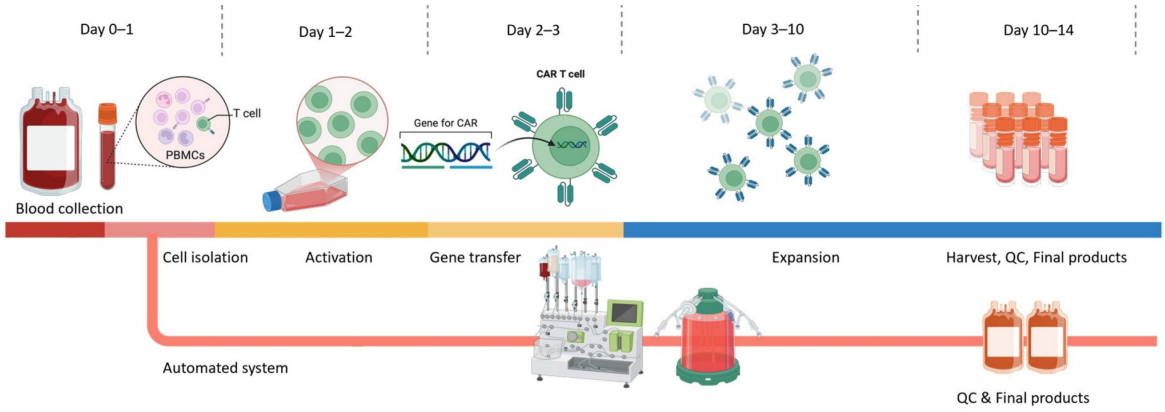

Figure 3. CAR T cell manufacturing process. The harvesting of material, T-cell isolation, activation, gene transfer by transduction and expansion, formulation and cryopreservation take ~ 14 days, followed by quality control. GMP-compliant, automated closed systems integrate the steps from cell isolation to expansion, improving standardization, reducing user-dependent variability, and enabling decentralized manufacturing. The final product is transferred to the clinical site. Adapted and reprinted from Qian *et al*. 2025[100], CC BY 4.0, (https://creativecommons.org/licenses/by/4.0/).

For example, the recommended dose of the recently FDA-approved CAR T cell therapy Aucatzyl is 410 × 10^6 CD19 CAR-positive viable cells, supplied in three to five infusion bags. In addition to CAR T cells, Aucatzyl may also contain non-transduced T cells and non-T cell populations as by-products. It is formulated in phosphate buffered saline (PBS)

containing 7.5 % dimethyl sulfoxide (DMSO), human serum albumin (HSA), and ethylenediaminetetraacetic acid (EDTA)[101].

1.2.3 Challenges and solutions

The current FDA-approved CAR T cell manufacturing protocols have an average vein-to-vein time of 3-6 weeks. During this period, the disease may progress to such an extent that treatment with CAR T cells is no longer possible, or, in the worst case, patients may die before therapy can be administered[96]. Manufacturing failures are frequent due to poor T cell quality, low yields and expansion, often linked to insufficient leukapheresis[102], and prolonged *ex vivo* cultivation impacts T cell phenotype and function[103]. In addition, autologous CAR T cell therapies are associated with very high costs, with list prices ranging from $424,000-543,828[104], and total treatment costs exceeding $500,000 in some cases, depending on the severity of therapy-related adverse effects[105]. These high costs are primarily attributable to the complexity of the multistep manufacturing process and the patient-specific nature of production and treatment, which together lead to high research and development costs. Consequently, these costs drastically limit patient access to CAR T cell therapy[104].

To address these challenges, CAR natural killer (NK) cell therapies are being developed as off-the-shelf therapies, whereby a single CAR NK cell product can be manufactured for multiple patients, thereby substantially reducing therapy costs and shortening time from diagnosis to treatment[106]. NK cells can be derived from multiple sources including induced pluripotent stem cells (iPSCs), umbilical cord blood (UCB) and NK cell lines and have a lower risk of graft-versus-host disease (GvHD) due to the absence of a T cell receptor[106]. In addition to CAR-mediated activity, CAR NK cells can use their natural cytotoxic functions, including antibody-dependent cellular cytotoxicity (ADCC) and recognition of cancer cells with downregulated MHC class I expression, leading to the secretion of granzyme B and perforin[107]. Because these pathways have a higher activation threshold and a more controlled cytokine release that CAR T cell therapy, CAR NK cell therapies are generally associated with fewer side effects[106]. A first phase 1/2 trial of allogeneic cord blood-derived NK cells expressing a CAR targeting CD19 and interleukin (IL)-15 reported a 1-year overall survival of 68%, with no observed toxicities such as CRS, neurotoxicity, or GvHD[108]. However, several challenges remain, including insufficient clinical efficacy attributable to the immunosuppressive milieu of the tumor microenvironment[109], the shorter

lifespan and reduced expansion capacity of NK cells compared with T cells[110], and tumor antigen escape[106].

Additional cost-reduction strategies include the decentralizing of CAR T cell manufacturing using fully good manufacturing practice (GMP)-compliant, automated closed systems such as Miltenyi CliniMACS Prodigy®[111,112]. These systems integrate steps from cell isolation to expansion, improving standardization, reducing user-dependent variability, and enabling decentralized manufacturing (Fig. 3)[100]. The Miltenyi CliniMACS Prodigy® has enabled local production with a vein-to-vein time of 9 days and manufacturing costs of only $35,107 (excluding LV costs), as demonstrated in India[111], thereby facilitating access for patients in developing countries[112]. Despite these advances, viral vectors remain the highest material production cost, with a viral batch for a single patient costing more than $16,000[113,114], underscoring the need to optimize retroviral transduction to improve efficiency and reduce vector usage.

1.2.4 Lentiviral and γ-retroviral vectors in CAR T cell therapy

As shown in Table 1, all 13 CAR T cell therapies approved worldwide use RVs or LVs for the CAR gene delivery. Both Yescarta and Tecartus use a non-self-inactivating MSCV-derived RV pseudotyped with the gibbon ape leukemia virus (GALV) glycoprotein, whereas the other FDA-approved products use HIV-1-based, replication-incompetent LVs pseudotyped with the vesicular stomatitis virus glycoprotein (VSV-G)[40]. For products approved in India and China, it is currently only reported that a lentiviral vector was used[40,115].

For the generation of LVs and RVs, non-essential viral components have been removed, and the remaining components have been separated onto three plasmids (transfer, packaging and envelope plasmids) to exclude the risk of producing replication-competent retroviruses (Fig. 4A)[116]. The transfer plasmid carries the transgene flanked by long terminal repeats (LTRs), which are required for genomic integration and contain promoter and enhancer regions[116]. To create self-inactivating (SIN) vectors, the transfer plasmid contains a deletion in the 3'LTR, that is copied to the 5'LTR during reverse transcription[117–119]. After integration into the host genome, transcription of the full-length virus is no longer possible[117,118]. In addition, only the transfer plasmid contains the RNA packaging signal ψ, which is responsible for packaging of the viral RNA (transgene flanked by LTRs) into the viral particle (Fig. 4A)[120].

The packaging plasmid encodes *gag* (matrix, capsid and nucleocapsid) and *pol* (reverse transcriptase, integrase, protease)[121]. Lentiviral accessory genes like *rev* , which mediates transport of viral mRNA from nucleus to cytoplasm[122], are often provided on a separate regulatory plasmid (Fig. 4A)[123]. The envelope plasmid contains *env*[123], with VSV-G being one of the most commonly used envelope protein due to its broad tropism[124]. However, VSV-G pseudotyped LVs do not efficiently transduce quiescent T cells, B cells, and HSCs due to low expression levels of the low-density lipoprotein receptor (LDL-R), the cellular receptor for VSV-G[124,125]. In contrast, GALV is often used for pseudotyping of RVs due to its efficient transduction of human hematopoietic cells[126,127]. GALV-RVs enter cells via the sodium-dependent phosphate transporter (PiT1, PiT2)[128–131].

The simplest method, and still the industry standard, for producing LVs and RVs is transient transfection of HEK293T cells using the above-mentioned plasmids (Fig. 4B)[132–134]. However, this approach is expensive and exhibits batch-to-batch variability in quality. Therefore, packaging cell lines such as PG13 were generated by stable integration of *gag*, *pol, env,* and *rev* (for LVs only), followed by transfection with the transfer plasmid (Fig. 4B)[40,135]. These cells can be further optimized to producer cell lines by stable integration of the transfer gene[134,136]. Both packaging and producer cell lines enable more cost-efficient and reproducible vector manufacturing[40,134].

However, the generation of these cell lines is complex and time-consuming[40]. In each case, the generated viral particles only contain the transgene cassette flanked by LTRs, making them replication-incompetent[137]. After harvesting and optional purification, retroviral particles can be used to transduce T cells, for example, to generate CAR T cells[40]. Upon transduction, the viral envelope protein binds to a specific target receptor on the cell membrane, leading to fusion of the viral particle with the cell (Fig. 4C)[138]. Depending on the virus, fusion can occur at the cell surface (pH-independent virus)[139,140] or after receptor-mediated endocytosis at the endosomal membrane (pH-dependent virus)[141,142]. This results in the release of two copies of positive-sense single stranded RNA, which are reverse-transcribed into DNA before being integrated into the host genome[138]. The integrated DNA encoding the CAR gene then undergoes transcription and translation, leading to the expression of the CAR protein on the cell surface (Fig. 4C)[143].

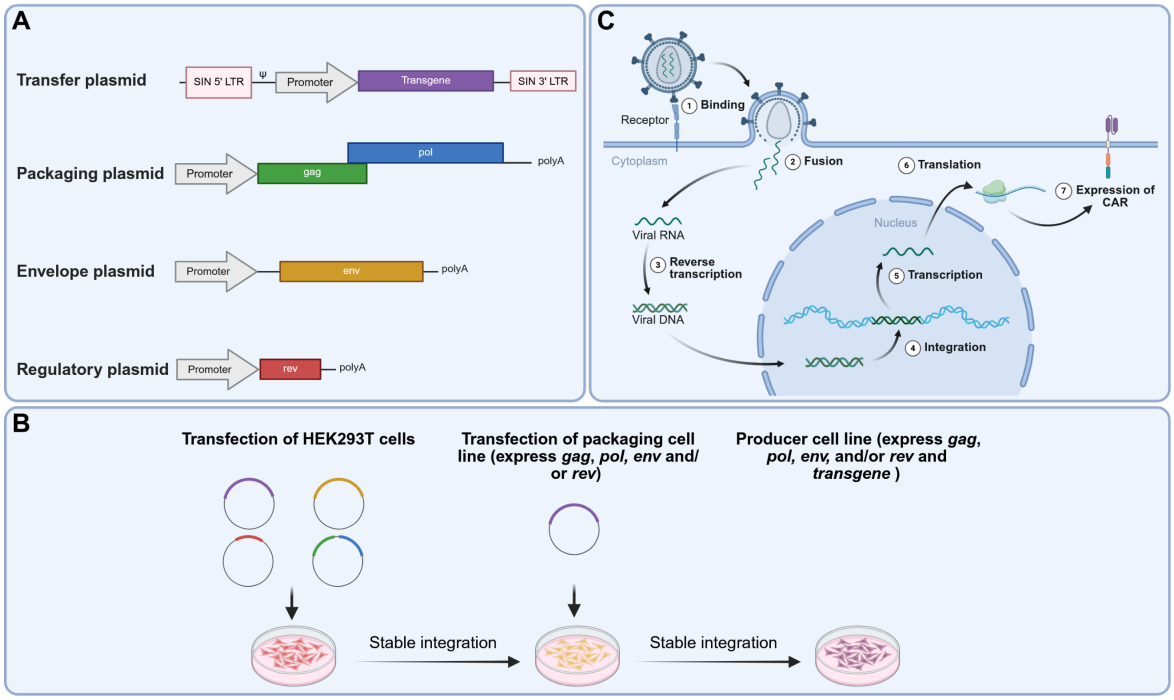

Figure 4. Production and transduction principle of lentiviral and γ-retroviral vectors. (**A**) Third-generation lentiviral plasmids. The transfer plasmid contains the transgene flanked by modified long terminal repeats (LTRs) and the packaging signal ψ. The packaging plasmid contains *gag* and *pol*. The envelope plasmid contains *env* and the regulatory plasmid contains *rev*. Adapted from BioRender template "Third-Generation Lentiviral Vector System". (**B**) Lentiviral (LVs) and γ-retroviral vectors (RVs) are produced by transient transfection of HEK293T cells. By stable integration of *gag*, *pol,* and *env* packaging cell lines are generated that only need transfection with the transfer plasmid. By stable integration of the transgene in the packaging cell lines, producer cell lines are generated. The manufactured LVs and RVs contain the transgene cassette, which renders them replication-incompetent (**C**) Scheme of LV/RV transduction process for the generation of CAR T cells**.** (**1**) The viral particle carrying the CAR gene binds to its target receptor via the envelope protein, leading to fusion of the viral and cellular membranes (**2**). (**3**) Reverse transcription converts viral RNA into DNA, which is then integrated into the host cell genome (**4**). (**5-7**) The integrated CAR gene is transcribed and translated, resulting in the expression of the CAR protein on the plasma membrane. Adapted from BioRender template "Retrovirus Life Cycle". Created in BioRender. Rauch, L. (2026) https://BioRender.com/iwu129g.

1.3 Optimization of retroviral transduction

In addition to the high vector costs, low transduction efficiencies resulting from low titers and limited binding rates of viral particles to target cells remain major challenges[144]. For successful transduction, viral particles must passively diffuse to the cell surface while overcoming the electrostatic repulsion between the negatively charged viral and cellular membranes[144]. Prior to receptor-binding via the envelope protein, viral particles bind nonspecifically to attachment factors like heparan sulfate proteoglycans (HSPGs)[145,146] and subsequently diffuse along the membrane to find their specific receptor[147]. To improve viral adsorption, various transduction enhancers have been developed[144].

Cationic polymers like polybrene and diethylaminoethyl (DEAE)-dextran enhance transduction by wrapping around viral particles, thereby neutralizing surface charge and promoting viral aggregation[144,148–150]. However, polybrene negatively affects cell

proliferation and shows cytotoxicity[151,152]. More biocompatible alternatives include polypeptides such as protamine sulfate and RetroNectin®[144]. Protamine sulfate, composed of cationic peptides derived from salmon or other fish sperm, shows lower cytotoxicity while achieving transduction enhancement comparable to polybrene[153,154]. A less toxic and more efficient transduction enhancer is RetroNectin[155]. This recombinant fibronectin fragment mediates interactions with viral particles via its heparin-binding domain and binds integrin receptors on the plasma membrane[156]. It efficiently enhances γ-retroviral and lentiviral transduction rates and has been widely used to generate CAR T cells[155,157–159]. Additionally, by mimicking fibronectin, it can promote T cell activation through engagement of VLA-4/VL-5 integrins as a costimulatory signal with anti-CD3, thereby stimulating proliferation of T cells[160–162]. However, RetroNectin has been reported to reduce expansion, cytokine production, viability and transduction efficiency of CAR T cells derived from CLL patient, potentially due to B-cell activation that interferes with manufacturing. Consequently, its use may be limited in patients with high tumor burden[163]. Furthermore, its application requires pre-coating of cell culture vessels, washing steps and often spinoculation/spinfection (centrifugation during transduction)[155,156,164], making the process time-consuming and costly[144]. In addition, RetroNectin is recombinantly expressed in *Escherichia coli* (*E.coli*)[165], which is a more expensive production method compared to peptide synthesis[166].

1.3.1 Peptide nanofibrils as transduction enhancer

In recent years, peptides that self-assemble into peptide nanofibrils (PNFs) have been identified as efficient transduction enhancers[167–171]. The first peptides reported to exhibit infection-enhancing activity were derived from the semen enzyme prostatic acid phosphatase (PAP)[167]. The most prominent peptide, PAP248-286, forms β-sheet PNFs termed semen-derived enhancer of viral infection (SEVI), which enhances HIV-1 infection as well as lentiviral and γ-retroviral gene transfer[167,172]. Structurally, SEVI fibrils resemble amyloid fibrils[167].

Subsequently, the 12-mer peptide enhancing factor-C (EF-C; QCKIKQIINMWQ), derived from the HIV-1 glycoprotein gp120, commercialized as Protransduzin™[173], was identified[168]. At physiological pH, EF-C assembles into positively charged β-sheet PNFs with a length of approximately 100–400 nm and a diameter of 3.4 ± 1.1 nm. EF-C PNFs enhance lentiviral and γ-retroviral transduction rates more efficiently than SEVI, DEAE-dextran, polybrene, and protamine sulfate while exhibiting lower cytotoxicity[168]. It

achieves transduction rates comparable to RetroNectin[168,173], but does not require time-consuming coating, washing, and spinoculation steps[168]. Moreover, EF-C PNFs do not induce inflammatory responses of monocyte-derived macrophages and plasmacytoid dendritic cells[174], nor do they impair HSC differentiation capacity[168]. EF-C PNFs have enabled successful transduction of murine bone marrow cells followed by effective transplantation into recipient mice, supporting their safety for *ex vivo* gene therapy applications[168]. However, EF-C PNFs exhibit chemical instability over time due to cyclization of the N-terminal glutamine to pyroglutamate[175] leading to large aggregate formation (Rauch-Wirth L., unpublished findings). This is a significant limitation, as chemical stability is a prerequisite for their implementation in GMP-compliant manufacturing processes for *ex vivo* gene therapy[176,177].

Another commercially available transduction enhancer is the amphiphilic, cationic 26-mer peptide Vectofusin®-1 (KKALLHAALAHLLALAHHLLALLKKA-NH_2). It belongs to the LAH4 peptide family, which promotes DNA delivery into mammalian cells[178,179]. In contrast to EF-C, it forms α-helical PNFs. These positively charged PNFs interact with negatively charged viral particles, promoting viral adhesion and fusion with the cellular membrane[180,181]. In addition to RetroNectin, Vectofusin-1 has been used to enhance retroviral gene transfer into HSCs and for the generation of CAR T cells and CAR NK cells[158,182–184]. Unlike RetroNectin, it can be applied directly by incubating with the viral vector for 5-30 min prior to adding it to the target cells, eliminating the need for vessel pre-coating. Higher transduction efficiencies can be achieved by applying spinoculation (1-2 h), and a washing step 6–24 h post-transduction is recommended[185]. Owing to its straightforward protocol, Vectofusin-1 has been integrated into the Miltenyi CliniMACS Prodigy® platform for the GMP-compliant CAR T cell production[158]. However, Vectofusin-1 does not promote gene transfer of VSV-G LVs in T cells[158,183,186], the most commonly used viral vector in CAR T cell therapy[40], likely due to the inhibition of endocytosis[186]. Furthermore, EF-C PNFs demonstrated superior transduction-enhancing activity for CAR T cell generation compared to Vectofusin-1[173].

1.3.2 Mechanism of transduction enhancing activity of β-sheet PNFs

From a biophysical perspective, several studies have demonstrated that peptides self-assembling into transduction-enhancing PNFs are typically cationic, amphiphilic, and possess a high isoelectric point (pI). Their positive surface charge enables them to capture negatively charged viral particles, thereby helping to overcome the electrostatic repulsion

between the viral and cellular membranes (Fig. 5)[168–171,187–189]. In addition, EF-C PNF/virus complexes were observed to be actively engaged by cellular protrusions such as filopodia, microvilli, and lamellipodia, which transport them to the cell surface, leading to increased viral adhesion and transduction efficiency[190]. In addition, a comprehensive data mining analysis of a peptide library derived from systematic substitutions, point mutations, and sequence scrambling of EF-C revealed that the formation of PNFs into µm-sized, β-sheet-rich aggregates with hydrophobic and positively charged surfaces (Fig. 5) is a key property for their transduction-enhancing effect[189].

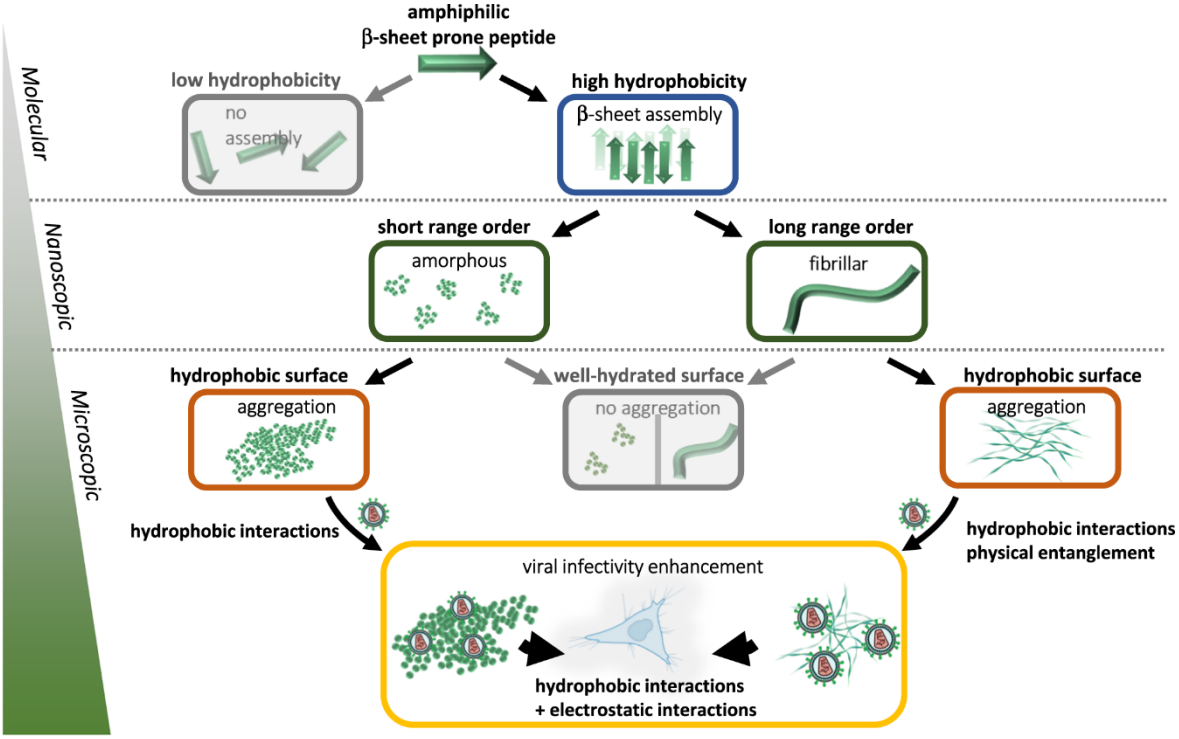

Figure 5. Proposed mode of action of PNFs as transduction enhancer from the molecular to microscopic level. Molecular: Cationic, amphiphilic peptides form β-sheet rich structures with high hydrophobicity. Nanoscopic: The degree of hydrophobicity determines the assembly in amorphous aggregates (short-range) or fibrils (long-range). Microscopic: Assembly in µm-size aggregates promotes interaction with viral particles and cell membranes via hydrophobic and electrostatic interactions. Reprinted from Kaygisiz *et al.* 2023[189], CC BY 4.0, (https://creativecommons.org/licenses/by/4.0/).

Notably, cationic amphiphilic peptides forming PNFs that assemble into many small aggregates show a better transduction-enhancing activity than those forming fewer and larger aggregates[189]. Importantly, previous studies have shown that SEVI does not enhance the infectivity of non-enveloped viruses such as AdV5 or enveloped viruses with high glycoprotein density, such as Zika virus[191]. Experiments using virions with varying envelope glycoprotein densities indicate that membrane accessibility is a key determinant of transduction enhancing activity, as a dense glycoprotein coat shields the viral lipid

membrane from interaction with PNFs[191]. Furthermore, several studies have reported that negatively charged PNFs can bind viral particles but fail to enhance infectivity or mediate cell binding[169,192]. It is predicted that PNF interaction with virions and cells is mediated by distinct mechanisms, likely arising from differences in lipid and protein composition as well as surface charge between viral and cellular membranes. These factors may differentially modulate interactions with positively charged or hydrophobic domains on the fibrillar surface[175,192].

1.4 Scientific aim

Peptide nanofibrils are a powerful tool for optimizing retroviral gene transfer in *ex vivo* gene therapy applications. It is well established that the transduction-enhancing activity of PNFs is driven by their assembly into positively charged aggregates, which capture viral particles and facilitate their transport to the cell surface via cellular protrusions. However, their safe implementation as transduction enhancers in clinical settings requires a comprehensive understanding of their underlying mechanisms, including cellular uptake and degradation pathways.

Accordingly, the first aim was to analyze the detailed interactions of EF-C PNFs with viral particles, as well as their uptake and degradation mechanisms. However, EF-C is chemically unstable over time, leading to the formation of large aggregates in cell culture. These aggregates may pose safety risks, such as immune reactions or vascular occlusions, if residual material is administered to patients. Furthermore, chemical stability is a requirement for integration into GMP-compliant processes.

Therefore, the second aim was to identify novel endogenous, non-immunogenic peptides that self-assemble into PNFs and efficiently enhance retroviral transduction rates without forming large aggregates.

Finally, we performed a comparative analysis of the newly identified transduction enhancer D4 and the clinically relevant Vectofusin-1 to investigate how their structural and morphological properties influence interactions with viral particles and the cell membrane, in order to elucidate the mechanisms underlying their transduction-enhancing effects.

2 Results and Discussion

2.1 Transduction enhancing EF-C peptide nanofibrils are endocytosed by macropinocytosis and subsequently degraded

This chapter describes data shown in Appendix 1 (Rauch-Wirth & Schütz *et al*. 2025[1]).

In a previous study, it was shown that EF-C PNFs enhance transduction by overcoming the electrostatic repulsion between viral and cellular membranes[168], which we confirmed by zeta potential measurements revealing a significant reduction of the negative surface charge of fluorescent MLV Gag-YFP derived virus-like particles (VLPs) upon EF-C PNF incubation. Furthermore, it is known that cellular protrusions capture EF-C PNFs and transport them toward the cell body, leading to increased virion attachment and transduction efficiency[190]. Additionally, it was observed that the interaction between PNFs and protrusions induced plasma membrane invaginations[190].

To elucidate the role of these invaginations, we analyzed the interaction of EF-C and HIV-1 virions with HeLa cells using transmission electron microscopy (TEM) and scanning electron microscopy (SEM). We observed that the induced plasma membrane invaginations increased the accessible surface area for HIV-1 virion attachment. In addition, these invaginations reduced the distance between plasma membrane and the nucleus, which was further confirmed by scanning transmission electron microscopy (STEM) tomography. Therefore, we propose that the reduced distance shortens the transport path of the viral capsid to the nucleus, thereby increasing the likelihood of successful transduction.

As the plasma membrane invaginations indicate the beginning of endocytosis[193], we next analyzed whether fluorescently labeled EF-C PNFs[194] are taken up by cells using flow cytometry and fluorescence microscopy analysis. Our experiments showed cell type-specific uptake kinetics: TZM-bl cells, being larger (~ 16 µm diameter[195,196]), showed a higher capacity for PNF internalization, whereas CD4+ T cells (5–10 µm diameter[197]) internalized EF-C PNFs more rapidly. Fluorescence microscopy showed that EF-C PNFs were taken up into large endosomal vesicles with diameters up to 5 µm, which, according to their size, are macropinosomes (diameter 0.2–5 µm)[198], indicating uptake by macropinocytosis. This was confirmed by pharmacological inhibition of different endocytosis pathways. These results are consistent with previous reports showing that amyloid fibrils, such as those formed by tau and α-synuclein, are taken up via macropinocytosis [199,200].

In addition, inhibition of endocytosis had no effect on HIV-1 infection, indicating that EF-C-mediated enhancement is independent of its uptake and consistent with the fact that HIV-1 enters cells mainly via fusion of viral and cellular membranes[201].

Next, EF-C PNF degradation was investigated using Förster resonance energy transfer (FRET) pair-labeled EF-C peptides. Correlative light and electron microscopy (CLEM) analysis revealed that assembled PNFs localized in macropinocytotic cups at the plasma membrane and within macropinosomes, while partially degraded forms accumulated in lysosomes, and fully disassembled PNFs were found in vesicles displaying features of lysosomes and multivesicular bodies (MVBs), suggesting fusion between these compartments. We therefore propose that PNFs progress from macropinosomes that either directly fuse with lysosomes or mature into MVBs that direct their cargo toward degradation[202].

Lysosomal degradation was further confirmed by colocalization of EF-C PNFs with lysosomes. In addition, inhibition of lysosomal activity with leupeptin, a lysosomal peptidase inhibitor[203], significantly reduced EF-C PNF disassembly. This indicates that EF-C PNFs are degraded by lysosomal enzymes and are not stored as amyloid deposits supporting their safe use as transduction enhancers for clinical applications. However, to ensure the absence of EF-C PNFs in the final product of *ex vivo* applications, such as CAR T cell therapy, degradation must be assessed over longer time points.

In summary, our study revealed that, in addition to overcoming electrostatic repulsions between negatively charged viral and cellular membranes[168,169] and being actively captured by cellular protrusions[190], EF-C PNFs enhance transduction by inducing plasma membrane invaginations. These invaginations increase the surface area for viral attachment and reduce the distance between the plasma membrane and the nucleus. Furthermore, EF-C PNFs are internalized via macropinocytosis, followed by lysosomal degradation (Fig. 6)[1].

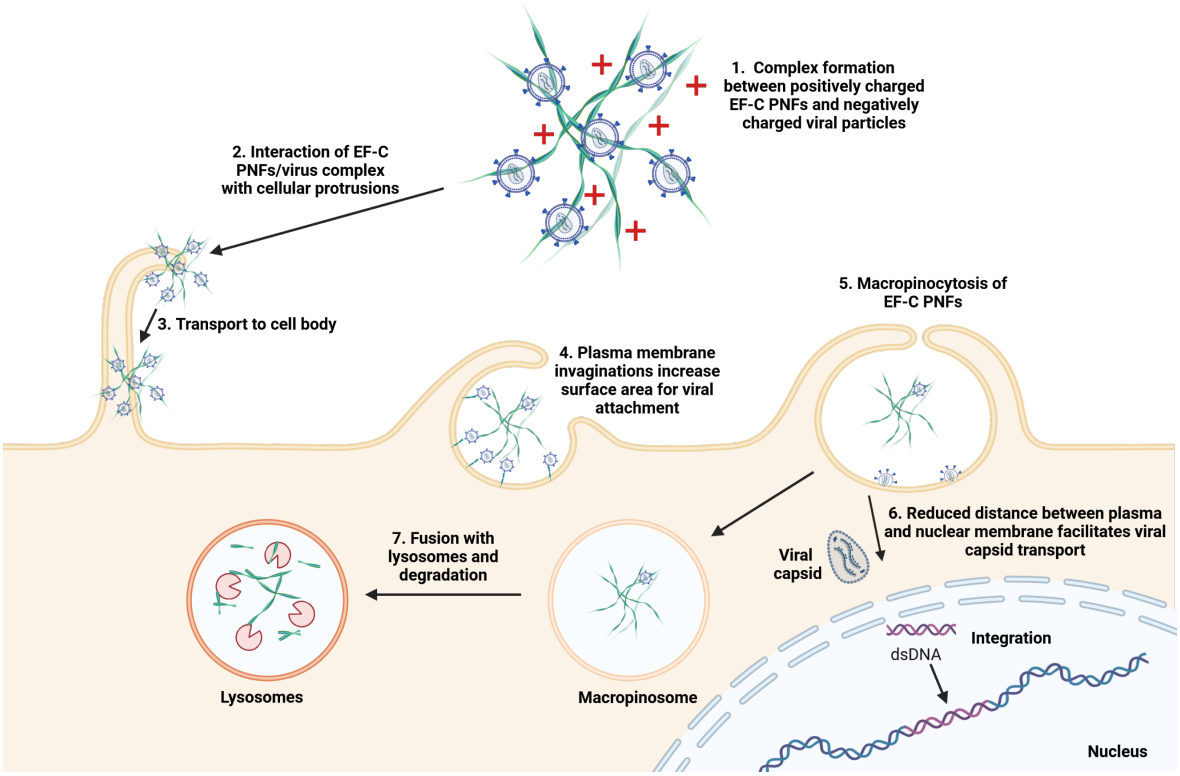

Figure 6. Transduction enhancing mechanism, uptake and degradation of EF-C PNFs. (**1**) Positively charged EF-C PNFs capture negatively charged viral particles. EF-C PNF/virus complex interacts with cellular protrusions (**2**), which transport the complex to the cell body (**3**). (**4**) EF-C PNFs induce plasma membrane invaginations that increase surface area for viral attachment. (**5**) EF-C PNFs are taken up via macropinocytosis. (**6**) Induced invaginations reduce travel distance for the viral capsid to the nucleus. (**7**) Fusion of EF-C PNF-containing macropinosome with lysosome. Created in BioRender. Rauch, L. (2025) https://BioRender.com/d35c025. Reprinted from Rauch-Wirth & Schütz *et al*. 2025[1], CC BY 4.0, (https://creativecommons.org/licenses/by/4.0/).

2.2 Optimized peptide nanofibrils as efficient transduction enhancers for *in vitro* and *ex vivo* gene transfer

This chapter describes data shown in Appendix 2 (Rauch-Wirth *et al*. 2023[2]).

EF-C efficiently enhance retroviral gene transfer, but its application in CAR T cell generation is limited by its chemical instability leading to large aggregates in cell culture and possible immunogenicity due to its derivation from HIV-1 gp120[168,175].

Therefore, we used an *in silico* screening approach to identify novel endogenous, non-immunogenic peptides assembling into positively charged PNFs that enhance retroviral transduction rates[2]. This approach identified a PNF-forming region in human IL-18, leading to the design of five cationic peptides. Among them, the shortest peptide RM-8 (RRIFIISM) formed chemically stable β-sheet PNFs with a positive surface charge that efficiently enhanced lentiviral and γ-retroviral transduction rates without showing toxicity. However, very large µm-sized aggregates were formed by RM-8 PNFs in cell culture. Although these

aggregates are necessary for the transduction-enhancing effect[189], some reached diameters exceeding 100 µm, potentially limiting cellular degradation and posing safety concerns, such as immune reactions[204] or vascular occlusions[205,206], if reintroduced into patients during CAR T cell therapy.

To address these limitations, RM-8 was optimized for aggregation properties and transduction enhancement using a structure-activity relationship (SAR) study, resulting in derivative D4 (RRIFIISM). D4 rapidly assembled into β-sheet-rich PNFs that remained chemically stable over time. Importantly, nanoparticle tracking analysis (NTA) and microscopic examination revealed that D4 formed significantly smaller aggregates compared to RM-8. We hypothesize that the increased positive net charge of D4, resulting from threonine-to-arginine substitution, limits the formation of large aggregates, likely through enhanced electrostatic repulsions[207].

Next, D4 was evaluated in a T cell transduction process based on CAR T cell protocol[208] using clinically relevant viral vectors. It significantly enhanced GALV-RV transduction in activated T cells without affecting viability (Fig. 7A, B) and was the only enhancer, alongside RetroNectin, to significantly improve transduction efficiency of VSV-G-LV mediated gene transfer, while no enhancing effect was seen for Vectofusin-1 (Fig. 7C, D).

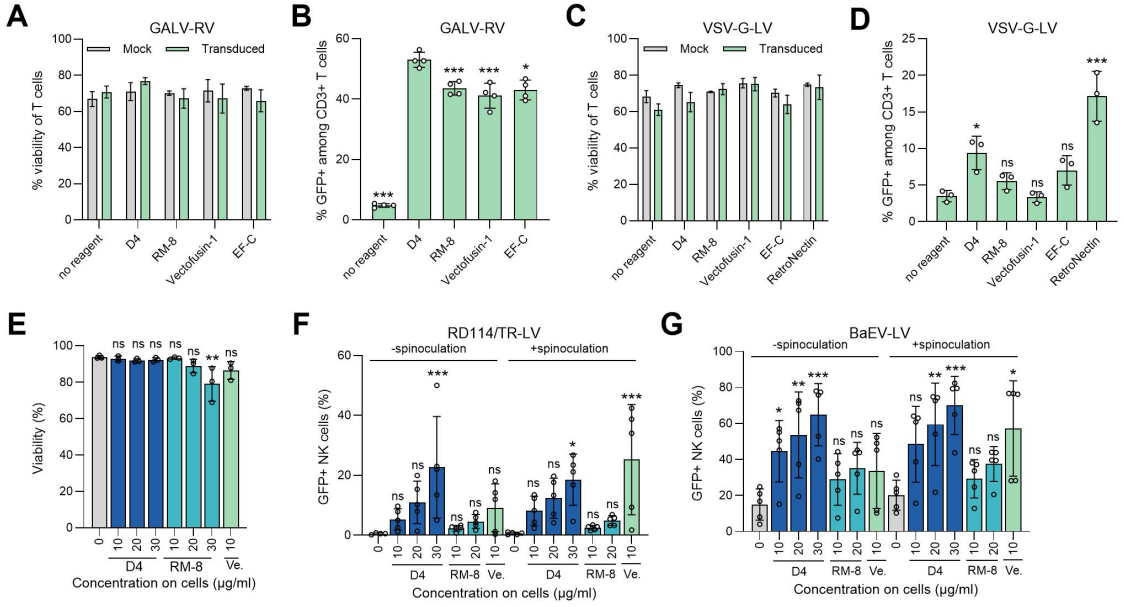

Figure 7. D4 as an efficient transduction enhancer for retroviral gene transfer in human T and NK cells. Viability (**A, C**) and transduction efficiency (**B, D**) of CD4+/CD8+ T cells 7 days after transduction with GALV-RV (A, B) or VSV-G-LV (C, D) using different transduction enhancers. Data are represented as mean values ± SD of four (GALV-RV) or three (VSV-G-LV) donors. (**E**) Viability of NK cells after treatment with different PNFs for 4 days. The transduction efficiency of NK cells was measured 4 days after they were transduced with RD114/TR-LV (**F**) or LV-BaEV-LV (**G**), both with and without spinoculation. Data are represented as mean values ± SD of three (E) or five (F, G) donors. For A and C, a two-way ANOVA with Šidák's multiple comparison test was performed, showing no significant differences between samples. For B and D–G a one-way ANOVA with Dunnett's multiple comparison test was performed. *p ≤ 0.05, **p ≤ 0.01,

***p ≤ 0.001. GALV, glycoprotein of gibbon ape leukemia virus; RD114/TR, chimeric envelope glycoprotein derived from feline leukemia virus with the cytoplasmic tail derived from the murine leukemia virus glycoprotein; LV, lentiviral vector; RV, γ-retroviral vector; Ve., Vectofusin-1; VSV-G, glycoprotein of vesicular stomatitis virus. Adapted and reprinted from Rauch-Wirth *et al*. 2023[2], CC BY 4.0, (https://creativecommons.org/licenses/by/4.0/).

This aligns with previous studies showing that Vectofusin-1 does not enhance VSV-G-LV delivery into T and B cells[158,183]. This differential enhancing effect may reflect distinct viral entry mechanisms. γ-retroviral vectors such as GALV-RVs mediate pH-independent fusion at the plasma membrane[209,210] whereas VSV-G-LVs enter cells via clathrin-mediated endocytosis followed by pH-dependent endosomal fusion[211]. Accordingly, it is suspected that Vectofusin-1 may reduce endocytic uptake of surface-bound vector particles[186].

As CAR NK cell therapy is being developed as an alternative to CAR T cell therapy[106], we evaluated D4 PNFs as a transduction enhancer for retroviral gene delivery in NK cells. D4 outperformed RM-8 and Vectofusin-1, enhancing the transduction of LVs pseudotyped with either chimeric envelope glycoprotein derived from feline leukemia virus with the cytoplasmic tail derived from the murine leukemia virus glycoprotein (RD114/TR) or the baboon endogenous virus glycoprotein (BaEV), two envelopes commonly used for NK cell gene delivery[184,212], while no cytotoxic effect was seen for D4 and Vectofusin-1 (Fig. 7E-G).

Unlike Vectofusin-1, which required spinoculation for efficient transduction, D4 was effective without this step, enabling a simplified protocol (Fig. 7F, G). Although spinoculation is widely used to enhance lentiviral and γ-retroviral transduction of T and NK cells [155,164,213–215], it can increase cellular stress, add process complexity, and limit scalability[216,217]. Moreover, several studies have demonstrated that T cell activation and transduction can be performed simultaneously without spinoculation, reducing cultivation time and potentially maintaining naive/stem memory T cells[218,219]. This population exhibits superior *in vivo* expansion, enhanced antitumor activity, and a lower risk of CRS compared to more differentiated CAR T cells[220].

Furthermore, we propose that the formation of smaller aggregates by D4 increases available surface area, thereby enhancing interactions with viral particles and cellular protrusions and may explain the superior transduction performance of D4 compared to RM-8 and Vectofusin-1. This aligns with our previous observation that smaller µm-sized aggregates correlate with improved transduction efficiency[189].

Aggregation and chemical modifications of proteins- or peptide-based therapeutics are frequently associated with immunogenicity[221–223]. For the potential use of D4 PNFs as a

transduction enhancer in gene therapy, no recognition by the innate immune system is essential to avoid inflammatory responses. D4, RM-8, EF-C, and Vectofusin-1 did not activate the nuclear factor- κB (NF-κB) and interferon regulatory factor (IRF) pathways, both important for the innate immune response[224], in the THP1-Dual monocyte cell line, nor did they induce an inflammatory response in CD4+ T cells, unlike the positive control lipopolysaccharide (LPS), which induced an inflammatory response in both cell types consistent with literature[225,226]. Importantly, T cell activation primarily depends on TCR stimulation by APCs[227], highlighting the need for further assays to assess T cell activation by D4 PNFs. Although our results indicate that D4 PNFs are non-immunogenic, further studies are necessary to determine whether they are fully degraded during a CAR T/NK cell manufacturing process, ensuring that no residual PNFs remain in the final therapeutic product.

Taken together, the patented D4 (EP4314030, status: examination is in progress)[228] is a potent and cost-effective transduction enhancer, outperforming Vectofusin-1 in lentiviral and γ-retroviral gene delivery into T and NK cells[2]. Its small size and ease of use, without requiring spinoculation, make it well-suited for automated, GMP-compliant manufacturing processes for the generation of CAR T/NK cells.

2.3 Structural morphology of peptide nanofibrils dictates viral capture and cellular uptake in gene therapy applications

This chapter describes data shown in Appendix 3 (Rauch-Wirth & La Roche *et al*. 2026[3]).

Recently, PNFs have emerged as promising tools for optimizing retroviral gene delivery in *ex vivo* gene therapy applications[2,168–171,181,182,189]. However, the impact of their structural morphology on viral binding and cellular interactions remains poorly understood. Here, we systematically compared the two clinically relevant PNFs, D4 and Vectofusin-1, using a combination of secondary structure analysis, molecular dynamics (MD) simulations, and electron- and fluorescence microscopy techniques to gain a deeper understanding of how their fibrillar architecture and aggregation behavior influence interactions with viral particles and host cells (Fig. 8)[3].

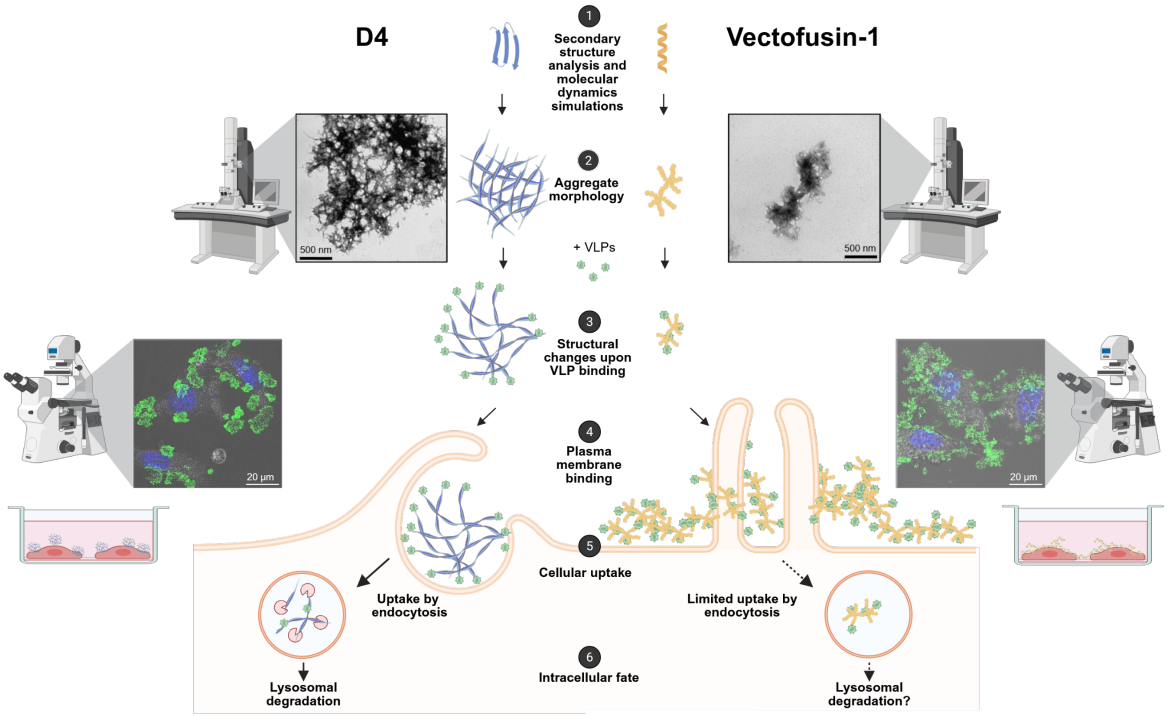

Figure 8. Systematic comparison of the transduction enhancer D4 and Vectofusin-1. (**1**) Secondary structure analysis and molecular dynamics simulations were conducted to understand their assembly into PNFs. (**2-6**) The morphology of PNF aggregates and their influence on virus-like particle (VLP) capture and interaction with the plasma membrane were investigated using a combination of electron- and fluorescence microscopy techniques. Created in BioRender. Rauch, L. (2026) https://BioRender.com/wheubqi. Reprinted from Rauch-Wirth & La Roche *et al*. 2026[3], CC BY 4.0, (https://creativecommons.org/licenses/by/4.0/).

2.3.1 Structural and morphological analysis of D4 and Vectofusin-1

We first analyzed D4 and Vectofusin-1 (KKALLHAALAHLLALAHHLLALLKKA-NH_2) by secondary structure analysis and MD simulations. Vectofusin-1 formed α-helical PNFs consistent with literature[181] that exhibited a positively charged and hydrophobic surface, primarily driven by lysine and leucine residues. The positively charged lysine residues localized at both N- and C-termini likely mediate interaction with negatively charged viral particles and membranes, while, according to literature, leucine residues promote coiled-coil assembly and histidine residues support fibril formation, as reported previously[181,183].

In contrast, D4 (RRIFIISM) monomers self-assembled into small antiparallel β-sheet oligomers composed of approximately 4–5 peptides, which associated into larger fibrillar aggregates. Hydrophobic isoleucine residues formed a buried central core, whereas phenylalanine and arginine side chains remained exposed at the surface, providing a hydrophobic and positive surface consistent with previous findings[2].

Negative-stain TEM and time-lapse imaging revealed distinct aggregation behaviors: D4 formed loosely packed, short PNFs that rapidly assembled into a few large, loosely connected µm-sized aggregates, while Vectofusin-1 formed shorter fibrils that aggregated

more slowly into numerous smaller, compact aggregates. In both cases, the observed PNF aggregates resembled the structures predicted by MD simulations. Together, these findings demonstrate that D4 and Vectofusin-1 differ not only in secondary structure but also in aggregate size, packaging density, and abundance.

2.3.2 Virus-like particle binding induces morphological and kinetic changes in PNFs

Upon incubation with VLPs (MLV Gag-YFP) morphological changes of both PNFs were observed: D4 formed larger, more loosely packed aggregates with faster kinetics. We suggest that binding of negatively charged VLPs partially neutralizes the cationic D4 surface and reduces the electrostatic repulsion thereby promoting fibril elongation. Consistent with our previous findings that EF-C PNFs significantly reduce viral surface charge[1], our results suggest a reciprocal effect in which virion binding can also modulate PNF charge. In contrast, VLP incubation led to the generation of more numerous small, loosely packed aggregates and well-defined fibrils were no longer detectable for Vectofusin-1 by TEM. Structural modeling suggests that VLP binding to lysine residues may interfere with adjacent histidine-mediated peptide-peptide interactions required for fibril growth[181], thereby impairing fibril maturation.

Time-lapse imaging and fluorescence microscopy revealed that D4 captured VLPs more efficiently, showing a ~4-fold higher binding capacity than Vectofusin-1, with uniform coating of aggregate surfaces consistent with exposed phenylalanine and arginine residues, which provide multiple hydrophobic and electrostatic interaction sites. This structural arrangement is similar to previously described peptide amphiphiles (PAs) that form fibrils with a hydrophobic core and cationic surface and exhibit the highest transduction enhancement activity among tested analogues[171]. Vectofusin-1 bound fewer VLPs with an irregular distribution, correlating with the heterogeneous lysine surface pattern predicted by MD simulations and a previous study[181].

In summary, D4's interaction with VLPs appears to enhance fibril growth, leading to larger and more open aggregates, whereas Vectofusin-1's interaction with VLPs appears to hinder fibril maturation, resulting in a high number of small aggregates. Moreover, D4's higher VLP binding capacity correlates with its greater ability to enhance γ-retroviral and lentiviral transduction compared to Vectofusin-1 under actual viral transduction conditions[2].

2.3.3 D4 PNFs are taken up via endocytosis followed by lysosomal degradation

The observed morphological differences resulted in distinct effects on plasma membrane dynamics. Filopodia surrounded and engulfed D4 aggregates, which bound as individual

structures to the cell surface, indicating active transport by filopodia (Fig. 9A). D4-treated cells also exhibited membrane ruffles and cup-like invaginations consistent with macropinocytosis[229], as previously reported for EF-C[1]. This membrane remodeling likely enhances viral attachment and uptake and is supported by the arginine-rich nature of D4, as arginine-rich peptides (e.g., HIV-1 Tat peptide and octaarginine) are known to induce actin-driven membrane ruffling and macropinocytosis via HSPG binding[230–232]. Consistently, SEM and STEM tomography demonstrated that the uniform VLP coating of D4 aggregates facilitated direct interactions with filopodia and the plasma membrane, supporting efficient VLP transport to cellular entry sites (Fig. 9B).

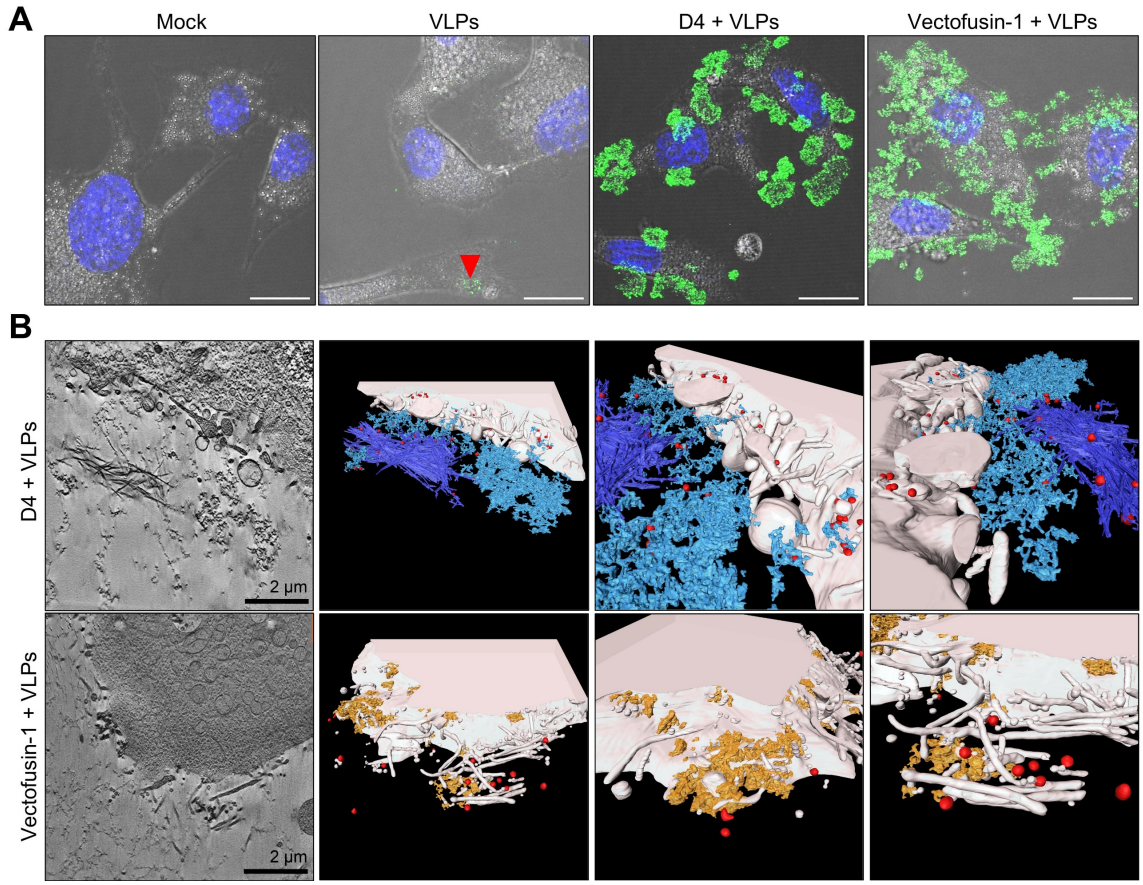

Figure 9. Aggregate morphology of D4 and Vectofusin-1 PNFs modulates plasma membrane dynamics and VLP-plasma membrane interactions. (**A**) (**B**) Fluorescence microscopy of HeLa cells incubated with PNFs (10 µg/ml) and VLPs for 1 h. The cell nucleus is shown in blue and VLPs in green (red arrowhead). A 63× objective with 2× zoom was used. Scale bar indicates 20 µm. (**B**) STEM tomography of HeLa cells (beige) incubated with PNFs (2 µg/ml) and VLPs (red) for 1 h. Long D4 PNFs are shown in blue, short D4 PNFs in cyan and Vectofusin-1 PNFs in orange. Adapted and reprinted from Rauch-Wirth & La Roche *et al.* 2026[3], CC BY 4.0, (https://creativecommons.org/licenses/by/4.0/).

Notably, similar mechanisms are exploited by retroviruses such as MLV and HIV-1[233], as well as by extracellular vesicles[234,235], which bind to filopodia and traffic toward the cell body. In contrast, Vectofusin-1 formed smaller aggregates that entangled filopodia,

indicating a more passive interaction. While membrane invaginations were occasionally observed, Vectofusin-1 predominantly formed mesh-like networks spanning adjacent cells (Fig. 9A), likely hindering efficient VLP transport.

Accordingly, SEM and STEM tomography demonstrated that VLPs were less frequently delivered to the plasma membrane (Fig.9B), suggesting that Vectofusin-1 mainly mediates static extracellular binding via electrostatic and hydrophobic interactions, whereas D4, in addition to these interactions, may also promote active endocytosis due to its high arginine content[236,237].

This difference in uptake behavior may explain the viral vector-specific effects previously observed[2]. Vectofusin-1 fails to enhance transduction of VSV-G-LVs[2,183,186], which enter cells via clathrin-mediated endocytosis through LDL-R[124,211], likely because its network-like structure hinders efficient internalization, while D4 enhances their transduction[2]. Both PNFs, however, efficiently enhance retroviral vectors such as GALV-RV [2,158,182,183], which fuse directly at the plasma membrane and do not rely on endocytic uptake[209].

Further experiments demonstrated that D4 PNFs are primarily internalized via macropinocytosis but can also enter cells through additional endocytic pathways in a size-dependent manner similar to what is seen for α-synuclein[199,238,239] and arginine-rich peptides[240], followed by lysosomal degradation. In contrast, Vectofusin-1 exhibited limited cellular uptake. For the safe clinical use of PNFs as transduction enhancers in *ex vivo* gene therapies such as CAR T cell therapy, side effects must be minimized. Ideally, PNFs should be internalized and degraded by target cells prior to infusion, as persistent aggregates could provoke immune responses or promote vascular occlusion[204–206].

To assess this, D4 uptake was evaluated under CAR T cell-like conditions using the pentameric form of formyl thiophene acetic acid (pFTAA), a dye that binds β-sheet-rich fibrils such as amyloid-β and tau fibrils[241,242] (Fig. 10A). Because pFTAA fluorescence decreases over time, matched input controls were generated prior to cell exposure, with medium changes and scaling steps performed in parallel. Compared to these controls, pFTAA-D4 fluorescence declined more rapidly and became undetectable after 7 days (Fig. 10B), with normalization showing a reduction to ~ 2% by day 3 (Fig. 10C). Importantly, no effects on T cell proliferation or viability were observed (Fig. 10D, E). In addition to cellular uptake and lysosomal degradation, gradual PNF disassembly and removal during medium exchange likely contribute to the observed fluorescence decline. Given that a typical CAR T cell process lasts ~14 days[100], these findings suggest that most

D4 PNFs are internalized and degraded during this period, supporting the safe clinical usage of D4 as a transduction enhancer.

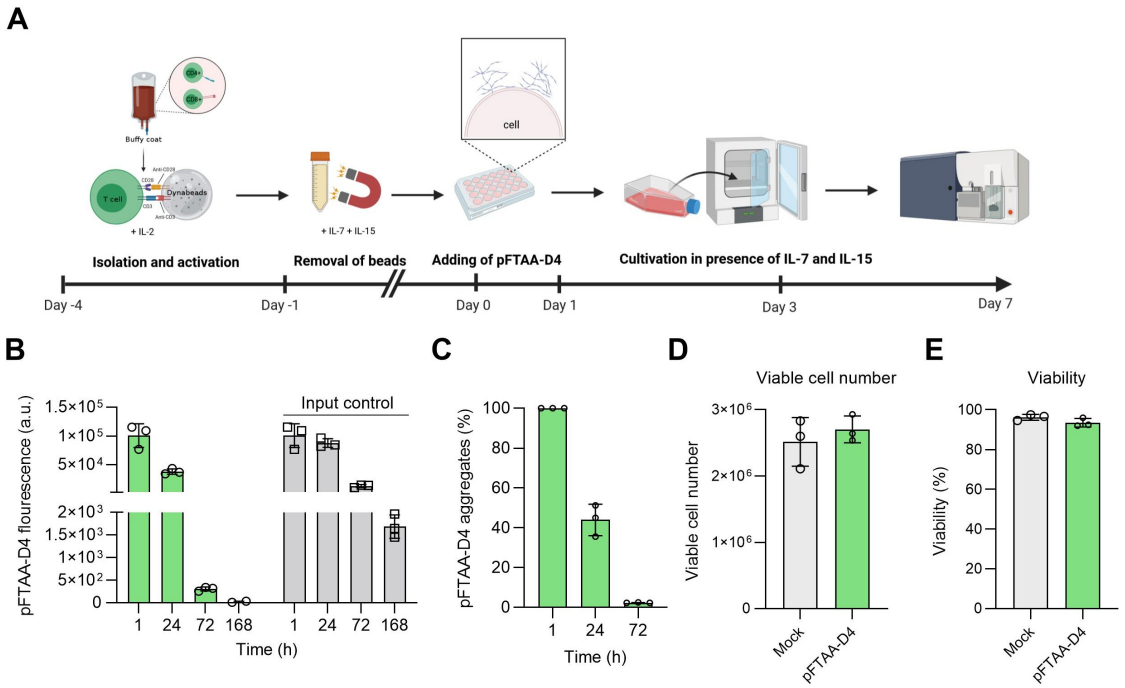

Figure 10. Decrease of pFTAA-D4 PNF aggregates during T cell cultivation. (**A**) Workflow of T cell cultivation under CAR T cell-like conditions including isolation, activation, and cultivation of human T cells. Activated CD4+/CD8+ T cells from three donors were incubated with pFTAA-labeled D4 PNFs (30 µg/ml) and incubated for 7 days, including medium changes and matched input controls. Created in BioRender. Rauch, L. (2026) https://BioRender.com/aate9gs. (**B**) Fluorescence was measured by flow cytometry over 7 days. (**C**) Normalized fluorescence to matched input control. Viable cell number (**D**) and viability (**E**) of T cells after cultivation for 7 days. Shown are mean values ±SD of three donors measured in triplicates or singlicates (mock). Reprinted from Rauch-Wirth & La Roche *et al.* 2026[3], CC BY 4.0, (https://creativecommons.org/licenses/by/4.0/).

Overall, our results demonstrate that the aggregate morphology of D4 and Vectofusin-1 directly influences their interactions with VLPs and the plasma membrane. D4 formed loosely packed β-sheet PNF aggregates with high VLP-binding capacity that induced plasma membrane invaginations, promoting uptake mainly via macropinocytosis followed by lysosomal degradation (Fig. 8)[3]. In contrast, Vectofusin-1 assembled into smaller α-helical PNF aggregates that formed large interconnected networks with lower VLP binding and limited cellular uptake, primarily entangling filopodia without clear membrane remodeling (Fig. 8). Notably, we showed that VLP interaction can directly influence PNF formation and aggregation behavior[3].

3 Summary

Peptide nanofibrils (PNFs) have emerged as a powerful and tunable platform to enhance retroviral gene delivery, addressing a central bottleneck in the manufacturing of chimeric antigen receptor (CAR) T and CAR NK cell therapies, namely inefficient viral transduction. Across the three studies, we systematically advanced the field from the identification and optimization of novel PNFs to a mechanistic and structural understanding of how these supramolecular assemblies mediate their biological function.

Initially, we elucidated the underlying mechanism of PNF-mediated transduction enhancement using EF-C PNFs as a model system. We demonstrated that PNFs act through a multi-step process involving viral capture, plasma membrane remodeling and active cellular uptake: First, the positively charged surface of PNFs binds viral particles with high efficiency, resulting in PNF/virus complexes and a significant reduction in virion surface charge. Second, these complexes interact with cellular protrusions like filopodia, which transport them to the cell body. This interaction induces pronounced plasma membrane invaginations that increase surface area for viral attachment and shorten the travel distance for viral capsids to reach the nucleus. Third, PNFs are internalized mainly via macropinocytosis and subsequently degraded by lysosomes. This degradation prevents intracellular accumulation of amyloid material and supports their safe use as transduction enhancers in *ex vivo* gene therapy applications. However, the chemical instability of EF-C, which leads to the formation of large aggregates in cell culture, limits its clinical applicability.

To address this, we established novel PNFs as effective transduction enhancers by exploiting intrinsic physicochemical properties such as positive charge and high β-sheet content. Cationic peptides assemble into positively charged, β-sheet-rich PNFs that capture negatively charged viral particles, thereby overcoming electrostatic interactions between viral and cellular membranes. Through an *in silico* screening approach, we predicted a fibril-forming segment in human interleukin-18 leading to the discovery of the 8-mer peptide RM-8, which was further optimized through a structure-activity relationship study to D4. D4 combines several advantageous features, including chemical stability, efficient self-assembly into PNFs and reduced formation of large aggregates. Functionally, D4 significantly enhanced γ-retroviral and lentiviral transduction rates in primary T and NK

cells, outperforming established enhancers such as Vectofusin-1 and EF-C. Additionally, no impact on cell viability or inflammatory responses was observed. These findings position D4 PNFs as a cost-effective and clinically relevant tool to improve gene transfer efficiency.

Building on this, we further refined this understanding by demonstrating that structural morphology across multiple length scales determines the activity of PNFs as transduction enhancers. By directly comparing the β-sheet forming peptide D4 with the α-helical Vectofusin-1, we show that differences in secondary structure translate into distinct supramolecular architectures and biological functions. D4 assembled into loosely packed, β-sheet-rich PNF aggregates with a heterogeneous, patchy surface composed of hydrophobic and positively charged regions. These aggregates exhibited a high capacity for viral binding, resulting in a dense and uniform coating of viral particles. Moreover, D4 aggregates were actively engaged by cellular protrusions and efficiently internalized via macropinocytosis, consistent with the mechanistic model established for EF-C.
In contrast, Vectofusin-1 formed more compact, α-helical PNFs that organized into an interconnected network displaying lower viral binding efficiency and heterogeneous virion association. Furthermore, these structures exhibited lower cellular uptake and primarily remained at the cell surface. Notably, D4 formed fewer but larger µm-sized aggregates, whereas Vectofusin-1 generated more numerous but smaller assemblies.

Together, these studies establish a mechanistic model in which the transduction-enhancing activity of PNFs arises from the interplay of (i) electrostatic viral capture, (ii) structural organization into supramolecular aggregates, and (iii) active engagement with cellular uptake pathways. Importantly, the data demonstrate that not only the peptide sequence but also higher-order assembly properties, such as fibril morphology, aggregate size, and surface topology, mediate biological activity. The identification of D4 as a structurally optimized, highly efficient and biologically well-tolerated PNF highlights the translational potential of this approach. More broadly, these findings provide a rational framework for the design of next-generation peptide-based materials to enhance gene delivery and may be extendable to other biomedical applications requiring controlled modulation of membrane interactions and cellular uptake.

4 References

1. Rauch-Wirth, L., Schütz, D., Groß, R., Rode, S., Glocker, B., Müller, J. A., Walther, P., Read, C. & Münch, J. Transduction enhancing EF-C peptide nanofibrils are endocytosed by macropinocytosis and subsequently degraded. *Biomaterials* **317**, 123044 (2025).
2. Rauch-Wirth, L., Renner, A., Kaygisiz, K., Weil, T., Zimmermann, L., Rodriguez-Alfonso, A. A., Schütz, D., Wiese, S., Ständker, L., Weil, T., Schmiedel, D. & Münch, J. Optimized peptide nanofibrils as efficient transduction enhancers for in vitro and ex vivo gene transfer. *Front. Immunol.* **14**, 1270243 (2023).
3. Rauch-Wirth, L., La Roche, J., Kaygisiz, K., Kuhn, A., Jeon, N., Stifel, U., Zech, F., Fischer-Posovszky, P., Weil, T., Read, C. & Münch, J. Structural morphology of peptide nanofibrils dictates viral capture and cellular uptake in gene therapy applications. *Nano Today* **69**, 103015 (2026).
4. What is Gene Therapy? FDA. https://www.fda.gov/vaccines-blood-biologics/cellular-gene-therapy-products/what-gene-therapy. Accessed on: 04.08.2025.
5. Rosenberg, S. A., Aebersold, P., Cornetta, K., Kasid, A., Morgan, R. A., Moen, R., Karson, E. M., Lotze, M. T., Yang, J. C., Topalian, S. L., Merino, M. J., Culver, K., Miller, A. D., Blaese, R. M. & Anderson, W. F. Gene Transfer into Humans — Immunotherapy of Patients with Advanced Melanoma, Using Tumor-Infiltrating Lymphocytes Modified by Retroviral Gene Transduction. *N. Engl. J. Med.* **323**, 570–578 (1990).
6. Ginn, S. L., Mandwie, M., Alexander, I. E., Edelstein, M. & Abedi, M. R. Gene therapy clinical trials worldwide to 2023—an update. *J. Gene Med.* **26**, e3721 (2024).
7. Gowing, G., Svendsen, S. & Svendsen, C. N. Chapter 4 - Ex vivo gene therapy for the treatment of neurological disorders. in *Progress in Brain Research* (eds Dunnett, S. B. & Björklund, A.) vol. 230 99–132 (Elsevier, 2017).
8. Mendell, J. R., Al-Zaidy, S. A., Rodino-Klapac, L. R., Goodspeed, K., Gray, S. J., Kay, C. N., Boye, S. L., Boye, S. E., George, L. A., Salabarria, S., Corti, M., Byrne, B. J. & Tremblay, J. P. Current Clinical Applications of *In Vivo* Gene Therapy with AAVs. *Mol. Ther.* **29**, 464–488 (2021).
9. Volodina, O. & Smirnikhina, S. The Future of Gene Therapy: A Review of In Vivo and Ex Vivo Delivery Methods for Genome Editing-Based Therapies. *Mol. Biotechnol.* **67**, 425–437 (2025).
10. Cavazza, A., Molina-Estévez, F. J., Reyes, Á. P., Ronco, V., Naseem, A., Malenšek, Š., Pečan, P., Santini, A., Heredia, P., Aguilar-González, A., Boulaiz, H., Ni, Q., Cortijo-Gutierrez, M., Pavlovic, K., Herrera, I., de la Cerda, B., Garcia-Tenorio, E. M., Richard, E., Granados-Principal, S., López-Márquez, A., Köber, M., Stojanovic, M., Vidaković, M., Santos-Garcia, I., Blázquez, L., Haughton, E., Yan, D., Sánchez-Martín, R. M., Mazini, L., Aseguinolaza, G. G., Miccio, A., Rio, P., Desviat, L. R., Gonçalves, M. A. F. V., Peng, L., Jiménez-Mallebrera, C., Molina, F. M., Gupta, D., Lainšček, D., Luo, Y. & Benabdellah, K. Advanced delivery systems for gene editing: A comprehensive review from the GenE-HumDi COST Action Working Group. *Mol. Ther. Nucleic Acids* **36**, 102457 (2025).
11. Gehl, J. Electroporation: theory and methods, perspectives for drug delivery, gene therapy and research. *Acta Physiol. Scand.* **177**, 437–447 (2003).
12. Barry, M. E., Pinto-Gonzalez, D., Orson, F. M., McKenzie, G. J., Petry, G. R. & Barry, M. A. Role of Endogenous Endonucleases and Tissue Site in Transfection and CpG-Mediated Immune Activation after Naked DNA Injection. *Hum. Gene Ther.* **10**, 2461–2480 (1999).

13. Felgner, P. L., Gadek, T. R., Holm, M., Roman, R., Chan, H. W., Wenz, M., Northrop, J. P., Ringold, G. M. & Danielsen, M. Lipofection: a highly efficient, lipid-mediated DNA-transfection procedure. *Proc. Natl. Acad. Sci.* **84**, 7413–7417 (1987).
14. Hawley, R. G., Lieu, F. H., Fong, A. Z. & Hawley, T. S. Versatile retroviral vectors for potential use in gene therapy. *Gene Ther.* **1**, 136–138 (1994).
15. Volkwein, W., Pavlovic, M., Anton, M., Haase, M., Stellberger, T., Jarrar, A., Busch, U. & Baiker, A. Detection and differentiation of murine leukemia virus (MLV) and murine stem cell virus (MSCV) and therefrom derived nucleic acids. *J. Virol. Methods* **299**, 114316 (2022).
16. Naldini, L., Blömer, U., Gallay, P., Ory, D., Mulligan, R., Gage, F. H., Verma, I. M. & Trono, D. In vivo gene delivery and stable transduction of nondividing cells by a lentiviral vector. *Science* **272**, 263–267 (1996).
17. Montini, E., Cesana, D., Schmidt, M., Sanvito, F., Bartholomae, C. C., Ranzani, M., Benedicenti, F., Sergi, L. S., Ambrosi, A., Ponzoni, M., Doglioni, C., Serio, C. D., Kalle, C. von & Naldini, L. The genotoxic potential of retroviral vectors is strongly modulated by vector design and integration site selection in a mouse model of HSC gene therapy. *J. Clin. Invest.* **119**, 964–975 (2009).
18. Ranzani, M., Cesana, D., Bartholomae, C. C., Sanvito, F., Pala, M., Benedicenti, F., Gallina, P., Sergi, L. S., Merella, S., Bulfone, A., Doglioni, C., von Kalle, C., Kim, Y. J., Schmidt, M., Tonon, G., Naldini, L. & Montini, E. Lentiviral vector–based insertional mutagenesis identifies genes associated with liver cancer. *Nat. Methods* **10**, 155–161 (2013).
19. Nienhuis, A. W., Dunbar, C. E. & Sorrentino, B. P. Genotoxicity of Retroviral Integration In Hematopoietic Cells. *Mol. Ther.* **13**, 1031–1049 (2006).
20. Jadlowsky, J. K., Hexner, E. O., Marshall, A., Grupp, S. A., Frey, N. V., Riley, J. L., Veloso, E., McConville, H., Rogal, W., Czuczman, C., Hwang, W.-T., Li, Y., Leskowitz, R. M., Farrelly, O., Karar, J., Christensen, S., Barber-Rotenberg, J., Gaymon, A., Aronson, N., Bernstein, W., Melenhorst, J. J., Roche, A. M., Everett, J. K., Zolnoski, S. A., McFarland, A. G., Reddy, S., Petrichenko, A., Cook, E. J., Lee, C., Gonzalez, V. E., Alexander, K., Kulikovskaya, I., Ramírez-Fernández, Á., Minehart, J. C., Ruella, M., Gill, S. I., Schuster, S. J., Cohen, A. D., Garfall, A. L., Shah, P. D., Porter, D. L., Maude, S. L., Levine, B. L., Siegel, D. L., Chew, A., McKenna, S., Lledo, L., Davis, M. M., Plesa, G., Herbst, F., Stadtmauer, E. A., Tebas, P., DiNofia, A., Haas, A., Haas, N. B., Myers, R., O'Rourke, D. M., Svoboda, J., Tanyi, J. L., Aplenc, R., Jacobson, J. M., Ko, A. H., Cohen, R. B., June, C. H., Bushman, F. D. & Fraietta, J. A. Long-term safety of lentiviral or gammaretroviral gene-modified T cell therapies. *Nat. Med.* **31**, 1134–1144 (2025).
21. Sayedahmed, E. E., Kumari, R. & Mittal, S. K. Current use of adenovirus vectors and their production methods. *Methods Mol. Biol. Clifton NJ* **1937**, 155–175 (2019).
22. Wold, W. S. M. & Toth, K. Adenovirus Vectors for Gene Therapy, Vaccination and Cancer Gene Therapy. *Curr. Gene Ther.* **13**, 421–433 (2013).
23. Duan, D., Yue, Y. & Engelhardt, J. F. Expanding AAV Packaging Capacity with *Trans*-splicing or Overlapping Vectors: A Quantitative Comparison. *Mol. Ther.* **4**, 383–391 (2001).
24. Brommel, C. M., Cooney, A. L. & Sinn, P. L. Adeno-Associated Virus-Based Gene Therapy for Lifelong Correction of Genetic Disease. *Hum. Gene Ther.* **31**, 985–995 (2020).
25. AlDallal, S. M. Yescarta: A New Era for Non-Hodgkin Lymphoma Patients. *Cureus* **12**, e11504 (2020).

26. Wang, M., Munoz, J., Goy, A., Locke, F. L., Jacobson, C. A., Hill, B. T., Timmerman, J. M., Holmes, H., Jaglowski, S., Flinn, I. W., McSweeney, P. A., Miklos, D. B., Pagel, J. M., Kersten, M.-J., Milpied, N., Fung, H., Topp, M. S., Houot, R., Beitinjaneh, A., Peng, W., Zheng, L., Rossi, J. M., Jain, R. K., Rao, A. V. & Reagan, P. M. KTE-X19 CAR T-Cell Therapy in Relapsed or Refractory Mantle-Cell Lymphoma. *N. Engl. J. Med.* **382**, 1331–1342 (2020).
27. Ali, S., Kjeken, R., Niederlaender, C., Markey, G., Saunders, T. S., Opsata, M., Moltu, K., Bremnes, B., Grønevik, E., Muusse, M., Håkonsen, G. D., Skibeli, V., Kalland, M. E., Wang, I., Buajordet, I., Urbaniak, A., Johnston, J., Rantell, K., Kerwash, E., Schuessler-Lenz, M., Salmonson, T., Bergh, J., Gisselbrecht, C., Tzogani, K., Papadouli, I. & Pignatti, F. The European Medicines Agency Review of Kymriah (Tisagenlecleucel) for the Treatment of Acute Lymphoblastic Leukemia and Diffuse Large B-Cell Lymphoma. *The Oncologist* **25**, e321–e327 (2020).
28. Sharma, P., Kanapuru, B., George, B., Lin, X., Xu, Z., Bryan, W. W., Pazdur, R. & Theoret, M. R. FDA Approval Summary: Idecabtagene Vicleucel for Relapsed or Refractory Multiple Myeloma. *Clin. Cancer Res. Off. J. Am. Assoc. Cancer Res.* **28**, 1759–1764 (2022).
29. Sharma, P., Lin, X., Xu, Z., Kanapuru, B., Theoret, M. R., Sokolic, R. & Fashoyin-Aje, L. A. FDA Approval Summary: Idecabtagene Vicleucel for the Treatment of Triple-Class–Exposed, Relapsed or Refractory Multiple Myeloma. *Clin. Cancer Res.* OF1–OF6 (2025).
30. Cappell, K. M. & Kochenderfer, J. N. Long-term outcomes following CAR T cell therapy: what we know so far. *Nat. Rev. Clin. Oncol.* **20**, 359–371 (2023).
31. Sadelain, M., Brentjens, R. & Rivière, I. The Basic Principles of Chimeric Antigen Receptor Design. *Cancer Discov.* **3**, 388–398 (2013).
32. Canelo-Vilaseca, M., Sabbah, M., Di Blasi, R., Cristinelli, C., Sureda, A., Caillat-Zucman, S. & Thieblemont, C. Lymphodepletion chemotherapy in chimeric antigen receptor-engineered T (CAR-T) cell therapy in lymphoma. *Bone Marrow Transplant.* **60**, 559–567 (2025).
33. Ninomiya, S., Narala, N., Huye, L., Yagyu, S., Savoldo, B., Dotti, G., Heslop, H. E., Brenner, M. K., Rooney, C. M. & Ramos, C. A. Tumor indoleamine 2,3-dioxygenase (IDO) inhibits CD19-CAR T cells and is downregulated by lymphodepleting drugs. *Blood* **125**, 3905–3916 (2015).
34. Gattinoni, L., Finkelstein, S. E., Klebanoff, C. A., Antony, P. A., Palmer, D. C., Spiess, P. J., Hwang, L. N., Yu, Z., Wrzesinski, C., Heimann, D. M., Surh, C. D., Rosenberg, S. A. & Restifo, N. P. Removal of homeostatic cytokine sinks by lymphodepletion enhances the efficacy of adoptively transferred tumor-specific CD8+ T cells. *J. Exp. Med.* **202**, 907–912 (2005).
35. Awasthi, R., Maier, H. J., Zhang, J. & Lim, S. Kymriah® (tisagenlecleucel) – An overview of the clinical development journey of the first approved CAR-T therapy. *Hum. Vaccines Immunother.* **19**, 2210046 (2023).
36. Tedder, T. F. CD19: a promising B cell target for rheumatoid arthritis. *Nat. Rev. Rheumatol.* **5**, 572–577 (2009).
37. Carpenter, R. O., Evbuomwan, M. O., Pittaluga, S., Rose, J. J., Raffeld, M., Yang, S., Gress, R. E., Hakim, F. T. & Kochenderfer, J. N. B-cell Maturation Antigen Is a Promising Target for Adoptive T-cell Therapy of Multiple Myeloma. *Clin. Cancer Res.* **19**, 2048–2060 (2013).
38. Cooper, L. J. N., Al-Kadhimi, Z., DiGiusto, D., Kalos, M., Colcher, D., Raubitschek, A., Forman, S. J. & Jensen, M. C. Development and application of CD19-specific T

cells for adoptive immunotherapy of B cell malignancies. *Blood Cells. Mol. Dis.* **33**, 83–89 (2004).
39. Davila, M. L. & Brentjens, R. J. CD19-Targeted CAR T Cells as Novel Cancer Immunotherapy for Relapsed or Refractory B-Cell Acute Lymphoblastic Leukemia. *Clin. Adv. Hematol. Oncol. HO* **14**, 802–808 (2016).
40. Yin, H. & Wei, X. The design of retroviral vectors used in the CAR-T products, risk management, and future perspective. *MedComm* **6**, e70067 (2025).
41. Liu, Y., Chen, X., Han, W. & Zhang, Y. Tisagenlecleucel, an approved anti-CD19 chimeric antigen receptor T-cell therapy for the treatment of leukemia. *Drugs Today Barc. Spain 1998* **53**, 597–608 (2017).
42. Rouce, R., Dolan, J. G., Phillips, C. L., Qayed, M., Pulsipher, M. A., Vernau, L. M., Galletta, T. J., Votaw, S., Llaurador Caraballo, G., Yang, H., Wang, Y., Ghantoji, S., Tesfaye, M., Lee, S., O'Sullivan, E. & Grupp, S. A. Impact of Current Manufacturing on Kymriah Real-World Effectiveness and Functional Persistence in Acute Lymphoblastic Leukemia (ALL) (KareALL): A Retrospective Study of Tisagenlecleucel (tisa-cel)-Treated Pediatric and Young Adult Patients (pts) with ALL. *Blood* **144**, 7724 (2024).
43. Novartis five-year Kymriah® data show durable remission and long-term survival maintained in children and young adults with advanced B-cell ALL. *Novartis* https://www.novartis.com/news/media-releases/novartis-five-year-kymriah-data-show-durable-remission-and-long-term-survival-maintained-children-and-young-adults-advanced-b-cell-all. Accessed on: 15.12.2025.
44. Neelapu, S. S., Chavez, J. C., Sehgal, A. R., Epperla, N., Ulrickson, M., Bachy, E., Munshi, P. N., Casulo, C., Maloney, D. G., de Vos, S., Reshef, R., Leslie, L. A., Oluwole, O. O., Yakoub-Agha, I., Khanal, R., Rosenblatt, J., Korn, R., Peng, W., Lui, C., Wulff, J., Shen, R., Poddar, S., Jung, A. S., Miao, H., Beygi, S. & Jacobson, C. A. Three-year follow-up analysis of axicabtagene ciloleucel in relapsed/refractory indolent non-Hodgkin lymphoma (ZUMA-5). *Blood* **143**, 496–506 (2024).
45. Jain, M. D., Spiegel, J. Y., Nastoupil, L. J., Tamaresis, J., Ghobadi, A., Lin, Y., Lekakis, L., Reagan, P., Oluwole, O., McGuirk, J., Deol, A., Dorritie, K. A., Sehgal, A. R., Goy, A., Hill, B. T., Andreadis, C., Munoz, J., Ulrickson, M., Westin, J., Chavez, J. C., Patel, D., Jacobs, M. T., Bansal, R., Bennani, N. N., Patel, V. G., Rapoport, A. P., Vose, J. M., Miklos, D. B., Neelapu, S. S., Locke, F. L., Lunning, M. & Dahiya, S. Five-Year Follow-Up of Standard-of-Care Axicabtagene Ciloleucel for Large B-Cell Lymphoma: Results From the US Lymphoma CAR T Consortium. *J. Clin. Oncol. Off. J. Am. Soc. Clin. Oncol.* **42**, 3581–3592 (2024).
46. Yescarta Is First CAR T cell Therapy to Report Five Year Survival Data From Pivotal Study Showing Durable Long Term Survival in Patients With Refractory Large B cell Lymphoma. https://www.gilead.com/news/news-details/2021/yescarta-is-first-car-t-cell-therapy-to-report-five-year-survival-data-from-pivotal-study-showing-durable-long-term-survival-in-patients-with-refractory-large-b-cell-lymphoma. Accessed on: 15.12.2025.
47. Kopmar, N. E. & Cassaday, R. D. Clinical Insights on Brexucabtagene Autoleucel for the Treatment of Patients with Relapsed or Refractory B-Cell Acute Lymphoblastic Leukemia. *Cancer Manag. Res.* **16**, 1587–1596 (2024).
48. Kite's Tecartus® Demonstrates Sustained Overall Survival in Adult Patients With Relapsed/Refractory B-cell Acute Lymphoblastic Leukemia. https://www.kitepharma.com/news/press-releases. Accessed on: 15.12.2025.
49. Longest Follow Up Data Reported for Kites Tecartus CAR T Cell Therapy at ASH 2024 Reinforce Durable Efficacy and Survival Benefits.

https://www.gilead.com/news/news-details/2024/longest-follow-up-data-reported-for-kites-tecartus-car-t-cell-therapy-at-ash-2024-reinforce-durable-efficacy-and-survival-benefits. Accessed on: 15.12.2025.

50. Riedell, P. A., Grady, C. B., Nastoupil, L. J., Luna, A., Ahmed, N., Maziarz, R. T., Hu, M., Brower, J., Hwang, W.-T., Schuster, S. J., Chen, A. I., Oluwole, O. O., Bachanova, V., McGurik, J. P., Perales, M.-A., Bishop, M. R. & Porter, D. L. Lisocabtagene maraleucel for relapsed/refractory large B-cell lymphoma: a cell therapy consortium real-world analysis. *Blood Adv.* **9**, 1232–1241 (2025).
51. Abramson, J. S., Palomba, M. L., Gordon, L. I., Lunning, M. A., Wang, M., Arnason, J., Mehta, A., Purev, E., Maloney, D. G., Andreadis, C., Sehgal, A., Solomon, S. R., Ghosh, N., Albertson, T. M., Garcia, J., Kostic, A., Mallaney, M., Ogasawara, K., Newhall, K., Kim, Y., Li, D. & Siddiqi, T. Lisocabtagene maraleucel for patients with relapsed or refractory large B-cell lymphomas (TRANSCEND NHL 001): a multicentre seamless design study. *Lancet Lond. Engl.* **396**, 839–852 (2020).
52. Kamdar, M., Solomon, S. R., Arnason, J., Johnston, P. B., Glass, B., Bachanova, V., Ibrahimi, S., Mielke, S., Mutsaers, P., Hernandez-Ilizaliturri, F., Izutsu, K., Morschhauser, F., Lunning, M., Maloney, D. G., Crotta, A., Montheard, S., Previtali, A., Stepan, L., Ogasawara, K., Mack, T., Abramson, J. S., & TRANSFORM Investigators. Lisocabtagene maraleucel versus standard of care with salvage chemotherapy followed by autologous stem cell transplantation as second-line treatment in patients with relapsed or refractory large B-cell lymphoma (TRANSFORM): results from an interim analysis of an open-label, randomised, phase 3 trial. *Lancet Lond. Engl.* **399**, 2294–2308 (2022).
53. Bristol Myers Squibb's Breyanzi Demonstrates Clinically Meaningful Outcomes Across Broad Range of B-Cell Malignancies in New Data Presented at 2024 ASCO® Annual Meeting. https://news.bms.com/news/details/2024/Bristol-Myers-Squibbs-Breyanzi-Demonstrates-Clinically-Meaningful-Outcomes-Across-Broad-Range-of-B-Cell-Malignancies-in-New-Data-Presented-at-2024-ASCO-Annual-Meeting/default.aspx. Accessed on: 15.12.2025.
54. Joseph, N., Parikh, R., Allada, S., Gupta, V., Hofmeister, C., Shah, N., Kaufman, J., Lonial, S. & Nooka, A. Real world evidence comparing idecabtagene vicleucel (Ide-cel, Abecma) versus ciltacabtagene autoleucel (Cilta-cel, Carvykti) chimeric antigen receptor T-cell (CART) therapy among patients with Relapsed/Refractory multiple myeloma (RRMM). *Blood* **146**, 2301 (2025).
55. Ying, Z., Yang, H., Guo, Y., Li, W., Zou, D., Zhou, D., Wang, Z., Zhang, M., Wu, J., Liu, H., Zhang, P., Yang, S., Zhou, Z., Zheng, H., Song, Y. & Zhu, J. Relmacabtagene autoleucel (relma-cel) CD19 CAR-T therapy for adults with heavily pretreated relapsed/refractory large B-cell lymphoma in China. *Cancer Med.* **10**, 999–1011 (2021).
56. Gao, F., Sun, C., Liu, J., Yu, J., He, J., Meng, X., Liu, X., Han, X., Li, L., Qiu, L., Qian, Z., Zhou, S., Xia, Z., Yang, S., Zhou, Z., Tian, A., Qin, Y., Wang, X. & Zhang, H. Survival Benefit of Relmacabtagene Autoleucel Versus Usual Care in Relapsed/Refractory Follicular Lymphoma: A Matching-Adjusted Indirect Analysis. *Hematol. Oncol.* **43**, e70051 (2025).
57. Shu, J., Xie, W., Mei, C., Ren, A., Ke, S., Ma, M., Zhou, Z., Hu, Y. & Mei, H. Safety and clinical efficacy of Relmacabtagene autoleucel (relma-cel) for systemic lupus erythematosus: a phase 1 open-label clinical trial. *eClinicalMedicine* **83**, (2025).
58. Carteyva (Relma-cel) CAR-T Therapy: 66.7% 4-Year Survival in R/R LBCL. *Advance of CAR-T Therapy in Blood Cancer* https://cartcellschina.com/relma-cel-achieves-66-7-4-year-survival-in-r-r-lbcl-asco-2024-reports/. Accessed on: 15.12.2025.

59. Natrajan, K., Kaushal, M., George, B., Kanapuru, B. & Theoret, M. R. FDA Approval Summary: Ciltacabtagene Autoleucel for Relapsed or Refractory Multiple Myeloma. *Clin. Cancer Res.* **30**, 2865–2871 (2024).
60. Sidana, S., Patel, K. K., Peres, L. C., Bansal, R., Kocoglu, M. H., Shune, L., Atrash, S., Smith, K., Midha, S., Ferreri, C., Dhakal, B., Dima, D., Costello, P., Wagner, C., Reshef, R., Hosoya, H., Mikkilineni, L., Atanackovic, D., Chhabra, S., Parrondo, R., Nadeem, O., Mann, H., Kalariya, N., Hovanky, V., De Avila, G., Freeman, C. L., Locke, F. L., Alsina, M., Wong, S., Herr, M., Htut, M., McGuirk, J., Sborov, D. W., Khouri, J., Martin, T., Janakiram, M., Lin, Y. & Hansen, D. K. Safety and efficacy of standard-of-care ciltacabtagene autoleucel for relapsed/refractory multiple myeloma. *Blood* **145**, 85–97 (2025).
61. Keam, S. J. Equecabtagene Autoleucel: First Approval. *Mol. Diagn. Ther.* **27**, 781–787 (2023).
62. Rehman, M. A. & Arshad, H. A Discount on the Cost of Cancer: India's Homegrown CAR-T Cell Therapy. *Blood Cell Ther.* **7**, 121–123 (2024).
63. Narula, G., Keerthivasagam, S., Jain, H., Dhamne, C., Tembhare, P., Subramanian, P. G., Patkar, N., Poojary, M., Nisar, A., Pandit, D., Pandit, K., Karulkar, A., Jaiswal, A. K., Khan, A., Shah, S., Firfiray, A., Pendhari, J., Asija, S., Chowdury, A., Banik, A., Roy Moulik, N., Srinivasan, S., Bhosle, S., Hiregoudar, S., Ojha, S., Nayak, L., Thorat, J., Bagal, B., Sengar, M., Jindal, N., Chichra, A., Mirgh, S., Gokarn, A., Punatar, S., Rajadhyaksha, S., Khattry, N., Banavali, S., Highfill, S., Shah, N. N. & Purwar, R. Evaluating the Safety of HCAR19 (Now Actalycabtagene Autoleucel- Actaly-Cel^{TM}), a Novel Humanized CD19-Directed Chimeric Antigen Receptor T-Cells in Pediatric, Adolescents, and Young Adults with Relapsed/ Refractory B- Acute Lymphoblastic Leukemia (ESHA) - Report of Phase-1B. *Blood* **142**, 6878 (2023).
64. Wang, Y., Lv, L., Song, Y., Wei, X., Zhou, H., Liu, Q., Xu, K., Yan, D., Zhang, C., Liu, S., Jin, J., Mei, H., Niu, T., Liang, A., Gu, R., Ren, J., Feng, Y., Jin, W., Zhou, Y., Deng, Y. & Wang, J. Inaticabtagene autoleucel in adult relapsed or refractory B-cell acute lymphoblastic leukemia. *Blood Adv.* **9**, 836–843 (2025).
65. Dhillon, S. Zevorcabtagene Autoleucel: First Approval. *Mol. Diagn. Ther.* **28**, 501–506 (2024).
66. Roddie, C., Sandhu, K. S., Tholouli, E., Logan, A. C., Shaughnessy, P., Barba, P., Ghobadi, A., Guerreiro, M., Yallop, D., Abedi, M., Pantin, J. M., Yared, J. A., Beitinjaneh, A. M., Chaganti, S., Hodby, K., Menne, T., Arellano, M. L., Malladi, R., Shah, B. D., Mountjoy, L., O'Dwyer, K. M., Peggs, K. S., Lao-Sirieix, P., Zhang, Y., Brugger, W., Braendle, E., Pule, M., Bishop, M. R., DeAngelo, D. J., Park, J. H. & Jabbour, E. Obecabtagene Autoleucel in Adults with B-Cell Acute Lymphoblastic Leukemia. *N. Engl. J. Med.* **391**, 2219–2230 (2024).
67. Lee, A. Obecabtagene Autoleucel: First Approval. *Mol. Diagn. Ther.* **29**, 419–423 (2025).
68. Martínez-Cibrián, N., Ortiz-Maldonado, V., Español-Rego, M., Alserawan, L., Navarro, S., Albiol, N., Lozano, M., Charry, P., Magnano, L., Rivero, A., Correa, J. G., Mozas, P., Cortés-Bullich, A., Jiménez-Vicente, C., Giné, E., Montoro-Lorite, M., Ramos, C., Ayora, P., Calderón, H., Sánchez-Castañón, M., Benítez-Ribas, D., Mata-Molanes, J. J., Rojas, K., Setoaín, X., Rodríguez, S., Murias, A., Alcubilla, P., Varea, S., Olesti, E., Bachiller, M., Calvo-Orteu, M., Sans-Pola, C., Sáez-Peñataro, J., de Larrea, C. F., López-Guillermo, A., González-Navarro, E. A., Juan, M. & Delgado, J. Efficacy and safety of the academic anti-CD19 chimeric antigen receptor T-cell product varnimcabtagene autoleucel for the treatment of relapsed/refractory follicular lymphoma. *HemaSphere* **9**, e70166 (2025).

69. Immuneel launches CAR-T therapy in India. *Cell & Gene Therapy review* https://www.cellgenetherapyreview.com/3972-News/617286-Immuneel-to-offer-India-s-first-CAR-T-therapy/?utm. Accessed on: 15.12.2025.
70. Cosenza, M., Sacchi, S. & Pozzi, S. Cytokine Release Syndrome Associated with T-Cell-Based Therapies for Hematological Malignancies: Pathophysiology, Clinical Presentation, and Treatment. *Int. J. Mol. Sci.* **22**, 7652 (2021).
71. Rice, J., Nagle, S., Randall, J. & Hinson, H. E. Chimeric Antigen Receptor T Cell-Related Neurotoxicity: Mechanisms, Clinical Presentation, and Approach to Treatment. *Curr. Treat. Options Neurol.* **21**, 40 (2019).
72. Golmohammadi, M., Noorbakhsh, N. & Kavianpour, M. CAR-T Cell Therapy: Managing Side Effects and Overcoming Challenges. *Adv. Biomed. Res.* **14**, 38 (2025).
73. Abid, M. B., Adnan, N. & Ahmed, N. From Risk to Reach: How Risk Evaluation and Mitigation Strategy Remediation Will Shape Access to Chimeric Antigen Receptor T Cell Therapy. *Transplant. Cell. Ther. Off. Publ. Am. Soc. Transplant. Cell. Ther.* **31**, 1051–1054 (2025).
74. REMS Compliance Program. FDA. https://www.fda.gov/drugs/risk-evaluation-and-mitigation-strategies-rems/rems-compliance-program. Accessed on: 14.01.2026.
75. FDA Eliminates Risk Evaluation and Mitigation Strategies (REMS) for Autologous Chimeric Antigen Receptor CAR T cell Immunotherapies. FDA. https://www.fda.gov/news-events/press-announcements/fda-eliminates-risk-evaluation-and-mitigation-strategies-rems-autologous-chimeric-antigen-receptor. Accessed on: 14.01.2026.
76. Si, S. & Teachey, D. T. Spotlight on Tocilizumab in the Treatment of CAR-T-Cell-Induced Cytokine Release Syndrome: Clinical Evidence to Date. *Ther. Clin. Risk Manag.* **16**, 705–714 (2020).
77. Ahmed, N., Mahmoudjafari, Z., Hamadani, M. & Hashmi, H. Bridging the Gap: Early Transition and Hybrid Models of Care to Improve Access to Chimeric Antigen Receptor T Cell Therapy. *Transplant. Cell. Ther.* **29**, 399–402 (2023).
78. Locke, F. L., Mahmoudjafari, Z., Kebriaei, P., Gardner, R. A., Frigault, M. J., Frey, N. V., Komanduri, K. V., Perales, M.-A. & Nikiforow, S. Awakening from REMS: ASTCT 80/20 Ongoing Recommendations for Safe Use of Chimeric Antigen Receptor T Cells. *Transplant. Cell. Ther.* **31**, 349.e1-349.e12 (2025).
79. FDA Eliminates Risk Evaluation and Mitigation Strategies (REMS) for Autologous Chimeric Antigen Receptor (CAR) T cell Immunotherapies. FDA. https://www.fda.gov/vaccines-blood-biologics/safety-availability-biologics/fda-eliminates-risk-evaluation-and-mitigation-strategies-rems-autologous-chimeric-antigen-receptor. Accessed on: 14.01.2026.
80. Wucherpfennig, K. W., Gagnon, E., Call, M. J., Huseby, E. S. & Call, M. E. Structural Biology of the T-cell Receptor: Insights into Receptor Assembly, Ligand Recognition, and Initiation of Signaling. *Cold Spring Harb. Perspect. Biol.* **2**, a005140 (2010).
81. Kuhns, M. S. & Badgandi, H. B. Piecing together the family portrait of TCR-CD3 complexes. *Immunol. Rev.* **250**, 120–143 (2012).
82. Lee, Y.-H. & Kim, C. H. Evolution of chimeric antigen receptor (CAR) T cell therapy: current status and future perspectives. *Arch. Pharm. Res.* **42**, 607–616 (2019).
83. Wang, D., Aguilar, B., Starr, R., Alizadeh, D., Brito, A., Sarkissian, A., Ostberg, J. R., Forman, S. J. & Brown, C. E. Glioblastoma-targeted $CD4^+$ CAR T cells mediate superior antitumor activity. *JCI Insight* **3**, (2018).
84. Sommermeyer, D., Hudecek, M., Kosasih, P. L., Gogishvili, T., Maloney, D. G., Turtle, C. J. & Riddell, S. R. Chimeric antigen receptor-modified T cells derived from defined

CD8+ and CD4+ subsets confer superior antitumor reactivity in vivo. *Leukemia* **30**, 492–500 (2016).
85. Fraietta, J. A., Lacey, S. F., Orlando, E. J., Pruteanu-Malinici, I., Gohil, M., Lundh, S., Boesteanu, A. C., Wang, Y., O'Connor, R. S., Hwang, W.-T., Pequignot, E., Ambrose, D. E., Zhang, C., Wilcox, N., Bedoya, F., Dorfmeier, C., Chen, F., Tian, L., Parakandi, H., Gupta, M., Young, R. M., Johnson, F. B., Kulikovskaya, I., Liu, L., Xu, J., Kassim, S. H., Davis, M. M., Levine, B. L., Frey, N. V., Siegel, D. L., Huang, A. C., Wherry, E. J., Bitter, H., Brogdon, J. L., Porter, D. L., June, C. H. & Melenhorst, J. J. Determinants of response and resistance to CD19 chimeric antigen receptor (CAR) T cell therapy of chronic lymphocytic leukemia. *Nat. Med.* **24**, 563–571 (2018).
86. Klebanoff, C. A., Gattinoni, L. & Restifo, N. P. Sorting Through Subsets: Which T-Cell Populations Mediate Highly Effective Adoptive Immunotherapy? *J. Immunother.* **35**, 651 (2012).
87. Korell, F., Berger, T. R. & Maus, M. V. Understanding CAR T cell-tumor interactions: Paving the way for successful clinical outcomes. *Med* **3**, 538–564 (2022).
88. Zarychta, J., Kowalczyk, A., Krawczyk, M., Lejman, M. & Zawitkowska, J. CAR-T Cells Immunotherapies for the Treatment of Acute Myeloid Leukemia—Recent Advances. *Cancers* **15**, (2023).
89. Watanabe, K., Kuramitsu, S., Posey, A. D. & June, C. H. Expanding the Therapeutic Window for CAR T Cell Therapy in Solid Tumors: The Knowns and Unknowns of CAR T Cell Biology. *Front. Immunol.* **9**, (2018).
90. Davenport, A. J., Cross, R. S., Watson, K. A., Liao, Y., Shi, W., Prince, H. M., Beavis, P. A., Trapani, J. A., Kershaw, M. H., Ritchie, D. S., Darcy, P. K., Neeson, P. J. & Jenkins, M. R. Chimeric antigen receptor T cells form nonclassical and potent immune synapses driving rapid cytotoxicity. *Proc. Natl. Acad. Sci.* **115**, E2068–E2076 (2018).
91. Xiong, W., Chen, Y., Kang, X., Chen, Z., Zheng, P., Hsu, Y.-H., Jang, J. H., Qin, L., Liu, H., Dotti, G. & Liu, D. Immunological Synapse Predicts Effectiveness of Chimeric Antigen Receptor Cells. *Mol. Ther.* **26**, 963–975 (2018).
92. Davenport, A. J., Jenkins, M. R., Cross, R. S., Yong, C. S., Prince, H. M., Ritchie, D. S., Trapani, J. A., Kershaw, M. H., Darcy, P. K. & Neeson, P. J. CAR-T Cells Inflict Sequential Killing of Multiple Tumor Target Cells. *Cancer Immunol. Res.* **3**, 483–494 (2015).
93. Davenport, A. J. & Jenkins, M. R. Programming a serial killer: CAR T cells form non-classical immune synapses. *Oncoscience* **5**, 69–70 (2018).
94. Mamonkin, M., Rouce, R. H., Tashiro, H. & Brenner, M. K. A T-cell–directed chimeric antigen receptor for the selective treatment of T-cell malignancies. *Blood* **126**, 983–992 (2015).
95. Benmebarek, M.-R., Karches, C. H., Cadilha, B. L., Lesch, S., Endres, S. & Kobold, S. Killing Mechanisms of Chimeric Antigen Receptor (CAR) T Cells. *Int. J. Mol. Sci.* **20**, (2019).
96. Agliardi, G., Dias, J., Rampotas, A., Garcia, J. & Roddie, C. Accelerating and optimising CAR T-cell manufacture to deliver better patient products. *Lancet Haematol.* **12**, e57–e67 (2025).
97. Pène, J., Rahmoun, M., Temmerman, S. & Yssel, H. Use of anti-CD3/CD28 mAb coupled magnetic beads permitting subsequent phenotypic analysis of activated human T cells by indirect immunofluorescence. *J. Immunol. Methods* **283**, 59–66 (2003).
98. Kabakibo, T. S., Arnold, E., Padhan, K., Lemieux, A., Ortega-Delgado, G. G., Routy, J.-P., Shoukry, N., Dubé, M. & Kaufmann, D. E. Artificial antigen-presenting cell system reveals CD28's role in modulating T cell functions during human immunodeficiency virus infection. *iScience* **27**, 110947 (2024).

99. Jassin, M., Silva, B. E., Ormenese, S., Baron, F., Ehx, G. & Caers, J. Comparable restimulation of human T cells activated with CD3/CD28 beads versus soluble antibody complexes. *Sci. Rep.* **16**, 9739 (2026).
100. Qian, Y., Ma, W. & Xu, X.-N. Breakthrough for Anticancer Immunotherapy: Current Advances in Manufacturing Protocols of Chimeric Antigen Receptor-Based Therapies. *Antibodies* **14**, (2025).
101. Package Insert - AUCATZYL. *FDA* https://www.fda.gov/media/183463/download?attachment. Accessed on: 15.01.2026.
102. Allen, E. S., Stroncek, D. F., Ren, J., Eder, A. F., West, K. A., Fry, T. J., Lee, D. W., Mackall, C. L. & Conry-Cantilena, C. Autologous lymphapheresis for the production of chimeric antigen receptor T cells. *Transfusion (Paris)* **57**, 1133–1141 (2017).
103. Ghassemi, S., Nunez-Cruz, S., O'Connor, R. S., Fraietta, J. A., Patel, P. R., Scholler, J., Barrett, D. M., Lundh, S. M., Davis, M. M., Bedoya, F., Zhang, C., Leferovich, J., Lacey, S. F., Levine, B. L., Grupp, S. A., June, C. H., Melenhorst, J. J. & Milone, M. C. Reducing Ex Vivo Culture Improves the Antileukemic Activity of Chimeric Antigen Receptor (CAR) T Cells. *Cancer Immunol. Res.* **6**, 1100–1109 (2018).
104. Cliff, E. R. S., Kelkar, A. H., Russler-Germain, D. A., Tessema, F. A., Raymakers, A. J. N., Feldman, W. B. & Kesselheim, A. S. High Cost of Chimeric Antigen Receptor T-Cells: Challenges and Solutions. *Am. Soc. Clin. Oncol. Educ. Book* e397912 (2023).
105. Keating, S. J., Gu, T., Jun, M. P. & McBride, A. Health Care Resource Utilization and Total Costs of Care Among Patients with Diffuse Large B Cell Lymphoma Treated with Chimeric Antigen Receptor T Cell Therapy in the United States. *Transplant. Cell. Ther.* **28**, 404.e1-404.e6 (2022).
106. Zhong, Y. & Liu, J. Emerging roles of CAR-NK cell therapies in tumor immunotherapy: current status and future directions. *Cell Death Discov.* **10**, 318 (2024).
107. Vivier, E., Tomasello, E., Baratin, M., Walzer, T. & Ugolini, S. Functions of natural killer cells. *Nat. Immunol.* **9**, 503–510 (2008).
108. Marin, D., Li, Y., Basar, R., Rafei, H., Daher, M., Dou, J., Mohanty, V., Dede, M., Nieto, Y., Uprety, N., Acharya, S., Liu, E., Wilson, J., Banerjee, P., Macapinlac, H. A., Ganesh, C., Thall, P. F., Bassett, R., Ammari, M., Rao, S., Cao, K., Shanley, M., Kaplan, M., Hosing, C., Kebriaei, P., Nastoupil, L. J., Flowers, C. R., Moseley, S. M., Lin, P., Ang, S., Popat, U. R., Qazilbash, M. H., Champlin, R. E., Chen, K., Shpall, E. J. & Rezvani, K. Safety, efficacy and determinants of response of allogeneic CD19-specific CAR-NK cells in CD19+ B cell tumors: a phase 1/2 trial. *Nat. Med.* **30**, 772–784 (2024).
109. Jia, H., Yang, H., Xiong, H. & Luo, K. Q. NK cell exhaustion in the tumor microenvironment. *Front. Immunol.* **14**, (2023).
110. Cooper, M. A., Fehniger, T. A. & Caligiuri, M. A. The biology of human natural killer-cell subsets. *Trends Immunol.* **22**, 633–640 (2001).
111. Palani, H. K., Arunachalam, A. K., Kulkarni, U., Yasar, M., Venkatraman, A., Palanikumar, S., Radhakrishnan, R. N., Solomon, M., Rajasekaran, A., Bankar, A., Datari, P. V. R., Selvarajan, S., Korula, A., Dash, P., Schneider, D., Wirthlin, L., Abraham, A., George, B. & Mathews, V. Safety, efficacy and total cost of point-of-care manufactured anti-CD19 CAR-T cell therapy in India: VELCART trial. *Mol. Ther. Oncol.* **33**, (2025).
112. Palani, H. K., Arunachalam, A. K., Yasar, M., Venkatraman, A., Kulkarni, U., Lionel, S. A., Selvarajan, S., Korula, A., Abraham, A., George, B., Adair, J. E., Orentas, R., Dropulic, B. & Mathews, V. Decentralized manufacturing of anti CD19 CAR-T cells

using CliniMACS Prodigy®: real-world experience and cost analysis in India. *Bone Marrow Transplant.* **58**, 160–167 (2023).
113. Abdo, L., Batista-Silva, L. R. & Bonamino, M. H. Cost-effective strategies for CAR-T cell therapy manufacturing. *Mol. Ther. Oncol.* **33**, 200980 (2025).
114. Mallapaty, S. Cutting-edge CAR-T cancer therapy is now made in India — at one-tenth the cost. *Nature* **627**, 709–710 (2024).
115. India Achieves Major Healthcare Milestone with World's First Humanized CAR-T Therapy | PackGene Biotech. *Packgene Biotech Inc.* https://www.packgene.com/frontier/110525-india/. Accessed on: 26.03.2026.
116. Zhang, X. & Godbey, W. T. Viral vectors for gene delivery in tissue engineering. *Adv. Drug Deliv. Rev.* **58**, 515–534 (2006).
117. Yu, S. F., von Rüden, T., Kantoff, P. W., Garber, C., Seiberg, M., Rüther, U., Anderson, W. F., Wagner, E. F. & Gilboa, E. Self-inactivating retroviral vectors designed for transfer of whole genes into mammalian cells. *Proc. Natl. Acad. Sci. U. S. A.* **83**, 3194–3198 (1986).
118. Barquinero, J., Eixarch, H. & Pérez-Melgosa, M. Retroviral vectors: new applications for an old tool. *Gene Ther.* **11**, S3–S9 (2004).
119. Zufferey, R., Dull, T., Mandel, R. J., Bukovsky, A., Quiroz, D., Naldini, L. & Trono, D. Self-Inactivating Lentivirus Vector for Safe and Efficient In Vivo Gene Delivery. *J. Virol.* **72**, 9873–9880 (1998).
120. Chameettachal, A., Mustafa, F. & Rizvi, T. A. Understanding Retroviral Life Cycle and its Genomic RNA Packaging. *J. Mol. Biol.* **435**, 167924 (2023).
121. Swanson, R. & Wills, J. Overview of Retroviral Assembly. in *Retroviruses* (eds Coffin, J. M., Hughes, S. H. & Varmus, H. E.) (Cold Spring Harbor Laboratory Press, 1997).
122. Lesnik, E. A., Sampath, R. & Ecker, D. J. Rev response elements (RRE) in lentiviruses: An RNAMotif algorithm-based strategy for RRE prediction. *Med. Res. Rev.* **22**, 617–636 (2002).
123. Ferreira, M. V., Cabral, E. T. & Coroadinha, A. S. Progress and Perspectives in the Development of Lentiviral Vector Producer Cells. *Biotechnol. J.* **16**, 2000017 (2021).
124. Finkelshtein, D., Werman, A., Novick, D., Barak, S. & Rubinstein, M. LDL receptor and its family members serve as the cellular receptors for vesicular stomatitis virus. *Proc. Natl. Acad. Sci.* **110**, 7306–7311 (2013).
125. Amirache, F., Lévy, C., Costa, C., Mangeot, P.-E., Torbett, B. E., Wang, C. X., Nègre, D., Cosset, F.-L. & Verhoeyen, E. Mystery solved: VSV-G-LVs do not allow efficient gene transfer into unstimulated T cells, B cells, and HSCs because they lack the LDL receptor. *Blood* **123**, 1422–1424 (2014).
126. von Kalle, C., Kiem, H., Goehle, S., Darovsky, B., Heimfeld, S., Torok-Storb, B., Storb, R. & Schuening, F. Increased gene transfer into human hematopoietic progenitor cells by extended in vitro exposure to a pseudotyped retroviral vector. *Blood* **84**, 2890–2897 (1994).
127. Ghani, K., Wang, X., de Campos-Lima, P. O., Olszewska, M., Kamen, A., Rivière, I. & Caruso, M. Efficient Human Hematopoietic Cell Transduction Using RD114- and GALV-Pseudotyped Retroviral Vectors Produced in Suspension and Serum-Free Media. *Hum. Gene Ther.* **20**, 966–974 (2009).
128. Olah, Z., Lehel, C., Anderson, W. B., Eiden, M. V. & Wilson, C. A. The cellular receptor for gibbon ape leukemia virus is a novel high affinity sodium-dependent phosphate transporter. *J. Biol. Chem.* **269**, 25426–25431 (1994).
129. Farrell, K. B., Tusnady, G. E. & Eiden, M. V. New Structural Arrangement of the Extracellular Regions of the Phosphate Transporter SLC20A1, the Receptor for Gibbon Ape Leukemia Virus*. *J. Biol. Chem.* **284**, 29979–29987 (2009).

130. Relander, T., Brun, A. C. M., Olsson, K., Pedersen, L. & Richter, J. Overexpression of Gibbon Ape Leukemia Virus (GALV) Receptor (GLVR1) on Human CD34+ Cells Increases Gene Transfer Mediated by GALV Pseudotyped Vectors. *Mol. Ther.* **6**, 400–406 (2002).
131. van Zeijl, M., Johann, S. V., Closs, E., Cunningham, J., Eddy, R., Shows, T. B. & O'Hara, B. A human amphotropic retrovirus receptor is a second member of the gibbon ape leukemia virus receptor family. *Proc. Natl. Acad. Sci.* **91**, 1168–1172 (1994).
132. Watanabe, N. & McKenna, M. K. Generation of CAR T-cells using γ-retroviral vector. *Methods Cell Biol.* **167**, 171–183 (2022).
133. Gouvarchin Ghaleh, H. E., Bolandian, M., Dorostkar, R., Jafari, A. & Pour, M. F. Concise review on optimized methods in production and transduction of lentiviral vectors in order to facilitate immunotherapy and gene therapy. *Biomed. Pharmacother.* **128**, 110276 (2020).
134. Tridgett, M., Mulet, M., Johny, S. P., Ababi, M., Raghunath, M., Fustinoni, C., Galabova, B., Fernández-Díaz, C., Mikalajūnaitė, I., Tomás, H. A., Kucej, M., Dunajová, L., Zgrundo, Z., Page, E., McCall, L., Parker-Manuel, R., Payne, T., Peckett, M., Kent, J., Holland, L., Asatryan, R., Montgomery, L., Chow, T. L., Beveridge, R., Salkauskaite, I., Alam, M. T., Hollard, D., Dowding, S., Gabriel, H. B., Branciaroli, C., Cawood, R., Valenti, W., Chang, D., Patrício, M. I. & Liu, Q. Lentiviral vector packaging and producer cell lines yield titers equivalent to the industry-standard four-plasmid process. *Mol. Ther. Methods Clin. Dev.* **32**, (2024).
135. Sheridan, P. L., Bodner, M., Lynn, A., Phuong, T. K., DePolo, N. J., de la Vega, D. J., O'Dea, J., Nguyen, K., McCormack, J. E., Driver, D. A., Townsend, K., Ibañez, C. E., Sajjadi, N. C., Greengard, J. S., Moore, M. D., Respess, J., Chang, S. M. W., Dubensky, T. W., Jolly, D. J. & Sauter, S. L. Generation of Retroviral Packaging and Producer Cell Lines for Large-Scale Vector Production and Clinical Application: Improved Safety and High Titer. *Mol. Ther.* **2**, 262–275 (2000).
136. Tomás, H. A., Rodrigues, A. F., Carrondo, M. J. T. & Coroadinha, A. S. LentiPro26: novel stable cell lines for constitutive lentiviral vector production. *Sci. Rep.* **8**, 5271 (2018).
137. Chang, T. & Yee, J.-K. Chapter one - General Principles of Retrovirus Vector Design. in *Methods in Enzymology* vol. 507 1–14 (Academic Press, 2012).
138. Kurian, K. M., Watson, C. J. & Wyllie, A. H. Retroviral vectors. *Mol. Pathol.* **53**, 173–176 (2000).
139. McClure, M. O., Sommerfelt, M. A., Marsh, M. & Weiss, R. A. The pH independence of mammalian retrovirus infection. *J. Gen. Virol.* **71**, 767–773 (1990).
140. McClure, M. O., Marsh, M. & Weiss, R. A. Human immunodeficiency virus infection of CD4-bearing cells occurs by a pH-independent mechanism. *EMBO J.* **7**, 513–518 (1988).
141. Nussbaum, O., Roop, A. & Anderson, W. F. Sequences determining the pH dependence of viral entry are distinct from the host range-determining region of the murine ecotropic and amphotropic retrovirus envelope proteins. *J. Virol.* **67**, 7402–7405 (1993).
142. Katen, L. J., Januszeski, M. M., Anderson, W. F., Hasenkrug, K. J. & Evans, L. H. Infectious Entry by Amphotropic as well as Ecotropic Murine Leukemia Viruses Occurs through an Endocytic Pathway. *J. Virol.* **75**, 5018–5026 (2001).
143. Gao, Y., Hu, J., An, N., Wen, X. & Li, C. In vivo engineering of CAR-T cells: delivery strategies and clinical translation. *Biomark. Res.* **14**, 23 (2026).
144. Meier, C., Weil, T., Kirchhoff, F. & Münch, J. Peptide nanofibrils as enhancers of retroviral gene transfer. *WIREs Nanomedicine Nanobiotechnology* **6**, 438–451 (2014).

145. Guibinga, G. H., Miyanohara, A., Esko, J. D. & Friedmann, T. Cell surface heparan sulfate is a receptor for attachment of envelope protein-free retrovirus-like particles and VSV-G pseudotyped MLV-derived retrovirus vectors to target cells. *Mol. Ther. J. Am. Soc. Gene Ther.* **5**, 538–546 (2002).
146. Pizzato, M., Marlow, S. A., Blair, E. D. & Takeuchi, Y. Initial Binding of Murine Leukemia Virus Particles to Cells Does Not Require Specific Env-Receptor Interaction. *J. Virol.* **73**, 8599–8611 (1999).
147. Marsh, M. & Helenius, A. Virus Entry: Open Sesame. *Cell* **124**, 729–740 (2006).
148. Davis, H. E., Rosinski, M., Morgan, J. R. & Yarmush, M. L. Charged Polymers Modulate Retrovirus Transduction via Membrane Charge Neutralization and Virus Aggregation. *Biophys. J.* **86**, 1234–1242 (2004).
149. Denning, W., Das, S., Guo, S., Xu, J., Kappes, J. C. & Hel, Z. Optimization of the transductional efficiency of lentiviral vectors: effect of sera and polycations. *Mol. Biotechnol.* **53**, 308–314 (2013).
150. Davis, H. E., Morgan, J. R. & Yarmush, M. L. Polybrene increases retrovirus gene transfer efficiency by enhancing receptor-independent virus adsorption on target cell membranes. *Biophys. Chem.* **97**, 159–172 (2002).
151. Lin, P., Correa, D., Lin, Y. & Caplan, A. I. Polybrene Inhibits Human Mesenchymal Stem Cell Proliferation during Lentiviral Transduction. *PLOS ONE* **6**, e23891 (2011).
152. Rajabzadeh, A., Hamidieh, A. A. & Rahbarizadeh, F. Spinoculation and retronectin highly enhance the gene transduction efficiency of Mucin-1-specific chimeric antigen receptor (CAR) in human primary T cells. *BMC Mol. Cell Biol.* **22**, 57 (2021).
153. Cornetta, K. & Anderson, W. F. Protamine sulfate as an effective alternative to polybrene in retroviral-mediated gene-transfer: implications for human gene therapy. *J. Virol. Methods* **23**, 187–194 (1989).
154. Levy, J. H., Ghadimi, K., Kizhakkedathu, J. N. & Iba, T. What's fishy about protamine? Clinical use, adverse reactions, and potential alternatives. *J. Thromb. Haemost.* **21**, 1714–1723 (2023).
155. Rajabzadeh, A., Hamidieh, A. A. & Rahbarizadeh, F. Spinoculation and retronectin highly enhance the gene transduction efficiency of Mucin-1-specific chimeric antigen receptor (CAR) in human primary T cells. *BMC Mol. Cell Biol.* **22**, 57 (2021).
156. Pollok, K. E., Hanenberg, H., Noblitt, T. W., Schroeder, W. L., Kato, I., Emanuel, D. & Williams, D. A. High-Efficiency Gene Transfer into Normal and Adenosine Deaminase-Deficient T Lymphocytes Is Mediated by Transduction on Recombinant Fibronectin Fragments. *J. Virol.* **72**, 4882–4892 (1998).
157. Nasiri, F., Muhammadnejad, S. & Rahbarizadeh, F. Effects of polybrene and retronectin as transduction enhancers on the development and phenotypic characteristics of VHH-based CD19-redirected CAR T cells: a comparative investigation. *Clin. Exp. Med.* **23**, 2535–2549 (2023).
158. Radek, C., Bernadin, O., Drechsel, K., Cordes, N., Pfeifer, R., Sträßer, P., Mormin, M., Gutierrez-Guerrero, A., Cosset, F., Kaiser, A. D., Schaser, T., Galy, A., Verhoeyen, E. & Johnston, I. C. D. Vectofusin-1 Improves Transduction of Primary Human Cells with Diverse Retroviral and Lentiviral Pseudotypes, Enabling Robust, Automated Closed-System Manufacturing. *Hum. Gene Ther.* **30**, 1477–1493 (2019).
159. Tumaini, B., Lee, D. W., Lin, T., Castiello, L., Stroncek, D. F., Mackall, C., Wayne, A. & Sabatino, M. Simplified process for the production of anti-CD19-CAR-engineered T cells. *Cytotherapy* **15**, 1406–1415 (2013).
160. Davis, L. S., Oppenheimer-Marks, N., Bednarczyk, J. L., McIntyre, B. W. & Lipsky, P. E. Fibronectin promotes proliferation of naive and memory T cells by signaling

through both the VLA-4 and VLA-5 integrin molecules. *J. Immunol.* **145**, 785–793 (1990).
161. Mizobata, S., Tanimura, H., Yamaue, H., Tani, M., Tsunoda, T., Iwahashi, M., Noguchi, K., Nishimoto, N., Hotta, T. & Arii, K. Fibronectin promotes the proliferation of cytotoxic T lymphocytes generated from cancer patients. *Br. J. Cancer* **74**, 1598–1604 (1996).
162. Han, L., Shang, Y.-M., Song, Y.-P. & Gao, Q.-L. Biological Character of RetroNectin Activated Cytokine-Induced Killer Cells. *J. Immunol. Res.* **2016**, 5706814 (2016).
163. Stock, S., Hoffmann, J.-M., Schubert, M.-L., Wang, L., Wang, S., Gong, W., Neuber, B., Gern, U., Schmitt, A., Müller-Tidow, C., Dreger, P., Schmitt, M. & Sellner, L. Influence of Retronectin-Mediated T-Cell Activation on Expansion and Phenotype of CD19-Specific Chimeric Antigen Receptor T Cells. *Hum. Gene Ther.* **29**, 1167–1182 (2018).
164. Berggren, W. T., Lutz, M. & Modesto, V. General Spinfection Protocol. in *StemBook* (Harvard Stem Cell Institute, Cambridge (MA), 2008).
165. Han, L., Shang, Y.-M., Song, Y.-P. & Gao, Q.-L. Biological Character of RetroNectin Activated Cytokine-Induced Killer Cells. *J. Immunol. Res.* **2016**, 5706814 (2016).
166. Chandrudu, S., Simerska, P. & Toth, I. Chemical methods for peptide and protein production. *Molecules* **18**, 4373–4388 (2013).
167. Münch, J., Rücker, E., Ständker, L., Adermann, K., Goffinet, C., Schindler, M., Wildum, S., Chinnadurai, R., Rajan, D., Specht, A., Giménez-Gallego, G., Sánchez, P. C., Fowler, D. M., Koulov, A., Kelly, J. W., Mothes, W., Grivel, J.-C., Margolis, L., Keppler, O. T., Forssmann, W.-G. & Kirchhoff, F. Semen-derived amyloid fibrils drastically enhance HIV infection. *Cell* **131**, 1059–1071 (2007).
168. Yolamanova, M., Meier, C., Shaytan, A. K., Vas, V., Bertoncini, C. W., Arnold, F., Zirafi, O., Usmani, S. M., Müller, J. A., Sauter, D., Goffinet, C., Palesch, D., Walther, P., Roan, N. R., Geiger, H., Lunov, O., Simmet, T., Bohne, J., Schrezenmeier, H., Schwarz, K., Ständker, L., Forssmann, W.-G., Salvatella, X., Khalatur, P. G., Khokhlov, A. R., Knowles, T. P. J., Weil, T., Kirchhoff, F. & Münch, J. Peptide nanofibrils boost retroviral gene transfer and provide a rapid means for concentrating viruses. *Nat. Nanotechnol.* **8**, 130–136 (2013).
169. Sieste, S., Mack, T., Lump, E., Hayn, M., Schütz, D., Röcker, A., Meier, C., Kaygisiz, K., Kirchhoff, F., Knowles, T. P. J., Ruggeri, F. S., Synatschke, C. V., Münch, J. & Weil, T. Supramolecular Peptide Nanofibrils with Optimized Sequences and Molecular Structures for Efficient Retroviral Transduction. *Adv. Funct. Mater.* **31**, 2009382 (2021).
170. Kaygisiz, K., Dutta, A., Rauch-Wirth, L., Synatschke, C. V., Münch, J., Bereau, T. & Weil, T. Inverse design of viral infectivity-enhancing peptide fibrils from continuous protein-vector embeddings. *Biomater. Sci.* **11**, 5251–5261 (2023).
171. Kaygisiz, K., Rauch-Wirth, L., Iscen, A., Hartenfels, J., Kremer, K., Münch, J., Synatschke, C. V. & Weil, T. Peptide Amphiphiles as Biodegradable Adjuvants for Efficient Retroviral Gene Delivery. *Adv. Healthc. Mater.* **13**, 2301364 (2024).
172. Wurm, M., Schambach, A., Lindemann, D., Hanenberg, H., Ständker, L., Forssmann, W. G., Blasczyk, R. & Horn, P. A. The influence of semen-derived enhancer of virus infection on the efficiency of retroviral gene transfer. *J. Gene Med.* **12**, 137–146 (2010).
173. Castro, A., Drosch, M., Liesenfeld, M., Kaan, T., Schilz, A., Wenschuh, H., Forsmann, W. & Kuhlke, K. Protransduzin™ - A novel transduction enhancer to accelerate en gros CAR-T production. *Cytotherapy* **21**, e14 (2019).
174. Rode, S. Elucidation of cell interaction and fate of EF-C peptide nanofibrils. Dissertation. (Ulm University, 2017).

175. Schütz, D. Mechanistic studies on transduction enhancing EF-C peptide nanofibrils and optimization for gene therapeutic applications. Dissertation. (Ulm University, 2021).
176. Guideline on the Development and Manufacture of Synthetic Peptides. *EMA* https://www.ema.europa.eu/en/documents/scientific-guideline/guideline-development-manufacture-synthetic-peptides_en.pdf. Accessed on: 02.11.2026.
177. Elsayed, Y. Y., Kühl, T. & Imhof, D. Regulatory Guidelines for the Analysis of Therapeutic Peptides and Proteins. *J. Pept. Sci.* **31**, e70001 (2025).
178. Fenard, D., Genries, S., Scherman, D., Galy, A., Martin, S. & Kichler, A. Infectivity enhancement of different HIV-1-based lentiviral pseudotypes in presence of the cationic amphipathic peptide LAH4-L1. *J. Virol. Methods* **189**, 375–378 (2013).
179. Kichler, A., Leborgne, C., Danos, O. & Bechinger, B. Characterization of the gene transfer process mediated by histidine-rich peptides. *J. Mol. Med.* **85**, 191–201 (2007).
180. Ingrao, D., Majdoul, S., Seye, A. K., Galy, A. & Fenard, D. Concurrent Measures of Fusion and Transduction Efficiency of Primary CD34+ Cells with Human Immunodeficiency Virus 1-Based Lentiviral Vectors Reveal Different Effects of Transduction Enhancers. *Hum. Gene Ther. Methods* **25**, 48–56 (2014).
181. Vermeer, L. S., Hamon, L., Schirer, A., Schoup, M., Cosette, J., Majdoul, S., Pastré, D., Stockholm, D., Holic, N., Hellwig, P., Galy, A., Fenard, D. & Bechinger, B. Vectofusin-1, a potent peptidic enhancer of viral gene transfer forms pH-dependent α-helical nanofibrils, concentrating viral particles. *Acta Biomater.* **64**, 259–268 (2017).
182. Piovan, C., Marin, V., Scavullo, C., Corna, S., Giuliani, E., Bossi, S., Galy, A., Fenard, D., Bordignon, C., Rizzardi, G. P. & Bovolenta, C. Vectofusin-1 Promotes RD114-TR-Pseudotyped Lentiviral Vector Transduction of Human HSPCs and T Lymphocytes. *Mol. Ther. Methods Clin. Dev.* **5**, 22–30 (2017).
183. Majdoul, S., Seye, A. K., Kichler, A., Holic, N., Galy, A., Bechinger, B. & Fenard, D. Molecular Determinants of Vectofusin-1 and Its Derivatives for the Enhancement of Lentivirally Mediated Gene Transfer into Hematopoietic Stem/Progenitor Cells. *J. Biol. Chem.* **291**, 2161–2169 (2016).
184. Müller, S., Bexte, T., Gebel, V., Kalensee, F., Stolzenberg, E., Hartmann, J., Koehl, U., Schambach, A., Wels, W. S., Modlich, U. & Ullrich, E. High Cytotoxic Efficiency of Lentivirally and Alpharetrovirally Engineered CD19-Specific Chimeric Antigen Receptor Natural Killer Cells Against Acute Lymphoblastic Leukemia. *Front. Immunol.* **10**, 3123 (2020).
185. MACS® GMP Vectofusin®-1. *Miltenyi Biotec* https://www.miltenyibiotec.com/DE-en/products/macs-gmp-vectofusin-1.html#170-076-165. Accessed on: 09.02.2026.
186. Jamali, A., Kapitza, L., Schaser, T., Johnston, I. C. D., Buchholz, C. J. & Hartmann, J. Highly Efficient and Selective CAR-Gene Transfer Using CD4- and CD8-Targeted Lentiviral Vectors. *Mol. Ther. Methods Clin. Dev.* **13**, 371–379 (2019).
187. Kim, K.-A., Yolamanova, M., Zirafi, O., Roan, N. R., Staendker, L., Forssmann, W.-G., Burgener, A., Dejucq-Rainsford, N., Hahn, B. H., Shaw, G. M., Greene, W. C., Kirchhoff, F. & Münch, J. Semen-mediated enhancement of HIV infection is donor-dependent and correlates with the levels of SEVI. *Retrovirology* **7**, 55 (2010).
188. Roan, N. R., Münch, J., Arhel, N., Mothes, W., Neidleman, J., Kobayashi, A., Smith-McCune, K., Kirchhoff, F. & Greene, W. C. The Cationic Properties of SEVI Underlie Its Ability To Enhance Human Immunodeficiency Virus Infection. *J. Virol.* **83**, 73–80 (2009).
189. Kaygisiz, K., Rauch-Wirth, L., Dutta, A., Yu, X., Nagata, Y., Bereau, T., Münch, J., Synatschke, C. V. & Weil, T. Data-mining unveils structure–property–activity correlation of viral infectivity enhancing self-assembling peptides. *Nat. Commun.* **14**, 5121 (2023).

190. Schütz, D., Rode, S., Read, C., Müller, J. A., Glocker, B., Sparrer, K. M. J., Fackler, O. T., Walther, P. & Münch, J. Viral Transduction Enhancing Effect of EF-C Peptide Nanofibrils Is Mediated by Cellular Protrusions. *Adv. Funct. Mater.* **31**, 2104814 (2021).
191. Müller, J.-A. The versatile role of semen and seminal amyloid in virus infection. Dissertation. (Ulm University, 2016).
192. Schütz, D., Read, C., Groß, R., Röcker, A., Rode, S., Annamalai, K., Fändrich, M. & Münch, J. Negatively Charged Peptide Nanofibrils from Immunoglobulin Light Chain Sequester Viral Particles but Lack Cell-Binding and Viral Transduction-Enhancing Properties. *ACS Omega* **6**, 7731–7738 (2021).
193. Dmitrieff, S. & Nédélec, F. Membrane Mechanics of Endocytosis in Cells with Turgor. *PLoS Comput. Biol.* **11**, e1004538 (2015).
194. Rode, S., Hayn, M., Röcker, A., Sieste, S., Lamla, M., Markx, D., Meier, C., Kirchhoff, F., Walther, P., Fändrich, M., Weil, T. & Münch, J. Generation and Characterization of Virus-Enhancing Peptide Nanofibrils Functionalized with Fluorescent Labels. *Bioconjug. Chem.* **28**, 1260–1270 (2017).
195. Borle, A. B. Kinetic analyses of calcium movements in HeLa cell cultures. I. Calcium influx. *J. Gen. Physiol.* **53**, 43–56 (1969).
196. James, M. B. & Giorgio, T. D. Nuclear-Associated Plasmid, but Not Cell-Associated Plasmid, Is Correlated with Transgene Expression in Cultured Mammalian Cells. *Mol. Ther.* **1**, 339–346 (2000).
197. Jiang, X., Dudzinski, S., Beckermann, K. E., Young, K., McKinley, E., McIntyre, J. O., Rathmell, J. C., Xu, J. & Gore, J. C. MRI of tumor T cell infiltration in response to checkpoint inhibitor therapy. *J. Immunother. Cancer* **8**, e000328 (2020).
198. Swanson, J. A. Shaping cups into phagosomes and macropinosomes. *Nat. Rev. Mol. Cell Biol.* **9**, 639–649 (2008).
199. Bayati, A., Banks, E., Han, C., Luo, W., Reintsch, W. E., Zorca, C. E., Shlaifer, I., Del Cid Pellitero, E., Vanderperre, B., McBride, H. M., Fon, E. A., Durcan, T. M. & McPherson, P. S. Rapid macropinocytic transfer of α-synuclein to lysosomes. *Cell Rep.* **40**, 111102 (2022).
200. Holmes, B. B., DeVos, S. L., Kfoury, N., Li, M., Jacks, R., Yanamandra, K., Ouidja, M. O., Brodsky, F. M., Marasa, J., Bagchi, D. P., Kotzbauer, P. T., Miller, T. M., Papy-Garcia, D. & Diamond, M. I. Heparan sulfate proteoglycans mediate internalization and propagation of specific proteopathic seeds. *Proc. Natl. Acad. Sci.* **110**, E3138–E3147 (2013).
201. Chen, B. Molecular Mechanism of HIV-1 Entry. *Trends Microbiol.* **27**, 878–891 (2019).
202. Racoosin, E. L. & Swanson, J. A. Macropinosome maturation and fusion with tubular lysosomes in macrophages. *J. Cell Biol.* **121**, 1011–1020 (1993).
203. Kovács, A. L., Reith, A. & Seglen, P. O. Accumulation of autophagosomes after inhibition of hepatocytic protein degradation by vinblastine, leupeptin or a lysosomotropic amine. *Exp. Cell Res.* **137**, 191–201 (1982).
204. Lundahl, M. L. E., Fogli, S., Colavita, P. E. & Scanlan, E. M. Aggregation of protein therapeutics enhances their immunogenicity: causes and mitigation strategies. *RSC Chem. Biol.* **2**, 1004–1020 (2021).
205. Hu, B.-R., Janelidze, S., Ginsberg, M. D., Busto, R., Perez-Pinzon, M., Sick, T. J., Siesjö, B. K. & Liu, C. L. Protein Aggregation after Focal Brain Ischemia and Reperfusion. *J. Cereb. Blood Flow Metab.* **21**, 865–875 (2001).

206. Take, Y., Chikai, Y., Shimamori, K., Kuragano, M., Kurita, H. & Tokuraku, K. Amyloid β aggregation induces human brain microvascular endothelial cell death with abnormal actin organization. *Biochem. Biophys. Rep.* **29**, 101189 (2022).
207. Roberts, C. J. Therapeutic Protein Aggregation: Mechanisms, Design, and Control. *Trends Biotechnol.* **32**, 372–380 (2014).
208. Gong, W., Hoffmann, J.-M., Stock, S., Wang, L., Liu, Y., Schubert, M.-L., Neuber, B., Hückelhoven-Krauss, A., Gern, U., Schmitt, A., Müller-Tidow, C., Shiku, H., Schmitt, M. & Sellner, L. Comparison of IL-2 vs IL-7/IL-15 for the generation of NY-ESO-1-specific T cells. *Cancer Immunol. Immunother.* **68**, 1195–1209 (2019).
209. Maetzig, T., Galla, M., Baum, C. & Schambach, A. Gammaretroviral Vectors: Biology, Technology and Application. *Viruses* **3**, 677–713 (2011).
210. Christodoulopoulos, I. & Cannon, P. M. Sequences in the Cytoplasmic Tail of the Gibbon Ape Leukemia Virus Envelope Protein That Prevent Its Incorporation into Lentivirus Vectors. *J. Virol.* **75**, 4129–4138 (2001).
211. Sun, X., Roth, S. L., Bialecki, M. A. & Whittaker, G. R. Internalization and fusion mechanism of vesicular stomatitis virus and related rhabdoviruses. *Future Virol.* **5**, 85–96 (2009).
212. Colamartino, A. B. L., Lemieux, W., Bifsha, P., Nicoletti, S., Chakravarti, N., Sanz, J., Roméro, H., Selleri, S., Béland, K., Guiot, M., Tremblay-Laganière, C., Dicaire, R., Barreiro, L., Lee, D. A., Verhoeyen, E. & Haddad, E. Efficient and Robust NK-Cell Transduction With Baboon Envelope Pseudotyped Lentivector. *Front. Immunol.* **10**, (2019).
213. Jung, D., Choi, E., Jeoung, Y.-H., Lee, J., Gong, E.-Y., Jo, S.-G., Noh, K., Ha, K., Wee, G., Kim, H., Jung, J. & Kim, S. Nanobody-Based CAR NK Cells for Possible Immunotherapy of Mesothelin+ Tumors. *Immune Netw.* **25**, e23 (2025).
214. Albinger, N., Müller, S., Kostyra, J., Kuska, J., Mertlitz, S., Penack, O., Zhang, C., Möker, N. & Ullrich, E. Manufacturing of primary CAR-NK cells in an automated system for the treatment of acute myeloid leukemia. *Bone Marrow Transplant.* **59**, 489–495 (2024).
215. Kim, Y., Lee, D. Y., Choi, J. U., Park, J. S., Lee, S. M., Kang, C. H. & Park, C. H. Optimized conditions for gene transduction into primary immune cells using viral vectors. *Sci. Rep.* **13**, 12365 (2023).
216. Napoleone, A., Sebastian, I. R., Marco, F. D., Molin, A., Hussein, M., Kramer, L., Jostock, T., Kelly, T. & Borth, N. Overcoming lentiviral delivery limitations in hard-to-transduce suspension cells for genome-wide CRISPR screening. *Mol. Ther. Adv.* **34**, (2026).
217. Guo, J., Wang, W., Yu, D. & Wu, Y. Spinoculation Triggers Dynamic Actin and Cofilin Activity That Facilitates HIV-1 Infection of Transformed and Resting CD4 T Cells. *J. Virol.* **85**, 9824–9833 (2011).
218. Tan, J. Y. M., Tan, J. C., Wang, C., Wu, L., Gascoigne, N. R. J. & Bhatt, S. Protocol for the simultaneous activation and lentiviral transduction of primary human T cells with artificial T cell receptors. *STAR Protoc.* **6**, 103685 (2025).
219. Delville, M., Soheili, T., Bellier, F., Durand, A., Denis, A., Lagresle-Peyrou, C., Cavazzana, M., Andre-Schmutz, I. & Six, E. A Nontoxic Transduction Enhancer Enables Highly Efficient Lentiviral Transduction of Primary Murine T Cells and Hematopoietic Stem Cells. *Mol. Ther. - Methods Clin. Dev.* **10**, 341–347 (2018).
220. Arcangeli, S., Bove, C., Mezzanotte, C., Camisa, B., Falcone, L., Manfredi, F., Bezzecchi, E., Khoury, R., Norata, R., Sanvito, F., Ponzoni, M., Greco, B., Moresco, M., Carrabba, M., Ciceri, F., Bonini, C., Bondanza, A. & Casucci, M. CAR T cell

manufacturing from naive/stem memory T lymphocytes enhances antitumor responses while curtailing cytokine release syndrome. *J. Clin. Invest.* **132**, (2022).
221. Rosenberg, A. S. Effects of protein aggregates: An immunologic perspective. *AAPS J.* **8**, E501–E507 (2006).
222. Cleland, J. L., Powell, M. F. & Shire, S. J. The development of stable protein formulations: a close look at protein aggregation, deamidation, and oxidation. *Crit. Rev. Ther. Drug Carrier Syst.* **10**, 307–377 (1993).
223. van Beers, M. M. C. & Bardor, M. Minimizing immunogenicity of biopharmaceuticals by controlling critical quality attributes of proteins. *Biotechnol. J.* **7**, 1473–1484 (2012).
224. Iwanaszko, M. & Kimmel, M. NF-κB and IRF pathways: cross-regulation on target genes promoter level. *BMC Genomics* **16**, 307 (2015).
225. Kuzmich, N. N., Sivak, K. V., Chubarev, V. N., Porozov, Y. B., Savateeva-Lyubimova, T. N. & Peri, F. TLR4 Signaling Pathway Modulators as Potential Therapeutics in Inflammation and Sepsis. *Vaccines* **5**, 34 (2017).
226. McAleer, J. P. & Vella, A. T. Understanding how lipopolysaccharide impacts CD4 T cell immunity. *Crit. Rev. Immunol.* **28**, 281–299 (2008).
227. Hilligan, K. L. & Ronchese, F. Antigen presentation by dendritic cells and their instruction of CD4+ T helper cell responses. *Cell. Mol. Immunol.* **17**, 587–599 (2020).
228. J. Münch, D. Schütz & L. Rauch. Fibril peptides. Patent (EP4314030). EPO. https://register.epo.org/application?lng=en&number=EP22713684.
229. Kay, R. R. Macropinocytosis: Biology and mechanisms. *Cells Dev.* **168**, 203713 (2021).
230. Nakase, I., Niwa, M., Takeuchi, T., Sonomura, K., Kawabata, N., Koike, Y., Takehashi, M., Tanaka, S., Ueda, K., Simpson, J. C., Jones, A. T., Sugiura, Y. & Futaki, S. Cellular Uptake of Arginine-Rich Peptides: Roles for Macropinocytosis and Actin Rearrangement. *Mol. Ther.* **10**, 1011–1022 (2004).
231. Nakase, I., Tadokoro, A., Kawabata, N., Takeuchi, T., Katoh, H., Hiramoto, K., Negishi, M., Nomizu, M., Sugiura, Y. & Futaki, S. Interaction of Arginine-Rich Peptides with Membrane-Associated Proteoglycans Is Crucial for Induction of Actin Organization and Macropinocytosis. *Biochemistry* **46**, 492–501 (2007).
232. Morimoto, K., Ishitobi, J., Noguchi, K., Kira, R., Kitayama, Y., Goto, Y., Fujiwara, D., Michigami, M., Harada, A., Takatani-Nakase, T., Fujii, I., Futaki, S., Kanada, M. & Nakase, I. Extracellular Microvesicles Modified with Arginine-Rich Peptides for Active Macropinocytosis Induction and Delivery of Therapeutic Molecules. *ACS Appl. Mater. Interfaces* **16**, 17069–17079 (2024).
233. Lehmann, M. J., Sherer, N. M., Marks, C. B., Pypaert, M. & Mothes, W. Actin- and myosin-driven movement of viruses along filopodia precedes their entry into cells. *J. Cell Biol.* **170**, 317–325 (2005).
234. Nolte-'t Hoen, E., Cremer, T., Gallo, R. C. & Margolis, L. B. Extracellular vesicles and viruses: Are they close relatives? *Proc. Natl. Acad. Sci.* **113**, 9155–9161 (2016).
235. Schneider, A. & Simons, M. Catching filopodia: Exosomes surf on fast highways to enter cells. *J. Cell Biol.* **213**, 143–145 (2016).
236. Wender, P. A., Mitchell, D. J., Pattabiraman, K., Pelkey, E. T., Steinman, L. & Rothbard, J. B. The design, synthesis, and evaluation of molecules that enable or enhance cellular uptake: Peptoid molecular transporters. *Proc. Natl. Acad. Sci.* **97**, 13003–13008 (2000).
237. Mitchell, D. j., Steinman, L., Kim, D. t., Fathman, C. g. & Rothbard, J. b. Polyarginine enters cells more efficiently than other polycationic homopolymers. *J. Pept. Res.* **56**, 318–325 (2000).

238. Medeiros, A. T., Bubacco, L. & Morgan, J. R. Impacts of increased α-synuclein on clathrin-mediated endocytosis at synapses: implications for neurodegenerative diseases. *Neural Regen. Res.* **13**, 647–648 (2018).
239. Shearer, L. J., Petersen, N. O. & Woodside, M. T. Internalization of α-synuclein oligomers into SH-SY5Y cells. *Biophys. J.* **120**, 877–885 (2021).
240. Ruseska, I. & Zimmer, A. Internalization mechanisms of cell-penetrating peptides. *Beilstein J. Nanotechnol.* **11**, 101–123 (2020).
241. Brelstaff, J., Ossola, B., Neher, J. J., Klingstedt, T., Nilsson, K. P. R., Goedert, M., Spillantini, M. G. & Tolkovsky, A. M. The fluorescent pentameric oligothiophene pFTAA identifies filamentous tau in live neurons cultured from adult P301S tau mice. *Front. Neurosci.* **9**, (2015).
242. Brelstaff, J., Spillantini, M. G. & Tolkovsky, A. M. pFTAA: a high affinity oligothiophene probe that detects filamentous tau in vivo and in cultured neurons. *Neural Regen. Res.* **10**, 1746–1747 (2015).

5 Appendices

5.1 Appendix 1

Rauch-Wirth, L.*, Schütz, D.*, Groß, R., Rode, S., Glocker, B., Müller, J. A., Walther, P., Read, C. & Münch, J. **Transduction enhancing EF-C peptide nanofibrils are endocytosed by macropinocytosis and subsequently degraded.** *Biomaterials* 317, 123044 (2025). https://doi.org/10.1016/j.biomaterials.2024.123044.
* These authors contributed equally.

Reference[1]

License: CC By 4.0 (https://creativecommons.org/licenses/by/4.0/)

Biomaterials 317 (2025) 123044



Contents lists available at ScienceDirect

Biomaterials

journal homepage: www.elsevier.com/locate/biomaterials





Transduction enhancing EF-C peptide nanofibrils are endocytosed by macropinocytosis and subsequently degraded

Lena Rauch-Wirth [a,1], Desiree Schütz [a,1], Rüdiger Groß [a], Sascha Rode [a], Bernhard Glocker [b,c], Janis A. Müller [a,d], Paul Walther [b], Clarissa Read [b], Jan Münch [a,*]

[a] Institute of Molecular Virology, Ulm University Medical Center, Ulm, 89081, Germany
[b] Central Facility for Electron Microscopy, Ulm University, Ulm, 89081, Germany
[c] Department of Ecosystem Biology, Faculty of Science, University of South Bohemia, České Budějovice, 37005, Czech Republic
[d] Institute of Virology, Philipps University Marburg, Marburg, 35043, Germany

ARTICLE INFO

Keywords:
Peptide nanofibrils
Transduction enhancer
Macropinocytosis
Lysosomal degradation
Retroviral transduction

ABSTRACT

Retroviral gene transfer is the preferred method for stable, long-term integration of genetic material into cellular genomes, commonly used to generate chimeric antigen receptor (CAR)-T cells designed to target tumor antigens. However, the efficiency of retroviral gene transfer is often limited by low transduction rates due to low vector titers and electrostatic repulsion between viral particles and cellular membranes. To overcome these limitations, peptide nanofibrils (PNFs) can be applied as transduction enhancers. Among these, PNFs derived from the 12-mer peptide EF-C are well-investigated and commercially available. EF-C PNFs enhance transduction by forming EF-C PNFs/virus complexes that overcome electrostatic repulsion through their polycationic surface and interaction with cellular protrusions. However, the safe application of PNFs as transduction enhancers in gene therapeutic applications requires a fundamental understanding of their transduction-enhancing mechanisms, uptake, and degradation. In this study, we demonstrate that EF-C PNFs induce plasma membrane invaginations, increasing the membrane surface for viral attachment and reducing the distance to the nuclear membrane, thereby facilitating viral entry and transport to the nucleus. Furthermore, we identified macropinocytosis as the main entry pathway for EF-C PNFs and their subsequent degradation by lysosomal peptidases. The lysosomal degradation of EF-C PNFs prevents their accumulation as amyloid deposits, mitigating potential side effects and supporting their safe use in clinical applications.

1. Introduction

For gene therapy, retroviral gene transfer is the preferred method for the stable and long-term integration of genetic material into cellular genomes [1,2]. Lentiviral and retroviral vectors are commonly used to generate chimeric antigen receptor (CAR)-T cells [3], which are autologous engineered T cells designed to target tumor antigens and elicit a potent antitumor immune response [4–6]. Despite its widespread use, the efficiency of retroviral gene transfer is often hampered by low transduction rates. This limitation arises primarily due to two factors: low vector titers and the electrostatic repulsion between the negatively charged viral particles and cellular membranes [7].

To overcome these limitations the 12-mer peptide EF-C (QCKIKQIINMWQ), which is derived from HIV-1 glycoprotein gp120, can be applied as transduction enhancer [8]. EF-C assembles into positively charged β-sheet peptide nanofibrils (PNFs) that form μm-sized aggregates [8,9]. These aggregates capture viral particles and interact with the cellular membrane leading to high attachment rates of viral particles and enhanced transduction efficiency [8]. Furthermore, EF-C PNFs are actively engaged by cellular protrusions such as filipodia, which pull them towards the cell body [10]. This explains the superior performance of EF-C PNFs over other commercially available transduction enhancers such as protamine sulphate, DEAE dextran and polybrene [8]. Furthermore, use of EF-C PNFs leads to similar transduction rates as RetroNectin and Vectofusin-1 [11], both commonly utilized transduction enhancers in the generation of CAR T cells [12–14].

In *ex vivo* clinical applications, such as CAR T cell therapy, cells are modified outside the body in a controlled laboratory setting and then

* Corresponding author. Institute of Molecular Virology, Ulm University Medical Center, Meyerhofstrasse 1, 89081 Ulm, Germany.
E-mail address: jan.muench@uni-ulm.de (J. Münch).
[1] Contributed equally.

https://doi.org/10.1016/j.biomaterials.2024.123044
Received 14 August 2024; Received in revised form 17 December 2024; Accepted 21 December 2024
Available online 25 December 2024
0142-9612/© 2025 The Authors. Published by Elsevier Ltd. This is an open access article under the CC BY license (http://creativecommons.org/licenses/by/4.0/).

reintroduced into the patient's body to treat or manage disease. It is crucial to ensure that the final product is free of harmful substances [15]. This includes the removal of residual fibrils post-transduction to prevent adverse effects like venous embolism [16]. In our previous study, we noticed a reduction in EF-C PNF aggregates over time in cell culture [9]. Despite these observations, a comprehensive understanding of the mechanisms enhancing transduction, along with the uptake and degradation of EF-C PNFs, remains elusive.

In this study, we demonstrate that EF-C PNFs create plasma membrane invaginations to aid viral attachment and support transduction by shortening the distance to the nuclear membrane. Through inhibiting endocytosis and electron microscopy, we pinpointed macropinocytosis as the primary pathway for EF-C PNF uptake. Our results confirm the degradation of these PNFs by lysosomes, highlighting their utility and safety as transduction enhancers in *ex vivo* gene therapy.

2. Results

2.1. Binding kinetics of viral particles to EF-C PNFs

To elucidate the mechanisms underlying the transduction-enhancing properties of EF-C PNFs, we systematically analyzed their interaction with viral particles, their cellular uptake pathways, and their intracellular degradation.

We began by characterizing the binding kinetics of EF-C PNFs with viral particles. Several studies have demonstrated that the positive surface charge of peptide nanofibrils (PNFs) plays a crucial role in their interaction with negatively charged viral particles [8,9,17–20]. EF-C (QCKIKQIINMWQ) possesses a positive surface charge at physiological pH, attributed to its two lysine side chains, which generate a hydrophilic surface with a high density of cationic charges [8]. To investigate this interaction in detail, we measured the zeta potential, an indicator of surface charge, of virus-like particles (VLPs, MLV Gag-YFP), which emit yellow fluorescence. Zeta potential measurements revealed that the positive surface charge of EF-C PNFs significantly reduced the negative surface charge of VLPs from −64.4 mV to −9.9 mV (Fig. S1A). Subsequently, we analyzed the binding kinetics of VLPs to EF-C PNFs. VLPs were incubated with EF-C PNFs (50 μg/ml) and their binding was quantified every 2 min for 30 min using nanoparticle tracking analysis (NTA) in the 488 nm fluorescence mode. NTA images indicated that while VLPs alone were randomly distributed, incubation with EF-C PNFs led to the formation of several large aggregates (Fig. S1B). This observation was corroborated by the NTA size distribution measurements, which showed the appearance of aggregates larger than the VLP diameter (~150 nm) over time, consistent with VLP binding to EF-C PNFs (Fig. S1C). From the NTA data, the percentage of free VLPs was quantified (Fig. S1D). After 0.5 min of incubation with EF-C PNFs, 66.2 % of VLPs remained unbound, which decreased to 18.4 % after 30.5 min. To assess how the binding kinetics of VLPs to EF-C PNFs affect viral transduction, EF-C PNFs were pre-incubated for 1, 5, 10, and 60 min with HIV-1 prior to infecting cells (Fig. S1E). At the highest EF-C PNF concentration (5 μg/ml) tested, HIV-1 infection was enhanced by 26-fold after 1 and 5 min. Infection rates after 10 min of pre-incubation were comparable to those observed at 60 min.

In summary, the positive surface charge of EF-C PNFs facilitates the binding of viral particles, effectively overcoming the electrostatic repulsion between the negatively charged viral particles and the cell membrane. NTA measurement and HIV-1 infection assay demonstrated that a 10-min incubation period is sufficient for EF-C PNFs to bind a major proportion of viral particles, achieving a high transduction efficiency.

2.2. EF-C PNFs lead to plasma membrane invaginations that promote HIV-1 binding

In a previous study we identified that the transduction enhancement by EF-C PNFs is not only attributed to overcoming the electrostatic repulsion between negatively charged viral particles and cell membranes but is also supported by the interaction with cellular protrusions [10]. Specifically, cellular protrusions capture EF-C PNFs and guide them towards the cellular body, potentially increasing the rates of virion attachment. Additionally, the binding of EF-C PNFs to cellular protrusion induced invaginations of the plasma membrane [10].

To elucidate the role of EF-C PNFs-induced plasma membrane invaginations in enhancing viral transduction, we analyzed the interactions of EF-C PNFs and HIV-1 virions alone or as PNFs/virus complexes with TZM-bl cells by transmission electron microscopy (TEM) after a 24 h incubation period (Fig. 1A–D). EF-C PNFs exhibited a characteristic star-shaped morphology, commonly observed for amyloid fibrils in cell culture [21,22]. They interacted with filipodia and were located in invaginations of the plasma membrane near the cell nucleus (Fig. 1B). The formation of invaginations substantially increased the membrane length measuring between approximately 14 and 17.8 μm in the cross section, compared to the theoretical length of membrane without invagination which ranged from 2.2 to 10.1 μm (Fig. S2A). The values (membrane length, distance from invagination to cell nucleus, number of HIV-1 particles) presented in Fig. S2 are exemplary measurements and do not represent a statistical analysis. In contrast to untreated control cells, we regularly observed a short distance between plasma membrane and nuclear membrane upon EF-C PNF treatment which could be as low as 70 nm (Fig. S2A). This shows that the invaginations reduce the distance between the cell membrane and nucleus.

To better visualize EF-C PNFs-induced invaginations and their interaction with cellular protrusions, 3D scanning electron microscopy (SEM) was used, capturing images from two different angles (Fig. S3). To further confirm that EF-C PNFs do not disrupt or damage the plasma membrane, scanning transmission electron microscopy (STEM) tomography was utilized. The STEM tomogram revealed no damaging of the plasma membrane by EF-C PNFs and further confirmed the reduced distance between invaginated plasma membrane and the nuclear envelope (Fig. S4, Movie S1).

Supplementary data related to this article can be found online at https://doi.org/10.1016/j.biomaterials.2024.123044

Following this, HIV-1 particles (exhibiting the same morphology as lentiviral vectors) were incubated with TZM-bl cells and analyzed by TEM. The viral particles with an average diameter of 100 nm are composed of viral envelope formed by a host-cell derived lipid bilayer and a capsid [23,24]. Without EF-C PNFs, only a small number of viral particles were located near the plasma membrane (Fig. 1C). In the presence of EF-C PNFs, we observed the formation of large invaginations similar to those found in the samples without viral particles (Fig. 1D). Here, several tens of HIV-1 particles accumulated around the star-like network of EF-C PNFs in close distance to the plasma membrane (Fig. 1D, Fig. S2).

For example, within an invagination measuring 27.9 μm in length and located 0.5 μm from the nuclear envelope in the TEM cross section, we identified 107 virus particles (Fig. S2B). Quantification for Fig. 1 D (left) showed 256 HIV-1 virions close to the plasma membrane. Thus, EF-C PNFs induce plasma membrane invaginations, resulting in a larger accessible cell surface for virion attachment, which likely enhances viral entry into the cell. Additionally, EF-C PNFs are responsible for bringing the plasma membrane closer to the nuclear envelope, which may further increase the likelihood of successful transduction, as HIV-1 needs to deliver its RNA into the nucleus.

2.3. EF-C PNFs are taken up by cell via macropinocytosis

Having demonstrated that EF-C PNFs induce plasma membrane invaginations, marking the initiation of endocytosis, we next examined whether these fibrils are subsequently internalized by cells. To investigate this, we incubated ATTO495-labeled EF-C PNFs (green

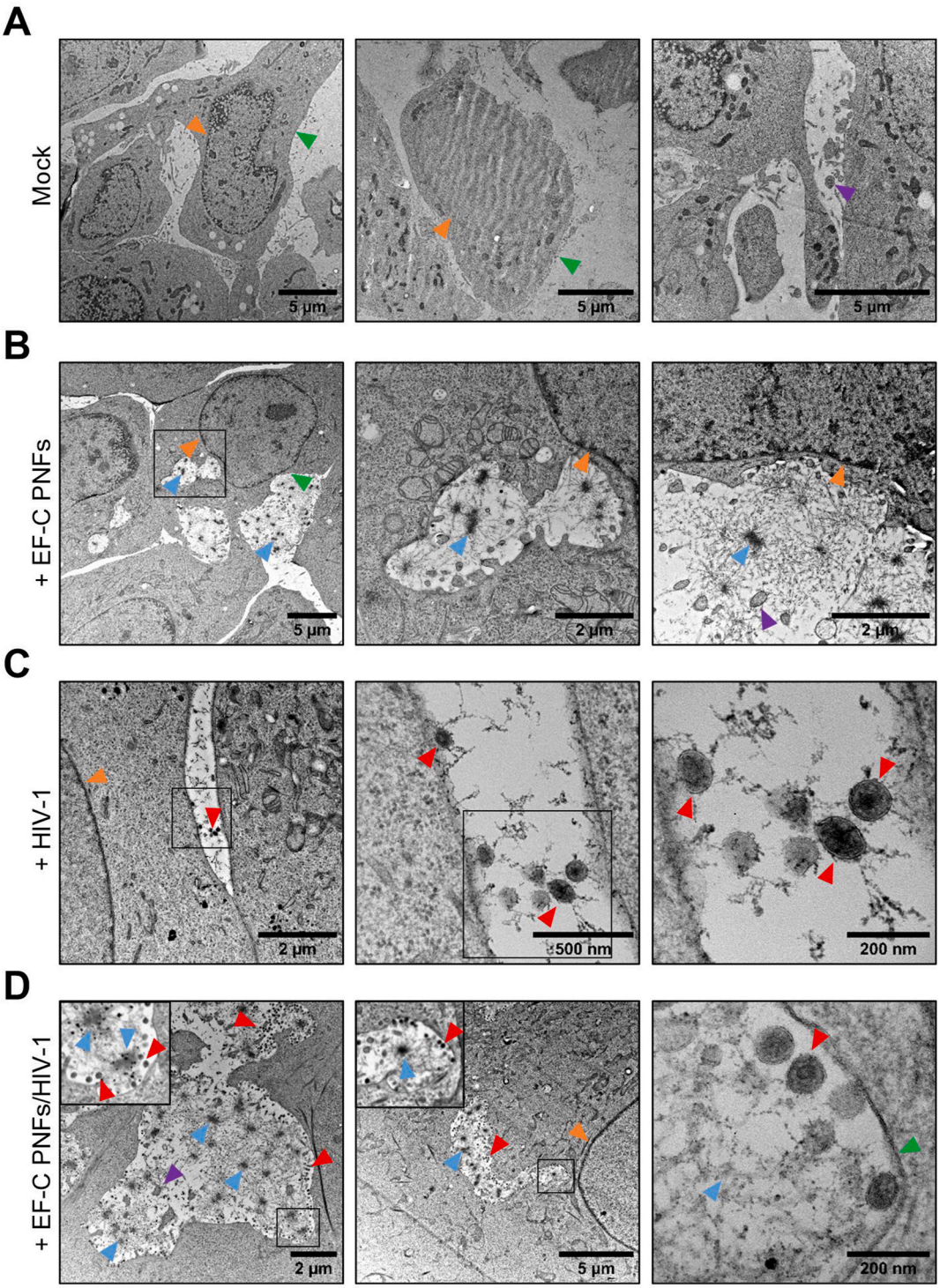

Fig. 1. EF-C PNFs lead to plasma membrane invaginations that promote HIV-1 binding. (A) TEM images of TZM-bl cells. The plasma membrane (green arrowheads), the nuclear membrane (orange arrowheads) and filopodia (purple arrowhead) are highlighted. A high-resolution version of the images is available as eSlide: VM07306, eSlide: VM07307, eSlide: VM07308. (B) TZM-bl cells were incubated with 5 µg/ml EF-C PNFs (blue arrowheads) for 24 h. A high-resolution version of the images is available as eSlide: VM07309, eSlide: VM07310, eSlide: VM07311. (C) TZM-bl cells were incubated with HIV-1 (red arrowheads) for 24 h. A high-resolution version of the images is available as eSlide: VM07312, eSlide: VM07313, eSlide: VM07314. (D) TZM-bl cells were infected with EF-C PNFs/HIV-1 complexes for 24 h. A high-resolution version of the images is available as eSlide: VM07315, eSlide: VM07316, eSlide: VM07318.

fluorescence) [25] with TZM-bl and $CD4^+$ T cells for 1 h and 24 h. To quench green fluorescence of extracellular EF-C PNFs, cells were incubated with trypan blue for 5 min followed by washing and analysis using confocal microscopy. Trypan blue quenching was employed to differentiate between intracellular and extracellular ATTO495-labeled EF-C PNFs. Internalized fibrils retain their green fluorescence (detected in FITC channel), whereas extracellular fibrils exhibit red fluorescence (detected in APC channel) after quenching with trypan blue. This effect is attributed to the absorption of light in the green-yellow spectrum by trypan blue, with a peak absorption around 590 nm in aqueous solution [26]. Additionally, it has been demonstrated that trypan blue binding to certain particles induces the emission of red fluorescence [27,28].

After 1 h of incubation, the majority of EF-C PNFs were bound to the surface of TZM-bl cells, with minimal intracellular green fluorescence detected (Fig. 2A upper panel). By 24 h, a significant proportion of fibrils had been internalized, as evidenced by a prominent intracellular green fluorescence signal. Intracellular EF-C PNFs were localized within endosomal vesicles, which are likely macropinosomes, with diameters reaching up to 5 μm. Macropinosomes are characterized as large, endocytic vesicles that typically measure between 0.2 and 5 μm in size [29]. The uptake process was further confirmed by time-lapse fluorescence microscopy capturing the internalization of ATTO647 N labeled EF-C in HeLa La.GFP cells (Movie S2). In contrast, $CD4^+$ T cells displayed a rapid uptake of EF-C PNFs within 1 h, but there was no

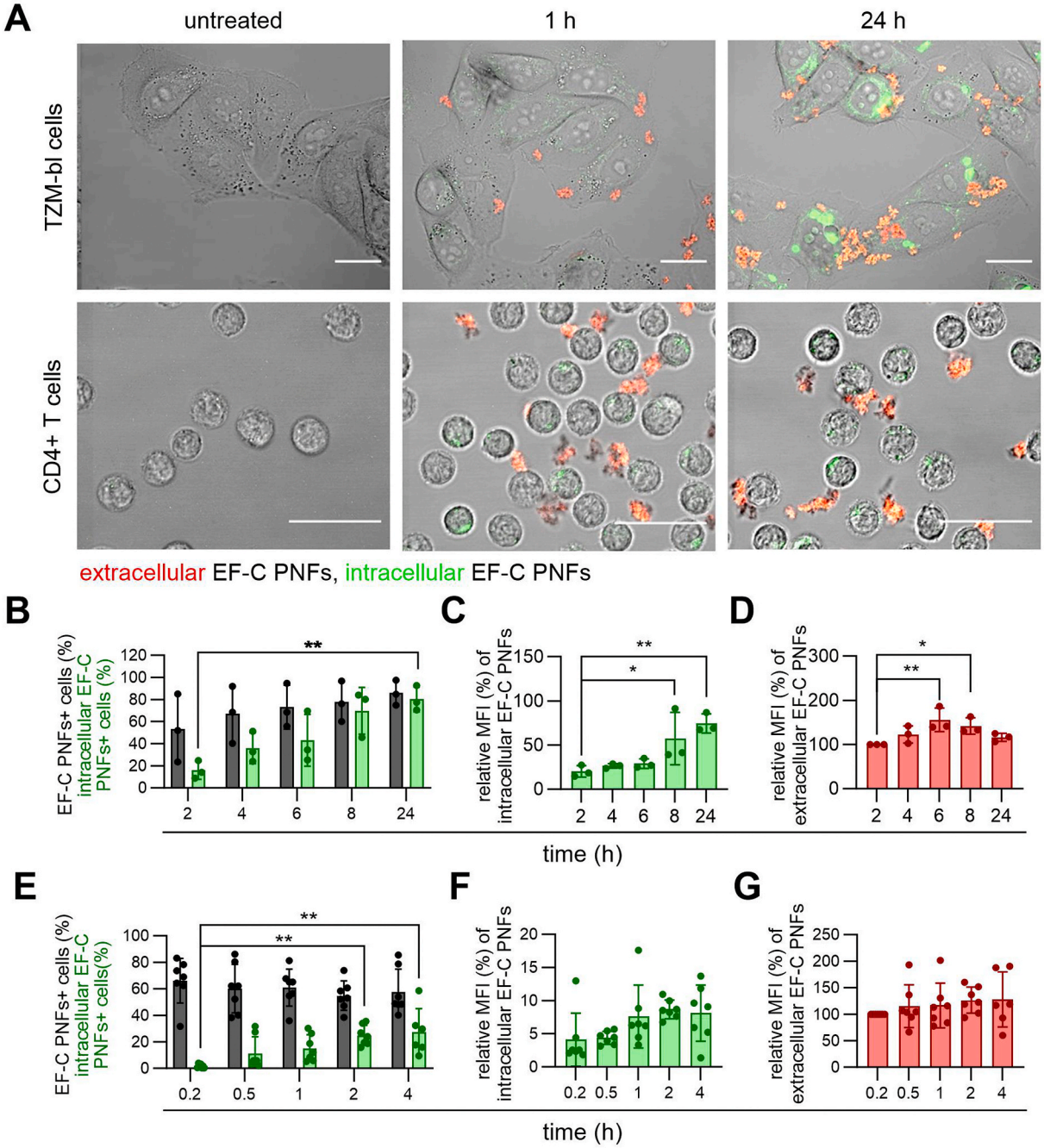

Fig. 2. EF-C PNFs bind to TZM-bl and $CD4^+$ T cells and are taken up. TZM-bl and $CD4^+$ T cells were incubated with ATTO495 labeled EF-C (5 μg/ml) for indicated time points. The green fluorescence of extracellular EF-C PNFs was quenched by incubation with trypan blue for 5 min, followed by washing. Scale bar indicates 20 μm. (A) Representative images of confocal microscopy analysis showing quenched, extracellular EF-C PNFs in red and intracellular EF-C PNFs in green. Flow cytometry analysis of EF-C PNF uptake kinetic in TZM-bl (B–D) and $CD4^+$ T cells (E–G). Mean values ± SD from three to seven independent experiments are shown, indicated as single symbols in each graph. (B, E) Percentage of EF-C PNFs positive cells and intracellular EF-C PNFs positive cells. (C, F) Relative mean fluorescence intensity (MFI) of intracellular EF-C PNFs + cells was determined by normalization to MFI of complete EF-C+ cell population. (D, G) MFI of extracellular EF-C PNFs + cells were normalized to the earliest time point. Significant differences to the earliest time point (2 h or 0.2 h) was determined using ordinary two-way ANOVA followed by Dunnett's multiple comparison test for B and E and one-way ANOVA followed by Dunnett's multiple comparison test for C, D, F and G. The time points not marked with an asterisk are not significantly different from the earliest time point. *$p < 0.033$; **$p < 0.002$; ***$p < 0.001$. A high-resolution version of the images of (A) is available as eSlide: VM07319, eSlide: VM07320, eSlide: VM07321, eSlide: VM07322, eSlide: VM07323, eSlide: VM07324.

significant increase in the extent of internalization after 24 h (Fig. 2A lower panel).

To quantitatively assess EF-C PNFs uptake, we incubated ATTO495-labeled EF-C PNFs with TZM-bl and CD4$^+$ T cells, at indicated time points extracellular EF-C PNFs were quenched using trypan blue and cells were analyzed by flow cytometry. The percentage of TZM-bl cells with surface-bound EF-C PNFs increased from 55 % at 2 h to 90 % at 24 h (Fig. 2B, grey bars). Correspondingly, the proportion of TZM-bl cells with internalized EF-C PNFs rose significantly from 15 % at 2 h to 80 % at 24 h (Fig. 2B, green bars). This was reflected in the relative mean fluorescence intensity (MFI) of intracellular fibril-positive TZM-bl cells, which increased from 20 % at 2 h to 77 % at 24 h (Fig. 2C). Additionally, the MFI of extracellular EF-C PNFs-bound TZM-bl cells showed an initial increase by 65 % at 6 h, followed by a decrease (Fig. 2D). This trend indicates that most fibrils were attached to the cells after 6 h, followed by a decrease of extracellular fibrils due to their internalization over time.

In CD4$^+$ T cells, the percentage of EF-C PNFs-positive cells remained constant at approximately 60 % over a 4-h-period (Fig. 2E, grey bars), while the proportion of cells with internalized EF-C PNFs increased significantly from 2 % at 0.2 h to 27 % at 4 h (Fig. 2E, green bars). Similarly, the MFI of intracellular fibrils rose from 4 % to 7.5 % over time, whereas the MFI of extracellular fibrils stayed constant.

In summary, TZM-bl cells, which are larger (15–20 μm diameter [30, 31]), exhibit a higher capacity for EF-C PNFs uptake compared to CD4$^+$ T cells (5–10 μm diameter [32]). However, CD4$^+$ T cells demonstrate more rapid uptake kinetics despite their smaller size.

Given that numerous studies have demonstrated the uptake of amyloid fibrils, such as tau fibrils [33] and α-synuclein fibrils [34], through macropinocytosis, we investigated whether EF-C PNFs are similarly internalized via this endocytic pathway. To study this, six endocytosis inhibitors, targeting different pathways, were used: macropinocytosis (wortmannin, cytochalasin D, EIPA, dynasore), clathrin-mediated endocytosis (chlorpromazine, dynasore) and caveola-mediated endocytosis (nystatin). The detailed mechanism of action of these inhibitors is described in Table S1. Possible cytotoxic effects were determined by MTT assay showing that some concentrations of cytochalasin D, EIPA, chlorpromazine and Nystatin reduced metabolic activity (Fig. 3, black line) after 4 h incubation time. Thus, TZM-bl cells were pre-incubated with sub-cytotoxic concentrations of each inhibitor for 30 min, followed by the addition of ATTO495 labeled EF-C PNFs for 4 h. After quenching with trypan blue, the extent of fibril internalization was determined by flow cytometry. The inhibitors of macropinocytosis significantly reduced the uptake of EF-C PNFs by TZM-bl cells while

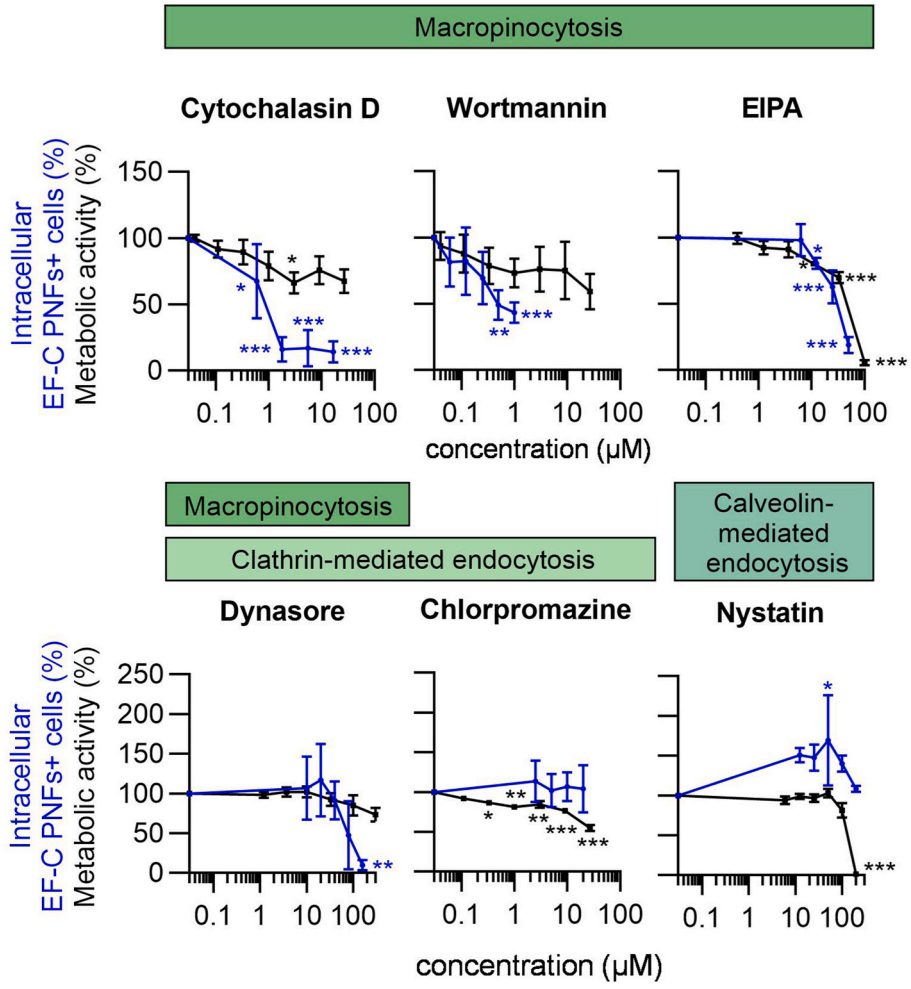

Fig. 3. Inhibition of cellular uptake of EF-C PNFs by macropinocytosis inhibitors. TZM-bl cells were treated with 6.25 μg/ml ATTO495 labeled EF-C PNFs for 4 h after cells were incubated with indicated endocytosis inhibitors for 30 min. Extracellular EF-C PNFs were quenched by incubation with trypan blue for 5 min, followed by a wash step and analyzed by flow cytometry (blue line). Shown are mean values ± SD from 3 (nystatin) or four independent experiments. Metabolic activity (black line) of TZM-bl cells was determined 4 h after micropinocytosis inhibitors treatment using MTT assay. Shown are mean values ± SEM from 3 independent experiments measured in triplicates. Percentage of intracellular EF-C PNFs + cells and metabolic activity was obtained by normalization to untreated cells. Significant differences to untreated cells were determined using ordinary one-way ANOVA, Dunnett's multiple comparison test. The concentrations not marked with an asterisk are not significantly different from the control (untreated cells). *$p < 0.033$; **$p < 0.002$; ***$p < 0.001$.

inhibitors of clathrin and caveolin-mediated endocytosis had no effect on the uptake (Fig. 3, blue line).

As we have shown that EF-C PNFs are internalized by cells via macropinocytosis, we aimed to determine whether this process also affects the uptake of HIV-1 particles and thereby influences infection. Therefore, cells were pre-incubated with sub-cytotoxic concentrations of each endocytosis inhibitor for 30 min, followed by the addition of HIV-1 in presence and absence of EF-C PNF. Treatment with endocytosis inhibitors did not reduce HIV-1 infection (Fig. S5), indicating that the observed enhancement of EF-C PNFs is facilitated by overcoming the electrostatic repulsion between negatively charged viral and cell membranes and the increased surface area provided by EF-C PNFs-induced plasma membrane invaginations.

To elucidate the degradation following the uptake of EF-C PNFs via macropinocytosis, we labeled EF-C peptide with a donor (ATTO488, green fluorescence) or an acceptor fluorophore (ATTO647, red fluorescence), which together form a Förster Resonance Energy Transfer (FRET) pair. TZM-bl cells were incubated with FRET pair labeled EF-C PNFs for 24 h using correlative light and electron microscopy (CLEM). Using the 488 nm laser the FRET labeling strategy enabled us to differentiate between assembled (red fluorescence, B690 channel) and disassembled (green fluorescence, FITC channel) fibrils, a differentiation confirmed in the CLEM experiments (Fig. 4A and B, Fig. S6A). Additionally, a yellow fluorescence signal, resulting from the overlap of both assembled and disassembled fibrils, was observed (Fig. 4B.1 and 4, Fig. S6A).

Initial imaging was performed using confocal light microscopy, where red fluorescence signals were predominantly associated with the plasma membrane, while green and yellow fluorescence signals were seen as large accumulations within the cytoplasm (Fig. 4 A.1, B.1 and Fig. S6A.1). Subsequent TEM analysis of the same locations revealed that the red fluorescence signal (assembled PNFs) corresponded with extracellular structures linked to membrane invaginations forming macropinocytic cups, which still displayed protrusions of the plasma membrane (Fig. 4A2-4, Fig. S6A.3). In contrast, the green (disassembled PNFs) and yellow (assembled and partially disassembled) fluorescence signals were found inside large membrane vesicles, disconnected from the extracellular space (Fig. 4, Fig. S6). Higher magnification images clearly showed morphological differences between assembled fibrils being endocytosed via macropinocytic cups and disassembled fibrils contained within vesicles (Fig. 4A4-5, B3-5). This finding clearly demonstrates that the fibrils are indeed degraded following their uptake.

The membrane profiles of vesicles containing yellow fluorescence signals showed less protrusion-like structures and their lumen a homogeneous electron dense texture. They regularly contained membrane whorls (Fig. 4B4, Fig. S6A.4). These properties are characteristic for lysosomal structures, allowing differentiation from endosomes [35]. Membrane whorls were also observed in vesicles containing green fluorescence (Fig. 4A5). In Fig. 4B5, the lumen of the vesicle containing disassembled EF-C PNFs displayed intraluminal vesicles and membrane whorls, suggesting a potential transition between a lysosome and a multivesicular body (MVB). MVBs are acidic endocytic organelles, enclosing numerous intraluminal vesicles with a diameter between 40 and 90 nm [36–38].

To provide a more detailed visualization of the macropinocytotic process, we generated a 3D segmentation of the tomogram depicted in Fig. S6A3 (Fig. S6B). The 3D data revealed that the macropinocytotic cup containing the assembled EF-C PNFs is characterized by the presence of numerous filipodia (Fig. S6B2). In contrast, the vesicle containing disassembled EF-C PNFs was defined by several intraluminal vesicles and membrane whorls along with filipodia that were in various stages of pinching off from the vesicle membrane and transition into globular structures (Fig. S6B1 and C).

These observations suggest that filipodia locally accumulate and interact with EF-C PNF during the formation of macropinocytic cups, facilitating their uptake into the cells. The process of macropinosome maturation involves the detachment and rounding off of filopodia within the endosomal lumen, a mechanism consistent with previous reports that describe the necessity for actin filament disassembly for the closure of macropinocytic cups to generate mature macropinosomes [39]. The data indicate that macropinocytotic cups appear to mature to macropinosomes that later fuse with lysosomes followed by the transition to MVBs. The observed morphological changes of EF-C PNF within these different organelle types correlated with the shift from red to green fluorescence. Taken together, this morphological data indicated that EF-C PNF are degraded by the lysosomal compartment.

2.4. EF-C PNFs are degraded by lysosomes

Since our previous results demonstrate that EF-C PNFs are taken up via macropinocytosis and indicate crosstalk with the lysosomal compartment, we took a closer look at the lysosomal degradation mechanism. To this end, TZM-bl cells were incubated with ATTO495 labeled EF-C PNFs for 24 h and we performed antibody staining of LAMP1, a lysosomal membrane protein [40]. Confocal microscopy demonstrated a colocalization of EF-C PNFs and lysosomes, manifesting as enlarged vesicular structures (Fig. 5). This observation suggests the fusion of macropinosomes containing EF-C PNFs with lysosomes, which confirm the results of TEM and STEM analysis.

To further confirm that internalized EF-C PNFs undergo lysosomal degradation, we pharmacologically inhibited lysosomal activity using two specific inhibitors: Leupeptin, a lysosomal peptidase inhibitor (serine protease, cysteine protease) [41], and chloroquine, which impedes autophagosome-lysosome fusion [42]. TZM-bl cells were treated with these inhibitors for 15 min followed by incubation with FRET pair labeled EF-C PNFs for 18 h. Confocal microscopy revealed that EF-C PNFs remained intact for 30 min; however, after 18 h fibril disassembly was indicated by increased yellow fluorescence. The disassembly was significantly reduced by leupeptin, as evidenced by the lack of fluorescence shift. In contrast, chloroquine had no impact on the degradation of EF-C PNFs (Fig. 6A). For quantification of lysosomal degradation, TZM-bl cells were incubated with Leupeptin for 15 min before FRET pair labeled EF-C PNFs were added. At indicated time points flow cytometry analysis was performed which showed a time-dependent increase in the percentage of cells containing disassembled EF-C PNFs, reaching up to 34 % after 48 h. This percentage was significantly reduced to 16 % in the presence of leupeptin (Fig. 6B). Similarly, the relative mean fluorescence intensity (MFI) increased over time but was markedly reduced by leupeptin from 100 % to 5 % after 48 h (Fig. 6C). These findings suggest that EF-C PNFs are degraded into non-amyloid material, a process that can be mitigated by inhibiting lysosomal activity.

3. Discussion

It has previously been shown that PNFs increase virion attachment by overcoming the electrostatic repulsion between negatively charged viral particles and cell membranes [8,43]. This mechanism is crucial for enhancing the initial stages of viral infection. Our previous study using a data-mining approach revealed that the transduction-enhancing effect depends on the fibril's hydrophobic surface pattern, high β-sheet content and a positive charge. Additionally, the study revealed that PNFs that form numerous smaller μm-sized aggregates exhibit a better transduction efficiency than those that form larger but fewer aggregates [18]. This finding aligns with our recent study on the 8-mer peptide D4, whose formation of small aggregates is probably related to its outstanding transduction enhancement [17]. We then observed that EF-C PNFs are also actively engaged by cellular protrusions. These protrusions not only facilitate the movement of fibril-virus complexes towards the cell body but also may serve as direct entry portals for viral particles [10]. It is described that several retroviruses including murine leukemia virus (MLV) and HIV-1 bind to receptors on filipodia and surf along these

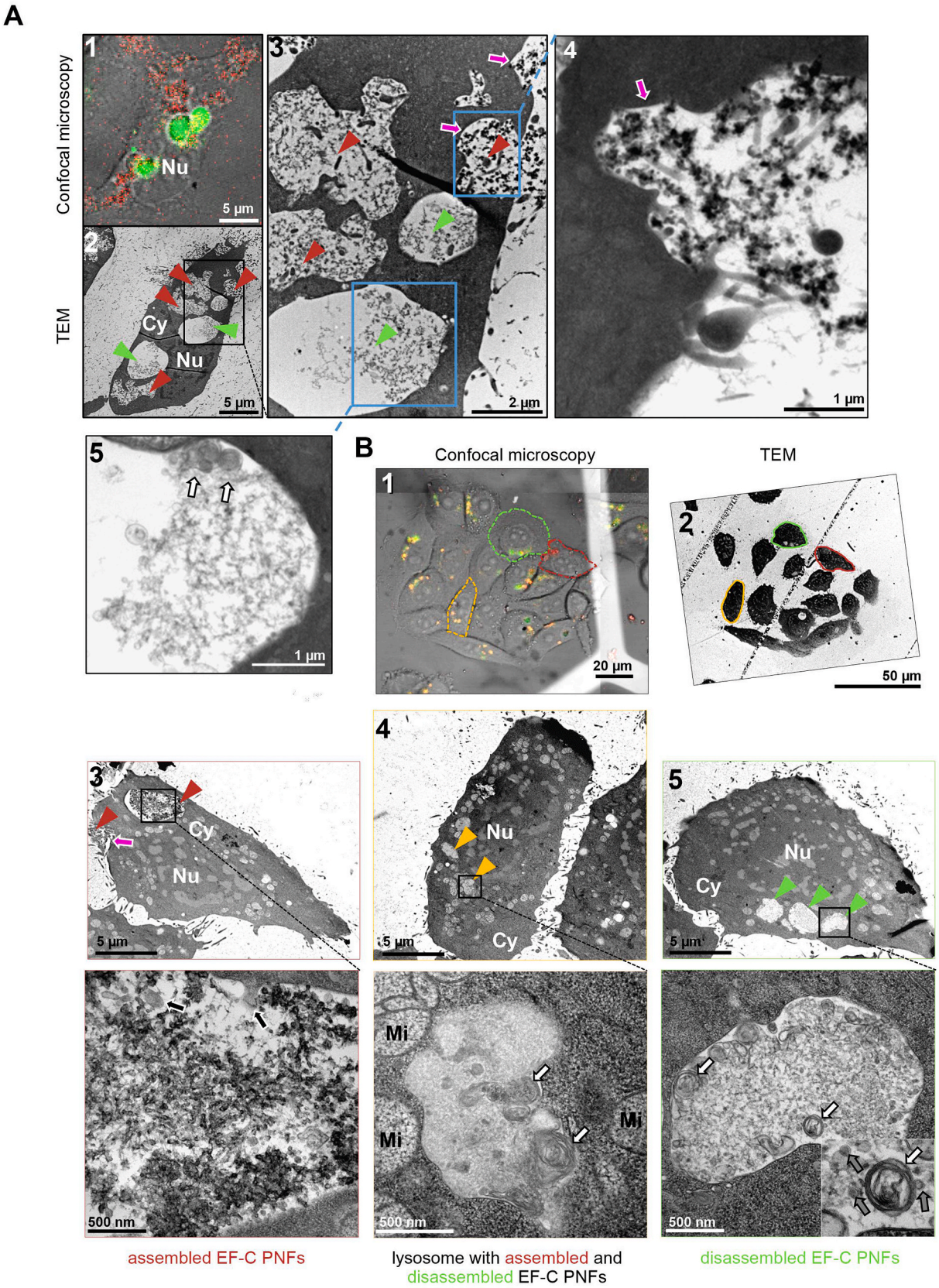

(caption on next page)

Fig. 4. Change of EF-C PNFs morphology during degradation. TZM-bl cells were treated with FRET pair labeled EF-C PNFs (5 μg/ml) for 24 h and were analyzed by correlative light and electron microscopy (CLEM). (A.1) Confocal microscopy image showing FRET pair labeled assembled EF-C PNFs in red and disassembled EF-C PNFs in green. (A.2) Transmission electron microscopy (TEM) image of the same cell as in A.1. Red arrowheads point at positions correlating with red fluorescence, green arrowheads with green fluorescence. (A.3) Magnification of the indicated area in A.2. Macropinocytic cups are marked with a pink arrow. (A.4) Magnification of the indicated area in A.3 showing assembled EF-C PNFs within a macropinocytic cup. (A.5) Magnification of the indicated area in A.3 showing dissembled EF-C PNFs within a vesicle. The disassembled fibril structures appear finer and less electron-dense and the vesicle contains membrane whorls (white arrows) (B) Higher magnifications reveal different morphologies of EF-C PNFs and the varied contents of invaginations/vesicles associated with EF-C PNFs. (B.1) Confocal microscopy image showing a group of cells. Assembled EF-C PNFs are shown in red, and disassembled EF-C PNFs are shown in green. The colocalization of red and green fluorescence results in a yellow signal. (B.2) TEM overview of the cells in B.1. (B.3) A cell labeled red showing assembled EF-C PNFs in a macropinocytic cup (pink arrow) and a macropinosome. Higher magnification of the macropinosome shows cellular protrusions on the membrane of this invagination (black arrows). (B.4) A cell labeled orange containing assembled and disassembled EF-C PNFs in lysosomes (orange arrowheads) which results in a yellow fluorescence signal. (B.5) Cell labeled in green containing disassembled EF-C PNFs in large vesicles (green arrowheads). Higher magnifications showing membrane whorls (white arrows) and intraluminal vesicles (grey arrows). Cy, cytoplasm; Nu, nucleus. A high-resolution version of the images of (A) is available as eSlide: VM07337, eSlide: VM07338, eSlide: VM07339. A high-resolution version of the images of (B) is available as eSlide: VM07340, eSlide: VM07341, eSlide: VM07342, eSlide: VM07343, eSlide: VM07344, eSlide: VM07345, eSlide: VM07346, eSlide: VM07347.

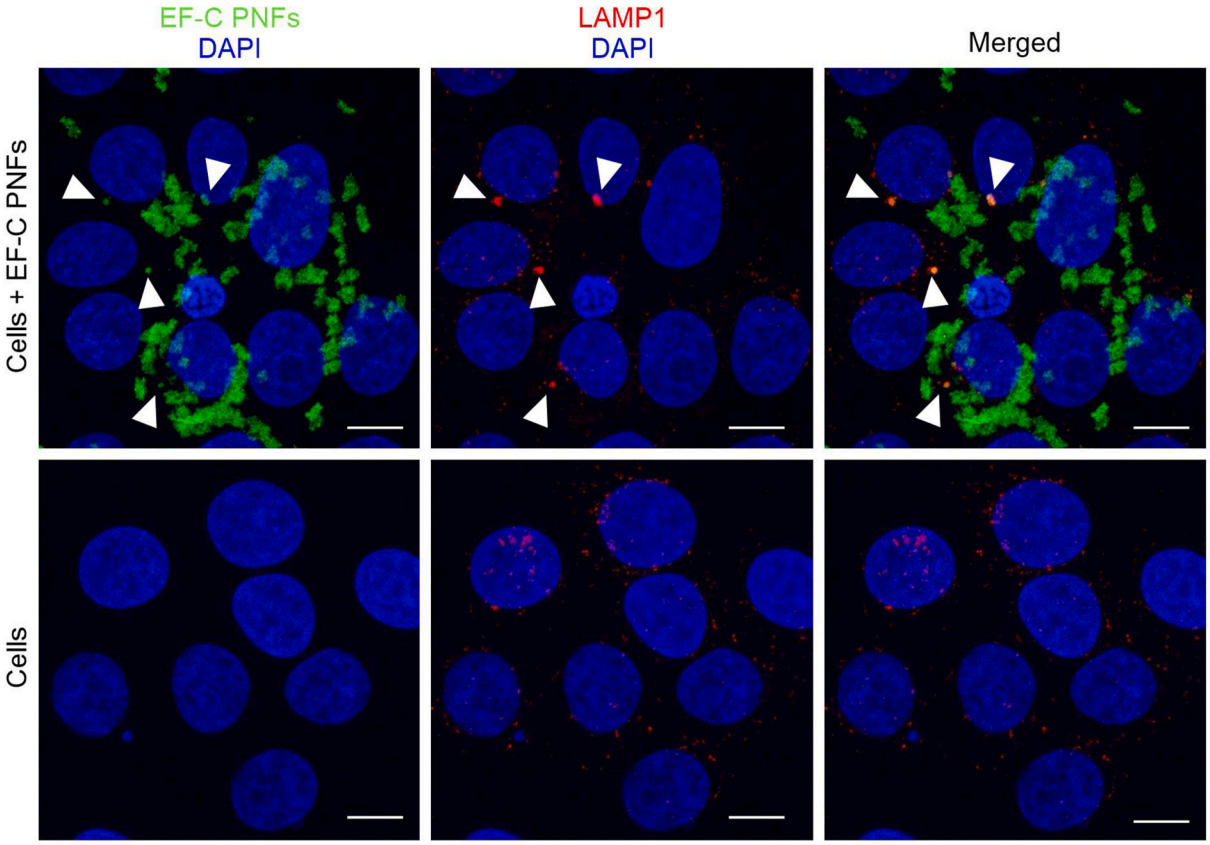

Fig. 5. EF-C PNFs colocalize with lysosomes stained by LAMP1. TZM-bl cells were incubated with ATTO495 labeled EF-C PNFs for 24 h. Cell nucleus was stained by DAPI and lysosomes using an anti-LAMP1 antibody. White arrowheads indicate colocalization of ATTO495 labeled EF-C PNFs and lysosomes. Scale bar indicates 10 μm. A high-resolution version of the images is available as eSlide: VM07325, eSlide: VM07326, eSlide: VM07327, eSlide: VM07328, eSlide: VM07329, eSlide: VM07330.

structures to reach the main body of the cell [44]. Furthermore, these viruses can use filipodia as bridges, called virus cytonemes, for their transfer between infected and uninfected cells [45].

In this study, we demonstrated that EF-C PNFs significantly reduced the negative charge of viral particles, facilitating their binding to the cell membrane. Moreover, analysis of viral binding kinetics revealed that a 10-min incubation period is sufficient for EF-C PNFs to capture a substantial proportion of viral particles, resulting in high transduction efficiency. Furthermore, we observed that EF-C PNFs induce plasma membrane invaginations thereby creating a larger accessible surface area for successful virion attachment and fusion. Moreover, these invaginations reduce the distance between the plasma membrane and nucleus, which may facilitate a more efficient viral infection. Retroviral infection starts with the binding of the envelope glycoprotein to its receptor and coreceptor leading to the fusion of viral and cellular membrane and subsequent entry of the viral particles. After uncoating and reverse transcription the viral capsid containing the viral genome is transported to the nucleus [46]. We here suggest that the regularly observed reduction in the proximity between the plasma and nuclear membrane shortens the transit path for the viral capsid to the nucleus, thereby enhancing the chances of successful transduction.

The formation of plasma membrane invaginations marks the initiation of endocytosis [47]. Using fluorescence microscopy, we showed that EF-C PNFs were internalized into large endosomal vesicles, likely macropinosomes, by TZM-bl cells and $CD4^+$ T cells. Macropinosomes are characterized by their size, typically ranging from 0.2 to 5 μm in diameter [29]. Flow cytometry revealed distinct uptake kinetics between these cell types. TZM-bl cells, being larger, internalized a greater

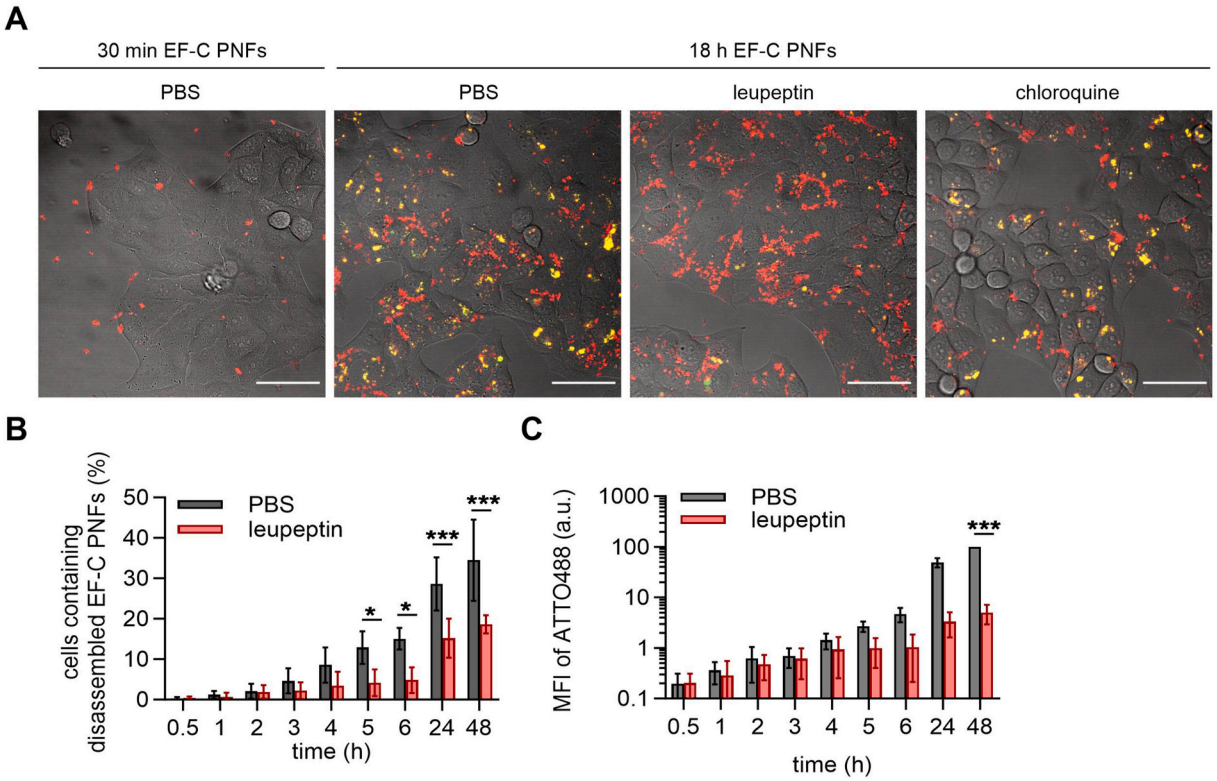

Fig. 6. Reduced disassembly of EF-C PNFs after lysosomal inhibition. TZM-bl cells were treated with indicated lysosomal inhibitors (0.1 mg/ml leupeptin, 1 μM chloroquine) for 15 min followed by incubation with FRET pair labeled EF-C PNFs (5 μg/ml) for indicated time points. ATTO488 acts as a donor and ATTO647 as an acceptor fluorophore. (A) Representative images of confocal microscopy analysis showing FRET pair labeled EF-C PNFs in red and disassembled EF-C PNFs in green. Colocalization of red and green fluorescence results in a yellow signal. Scale bar indicates 50 μm. (B) Disassembled EF-C PNFs (percentage and MFI) after leupeptin treatment was evaluated by flow cytometry. Significant differences to untreated cells (PBS) were determined using ordinary one-way ANOVA followed by Bonferroni's multiple comparison test. Bars without asterisk are not significantly different from the control. *$p < 0.033$; ***$p < 0.001$. A high-resolution version of the images of (A) is available as eSlide: VM07331, eSlide: VM07332, eSlide: VM07333, eSlide: VM07334.

quantity of fibrils compared to $CD4^+$ T cells, which, however, exhibited a faster rate of EF-C PNFs internalization. By pharmacological inhibition of different endocytosis pathways, we identified macropinocytosis as the main entry way of EF-C PNFs into cells. This is consistent with literature describing that tau fibrils (30) and α-synuclein fibrils [34] are endocytosed via macropinocytosis. Macropinocytosis is a non-specific endocytosis pathway for the uptake of extracellular liquid, membrane components and solids [48,49]. In addition to nutrient uptake, macropinocytosis plays a role in a variety of cellular processes such as immune surveillance [50], pathogen invasion, propagation of protein aggregates in neurodegeneration and synaptic function [51]. It is initiated by the formation of actin-dependent protrusions, so-called membrane ruffles [48]. The leading edges of these ruffles are then extended outwards, while the base remains static, allowing to enclose the cargo [52]. The resulting macropinosome can have a diameter up to 5 μm [29]. The inhibition of macropinocytosis did not reduce HIV-1 infection, suggesting that the enhancing activity of EF-C PNFs is independent of its uptake. Instead, this enhancement is mediated through several mechanisms: the interaction with filopodia, which transport virus-fibril complexes to the cell body; the increased attachment surface area for virus particles provided by plasma membrane invaginations; and the reduced distance between the plasma and nuclear membranes, which facilitates more efficient viral capsid transport to the nucleus.

To further investigate the macropinocytosis of EF-C PNFs, we applied CLEM analysis of FRET pair labeled EF-C PNFs. This analysis revealed that assembled EF-C PNFs (red fluorescence) were encapsulated by membrane rufflings, forming macropinocytic cups. Moreover, STEM tomograms revealed that filipodia were detached and rounding off within endosomal lumen, a mechanism consistent with necessity of actin filament disassembly for the closure of macropinocytic cups and the formation of mature macropinosomes [39]. Morphological differences were observed between fibrils (red fluorescence) in macropinocytic cups and fibrils (green and yellow fluorescence) located in intracellular vesicles, correlating with fluorescence signals indicative of fibril degradation. This is supported by STEM and confocal microscopy showing the colocalization of EF-C PNFs with yellow fluorescence in lysosomes, suggesting fusion events between macropinosomes and lysosomes which results in the degradation of EF-C PNF. Such fusion can occur through direct fusion between lysosomes and macropinosomes [53] or by a process called pyranhalysis [54] or kiss and run [55], where endolysosomes surround and repeatedly fuse with macropinosomes as they shrink. Disassembled EF-C PNFs were also detected in a vesicle exhibiting characteristics of both lysosomes and multivesicular bodies (MVBs), suggesting a possible lysosome-to-MVB transition. MVBs are late endosomes containing small intraluminal vesicles that include nucleic acids, proteins, and lipids [56]. While most MVBs fuse with lysosomes to degrade their cargo [57], some fuse with the plasma membrane, releasing their intraluminal vesicles as exosomes into the extracellular space [58]. The observed lysosome-to-MVB transition and the presence of disassembled EF-C PNFs (green fluorescence) suggest the early stages of exosome formation. However, it is also noted that macropinosomes can form intravacuolar vesicle inclusions with a morphology similar to MVBs, as demonstrated in macrophages [59]. Furthermore, macropinocytosis can occur rapidly, as demonstrated by the uptake of α-synuclein preformed fibrils, which are internalized via macropinocytosis and transported to lysosomes within approximately 2 min. Consequently, it remains unclear whether macropinosomes fuse with MVBs and lysosomes or if they mature into these structures [60].

After internalization of EF-C PNFs they were degraded by lysosomes. This degradation process was confirmed by inhibiting lysosomal activity with specific inhibitors (leupeptin and chloroquine). Leupeptin significantly reduced fibril disassembly, indicating the involvement of lysosomal peptidases in the degradation process. Confocal microscopy and flow cytometry analyses showed a time-dependent increase in the percentage of cells containing disassembled EF-C PNFs. The presence of leupeptin significantly reduced the degradation, highlighting the role of lysosomal enzymes in the disassembly of EF-C PNFs. However, to ensure that there are no more EF-C PNFs in the final product of *ex vivo* clinical applications, including CAR T cell therapy, the degradation process must be analyzed over a longer time period.

In summary, our data demonstrate that EF-C PNFs induce plasma membrane invaginations, increasing the membrane surface area for viral attachment and reducing the distance between the plasma and nuclear membrane. This reduction in distance potentially facilitates the travel of the viral capsid to the nucleus, thereby enhancing viral transduction. Additionally, EF-C PNFs are internalized into cells via macropinocytosis and subsequently degraded by lysosomal peptidases. The efficient intracellular degradation of EF-C PNFs prevents their accumulation as amyloid deposits, alleviating concerns about potential side effects. This degradation supports the safe application of EF-C PNFs in clinical settings, particularly for *ex vivo* gene therapy applications.

4. Material and methods

Cells: TZM-bl reporter cells (AIDS reagent and reference programme, Saic Frederick, USA), HEK 293T cells (ATCC, CRL-3216) and HeLa LA. GFP cells which F-actin is labeled with Lifeact-GFP (kindly provided by Prof. Dr. Oliver Fackler Department of Infectious Diseases, Virology, Heidelberg.) were cultured in Dulbecco's Modified Eagle Medium (DMEM, Gibco, 11965092) supplemented with 100 U/ml penicillin, 100 μg/ml streptomycin (PAN-Biotech, P06-07050), 2 mM L-glutamine (PAN-Biotech, P04-80050, and 10 % inactivated fetal calf serum (FCS, Gibco, 10437028).

$CD4^+$ T cell preparation: $CD4^+$ T cells were isolated from Buffy coats of healthy donors using lymphocyte separation medium (Biocoll separating solution; Biochrom, Berlin, Germany) and RosetteSep Human CD4 +T Cell Enrichment Cocktail (STEMCELL Technologies, 15063) according to manufacturer's protocol. Cells were maintained in RPMI medium supplemented with 100 U/ml penicillin, 100 μg/ml streptomycin, 2 mM L-glutamine and 10 % FCS.

Peptide synthesis: Peptides were chemically synthesized and purified by high-performance liquid chromatography (HPLC) with a purity of >95 % by Synpeptide Co.,Ltd. (Shanghai, China). EF-C has the sequence QCKIKQIINMWQ. ATTO 647 N and ATTO 495 NHS ester were purchased from ATTO-TEC GmbH (Siegen, Germany). For the labeling reaction 10 mg/ml EF-C DMSO solution was mixed with 1 mg ATTO dye according to the manufacture's protocol and Rode et al. [25]. In this labeling reaction the free amino groups of the EF-C peptide were coupled to the ATTO 647 N and ATTO 495 NHS ester dyes. To generate labeled fibrils, 1 % ATTO 647N- or ATTO 495-labeled EF-C peptides from the labeling reaction were mixed with 99 % unlabeled peptide in DMSO. To generate FRET labeled fibrils, 1 % ATTO 647N- and 1 % ATTO 488-labeled EF-C peptides were mixed with 98 % unlabeled peptide in DMSO. Fibrillation of ATTO labeled EF-C was initiated by diluting the peptide mixture in PBS to 1 mg/ml and incubation for 10 min. Unbound dye was removed by centrifugation at 20,817×*g* for 15 min followed by washing and resuspension in equal amount of PBS. For inducing fibril formation of unstained EF-C, 10 mg/ml DMSO solution was diluted in PBS to 1 mg/ml and incubated overnight at room temperature.

Zeta potential: For the analysis of zeta potential, which is an indicator for the surface charge, MLV Gag-YFP virus-like particles (VLPs, 1:1000 diluted) and EF-C PNFs (30 μg/ml) were diluted in 1 ml 1 mM KCl (Merck, 104936) so that 100–400 traced particles were obtained. After incubation of VLPs/EF-C PNFs mix for 2 min. Zeta potential was determined using ZetaView TWIN (Particle Metrix) and the corresponding Software ZetaView (Zetaview Nanoparticle Tracking Analyzer RRID: SCR_016647). Samples with VLPs (emit yellow fluorescence) were measured using the 488 nm fluorescence mode (500 nm filter wavelength). EF-C PNFs (1 μg/ml) were measured in the scatter mode.

Nanoparticle tracking analysis (NTA): VLPs were injected into ZetaView TWIN after either being mock-treated with PBS or incubated with of EF-C PNFs (50 μg/ml). Samples were injected via the pump at 5 m/min flow rate. Due to mixing, injection and measurement initiation delay, the first size distribution measurement was initiated at after 0.5 min. Afterwards, a size-distribution measurement was taken in 488 nm fluorescence mode every 2 min for a total of 30 min. After each measurement, one pump stroke was automatically performed to draw more sample from the syringe to reduce loss of tracked particles due to bleaching of VLPs. Note that in 488 mode, (unstained) fibrils are not visible and only VLPs are tracked – either free (small, single particles) as aggregates (large, multiple particles). Changes in the number of free VLPs were thus evaluated as a measurement for fibril binding. Evaluation of NTA data was carried out by FlowJo™ (Version 10.8.1).

Confocal microcopy: For the uptake experiment 40,000 TZM-bl cells were seeded in 8-well μ-Slides (Ibidi, 80826). Next day, TZM-bl cells and 250,000 $CD4^+$ T cells were treated with 5 μg/ml ATTO495 EF-C PNFs for 1 or 24 h. To quench green fluorescence of extracellular EF-C PNFs, cells were incubated with trypan blue (0.05 % diluted in PBS), which absorbs light in the range of 450–550 nm and emits red fluorescence, for 5 min followed by washing. After $CD4^+$ T cells were transferred into 8-well μ-Slides, cells were analyzed by confocal microscopy (LSM 710 confocal microscope, Zeiss). Green fluorescence was measured in the FITC channel (488 nm laser, 525/40 filter) and red fluorescence in the APC channel (638 nm laser, 660/10 filter).

For inhibition of lysosomal activity, 40,000 TZM-bl cells were seeded in 8-well μ-Slides followed by treatment with 0.1 mg/ml leupeptin (Sigma, L2884-.5 MG) and 1 μM chloroquine (Santa Cruz Biotechnology, sc-205629) for 15 min on the next day. FRET pair labeled EF-C PNFs (5 μg/ml) were added and cells were analyzed by confocal microscopy and flow cytometry after 18 h. EF-C PNFs uptake in cells was visualized by life cell imaging. Therefore, 30,000 HeLa LA.GFP cells were seeded and on the next day treated with 5 μg/ml ATTO647 labeled EF-C PNFs for 30 min to allow sedimentation of fibril and cells were analyzed by time-laps imaging every 5 min for 14 h and 55 min.

For colocalization of EF-PNFs and lysosomes, 60,000 TZM-bl cells were seeded in a 8-well Ibidi slide. Next day cells were treated with 5 μg/ml ATTO495 labeled EF-C PNFs. After 24 h cells were washed with PBS, fixed with 4 % PFA for 20 min and permeabilized and blocked (0.5 % Triton X-100 in PBS containing 5 % FCS) for 60 min. After washing three times, cells were stained using an anti-LAMP1 Rabbit antibody (Cell signaling Technology, 9091) 1:200 diluted in Staining buffer (1 % FCS in PBS) at 4 °C for 2 h. Cells were washed three times with 0.1 % Tween20 in PBS and 1:400 diluted Goat anti-Rabbit IgG Alexa Fluor 647 secondary antibody (Invitrogen, A-21245) and 1:1000 diluted DAPI (Roche), both diluted in staining buffer, were added for 2 h at 4 °C. After three times washing with 0.1 % Tween20 in PBS, cells were analyzed by confocal microscopy.

Uptake kinetics: To analyze the uptake kinetics of EF-C PNF, 200,000 TZM-bl cells were seeded one day prior experiment. TZM-bl cells and $CD4^+$ T cells (150,0000) were incubated with 5 μg/ml ATTO495 labeled EF-C PNFs for indicated time points. After incubation times, green fluorescence of extracellular fibrils was quenched by incubation with typan blue for 5 min followed by washing. To distinguish between dead cells and extracellular fibrils, cells were stained with Fixable Viability Dye eFluor™ 450 (eBioscience, 405 laser, 450/45 filter) according to manufacturer's protocol. TZM-bl cells and $CD4^+$ T cells were analyzed for intracellular and extracellular fibrils via the green (FITC, 488 nm laser, 525/40 filter) and red fluorescence (APC, 638 nm laser, 660/10) channel using flow cytometry (BD FACSCanto II, BD Bioscience).

Toxicity: For analysis of metabolic activity via a MTT (Thiazolyl blue

tetrazolium bromide) Cell Growth Assay (Merck, CT02), 10,000 TZM-bl cells were seeded in a 96-well plate one day before experiment and cells were treated with indicated concentrations of cytochalasin D, wortmannin, EIPA, dynasore, chlorpromazine or nystatin for 4 or 24 h. Subsequently supernatant was removed, replaced by 100 µl MTT (0.5 mg/ml) and incubated 2.5 h. The supernatant was removed and 100 µl 1:1 DMSO-Ethanol solution was added. The absorption was measured at 590 nm with baseline-corrected at 650 nm using VersaMax Microplate Reader (Molecular Devices). Metabolic activity in % was calculated by dividing the mean of every concentration by the values of the untreated cells.

Pharmacological inhibition of endocytosis: 50,000 TZM-bl cells were seeded and on the next day treated with indicated concentrations of cytochalasin D (Enzo, BML-T109-0001), EIPA (MCE, HY-101840), wortmannin (abcam, ab120148), chlorpromazine (CPZ, Sigma, C8138-5G), dynasore (Sigma, 324410-10 MG) or nystatin (sigma, N6261–500KU) for 30 min at 37 °C. Next, 6.25 µg/ml ATTO495 labeled EF-C PNFs were added for 4 h (to get a final concentration of 6.25 µg/ml on cells). Quenching with trypan blue was performed as described above and cells were analyzed by flow cytometry.

Pharmacological inhibition of lysosomal degradation: For analysis of the impact of leupeptin to the disassembly of EF-C PNF, 20,000 TZM-bl cells were seeded. Next day, cells were treated with 100 µg/ml leupeptin for 15 min followed by incubation with 5 µg/ml FRET pair EF-C PNFs for indicated time points. Cells were analyzed by flow cytometry. Assembled fibrils (ATTO647, red fluorescence) was measured using the 488 nm laser and filter 690/50 (B690 channel) and disassembled fibrils (ATTO488, green fluorescence) was measured using the same laser but the 525/40 filter (FITC channel).

Production of virus stock: For transfection 800,000 HEK293T cells were seeded in a 6-well-plate. One day later cells were transfected using CalPhos™ Mammalian Transfection Kit (Takara, 631312) with 5 µg DNA/well. For generation of HIV-1 stocks the plasmid pBRNL4-3_92TH014.12 was used [61]. For TEM analysis virus stocks were further purified with a 0.4 µm filter and ultracentrifugation (90 min, 141,000×*g*, 4 °C). Titer of HIV-1 stock was determined using in house p-24-antigen ELISA.

For VLP stock generation, 15×10^6 HEK293T cells were initially seeded in a T-175 flask (Sarstedt), followed by transfection using the plasmid MLV Gag-YFP (41.7 µg) and TransIT-LT1 Transfection Reagent (Mirus Bio, Cat: Mir 2305) according to the manufacturer's protocol on the next day. MLV Gag-YFP was a gift from Walther Mothes (Addgene plasmid # 1813) [62]. Murine leukemia virus (MLV) gag is fused to yellow fluorescent protein (YFP). The resulting virus particles are non-infectious and emit a yellow fluorescence. Two days after transfection, VLP stock was harvested and centrifuged (5 min, 1300 rpm, 4 °C). The supernatant was purified using 20 % sucrose and centrifugation (3 h, 14,0000 rpm, 4 °C). Therefore, 5 vol of VLP supernatant was layered on top of one volume of 20 % sucrose. Viral pellet was resuspended in PBS and stored at −80 °C.

HIV-1 infection assay: The impact of endocytosis inhibition on transduction enhancement was analyzed by transducing cells with HIV-1 after they were incubated with endocytosis inhibitors as described before. Therefore, 10,000 TZM-bl cells were seeded one day before transduction. HIV-1 (final dilution factor 640) was incubated with EF-C PNFs (final concentration of 2 µg/ml) before TZM-bl cells were infected. After 3 days HIV-1 infection was measured by analysis of Tat-inducible β-galactosidase activity according to Rauch-Wirth et al. [17].

For the analysis of interaction of EF-C PNFs with HIV-1, dilution series of EF-C were incubated with HIV-1 for 0 min, 5 min, 10 min and 60 min before TZM-bl cells were infected as described above. β-galactosidase activity was measured three days after infection.

Transmission electron microscopy (TEM): 200,000 TZM-bl cells were seeded on carbon-coated sapphire discs (3-mm diameter, 50-µm thickness, Wohlwend GmbH) in a 12 well plate and on the next day 5 µg/ml EF-C PNFs or EF-C PNFs mixed with HIV-1 (773 µg p24 on 20,000 cells) were added. Samples with HIV-1 were pre-fixed by replacing 50 % of culture media with 2.5 % glutaraldehyde fixation solution for at least 1 h and further prepared as described previously [63]. Samples were imaged using a JEM-1400 electron microscope (JEOL) with an accelerating voltage of 120 kV.

Scanning electron microscopy (SEM): To visualize cell surfaces SEM was used. 200,000 TZM-bl cells were seeded on cover glasses in a 12 well plate. Next day EF-C PNFs (5 µg/ml) were added to cells. After incubation for 4 or 24 h, cells were fixed with SEM fixation solution (2.5 % glutaraldehyde, 1 % sucrose in 0.2 M Phosphate Buffer, pH 7.3) overnight at 4 °C. Further preparation was performed as described previously [63] and cells were imaged using a S-5200 field emission scanning electron microscope (Hitachi). Anaglyph stereo pairs were generated by recording of two images with different angles to the object: 3.5° and –3.5°. Using Adobe Photoshop images were merged and digitally colorized.

Correlative light and electron microscopy (CLEM): For degradation experiments, 5000 TZM-bl cells were seeded on carbon-coated sapphire discs with coordinate system (3-mm diameter, 50-µm thickness, Wohlwend GmbH). Next day cells were treated with 5 µg/ml FRET pair labeled EF-C PNFs for 24 h and red and green fluorescence was analyzed by confocal microscopy. Afterwards, samples were fixed by high pressure freezing (HPF Compact 01, Wohlwend GmbH) and freeze substitution (EM AFS2, Leica), embedded in Epon and ultra-thin sectioned (~70 nm thick). Sections were mounted on glow discharged copper grids coated with formvar and carbon and were imaged with a JEM-1400 electron microscope (JEOL).

Scanning transmission electron microscopy tomography (STEM): TEM samples were used and 700 nm-thick sections were cut, mounted on a 300-mesh copper grid (Plano GmbH) and imaged using JEM-2100F electron microscope (JEOL) with 200 kV in STEM mode as described previously [21]. Different tilt angles ranging from −70° to +70° were applied for imaging and for each samples a series containing 94 images were taken. Gold particles were used as a marker to align image stack with IMOD software package (University of Colorado). 3D structures of the tomograms were visualized by the Avizo lite software (Thermo Fisher Scientific).

Statistics: Statistical analysis were performed using GraphPad Prism version 10.1.0.

CRediT authorship contribution statement

Lena Rauch-Wirth: Writing – review & editing, Writing – original draft, Visualization, Validation, Methodology, Investigation, Formal analysis, Data curation, Conceptualization. **Desiree Schütz:** Visualization, Investigation, Formal analysis, Data curation, Conceptualization. **Rüdiger Groß:** Conceptualization, Data curation, Formal analysis, Investigation. **Sascha Rode:** Visualization, Investigation, Data curation, Conceptualization. **Bernhard Glocker:** Visualization, Investigation, Data curation. **Janis A. Müller:** Methodology, Data curation. **Paul Walther:** Resources, Methodology, Funding acquisition. **Clarissa Read:** Writing – review & editing, Supervision, Resources, Project administration, Methodology, Investigation, Funding acquisition, Formal analysis, Data curation, Conceptualization. **Jan Münch:** Writing – review & editing, Writing – original draft, Supervision, Resources, Project administration, Funding acquisition, Formal analysis, Conceptualization.

Ethics statement

CD4+T cells from healthy donors were isolated from buffy coats aquired from the Blutspendezentrale Ulm, ethic vote number 151/22 FSt/bal.

Declaration of generative AI and AI-assisted technologies in the writing process

During the preparation of this work the author used ChatGPT (May 16 version)/OpenAI in order to improve the readability and language of the manuscript. After using this tool/service, the authors reviewed and edited the content as needed and take full responsibility for the content of the publication.

Declaration of competing interest

The authors declare the following financial interests/personal relationships which may be considered as potential competing interests: Jan Muench has patent issued to Assignee. Lena-Rauch Wirth has patent pending to Assignee. Desiree Schuetz has patent pending to Assignee. If there are other authors, they declare that they have no known competing financial interests or personal relationships that could have appeared to influence the work reported in this paper.

Acknowledgements

This project has received funding through a Collaborative Research Centre grant of the German Research Foundation (316249678 – SFB 1279) to JM, CR, and PW.

Appendix A. Supplementary data

Supplementary data to this article can be found online at https://doi.org/10.1016/j.biomaterials.2024.123044.

Data availability

Data will be made available on request.

References

[1] X. Zhang, W.T. Godbey, Viral vectors for gene delivery in tissue engineering, Adv. Drug Deliv. Rev. 58 (2006) 515–534, https://doi.org/10.1016/j.addr.2006.03.006.
[2] J. Barquinero, H. Eixarch, M. Pérez-Melgosa, Retroviral vectors: new applications for an old tool, Gene Ther. 11 (2004) S3–S9, https://doi.org/10.1038/sj.gt.3302363.
[3] M. Irving, E. Lanitis, D. Migliorini, Z. Ivics, S. Guedan, Choosing the right tool for genetic engineering: clinical lessons from chimeric antigen receptor-T cells, Hum. Gene Ther. 32 (2021) 1044–1058, https://doi.org/10.1089/hum.2021.173.
[4] M. Sadelain, CD19 CAR T cells, Cell 171 (2017) 1471, https://doi.org/10.1016/j.cell.2017.12.002.
[5] J.N. Kochenderfer, M.E. Dudley, S.A. Feldman, W.H. Wilson, D.E. Spaner, I. Maric, M. Stetler-Stevenson, G.Q. Phan, M.S. Hughes, R.M. Sherry, J.C. Yang, U. S. Kammula, L. Devillier, R. Carpenter, D.-A.N. Nathan, R.A. Morgan, C. Laurencot, S.A. Rosenberg, B-cell depletion and remissions of malignancy along with cytokine-associated toxicity in a clinical trial of anti-CD19 chimeric-antigen-receptor-transduced T cells, Blood 119 (2012) 2709–2720, https://doi.org/10.1182/blood-2011-10-384388.
[6] C.H. June, M. Sadelain, Chimeric antigen receptor therapy, N. Engl. J. Med. 379 (2018) 64–73, https://doi.org/10.1056/NEJMra1706169.
[7] R.K. Iyer, P.A. Bowles, H. Kim, A. Dulgar-Tulloch, Industrializing autologous adoptive immunotherapies: manufacturing advances and challenges, Front. Med. 5 (2018) 150, https://doi.org/10.3389/fmed.2018.00150.
[8] M. Yolamanova, C. Meier, A.K. Shaytan, V. Vas, C.W. Bertoncini, F. Arnold, O. Zirafi, S.M. Usmani, J.A. Müller, D. Sauter, C. Goffinet, D. Palesch, P. Walther, N.R. Roan, H. Geiger, O. Lunov, T. Simmet, J. Bohne, H. Schrezenmeier, K. Schwarz, L. Ständker, W.-G. Forssmann, X. Salvatella, P.G. Khalatur, A. R. Khokhlov, T.P.J. Knowles, T. Weil, F. Kirchhoff, J. Münch, Peptide nanofibrils boost retroviral gene transfer and provide a rapid means for concentrating viruses, Nat. Nanotechnol. 8 (2013) 130–136, https://doi.org/10.1038/nnano.2012.248.
[9] K. Kaygisiz, L. Rauch-Wirth, A. Iscen, J. Hartenfels, K. Kremer, J. Münch, C. V. Synatschke, T. Weil, Peptide amphiphiles as biodegradable adjuvants for efficient retroviral gene delivery, Adv. Healthcare Mater. 13 (2024) 2301364, https://doi.org/10.1002/adhm.202301364.
[10] D. Schütz, S. Rode, C. Read, J.A. Müller, B. Glocker, K.M.J. Sparrer, O.T. Fackler, P. Walther, J. Münch, Viral transduction enhancing effect of EF-C peptide nanofibrils is mediated by cellular protrusions, Advanced Functional Materials n/a (2021) 2104814, https://doi.org/10.1002/adfm.202104814.
[11] A. Castro, M. Drosch, M. Liesenfeld, T. Kaan, A. Schilz, H. Wenschuh, W. Forsmann, K. Kuhlke, Protransduzin™ - A novel transduction enhancer to accelerate en gros CAR-T production, Cytotherapy 21 (2019) e14, https://doi.org/10.1016/j.jcyt.2019.04.044.
[12] C. Radek, O. Bernadin, K. Drechsel, N. Cordes, R. Pfeifer, P. Sträßer, M. Mormin, A. Gutierrez-Guerrero, F. Cosset, A.D. Kaiser, T. Schaser, A. Galy, E. Verhoeyen, I.C. D. Johnston, Vectofusin-1 improves transduction of primary human cells with diverse retroviral and lentiviral pseudotypes, enabling robust, automated closed-system manufacturing, Hum. Gene Ther. 30 (2019) 1477–1493, https://doi.org/10.1089/hum.2019.157.
[13] A. Rajabzadeh, A.A. Hamidieh, F. Rahbarizadeh, Spinoculation and retronectin highly enhance the gene transduction efficiency of Mucin-1-specific chimeric antigen receptor (CAR) in human primary T cells, BMC Molecular and Cell Biology 22 (2021) 57, https://doi.org/10.1186/s12860-021-00397-z.
[14] F. Nasiri, S. Muhammadnejad, F. Rahbarizadeh, Effects of polybrene and retronectin as transduction enhancers on the development and phenotypic characteristics of VHH-based CD19-redirected CAR T cells: a comparative investigation, Clin. Exp. Med. (2022), https://doi.org/10.1007/s10238-022-00928-8.
[15] M. Perez, A. Maiguy-Foinard, C. Barthélémy, B. Décaudin, P. Odou, Particulate matter in injectable drugs: evaluation of risks to patients, Pharmaceutical Technology in Hospital Pharmacy 1 (2016) 91–103, https://doi.org/10.1515/pthp-2016-0004.
[16] J. Wong, A. Brugger, A. Khare, M. Chaubal, P. Papadopoulos, B. Rabinow, J. Kipp, J. Ning, Suspensions for intravenous (IV) injection: a review of development, preclinical and clinical aspects, Adv. Drug Deliv. Rev. 60 (2008) 939–954, https://doi.org/10.1016/j.addr.2007.11.008.
[17] L. Rauch-Wirth, A. Renner, K. Kaygisiz, T. Weil, L. Zimmermann, A.A. Rodriguez-Alfonso, D. Schütz, S. Wiese, L. Ständker, T. Weil, D. Schmiedel, J. Münch, Optimized peptide nanofibrils as efficient transduction enhancers for in vitro and ex vivo gene transfer, Front. Immunol. 14 (2023), https://doi.org/10.3389/fimmu.2023.1270243.
[18] K. Kaygisiz, L. Rauch-Wirth, A. Dutta, X. Yu, Y. Nagata, T. Bereau, J. Münch, C. V. Synatschke, T. Weil, Data-mining unveils structure–property–activity correlation of viral infectivity enhancing self-assembling peptides, Nat. Commun. 14 (2023) 5121, https://doi.org/10.1038/s41467-023-40663-6.
[19] K. Kaygisiz, A. Dutta, L. Rauch-Wirth, C.V. Synatschke, J. Münch, T. Bereau, T. Weil, Inverse design of viral infectivity-enhancing peptide fibrils from continuous protein-vector embeddings, Biomater. Sci. 11 (2023) 5251–5261, https://doi.org/10.1039/D3BM00412K.
[20] S. Sieste, T. Mack, E. Lump, M. Hayn, D. Schütz, A. Röcker, C. Meier, K. Kaygisiz, F. Kirchhoff, T.P.J. Knowles, F.S. Ruggeri, C.V. Synatschke, J. Münch, T. Weil, Supramolecular peptide nanofibrils with optimized sequences and molecular structures for efficient retroviral transduction, Adv. Funct. Mater. 31 (2021) 2009382, https://doi.org/10.1002/adfm.202009382.
[21] M. Kollmer, K. Meinhardt, C. Haupt, F. Liberta, M. Wulff, J. Linder, L. Handl, L. Heinrich, C. Loos, M. Schmidt, T. Syrovets, T. Simmet, P. Westermark, G. T. Westermark, U. Horn, V. Schmidt, P. Walther, M. Fändrich, Electron tomography reveals the fibril structure and lipid interactions in amyloid deposits, Proc. Natl. Acad. Sci. USA 113 (2016) 5604–5609, https://doi.org/10.1073/pnas.1523496113.
[22] S. Han, M. Kollmer, D. Markx, S. Claus, P. Walther, M. Fändrich, Amyloid plaque structure and cell surface interactions of β-amyloid fibrils revealed by electron tomography, Sci. Rep. 7 (2017) 43577, https://doi.org/10.1038/srep43577.
[23] T. Do, G. Murphy, L.A. Earl, G.Q. Del Prete, G. Grandinetti, G.-H. Li, J.D. Estes, P. Rao, C.M. Trubey, J. Thomas, J. Spector, D. Bliss, A. Nath, J.D. Lifson, S. Subramaniam, Three-dimensional imaging of HIV-1 virological synapses reveals membrane architectures involved in virus transmission, J. Virol. 88 (2014) 10327–10339, https://doi.org/10.1128/jvi.00788-14.
[24] K. Pritschet, N. Donhauser, P. Schuster, M. Ries, S. Haupt, N.A. Kittan, K. Korn, S. Pöhlmann, G. Holland, N. Bannert, E. Bogner, B. Schmidt, CD4- and dynamin-dependent endocytosis of HIV-1 into plasmacytoid dendritic cells, Virology 423 (2012) 152–164, https://doi.org/10.1016/j.virol.2011.11.026.
[25] S. Rode, M. Hayn, A. Röcker, S. Sieste, M. Lamla, D. Markx, C. Meier, F. Kirchhoff, P. Walther, M. Fändrich, T. Weil, J. Münch, Generation and characterization of virus-enhancing peptide nanofibrils functionalized with fluorescent labels, Bioconjugate Chem. 28 (2017) 1260–1270, https://doi.org/10.1021/acs.bioconjchem.7b00079.
[26] S. Busetto, E. Trevisan, P. Patriarca, R. Menegazzi, A single-step, sensitive flow cytofluorometric assay for the simultaneous assessment of membrane-bound and ingested Candida albicans in phagocytosing neutrophils, Cytometry 58A (2004) 201–206, https://doi.org/10.1002/cyto.a.20014.
[27] J.D. Loike, S.C. Silverstein, A fluorescence quenching technique using trypan blue to differentiate between attached and ingested glutaraldehyde-fixed red blood cells in phagocytosing murine macrophages, J. Immunol. Methods 57 (1983) 373–379, https://doi.org/10.1016/0022-1759(83)90097-2.
[28] L. Lipoglavšek, G. Avguštin, Application of flow cytometry for ecological monitoring of the rumen microbial ecosystem, Folia Microbiol. 46 (2001) 53–55, https://doi.org/10.1007/BF02825885.
[29] J.A. Swanson, Shaping cups into phagosomes and macropinosomes, Nat. Rev. Mol. Cell Biol. 9 (2008) 639–649, https://doi.org/10.1038/nrm2447.
[30] A.B. Borle, Kinetic analyses of calcium movements in HeLa cell cultures. I. Calcium influx, J. Gen. Physiol. 53 (1969) 43–56, https://doi.org/10.1085/jgp.53.1.43.
[31] M.B. James, T.D. Giorgio, Nuclear-associated plasmid, but not cell-associated plasmid, is correlated with transgene expression in cultured mammalian cells, Mol. Ther. 1 (2000) 339–346, https://doi.org/10.1006/mthe.2000.0054.
[32] X. Jiang, S. Dudzinski, K.E. Beckermann, K. Young, E. McKinley, J.O. McIntyre, J. C. Rathmell, J. Xu, J.C. Gore, MRI of tumor T cell infiltration in response to

checkpoint inhibitor therapy, J Immunother Cancer 8 (2020) e000328, https://doi.org/10.1136/jitc-2019-000328.
[33] B.B. Holmes, S.L. DeVos, N. Kfoury, M. Li, R. Jacks, K. Yanamandra, M.O. Ouidja, F.M. Brodsky, J. Marasa, D.P. Bagchi, P.T. Kotzbauer, T.M. Miller, D. Papy-Garcia, M.I. Diamond, Heparan sulfate proteoglycans mediate internalization and propagation of specific proteopathic seeds, Proc. Natl. Acad. Sci. USA 110 (2013) E3138–E3147, https://doi.org/10.1073/pnas.1301440110.
[34] P. Hivare, J. Gadhavi, D. Bhatia, S. Gupta, α-Synuclein fibrils explore actin-mediated macropinocytosis for cellular entry into model neuroblastoma neurons, Traffic 23 (2022) 391–410, https://doi.org/10.1111/tra.12859.
[35] D.C. Barral, L. Staiano, C. Guimas Almeida, D.F. Cutler, E.R. Eden, C.E. Futter, A. Galione, A.R.A. Marques, D.L. Medina, G. Napolitano, C. Settembre, O.V. Vieira, J.M.F.G. Aerts, P. Atakpa-Adaji, G. Bruno, A. Capuozzo, E. De Leonibus, C. Di Malta, C. Escrevente, A. Esposito, P. Grumati, M.J. Hall, R.O. Teodoro, S.S. Lopes, J.P. Luzio, J. Monfregola, S. Montefusco, F.M. Platt, R. Polishchuck, M. De Risi, I. Sambri, C. Soldati, M.C. Seabra, Current methods to analyze lysosome morphology, positioning, motility and function, Traffic 23 (2022) 238–269, https://doi.org/10.1111/tra.12839.
[36] M.J. Clague, S. Urbé, Multivesicular bodies, Curr. Biol. 18 (2008) R402–R404, https://doi.org/10.1016/j.cub.2008.02.068.
[37] J. Gruenberg, H. Stenmark, The biogenesis of multivesicular endosomes, Nat. Rev. Mol. Cell Biol. 5 (2004) 317–323, https://doi.org/10.1038/nrm1360.
[38] J. Neefjes, CIIV, MIIC and other compartments for MHC class II loading, Eur. J. Immunol. 29 (1999) 1421–1425, https://doi.org/10.1002/(SICI)1521-4141(199905)29:05<1421::AID-IMMU1421>3.0.CO;2-C.
[39] W.S. Garrett, I. Mellman, Chapter 16 - studies of endocytosis, in: M.T. Lotze, A. W. Thomson (Eds.), Dendritic Cells, second ed., Academic Press, London, 2001, p. 213, https://doi.org/10.1016/B978-012455851-9/50055-9, cp.1.
[40] Q. Wang, J. Yao, Q. Jin, X. Wang, H. Zhu, F. Huang, W. Wang, J. Qiang, Q. Ni, LAMP1 expression is associated with poor prognosis in breast cancer, Oncol. Lett. 14 (2017) 4729–4735, https://doi.org/10.3892/ol.2017.6757.
[41] A.L. Kovács, A. Reith, P.O. Seglen, Accumulation of autophagosomes after inhibition of hepatocytic protein degradation by vinblastine, leupeptin or a lysosomotropic amine, Exp. Cell Res. 137 (1982) 191–201, https://doi.org/10.1016/0014-4827(82)90020-9.
[42] M. M, O. I, R. C, Z. X, L. M, H. Kj, C. Rp, E. N, M. M, R. F, Chloroquine inhibits autophagic flux by decreasing autophagosome-lysosome fusion, Autophagy 14 (2018), https://doi.org/10.1080/15548627.2018.1474314.
[43] C. Meier, T. Weil, F. Kirchhoff, J. Münch, Peptide nanofibrils as enhancers of retroviral gene transfer, WIREs Nanomedicine and Nanobiotechnology 6 (2014) 438–451, https://doi.org/10.1002/wnan.1275.
[44] M.J. Lehmann, N.M. Sherer, C.B. Marks, M. Pypaert, W. Mothes, Actin- and myosin-driven movement of viruses along filopodia precedes their entry into cells, J. Cell Biol. 170 (2005) 317–325, https://doi.org/10.1083/jcb.200503059.
[45] N.M. Sherer, M.J. Lehmann, L.F. Jimenez-Soto, C. Horensavitz, M. Pypaert, W. Mothes, Retroviruses can establish filopodial bridges for efficient cell-to-cell transmission, Nat. Cell Biol. 9 (2007) 310–315, https://doi.org/10.1038/ncb1544.
[46] F.S. Pedersen, M. Pyrz, M. Duch, Retroviral replication, in: eLS, John Wiley & Sons, Ltd, 2011, https://doi.org/10.1002/9780470015902.a0000430.pub3.
[47] S. Dmitrieff, F. Nédélec, Membrane mechanics of endocytosis in cells with turgor, PLoS Comput. Biol. 11 (2015) e1004538, https://doi.org/10.1371/journal.pcbi.1004538.
[48] J.P. Lim, P.A. Gleeson, Macropinocytosis: an endocytic pathway for internalising large gulps, Immunol. Cell Biol. 89 (2011) 836–843, https://doi.org/10.1038/icb.2011.20.
[49] R.R. Kay, Macropinocytosis: biology and mechanisms, Cells & Development 168 (2021) 203713, https://doi.org/10.1016/j.cdev.2021.203713.
[50] J. Canton, Macropinocytosis: new insights into its underappreciated role in innate immune cell surveillance, Front. Immunol. 9 (2018), https://doi.org/10.3389/fimmu.2018.02286.
[51] G. Bloomfield, R.R. Kay, Uses and abuses of macropinocytosis, J. Cell Sci. 129 (2016) 2697–2705, https://doi.org/10.1242/jcs.176149.
[52] D.M. Veltman, T.D. Williams, G. Bloomfield, B.-C. Chen, E. Betzig, R.H. Insall, R. R. Kay, A plasma membrane template for macropinocytic cups, Elife 5 (2016) e20085, https://doi.org/10.7554/eLife.20085.
[53] J.A. Swanson, S. Yoshida, Macropinosomes as units of signal transduction, Philos. Trans. R. Soc. Lond. B Biol. Sci. 374 (2019) 20180157, https://doi.org/10.1098/rstb.2018.0157.
[54] M.C. Willingham, S.S. Yamada, A mechanism for the destruction of pinosomes in cultured fibroblasts. Piranhalysis, J. Cell Biol. 78 (1978) 480–487, https://doi.org/10.1083/jcb.78.2.480.
[55] M. Desjardins, Biogenesis of phagolysosomes: the "kiss and run" hypothesis, Trends Cell Biol. 5 (1995) 183–186, https://doi.org/10.1016/s0962-8924(00)88989-8.
[56] M.P. Bebelman, P. Bun, S. Huveneers, G. van Niel, D.M. Pegtel, F.J. Verweij, Real-time imaging of multivesicular body–plasma membrane fusion to quantify exosome release from single cells, Nat. Protoc. 15 (2020) 102–121, https://doi.org/10.1038/s41596-019-0245-4.
[57] J. Huotari, A. Helenius, Endosome maturation, EMBO J. 30 (2011) 3481–3500, https://doi.org/10.1038/emboj.2011.286.
[58] G. van Niel, G. D'Angelo, G. Raposo, Shedding light on the cell biology of extracellular vesicles, Nat. Rev. Mol. Cell Biol. 19 (2018) 213–228, https://doi.org/10.1038/nrm.2017.125.
[59] J. Lou, S.T. Low-Nam, J.G. Kerkvliet, A.D. Hoppe, Delivery of CSF-1R to the lumen of macropinosomes promotes its destruction in macrophages, J. Cell Sci. 127 (2014) 5228–5239, https://doi.org/10.1242/jcs.154393.
[60] A. Bayati, E. Banks, C. Han, W. Luo, W.E. Reintsch, C.E. Zorca, I. Shlaifer, E. Del Cid Pellitero, B. Vanderperre, H.M. McBride, E.A. Fon, T.M. Durcan, P. S. McPherson, Rapid macropinocytic transfer of α-synuclein to lysosomes, Cell Rep. 40 (2022) 111102, https://doi.org/10.1016/j.celrep.2022.111102.
[61] A. Papkalla, J. Münch, C. Otto, F. Kirchhoff, Nef enhances human immunodeficiency virus type 1 infectivity and replication independently of viral coreceptor tropism, J. Virol. 76 (2002) 8455–8459, https://doi.org/10.1128/JVI.76.16.8455-8459.2002.
[62] N.M. Sherer, M.J. Lehmann, L.F. Jimenez-Soto, A. Ingmundson, S.M. Horner, G. Cicchetti, P.G. Allen, M. Pypaert, J.M. Cunningham, W. Mothes, Visualization of retroviral replication in living cells reveals budding into multivesicular bodies, Traffic 4 (2003) 785–801, https://doi.org/10.1034/j.1600-0854.2003.00135.x.
[63] A. Bauer, N. Subramanian, C. Villinger, G. Frascaroli, T. Mertens, P. Walther, Megapinocytosis: a novel endocytic pathway, Histochem. Cell Biol. 145 (2016) 617–627, https://doi.org/10.1007/s00418-015-1395-2.

5.2 Appendix 2

Rauch-Wirth, L., Renner, A., Kaygisiz, K., Weil, T., Zimmermann, L., Rodriguez-Alfonso, A. A., Schütz, D., Wiese, S., Ständker, L., Weil, T., Schmiedel, D. & Münch, J. **Optimized peptide nanofibrils as efficient transduction enhancers for in vitro and ex vivo gene transfer.** *Front. Immunol.* **14**, 1270243 (2023).
https://doi.org/10.3389/fimmu.2023.1270243.

Reference[2]

License: CC By 4.0 (https://creativecommons.org/licenses/by/4.0/)

frontiers | Frontiers in Immunology

TYPE Original Research
PUBLISHED 09 November 2023
DOI 10.3389/fimmu.2023.1270243

Check for updates

OPEN ACCESS

EDITED BY
Michael Hudecek,
University Hospital Würzburg, Germany

REVIEWED BY
Di Yu,
Uppsala University, Sweden
Jessica Hartmann,
Paul-Ehrlich-Institut (PEI), Germany

*CORRESPONDENCE
Jan Münch
jan.muench@uni-ulm.de

RECEIVED 31 July 2023
ACCEPTED 24 October 2023
PUBLISHED 09 November 2023

CITATION
Rauch-Wirth L, Renner A, Kaygisiz K, Weil T, Zimmermann L, Rodriguez-Alfonso AA, Schütz D, Wiese S, Ständker L, Weil T, Schmiedel D and Münch J (2023) Optimized peptide nanofibrils as efficient transduction enhancers for *in vitro* and *ex vivo* gene transfer. *Front. Immunol.* 14:1270243. doi: 10.3389/fimmu.2023.1270243

COPYRIGHT
© 2023 Rauch-Wirth, Renner, Kaygisiz, Weil, Zimmermann, Rodriguez-Alfonso, Schütz, Wiese, Ständker, Weil, Schmiedel and Münch. This is an open-access article distributed under the terms of the Creative Commons Attribution License (CC BY). The use, distribution or reproduction in other forums is permitted, provided the original author(s) and the copyright owner(s) are credited and that the original publication in this journal is cited, in accordance with accepted academic practice. No use, distribution or reproduction is permitted which does not comply with these terms.

Optimized peptide nanofibrils as efficient transduction enhancers for *in vitro* and *ex vivo* gene transfer

Lena Rauch-Wirth[1], Alexander Renner[2], Kübra Kaygisiz[3], Tatjana Weil[1], Laura Zimmermann[1], Armando A. Rodriguez-Alfonso[4,5], Desiree Schütz[1], Sebastian Wiese[5], Ludger Ständker[4], Tanja Weil[3], Dominik Schmiedel[2] and Jan Münch[1,4]*

[1]Institute of Molecular Virology, Ulm University Medical Center, Ulm, Germany, [2]Department for Cell and Gene Therapy Development, Fraunhofer Institute for Cell Therapy and Immunology (IZI), Leipzig, Germany, [3]Department Synthesis of Macromolecules, Max Planck Institute for Polymer Research, Mainz, Germany, [4]Core Facility Functional Peptidomics, Ulm University Medical Center, Ulm, Germany, [5]Core Unit of Mass Spectrometry and Proteomics, Ulm University Medical Center, Ulm, Germany

Chimeric antigen receptor (CAR)-T cell therapy is a groundbreaking immunotherapy for cancer. However, the intricate and costly manufacturing process remains a hurdle. Improving the transduction rate is a potential avenue to cut down costs and boost therapeutic efficiency. Peptide nanofibrils (PNFs) serve as one such class of transduction enhancers. PNFs bind to negatively charged virions, facilitating their active engagement by cellular protrusions, which enhances virion attachment to cells, leading to increased cellular entry and gene transfer rates. While first-generation PNFs had issues with aggregate formation and potential immunogenicity, our study utilized *in silico* screening to identify short, endogenous, and non-immunogenic peptides capable of enhancing transduction. This led to the discovery of an 8-mer peptide, RM-8, which forms PNFs that effectively boost T cell transduction rates by various retroviral vectors. A subsequent structure-activity relationship (SAR) analysis refined RM-8, resulting in the D4 derivative. D4 peptide is stable and assembles into smaller PNFs, avoiding large aggregate formation, and demonstrates superior transduction rates in primary T and NK cells. In essence, D4 PNFs present an economical and straightforward nanotechnological tool, ideal for refining *ex vivo* gene transfer in CAR-T cell production and potentially other advanced therapeutic applications.

KEYWORDS

transduction enhancer, peptide nanofibrils, gene delivery, CAR-T cells, CAR-NK cells, lentiviral vector, retroviral vector

1 Introduction

Over the past few years, chimeric antigen receptor (CAR)-T cell therapy has gained prominence as an efficient treatment for various hematological malignancies such as B cell lymphoma, B cell acute lymphoblastic leukemia, and multiple myeloma (1–5). CAR-T cells are autologous engineered T cells that target specific tumor antigens leading to an antitumor immune response (6–8). So far, four CAR-T cell products targeting cluster of differentiation 19 (CD19) (axicabtagene ciloleucel (1), tisagenlecleucel (3), lisocabtagene maraleucel (9, 10) and brexucabtagene autoleucel (2)) and two B cell maturation antigen (BCMA)-targeted CAR-T cell products (idecabtagene vicleucel (11) and ciltacabtagene autoleucel (12)) are approved in the US and the EU by the FDA and the European Commission, respectively. All these products are generated by *ex vivo* viral transduction of patients' T cells using lentiviral or γ-retroviral vectors (13).

Recently, CAR-Natural Killer (NK) cell therapy has gained attention due to its notable advantages compared to CAR-T cell therapy. These advantages include a superior safety profile attributed to a decreased risk of cytokine-release syndrome and neurotoxicity (14), as well as multiple CAR-independent ways to activate cytotoxic activity (15, 16). Furthermore, CAR-NK cell therapy carries a reduced risk for graft-versus-host disease (GvHD), enabling the potential production of a single CAR-NK cell product for multiple patients (17, 18). The viral gene delivery of primary NK cells, which is significantly less efficient compared to primary T cells, poses a significant challenge in using CAR-NK cells for immunotherapy (19).

The manufacturing and administration of CAR-T and CAR-NK cells involve labor-intensive processes and significant costs. One crucial component contributing to these costs is the viral vector required for *ex vivo* cell manufacturing (20). However, by improving the transduction efficiency of target cells, it becomes possible to reduce the quantity of viral vectors needed, leading to potential cost savings (21). Beyond cost reduction, increased transduction efficiency plays a critical role in the success of CAR-T/NK cell therapy, as an adequate number of successfully transduced cells is essential for effective treatment (22). Therefore, focusing on improving transduction rates holds the key to not only potential cost savings but also enhancing the overall success rate of CAR-T and CAR-NK cell therapies.

To enhance transduction efficiency, various transduction enhancers have been developed, including polymers (23), lipids (24), peptides (21, 25), and polypeptides (26). Notably, two transduction enhancers, RetroNectin and Vectofusin-1, have been specifically employed in CAR-T and CAR-NK cell therapies (21, 22, 27, 28). RetroNectin, a recombinant human fibronectin fragment, facilitates lentiviral and γ-retroviral gene transfer by promoting the interaction between virus particles and cells through its heparin-binding domain, as well as its binding to cellular integrin receptors (29). While RetroNectin has demonstrated successful use in generating CAR-T cells (22, 28), its application is time-consuming, requiring pre-coating of cell culture flasks and sometimes centrifugation for improved transduction enhancement (22). On the other hand, Vectofusin-1 offers an alternative transduction enhancer approach. It is a self-assembling cationic 26-mer peptide that forms α-helical nanofibrils (30). Vectofusin-1 has shown efficacy in enhancing γ-retroviral and lentiviral transduction rates and is implemented in an automated and closed system, such as the CliniMACS Prodigy™, for CAR-T cell production (21).

Another promising transduction enhancer is Protransduzin, previously described as enhancing factor C (EF-C), a 12-mer peptide derived from Human immunodeficiency virus 1 (HIV-1) glycoprotein gp120, that forms β-sheet peptide nanofibrils (PNF) (25). These PNFs possess a positive surface charge, enabling them to effectively capture negatively charged viral particles. This interaction enhances the attachment of the viral particles to target cells, leading to increased transduction rates (25). Studies have further revealed that Protransduzin's transduction enhancing activity is actively mediated by cellular protrusions. This mechanism explains its superior performance compared to other additives (31). Protransduzin offers advantages over other transduction enhancers, such as Vectofusin-1 and RetroNectin, due to its shorter length and independence from additional steps like centrifugation or coating. This makes it a more cost-effective and user-friendly alternative. However, the chemical instability of Protransduzin, caused by the cyclization of its N-terminal glutamine to pyroglutamate, presents a challenge, which leads to significant aggregate formation in cell culture (32).

In this study we screened for novel short endogenous and non-immunogenic peptides that assemble into PNFs that efficiently enhance viral transduction rates but do not form large aggregates in cell culture, using an *in silico* screening approach. We discovered an 8-mer peptide, termed RM-8, derived from human interleukin-18, that forms chemically stable β-sheet PNFs, which effectively boost γ-retroviral and lentiviral gene transfer. By applying a structure-activity relationship (SAR) study RM-8 was optimized regarding aggregate formation to its derivative D4, which shows comparable or better transduction rates in primary T and NK cells than RM-8, Vectofusin-1, and EF-C. Thus, D4 PNFs represent a novel, easy-to-apply nanotechnological tool to increase viral transduction rates in the laboratory, and to optimize the production of CAR-T and CAR-NK cells.

2 Materials and methods

2.1 Cell culture

TZM-bl (AIDS reagent and reference programme, Saic Frederick, USA) and HEK293T cells (ATCC, CRL-3216) were cultured in Dulbecco´s Modified Eagle Medium (DMEM, Gibco, Catalog number (Cat): 11965092) supplemented with 10% inactivated fetal calf serum (FCS, Gibco, Cat: 10437028), 2 mM L-glutamine (PAN-Biotech, Cat: P04-80050), 100 U/ml penicillin and 100 µg/ml streptomycin (PAN-Biotech, P06-07050). Jurkat cells (ATCC, TIB-152) and THP1-Dual cells (InvivoGen, Cat: thpd-nfis) were cultured in Roswell Park Memorial Institute 1640 Medium (RPMI, Gibco, Cat: 11875093) supplemented with 10% FCS, 2 mM L-glutamine, 100 U/ml penicillin and 100 µg/ml

streptomycin. T cells were cultured in RPMI medium supplemented with 10% FCS, 2 mM L-glutamine, 100 U/ml penicillin, and 100 µg/ml streptomycin and different interleukins as described below.

2.2 Cell viability

To determine the effect of peptides on cellular metabolic activity, MTT (Thiazolyl blue tetrazolium bromide) Cell Growth Assay (Merck, Cat: CT02) and CellTiter-Glo Luminescent Cell Viability Assay (Promega, Cat: G7571) were performed. 10,000 TZM-bl cells or 50,000 Jurkat cells were seeded into 96-well plates and treated with indicated concentrations of peptides. For TZM-bl cells, the supernatants were removed after three days and 100 µl MTT (0.5 mg/ml) was added and incubated for 2.5 hours. For Jurkat cells, supernatants were removed after two days, and cells were incubated with 40 µl MTT (1 mg/ml) for 5 hours. Then the MTT solution was removed, and 100 µl 1:1 DMSO-Ethanol was added. The absorption was measured at 590 nm with baseline-corrected at 650 nm using VersaMax Microplate Reader (Molecular Devices). The CellTiter-Glo assay was performed according to the manufacturing protocol. 100 µl CellTiter-Glo Reagent 1:1 diluted in PBS (Gibco, 14200075) was added to pelleted Jurkat cells for 10 min followed by transferring 50 µl to white microplate, and luminescence was recorded by Orion microplate luminometer (Berthold).

2.3 *In-silico* screening for endogenous peptide nanofibrils (PNFs)

The Human proteins serum albumin (HSA, P02768), glyceraldehyde-3-phosphate dehydrogenase (GAPDH, P04406), signal transducing adapter molecule 2 (Stam2, O75886), and interleukin-18 (IL-18, Q14116) were analyzed by the amyloid prediction tools ZipperDB (33), Tango (34–36) and PASTA 2.0 (37). The amino acid sequence of the above proteins derived from UniProt was used. With the help of the ZipperDB the Rosetta energy was determined to predict fibrillation propensity, and hexapeptides showing a Rosetta energy below -23 kcal/mol were chosen based on Goldschmidt et al., 2010 (33). Additionally, the statistical mechanics algorithm TANGO was used. Fernandez-Escamilla et al., 2004 demonstrated that a TANGO score (percentage β-aggregation per residue) above 5% in a window of at least five residues is a good predictor for aggregation (35), which was also used for the analysis of HSA, GAPDH, Stam2, and IL-18. The following conditions were used for TANGO analysis: pH = 7, temperature = 25°C, ionic strength = 0.02 M, and concentration = 1 M. Using the server PASTA 2.0 for the analysis, an energy cut-off -5 Pasta Energy Unit (PEU) based on Walsh et al., 2014 (37), and a top pairing energy of 20 was selected for the analysis of the above-mentioned proteins. 1 PEU corresponds to 1.192 kcal/mol. The molecular weight and theoretical pI of the endogenous peptides were determined using ProtParam, a tool for the computation of various physical and chemical parameters (38).

2.4 Preparation of peptide nanofibrils

Peptides were synthesized by KE Biochem Co. (Shanghai City, China), Core Facility Functional Peptidomics (Ulm University Medical Centre, Ulm, Germany) and GaloreTx Pharmaceuticals (Udupi, India). Peptides were dissolved in DMSO (Merck, Cat: 67-68-5) to 10 mg/ml and stored at 4°C. For each experiment, the peptides were freshly dissolved in PBS to 2 mg/ml and incubated for 10 min at room temperature to generate peptide nanofibrils (PNFs). Unless otherwise described, this concentration was used for the experiments. Vectofusin-1 (Miltenyi Biotec, Cat: 130-111-163) was solved in sterile water to 1 mg/ml and stored at -80°C according to manufacturing protocol.

2.5 Thioflavin T (ThT) assay

To monitor the presence of PNFs, 25 µl PNFs solution was mixed with 24 µl PBS and 1 µl 2.5 mM ThT (Sigma, Cat: T3516) and incubated for 10 min at dark before fluorescence was measured at an excitation wavelength of 450 nm and an emission endpoint of 482 nm using a Synergy H1 hybrid multi-mode reader (Biotek).

2.6 Zeta potential

To determine the surface charge of fibrils, the zeta potential was measured. PNFs solutions were diluted in 1 ml 1 mM KCl (Merck, Cat: 104936) so that a number of traced particles of 100-400 was obtained. The zeta potential derived from the electrophoretic mobility of the PNFs was measured using the ZetaView TWIN (Particle Metrix) and the corresponding Software ZetaView (Zetaview Nanoparticle Tracking Analyzer RRID: SCR_016647).

2.7 Nanoparticle tracking analysis (NTA)

NTA to determine the size distribution of PNFs was performed using ZetaView TWIN. 2 mg/ml PNFs and 1 mg/ml Vectofusin-1 solutions were diluted in particle-free PBS, and videos of the light-refracting particles were recorded with the following settings: 25°C fixed temperature, 11 positions, 1 cycle, sensitivity 70, shutter 100, 15 fps, 2 s videos/position, 3 measurements. The chamber was rinsed between the samples with particle-free PBS.

2.8 Attenuated total reflection Fourier transform infrared (ATR-FTIR) spectroscopy

To analyze the secondary structure PNFs solutions were freshly prepared by diluting the DMSO stock (c = 10 mg/ml) tenfold using PBS (c = 1 mg/ml). 200 µl of samples were lyophilized, and all spectra were recorded on a Bruker Tensor 27 spectrometer with a diamond crystal as ATR element (PIKE MiracleTM, spectral resolution 2 cm^{-1}) according to a previous report (39).

2.9 Conversion rate (CR)

The CR determines the ratio of peptide monomers that convert into aggregated structures. To measure the CR, 1 mg/ml of PNFs were incubated in PBS for one day and the assay was performed according to a previous report (40).

2.10 Transmission electron microscopy (TEM)

5 µl PNFs solution (2 mg/ml) was incubated on a glow-discharged carbon copper grid for 5 min. The liquid on the grid was removed by Whatman™ filter paper (Merck) followed by three washing steps using 10 µl water each and then stained three times with 10 µl 0.5% (w/v) uranyl acetate (Merck). Remaining uranyl acetate was removed, and the grid was dried. Samples were imaged with the JEM-1400 120kV transmission electron microscope (Jeol).

2.11 Microscopic analysis of PNFs

To visualize aggregates of PNFs, microscopic images were taken of 2 mg/ml PNFs using Cytation 5 and 4x phase contrast (BioTek).

2.12 High-performance liquid chromatography (HPLC) analysis

RM-8 and D4 were prepared at 2 mg/ml in PBS and were incubated at room temperature (RT) or 37°C for 10 min, 1 hour, 24 hours, and 10 days. Aliquots (25 µL) of both samples were separated after 10 minutes, 1 hour, 24 hours, and 10 days and centrifuged at 13,000 x g for one minute. Supernatants were diluted with 100 µL 10% acetic acid, whereas the pellets were dissolved in 125 µL 6 M guanidinium chloride. All samples were analyzed in an Agilent 1100 Series HPLC system, using a reversed-phase BioBasicTM 18-HPLC column (Thermo Scientific) of dimensions 2.1 x 100 mm and particle size of 5 µm. Gradient elution was used for elution as follows (RM-8): 0 min/5%B, 1 min/20%B, and 15 min/40%B; and for D4: 0 min/5%B, 1 min/15%B, and 15 min/35/%B), being A, 0.1% TFA in water, and B, 0.1% TFA in acetonitrile. The flow rate was 0.5 mL/min, and the detection was monitored online by UV absorption at 214 nm. ChemStation (version B.04.03, Agilent) was used for data acquisition and the HPLC system's control.

2.13 Matrix assisted laser desorption ionization-time of flight mass spectrometry (MALDI-TOF MS) analysis

Mass spectra were obtained with an Axima Confidence MALDI-TOF mass spectrometer (Shimadzu). Measurements were performed in positive ion reflectron mode. The mass range was 100–10000 Da. For each sample, 20 shots were accumulated per profile (100 profiles per spectra) using a laser power of 42% and a laser frequency of 50 Hz. TOFMix MALDI kit (Shimadzu) was used for external mass calibration. Shimadzu Biotech Launchpad software (version 2.9.8.1, Kratos Analytical, UK) was used for spectra visualization and equipment control.

2.14 Virus stocks

For virus stock generation, 800,000 HEK293T cells were initially seeded, followed by transfection using different plasmids and TransIT-LT1 Transfection Reagent (Mirus Bio, Cat: Mir 2305) according to the manufacturer's protocol on the next day. After two days, virus stocks were harvested, centrifuged (3 min at 1300 rpm) and supernatants were stored at -80°C. Infectious HIV-1 stocks were produced by transfection of HEK293T cells using pBRNL4.39-92TH14 (5 µg), a plasmid containing a CCR5 tropic molecular HIV-1 clone (41). For GALV γ-retroviral vector (GALV-RV) production, HEK293T cells were cotransfected with the following plasmids: GFP expressing Murine leukemia virus (MLV) vector E200 pcmE26-gfp (1.15 µg), E848 pCsGPpA-ed (0.95 µg) and glycoprotein derived from Gibbon ape Leukemia Virus (GALV, 0.4 µg) (39). GALV-RV was titrated on Jurkat cells and transduction efficiency was determined by flow cytometry after two days. The GALV-RV titer was determined as transducing units per volume (TU/ml). GFP-expressing VSV-G pseudotyped lentiviral vector (VSV-G-LV) was generated by cotransfection of HEK293T cells with the plasmids pRSV-rev (0.25 µg, Addgene plasmid # 12253, a gift from Didier Trono) (42), pRRL.cPPT.SF-eGFP.pre (1 µg) (25), pMDLg/pRRE (3 µg, Addgene plasmid # 12251, a gift from Didier Trono) (42) and Vesicular Stomatitis Virus glycoprotein (VSV-G, 0.5 µg). Luciferase expressing VSV-G-LV was generated by cotransfection of HEK293T cells with the plasmids pSEW-luc2 (2 µg) and pCMV-dR8.91 (2 µg) and VSV-G (1 µg) (39). Luciferase-expressing RD114/TR pseudotyped lentiviral vector (RD114/TR-LV) was generated by cotransfection of HEK293T cells with an env deleted pBRHIV-1 NL4_3 derivative (2.5 µg) encoding luciferase instead of nef and phCMV-RD114/TR (0.31 µg) encoding chimeric envelope glycoproteins derived from Feline Leukemia Virus (RD114) with the cytoplasmic tail derived from the MLV glycoprotein (25). For RD114/TR γ-retroviral vector (RD114/TR-RV) production, HEK293T cells were cotransfected with the following plasmids: GFP expressing Murine leukemia virus (MLV) vector E200 pcmE26-gfp (1.15 µg), E848 pCsGPpA-ed (0.95 µg) and RD114/TR glycoprotein (0.4 µg). RD114/TR-RV was titrated on HEK293T cells and transduction efficiency was determined by flow cytometry after two days. GFP-encoding lentiviral vectors (LV) were generated by transfection of HEK293T cells (150,000 cells were seeded 1 day prior transfection) using following plasmids: 0.667 µg of pMDLg/pRRE-gagpol (Addgene plasmid # 12251, a gift from Didier Trono), 0.167 µg pRSV-Rev (Addgene plasmid # 12253, a gift from Didier Trono) (42), 1 µg of pCDH-CMV-MCS-EF1-GreenPuro (System Biosciences, Cat: CD513B-1) and an envelope plasmid (0.167 µg) for pseudotyping. RD114-TR (pLTR-RD114A, Addgene plasmid # 17576, a gift from Jakob Reiser) (43) or baboon envelope (BaEV, pTwist-BaEVRless) (44) were used as envelope

proteins. Two days after transfection, the cell culture supernatant was collected and filtered using a 0.45 µm syringe filter. LV containing supernatants were stored at -80°C.

2.15 Effect of PNFs on HIV-1 infection

To determine the effect of PNFs on HIV-1 infection 10,000 TZM-bl cells, which contain the reporter gene β-galactosidase under the control of the HIV-1 long terminal repeat (LTR) promoter, were seeded in a 96-well plate in 180 µl supplemented DMEM one day prior to infection. The cells were inoculated with 20 µl PNFs solution 1:1 (v/v) mixed with virus (2500 dilution on cells) after an incubation time of 10 min to allow the binding of virus particles to PNFs. Three days post HIV-1 infection, the cell culture medium was removed, and 42 µl of 1:8 diluted Gal-screen substrate (Thermo Fisher, Cat: T1027) in PBS was added. After incubation for 30-40 min, 36 µl of lysates were transferred to white microtiter plates, and β-galactosidase activity was recorded as relative light units (RLU) by Orion II Microplate Luminometer (Berthold).

2.16 Effect of PNFs on lentiviral transduction

To detect transduction rates of luciferase encoding lentiviral vectors (VSV-G-LVs, RD114/TR-LVs), 10,000 HEK293 cells were seeded in a 96-well plate in 180 µl supplemented DMEM one day prior to infection. The cells were inoculated with 20 µl PNFs solution 1:1 (v/v) mixed with virus (1:640 dilution on cells for VSV-G-LV and 1:80 dilution on cells for RD114/TR-LV) after an incubation time of 10 min. Two days after VSV-G-LV infection and three days after RD114/TR-LV infection the supernatant of cells was removed and cells were lysed in 40 µl 1-fold diluted Luciferase Cell Culture Lysis Reagent (Promega). After 10 min, cells were resuspended and 30 µl of the lysates were transferred into white microtiter plates. Thereafter, 50 µl luciferase substrate reconstituted in luciferase buffer (Luciferase Assay system, Promega) was added, and luminescence was measured as RLU using Orion II Microplate Luminometer (Berthold).

2.17 Effect of PNFs on γ-retroviral transduction

For the determination of infectivity enhancement of GALV-RV, 50,000 Jurkat cells were seeded in 180 µl supplemented RPMI. The cells were inoculated with 20 µl PNFs solution 1:1 (v/v) mixed with GALV-RV after an incubation time of 10 min. Two days post infection, GFP-expression was analyzed by flow cytometry using CytoFlex (Beckmann Coulter) and the evaluation was carried out with FlowJo™ (Version 10.8.1) according to the gating strategy shown in Figure S1. For analyzing the transduction enhancement of RD114/TR-RV, 10,000 HEK293T cells were seeded in a 96-well plate in 100 µl supplemented DMEM one day prior to infection. The cells were inoculated with 100 µl PNFs solution 1:1 (v/v) mixed with virus after an incubation time of 10 min. Transduction efficiency was determined three days later by flow cytometry.

2.18 γ-retroviral and lentiviral transduction of human T cells

Human CD4+ and CD8+ T cells were isolated from Buffy coats of healthy donors using RosetteSep™ Human CD4+ Enrichment Cocktail (STEMCELL Technologies, Cat: 15062) and CD8+ Enrichment Cocktail (STEMCELL Technologies, Cat: 15063) according to manufacturer's protocol. Isolated T cells were activated using Dynabeads™ Human T-Activator CD3/CD28 (Gibco, Cat: 11131D) according to manufacturer's protocol in supplemented RPMI in presence of 10 ng/ml IL-2 (Miltenyi Biotec, Cat: 130-097-748) for three days. The purity of isolated T cells was determined by flow cytometry using CD4, CD8, and CD11c antibodies and their corresponding isotype control (Table S1). After three days, the magnetic Dynabeads were removed, and T cells were cultured in supplemented RPMI in presence of 450 IU/ml IL-7 (Miltenyi Biotec, Cat: 130-095-362) and 50 IU/ml IL-15 (Miltenyi Biotec, Cat: 130-095-764). After one day 5×10^5 T cells were transduced with GALV-RV (1:4 dilution on cells) or VSV-G-LV (1:40 dilution on cells) in absence and presence of RM-8 (30 or 50 µg/ml), D4 (30 µg/ml), EF-C (30 or 50 µg/ml), 10 µg/ml Vectofusin-1 (Miltenyi Biotec, Cat: 130-111-163), or 20 µg/ml RetroNectin (Takara Bio, Cat: T100B). The 24-well plate was coated with RetroNectin and incubated overnight at 4°C. Wells were blocked with PBS containing 2% BSA (Gibco, Cat: 15260037) for 30 min and washed twice with PBS. Virus was centrifuged onto coated wells at 2,000 g at 32°C for 2 h. Viral supernatant was removed and T cells were added and subsequently spin-infected (300 g for 10 min). One day after transduction, the medium was exchanged. T cells were cultured with a cell density of 1×10^6 cells/ml for seven days. T cells were analyzed for CD3 expression using an antibody and its corresponding isotype controls shown in Table S1. Furthermore, viability using LIVE/DEAD™ Fixable Aqua Dead Cell Stain Kit (ThermoFisher Scientific, Cat: L34957) and Trypan blue stain (Invitrogen, Cat: T10282) according to the manufacturer's protocol and transduction efficiency (% GFP+ cells) were determined. Flow cytometry analysis were performed using CytoFlex (Beckmann Coulter) and evaluation was carried out with FlowJo™ (Version 10.8.1). The gating strategy shown in Figure S2 was applied.

2.19 Lentiviral transduction of human NK cells

NK cells were isolated from buffy coats of healthy donors by standard density-gradient centrifugation, using Ficoll-Paque (VWR, Cat: 17-1440-03) using the RosetteSep™ Human NK Cell Enrichment Cocktail (STEMCELL Technologies, Cat: 15065). NK cells were cultured at 1×10^6 cells/ml in NK MACS medium

10.3389/fimmu.2023.1270243

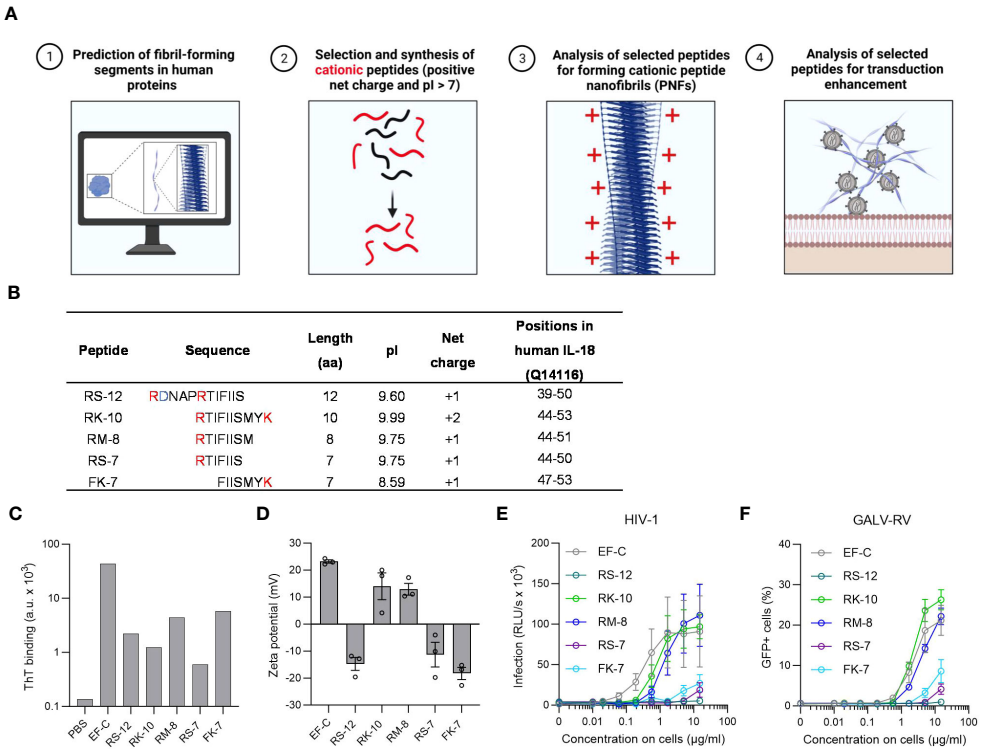

Peptide	Sequence	Length (aa)	pI	Net charge	Positions in human IL-18 (Q14116)
RS-12	RDNAPRTIFIIS	12	9.60	+1	39-50
RK-10	RTIFIISMYK	10	9.99	+2	44-53
RM-8	RTIFIISM	8	9.75	+1	44-51
RS-7	RTIFIIS	7	9.75	+1	44-50
FK-7	FIISMYK	7	8.59	+1	47-53

FIGURE 1
In silico identification and characterization of IL-18 derived PNF as potential enhancers for viral transduction. **(A)** *In silico* screening for endogenous PNFs as transduction enhancers using different amyloid aggregation algorithms (Tango, PASTA 2.0, and ZipperDB). Created with BioRender.com. **(B)** Physical and chemical parameters of selected IL-18 derived peptides with positive net charge based on *in silico* screening results. The positively charged amino acids are marked in red, and the negatively charged residues in blue. The positions of the peptides correspond to human IL-18 (UniProtKB: Q14116) without the propeptide. **(C)** ThT fluorescence intensities of tested peptides. Shown is one measurement from one experiment. **(D)** Zeta potential, an indicator of the surface charge, of IL-18 derived PNFs. The results shown are average values (± SEM) of duplicates measurement from three independent experiments. **(E)** RM-8 and RK-10 PNFs increase HIV-1 infection of TZM-bl cells. HIV-1 was treated with PNFs and mixtures were used to infect TZM-bl cells. Tat-inducible β-galactosidase activity was measured three days later. The results shown are average values (± SEM) of triplicate measurements from three independent experiments. **(F)** RM-8 and RK-10 PNFs enhance GALV-RV infection of Jurkat cells. GFP-expressing GALV-RV was treated with PNFs and mixtures were used to infect Jurkat cells. GFP positive (GFP+) cells were determined two days later by flow cytometry. The results shown are average values (± SD) of three independent experiments. GALV, glycoprotein of gibbon ape leukemia virus; HIV-1, Human immunodeficiency virus 1; IL-18, interleukin-18; PNFs, peptide naofibrils; RLU/s, relative light units per second; RV, γ-retroviral vector; ThT; Thioflavin T; SEM, standard error of the mean.

(Miltenyi Biotec, Cat: 130-114-429) with 5% human AB serum (Sigma Aldrich, Cat: H4522-100ML), 500 U/ml IL-2 (Peprotech, Cat: 200-02) and 140 U/ml IL-15 (Peprotech, Cat: 200-15). After seven days of culturing, NK cells were transduced with lentiviral particles. 1.25×10^5 NK cells were seeded per well in a 48-well plate. 250 µl of lentiviral supernatant (undiluted RD114/TR-LV stock, 1:3 diluted BaEV-LV stock in HEK293T culture medium) was mixed with transduction enhancers to final concentrations of 10 µg/ml for Vectofusin-1 and either 10, 20 or 30 µg/ml for RM-8 and D4 peptides and then incubated at room temperature for 10 min prior to adding to the NK cells. After incubation at 37°C for 1 h, 250 µl of fresh complete NK MACS medium was added to the transduced cells. For spinfection, cells were centrifuged (400 g, 1 h at 37°C) after virus and transduction enhancer were added. Transduction efficiency (GFP+ cells) was assessed four days after transduction using flow cytometry (MACSQuant10, Miltenyi Biotec). Propidium Iodide (PI) (Miltenyi Biotec, Cat: 130-093-233) staining was used to determine the viability of NK cells.

2.20 PNFs stimulation of THP1-Dual cells

To analyze if PNFs stimulate an immune response, different PNFs concentrations (5, 10, 30 and 50 µg/ml) and 0.1 µg/ml lipopolysaccharide (LPS, InvivoGen, Cat: tlrl-eklps) as a positive control were incubated with 70,000 THP1-Dual cells, a monocyte cell line that allows the simultaneous analysis of the NF-κB and interferon regulatory factor (IRF) pathway, which are major effectors of the innate immune response (45). After 24 h, cellular supernatants were analyzed for the activation of the NF-κB pathway by measuring the activity of secreted alkaline phosphatase (SEAP). Therefore, 20 µl supernatant was mixed with 120 µl Alkaline Phosphatase Blue Microwell Substrate (Sigma Aldrich, Cat: AB0100-1KT). After 10 min, 30 µl Alkaline Phosphatase Stop Solution (Sigma Aldrich, Cat: A5852) was added and adsorption at 620 nm was measured using VersaMax Microplate Reader (Molecular Devices). For analysis of IRF pathway, secreted Gaussia Luciferase was measured. 25 µl supernatant was

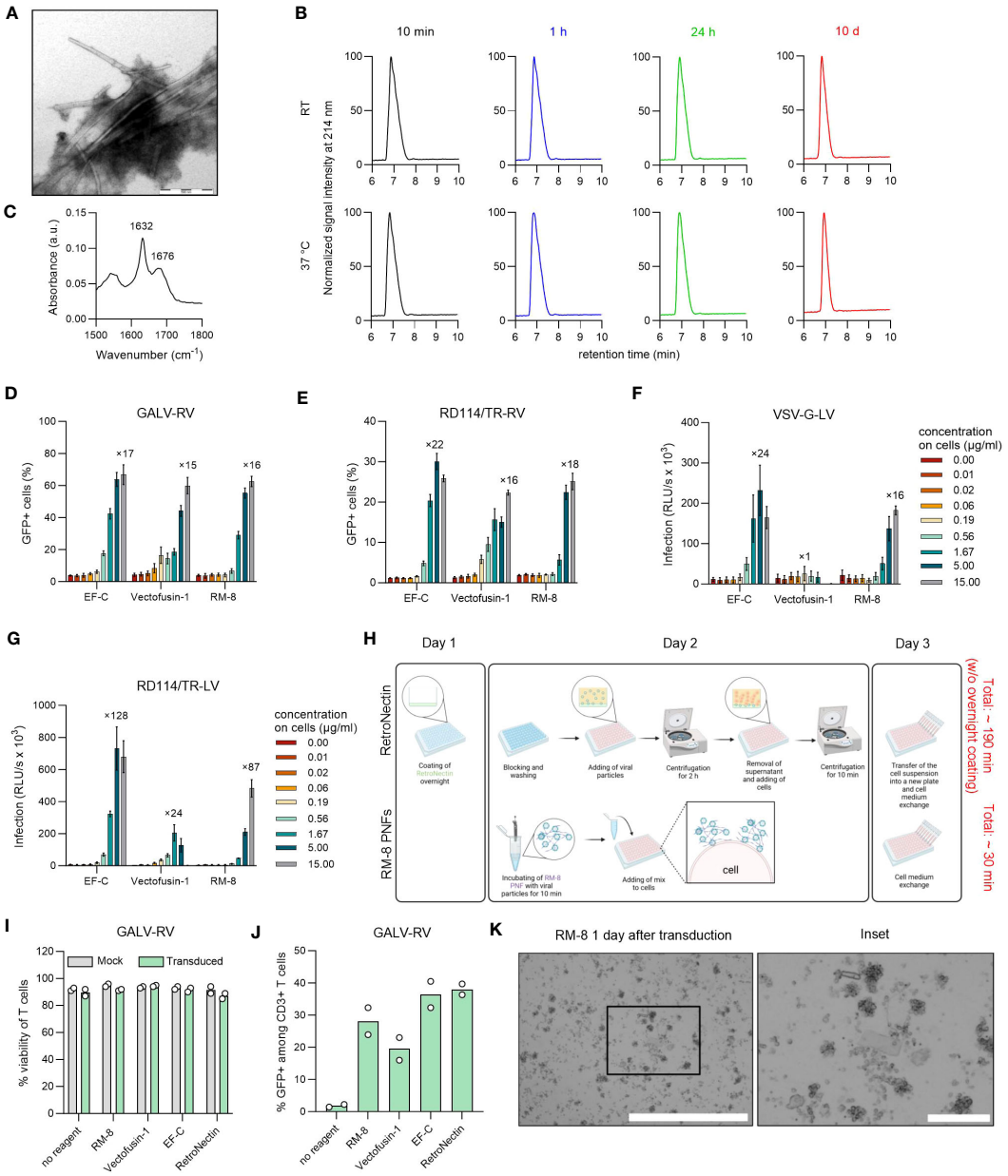

FIGURE 2
Biophysical and functional characterization of RM-8 PNFs. **(A)** TEM image of RM-8 PNFs. Scale bar indicates 500 nm. **(B)** RM-8 PNFs are chemically stable for 10 days, as analyzed by HPLC. **(C)** ATR-FTIR spectrum of RM-8, showing spectral maxima in the amide I region indicating β-sheet structure. **(D)** RM-8 PNFs efficiently enhance transduction rates of GFP-expressing GALV-RV in Jurkat cells. Two days after transduction GFP+ cells were determined by flow cytometry. Shown are average values (± SD) of three independent experiments. **(E)** RM-8 PNFs efficiently enhance transduction rates of GFP-expressing RD114/TR-RV in HEK293T cells. Three days after transduction GFP+ cells were determined by flow cytometry. Shown are average values (± SD) of three independent experiments. **(F)** RM-8 PNFs efficiently enhance transduction rates of Luciferase-expressing VSV-G-LV in HEK293T cells. Two days after transduction infection rates were determined by measuring Luciferase signal. Shown are average values of triplicates (± SEM) of three independent experiments. **(G)** RM-8 PNFs efficiently enhance transduction rates of Luciferase-expressing RD114/TR-LV in HEK293T cells. Three days after transduction infection rates were determined by measuring Luciferase signal. Shown are average values of triplicates (± SEM) of three independent experiments. In D-F the numbers above the bars show the n-fold enhancement of infection relative to the average of controls without peptide. **(H)** Transduction protocol for using RetroNectin and RM-8 PNFs as transduction enhancer in an *ex vivo* gene transfer. Created with BioRender.com. **(I)** Viability of T cells was determined using trypan blue staining after 7 days. Shown are average values (± SD) of two donors. **(J)** RM-8 PNFs enhance retroviral transduction of T cells similar to Vectofusin-1 and RetroNectin. GALV-RV was incubated with indicated transduction enhancers before transducing activated T cells according to protocol of **(H)** GFP+ cells were determined by flow cytometry after 7 days. Shown are values of two donors. **(K)** RM-8 forms aggregates 1 day after transduction. Scale bar indicates 1000 µm and for the inset 200 µm. ATR-FTIR, Attenuated total reflection Fourier transform infrared spectroscopy; A.u., arbitrary units; centrif., centrifugation step; GALV, glycoprotein of gibbon ape leukemia virus; HPLC, high-performance liquid chromatography; LV, lentiviral vector; RD114/TR, chimeric envelope glycoprotein derived from feline leukemia virus with the cytoplasmic tail derived from the murine leukemia virus glycoprotein; RV; γ-retroviral vector; SEM, standard error of mean; TEM, Transmission electron microscopy; VSV-G, glycoprotein of vesicular stomatitis virus.

transferred to a white 96 well microtiter plate and Gaussia substrate (82.6 µg/ml Colenterazine, PJK, Cat: 102172) was automatically added according to manufacturer's protocol and Luminescence was measured by Orion II Microplate Luminometer (Berthold).

2.21 PNFs stimulation of CD4+ T cells

For the investigation of T cell immune response after PNFs stimulation, 50,000 CD4+ T cells were incubated with different PNFs concentrations (5, 10, 30 and 50 µg/ml) and 0.1 µg/ml LPS as a positive control. After 24 h, supernatants were analyzed by flow cytometry, using the LEGENDplex Human Inflammation Panel 1 (Biolegend, Cat: 740809), a bead-based multiplex assay to quantify human inflammatory cytokines/chemokines, according to manufacturing protocol. Mean fluorescence of the samples were normalized to the untreated control.

2.22 Statistics

Statistical analysis including one-way ANOVA with Dunnett's multiple comparison test were performed using GraphPad Prism version 9.5.1.

2.23 Ethics statement

NK cells from healthy donors were isolated from buffy coats acquired from the blood bank of the University Hospital Leipzig; ethic vote number 327/22-ek. T cells from healthy donors were isolated from buffy coats acquired from the Blutspendezentrale Ulm; ethic vote number 151/22 FSt/bal.

3 Results

3.1 *In silico* screening for peptide nanofibrils as transduction enhancer

We previously identified the 12-mer peptide EF-C that self-assembles into peptide nanofibrils (PNFs) and efficiently enhances γ-retroviral gene transfer in various *in vitro* settings (25). The application of EF-C for CAR-T cell generation is however limited due to its time-dependent chemical instability and the formation of large aggregates under cellular conditions (32). Additionally, its sequence is derived from HIV-1 glycoprotein gp120 (25), which may potentially induce immunogenicity. Therefore, our goal was to identify novel endogenous and non-immunogenic peptides that assemble into PNFs and efficiently enhance viral transduction without forming larger aggregates.

For this, we analyzed arbitrary human proteins (serum albumin (HSA), glyceraldehyde-3-phosphate dehydrogenase (GAPDH), signal transducing adapter molecule 2 (Stam2) and interleukin-18 (IL-18)) by an *in silico* screening approach using a combination of amyloid prediction algorithms (Figure 1A). As selection criteria, proteins were chosen according to their expression (high: HSA and GAPDH, low: Stam2 and IL-18) and localization (extracellular: HSA, IL-18, intracellular: GAPDH, Stam2). The algorithms Tango, PASTA 2.0, and ZipperDB collectively offer predictive capabilities for identifying various aspects of protein aggregation and have been evaluated by us in a previous report to perform well for the prediction of short self-assembling peptides (46). TANGO predicts aggregation areas in unfolded polypeptide chains (34–36), PASTA 2.0 predicts amyloid fibril regions in proteins (37), and ZipperDB predicts fibril-forming segments capable of forming the steric zipper, the backbone of an amyloid fibril (33). By *in-silico* screening, a fibril-forming segment (position 39-53) was determined for IL-18 by all three algorithms (Figure S3). For the other proteins only a hexapeptide in HSA was predicted to self-assemble which could not be experimentally confirmed.

Based on the predicted region in IL-18 five different cationic peptides named RS-12, RK-10, RM-8, RS-7, and FK-7 were chemically synthesized and further analyzed (Figure 1B). PNFs formation of the five peptides was achieved by dilution of their DMSO stock (10 mg/ml) in PBS (2 mg/ml) and incubation for 10 min at room temperature (RT). To test the peptides' ability to form PNFs, they were incubated with the amyloid dye Thioflavin T (ThT), showing a clear ThT fluorescence for all peptides (Figure 1C). Since we previously showed that the positive charge of PNFs is essential for their transduction enhancing property (25, 39, 47), the zeta potential (ZP), an indicator for the surface charge, was measured. ZP measurements revealed a positive ZP for RK-10 and RM-8 PNFs (Figure 1D). In fact, both PNFs efficiently enhanced HIV-1 infection of TZM-bl cells (Figure 1E) while not being cytotoxic (Figure S4A). Moreover, RM-8 PNF also increased transduction rates of T cells with a γ-retroviral vector pseudotyped with the glycoprotein of gibbon ape leukemia virus glycoprotein (GALV-RV), within a comparable range to EF-C PNFs, while exhibiting no cytotoxic effects (Figures 1F, S4).

3.2 RM-8 PNFs efficiently enhance γ-retroviral and lentiviral transduction

Due to its simplicity and cost-effectiveness in synthesis, we continued our further study with the shortest 8-mer peptide RM-8. PNFs formation of RM-8 was confirmed by transmission electron microscopy (TEM, Figure 2A). Furthermore, a high conversion rate (CR) of 97% was determined. The CR indicates the percentage of monomers that self-assemble into aggregated structures (40). To analyze the chemical stability of RM-8, respective PNFs were incubated for 10 min, 1 h, 24 h or 10 d at room temperature (RT) or 37°C, followed by high performance liquid chromatography (HPLC) analysis. Chromatograms show one peak at the same retention time for each time point (Figure 2B), indicating that RM-8 PNFs are chemically stable over time. Further biophysical analysis using attenuated total reflection fourier transform infrared (ATR-FTIR) spectroscopy revealed the amide I maxima at approximately 1632 and 1676 cm^{-1} (Figure 2C), which are characteristic for the presence of β-sheet structures (48).

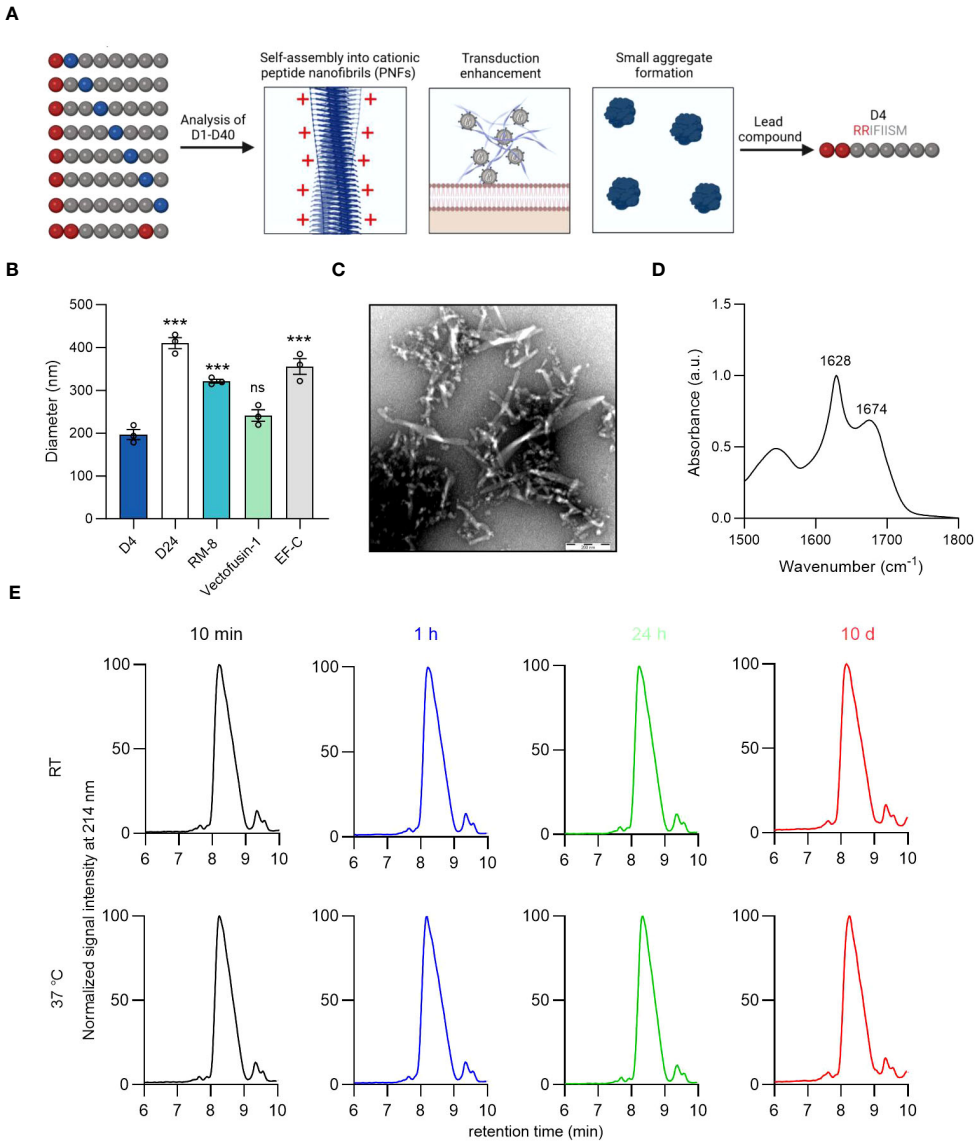

FIGURE 3
Identification of lead candidate D4 by a structure-activity relationship study of RM-8. **(A)** Optimization of RM-8 in regard to aggregate formation and transduction enhancing activity by a SAR study. 40 RM-8 derivatives (D1-D40) were generated by replacing the amino acids at position 2-8 with the following amino acids: isoleucine (I), proline (P), glycine (G), threonine (T), lysine (K) or arginine (R), which are shown in blue. Furthermore a derivative was generated containing three arginines (shown in red). The N-terminal R was not replaced as it is responsible for the positive charge of RM-8. Created with BioRender.com. **(B)** Diameter of D4, D24, RM-8, Vectofusin-1 and EF-C PNFs measured by NTA. The results shown are average values (± SD) of triplicates from three independent measurements. One-way ANOVA, Dunnett's multiple comparison test. ***$p \leq 0.001$ **(C)** TEM image of D4 PNFs. Scale bar indicates 200 nm. **(D)** FTIR spectrum of D4. The values in the plot refer to spectral maxima in the amide I region. **(E)** D4 PNF are chemically stable for 10 days. D4 PNFs (2 mg/ml) were incubated at room temperature and 37°C and after 10 min, 1 h, 24 h and 10 days, the chemical stability was analyzed using HPLC. Also, MALDI-TOF MS measurements were done on D4 PNFs after incubation for 10 days at RT and 37°C (Figure S7) to confirm that the monoisotopic mass did not change due to any modification. ATR-FTIR, Attenuated total reflection Fourier transform infrared spectroscopy; HPLC, high-performance liquid chromatography MALDI-TOF MS, Matrix assisted laser desorption ionization-time of flight mass spectrometry; NTA, nanoparticle tracking analysis; TEM, Transmission electron microscopy; SAR, structure-activity relationship.

Since all CAR-T cell therapies approved to date are manufactured using γ-retroviral and lentiviral vectors (13), we analyzed RM-8 PNFs' ability to enhance these vectors in comparison to the commercially available transduction enhancer Vectofusin-1, which is a 26-mer amphipathic peptide (30). RM-8 PNFs increased transduction of GFP-expressing γ-retroviral vector pseudotyped with the glycoprotein of GALV, or from feline leukemia virus (RD114/TR-RV) in a similar range as Vectofusin-1, from around 4% to 60% GFP+ cells for GALV-RV (Figures 2D, S5B) and from around 2% to 25% GFP+ cells for RD114/TR-RV (Figures 2E, S5C) without showing cytotoxicity (Figures S4B, C). Of note, RM-8 PNFs promoted transduction of luciferase encoding LVs carrying the G protein of the Vesicular Stomatitis Virus (VSV-G) or RD114 more efficiently than Vectofusin-1 (Figures 2F, G).

To test RM-8 PNFs in a more clinically relevant setting, activated human CD4+ and CD8+ T cells were transduced with

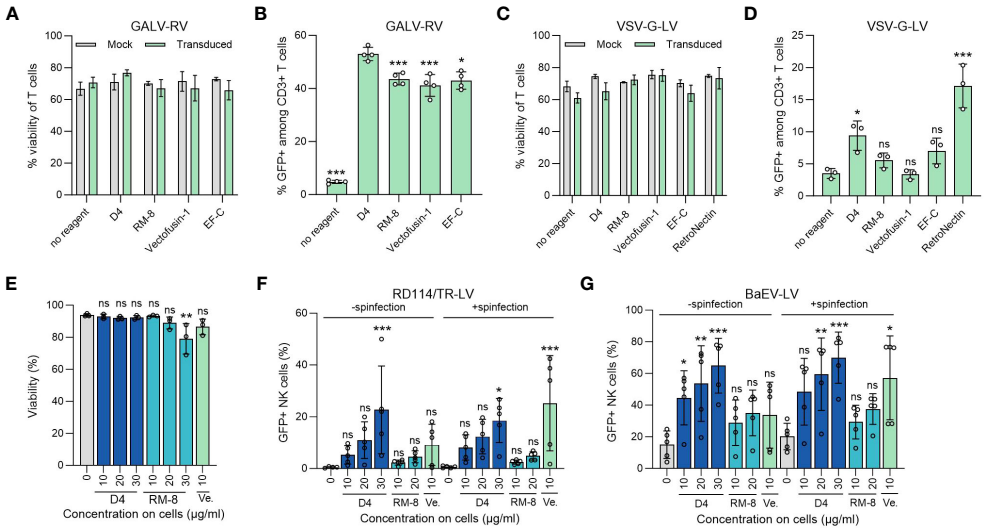

FIGURE 4
D4 as an efficient transduction enhancer for γ-retroviral and lentiviral transduction of human T and NK cells. **(A)** Viability of T cells was determined using trypan blue staining 7 days after GALV-RV transduction. Shown are average values (± SD) of four donors. Two-way ANOVA, Šidák's multiple comparison test. No significant differences in viability between no reagent and the transduction enhancers were determined. **(B)** D4 PNFs more efficiently enhance GALV-RV transduction of T cells than RM-8, Vectofusin-1 and EF-C PNFs. GFP+ cells were determined by flow cytometry after 7 days. Data are presented as mean ± SD of four donors. One-way ANOVA, Dunnett's multiple comparison test. **p ≤ 0.01, ***p ≤ 0.001. **(C)** Viability of T cells was determined using trypan blue staining 7 days after VSV-G-LV transduction. Shown are average values (± SD) of three donors. Two-way ANOVA, Šidák's multiple comparison test. No significant differences in viability between no reagent and the transduction enhancers were determined. **(D)** D4 PNFs more efficiently enhance transduction rates of GFP-expressing VSV-G-LV in T cells than RM-8, Vectofusin-1 and EF-C PNFs. GFP+ cells were determined by flow cytometry after 7 days. Data are presented as mean ± SD of three donors. One-way ANOVA, Dunnett's multiple comparison test. **p ≤ 0.01, ***p ≤ 0.001. **(E)** D4 PNFs do not reduce viability of human NK cells. Activated NK cells of three donors were incubated with different concentrations of D4 and RM-8 PNFs, and viability was determined by propidium iodide staining after 4 days. One-way ANOVA, Dunnett's multiple comparison test. *p ≤ 0.05. Activated NK cells of five donors were transduced with a GFP-expressing LV pseudotyped with RD114/TR **(F)** or a baboon endogenous virus derived envelope (BaEV, **G**) with and without spinfection. GFP+ cells were determined by flow cytometry after 4 days. Shown are average values (± SD) of five donors. One-way ANOVA, Dunnett's multiple comparison test. *p ≤ 0.05, **p ≤ 0.01, ***p ≤ 0.001. GALV, glycoprotein of gibbon ape leukemia virus; RD114/TR, chimeric envelope glycoprotein derived from feline leukemia virus with the cytoplasmic tail derived from the murine leukemia virus glycoprotein; LV, lentiviral vector; RV, γ-retroviral vector; Ve., Vectofusin-1; VSV-G, glycoprotein of vesicular stomatitis virus.

GALV-RV in presence of different transduction enhancers (RM-8, EF-C, Vectofusin-1 and RetroNectin), according to the protocol described in Figure 2H. After cultivation for seven days, viability and transduction efficiencies were determined. RM-8 PNFs allowed similar transduction rates of T cells of around 28% GFP+ cells as Vectofusin-1 and RetroNectin while not showing any cytotoxic effect (Figures 2I, J, S5E). However, during the T cell transduction process large µm-sized fibrillar aggregates were observed for RM-8 PNFs (Figure 2K).

3.3 Optimization of RM-8 to its derivate D4 by a structure-activity relationship study

The µm-scale RM-8 aggregates that formed in the T cell cultures could potentially hinder approval of RM-8 PNFs as a transduction enhancer in clinical settings. To address this, we fine-tuned RM-8 based on a structure-activity relationship (SAR) study, with a specific focus on minimizing aggregation (Figure 3A). For stability, we excluded amino acids prone to oxidation (phenylalanine, tryptophan, tyrosine, histidine, cysteine and methionine), intra- and inter-residue cyclization (asparagine, glutamine, aspartic and glutamic acid), and β-elimination (cysteine, serine and threonine) (49) from the SAR study, except for threonine, which was already present in RM-8 and did not induce instability.

We opted to evaluate a large peptide library composed of 40 RM-8 derivatives (Table S2). This was accomplished by mutating the amino acids at positions 2-8 of RM-8 with isoleucine (I), proline (P), glycine (G), threonine (T), lysine (K), and arginine (R). The C-terminal R remained unchanged due to its critical role in contributing to the positive surface charge and hence the enhancement activity. We picked the positively charged amino acids L and R with the prospect that an increase in net charge could diminish aggregation propensity through electrostatic repulsion (50), potentially leading to the formation of smaller, more beneficial aggregates. Our findings revealed that, with the exception of D17, D18, D25, and D26, all derivatives exhibited an amyloid-specific enhancement in ThT binding, as illustrated in Figure S6A. Additionally, out of the 40 RM-8 derivatives tested, only 10 displayed a positive ZP, as shown in Figure S6B. Most of the derivatives amplified γ-retroviral transduction rates in Jurkat cells comparably to RM-8 PNFs, without any noticeable cytotoxic effect (Figures S6C, S6D).

Microscopic imaging of derivatives with similar transduction enhancing activity to RM-8 showed no significant aggregation in

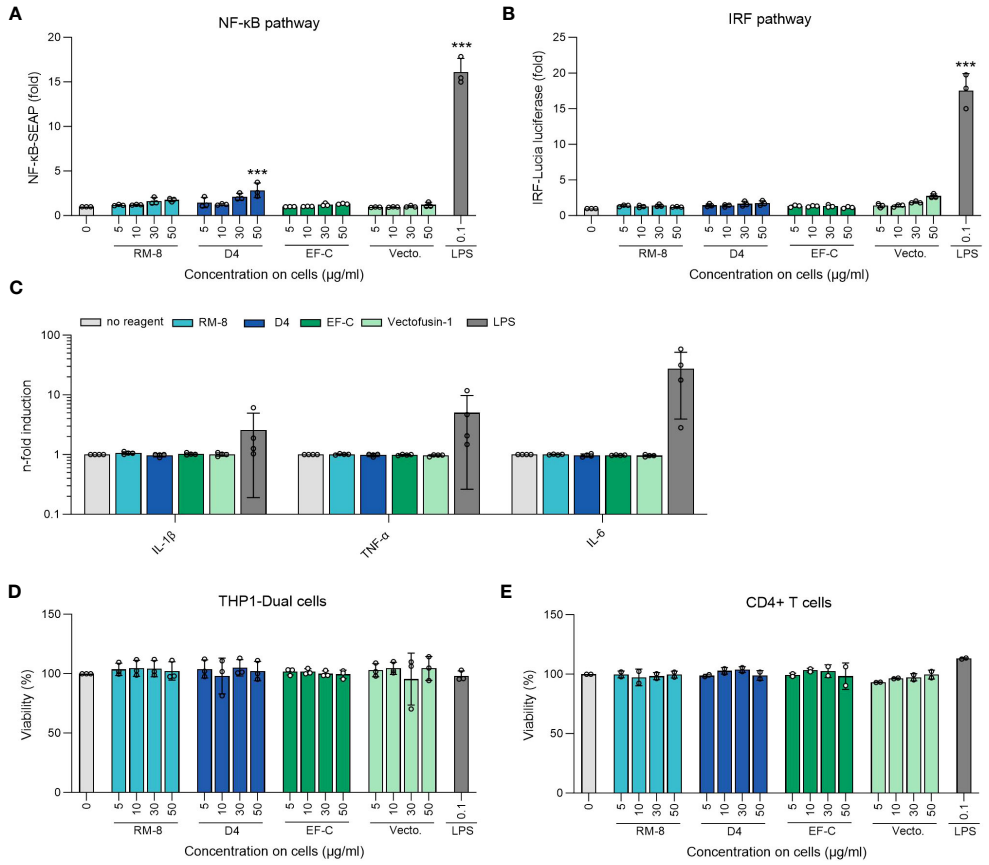

FIGURE 5
Analysis of inflammatory response of THP1-Dual and CD4+ T cells after PNFs stimulation. **(A)** Analysis of NF-κB pathway of THP1-Dual cells after PNFs and LPS stimulation. One-way ANOVA, Dunnett's multiple comparison test. ***p ≤ 0.001. **(B)** Analysis of IRF pathway of THP1-Dual cells after PNFs and LPS stimulation. One-way ANOVA, Dunnett's multiple comparison test. ***p ≤ 0.001. For A and B THP1-Dual cells, a monocyte-derived cell line, were treated with different PNFs (RM-8, D4, EF-C and Vectofusin-1) concentrations and 0.1 µg/ml LPS as a positive control. After one day the supernatants were simultaneously analyzed for activation of NF-κB pathway and the IRF pathway. Values were normalized to the PBS control. Shown are mean values (± SEM) of triplicate measurements from three independent experiments. **(C)** Analysis of different human inflammatory cytokines/chemokines after PNFs stimulation of CD4+ T cells using LEGENDplex Human Inflammation Panel 1. CD4+ T cells were treated with 30 µg/ml PNFs (RM-8, D4, EF-C and Vectofusin-1) and 0.1 µg/ml LPS as a positive control. After one day the cytokines/chemokines levels were analyzed using flow cytometry. Values were normalized to the untreated cells. Shown are mean values (± SEM) of duplicates of four donors. **(D)** Viability of THP1-Dual cells after PNFs and LPS stimulation. 24 h after stimulation viability was determined using CellTiter-Glo Luminescent Cell Viability Assay. Shown are mean values (± SEM) of triplicate measurements from three independent experiments. **(E)** Viability of CD4+ T cells after PNFs and LPS stimulation. 24 h after stimulation, viability was determined using CellTiter-Glo Luminescent Cell Viability Assay. Shown are mean values (± SEM) of duplicates of two donors. IL, interleukin; IRF, interferon regulatory factor; LPS, lipopolysaccharides; TNF-α, tumor necrosis factor alpha; SEAP, secreted alkaline phosphatase; Vecto., Vectofusin-1.

D4 and D24 (Figure S7). Using nanoparticle tracking analysis (NTA), we found D4's diameter to be around 200 nm, similar to Vectofusin-1, while D24, RM-8, and EF-C showed considerably larger diameters (Figure 3B). It is important to note that NTA can only measure particle sizes from about 30 to 1000 nm (51), thus making it unable to measure PNFs larger than 1 µm. This led us to identify D4 (RRIFIISM), where a threonine was replaced by an arginine at position 2, as the lead candidate from the SAR study. TEM analysis depicted that the D4 peptide assembled into short PNFs (Figure 3C). Additionally, a CR of 98% was determined, and ATR-FTIR spectroscopy analysis confirmed a high β-sheet content (Figure 3D).

Peptides can undergo modifications during storage that may affect their functionality (49). Given that D4 contains a serine residue prone to β-elimination (49), and the oxidation-sensitive amino acids methionine and phenylalanine (52, 53), we assessed its stability using HPLC and MALDI-TOF MS. HPLC analysis consistently showed a single peak with unchanged retention time across different time points (Figure 3E). Similarly, MALDI-TOF MS confirmed the consistent monoisotopic mass of D4 before and after a 10-day incubation (Figure S8).

3.4 D4 PNFs efficiently enhance γ-retroviral and lentiviral transduction of human T and NK cells

Our lead candidate, D4, underwent evaluation in a T cell transduction procedure. This process entailed incubating different transduction enhancers with a GFP-expressing GALV-RV, followed

by transduction of activated T cells. After 7 days, we assessed both the viability and the percentage of GFP+ T cells. Importantly, neither D4 PNF nor the other transduction enhancers affected T cell viability (Figure 4A). Furthermore, D4 PNFs amplified γ-retroviral transduction from 5% to 53% GFP+ cells, a thus a slightly increased enhancing activity as compared to RM-8 PNF, Vectofusin-1, and EF-C PNFs (Figure 4B). As 4 of 6 authorized CAR-T cell products are generated using a lentiviral vector pseudotyped with the glycoprotein of vesicular stomatitis virus (VSV-G-LV) for CAR gene tranfer (13), we analyzed D4 PNF and other transduction enhancers in a T cell transduction process using a GFP-expressing VSV-G-LV. None of the transduction enhancer reduced viability of T cells and only D4 PNFs and RetroNectin significantly enhanced transduction rates (Figures 4C, D).

The limited efficiency of viral gene delivery in primary NK cells, which is less effective when compared to primary T cells, presents a noteworthy challenge in the application of NK-cell based immunotherapy (19). Therefore, we chose to test the potential of D4 PNFs as transduction enhancer for primary NK cells. To exclude cytotoxic effects of PNFs on NK cells, a viability assay using propidium iodide staining was performed. After a 4-day incubation period, the highest concentration of RM-8 (30 μg/ml) slightly reduced cell viability while D4 and Vectofusin-1 did not show any impact on cell viability (Figure 4E). Following this, activated NK cells were transduced with lentiviral vectors in the presence of different PNFs, both with and without spinfection. Transduction efficiencies were assessed after 4 days. Due to the inefficient enhancement of transduction rates in NK cells using VSV-G-LVs (54), RD114 was selected for pseudotyping. RD114 specifically binds to the sodium-dependent neutral amino acid transporter (ASCT2) (55, 56), which is expressed on hematopoietic cells (57). Without spinfection, D4 PNFs significantly increased transduction rates of RD114-LV from 0.4% to approximately 23% GFP+ NK cells, while RM-8 and Vectofusin-1 did not exhibit a significant increase at tested concentrations (Figures 4F, S5G). However, with spinfection, both D4 and Vectofusin-1 significantly enhanced lentiviral transduction rates (Figures 4F, S5G).

An alternative envelope, derived from the baboon endogenous virus glycoprotein (BaEV), which binds to ASCT1 and ASCT2 (44), was also considered. Without spinfection, all concentrations of D4 PNFs significantly increased transduction rates of BaEV-LV from 15% to approximately 65% GFP+ NK cells, while RM-8 and Vectofusin-1 were only slightly active (Figures 4G. S5H). The lentiviral transduction rates were additionally significantly enhanced by both D4 PNF and Vectofusin-1 when spinfection was employed (Figures 4G, S5H).

3.5 D4 PNFs elicit no inflammatory response

Aggregates in protein or peptide-based therapeutics often correlate with immunogenicity (58, 59). Given the potential application of D4 PNFs as a transduction enhancer in gene therapy, it's crucial that they remain undetected by the innate immune system to prevent inflammation. To assess this, we examined the ability of D4, RM-8, EF-C, and Vectofusin-1 PNFs to trigger an immune response in THP1-Dual cells. This monocyte cell line is adept at simultaneously evaluating the NF-κB and interferon regulatory factor (IRF) pathways, both pivotal in the innate immune response (45). Different PNFs concentrations and lipopolysaccharides (LPS) as a positive control were incubated with THP-1 Dual cells for 24 h before supernatants were analyzed for activation of NF-κB and IRF pathway. Notably, only the 50 μg/ml concentration of D4 PNFs, which is not the concentration used in transduction experiments, showed significant activation of the NF-kB pathway (Figure 5A). As expected, LPS activated both pathways (Figures 5A, B). Next, we incubated PNFs with freshly isolated human CD4+ T cells for 24 h and subsequently used the LEGENDplex™ Human Inflammation Panel 1, a bead-based multiplex assay, to quantify human inflammatory cytokines/chemokines. Only LPS induced the expression of IL-1β, TNF-α and IL-6 of CD4+ T cells while the PNFs did not induce an inflammatory response (Figures 5C, S9). We also confirmed that neither the PNFs nor LPS exhibited cytotoxic effects (Figures 5D, E).

4 Discussion

The manufacturing and administration of CAR-T and CAR-NK cells involve labor-intensive procedures and significant costs, with the viral vector being a particularly expensive component (20). Enhancing target cell transduction efficiency can reduce the required quantity of viral vectors, potentially leading to cost savings (21); more importantly, it may enhance the success rate of the therapy by ensuring high transduction rates necessary for effective treatment (22). In this study, we demonstrate that D4 PNFs amplify retroviral transduction in primary T and NK cells, without inducing cytotoxicity or triggering inflammatory reactions. When juxtaposed with other transduction enhancers, D4 PNFs stand out for their simplicity and cost-efficiency. Their application is straightforward, involving a mere addition to the vector mix, sidestepping the labor-intensive coating or equipment-dependent spin infection processes associated with agents like RetroNectin or Vectofusin-1. Given its concise eight-residue structure, D4 can be synthesized more economically than lengthier peptides, such as Vectofusin-1. Moreover, D4 PNFs outperform Vectofusin-1 by bolstering VSV-G-LV mediated T cell transduction. These attributes of D4 PNF, including its prevention of extensive aggregate formation, non-toxicity, and non-inflammatory nature, position it as a pioneering tool for enhancing viral gene transfer. This potential is evident not just for research purposes but also holds promise for broader clinical applications.

Using an *in silico* screening approach, we searched for endogenous, non-immunogenic peptides that form into PNFs, effectively amplifying viral transduction rates. Leveraging amyloid prediction algorithms Tango, PASTA 2.0 and ZipperDB, a fibril-forming segment was determined within the IL-18 sequence. Based on this region, we synthesized five different cationic peptides named RS-12, RK-10, RM-8, RS-7 and FK-7 and subjected them to analysis. Among these, only RK-10 and RM-8 exhibited a positive ZP, making them effective in enhancing viral transduction. Notably, RM-8, an 8-mer peptide, swiftly self-organized into cationic,

chemically stable β-sheet PNFs. Even though D4 contains a serine, which is sensitive to β-elimination (49), and the oxidation sensitive methionine and phenylalanine (52, 53), it stayed chemically stable over 10 days as shown by HPLC and MALDI-TOF analysis. It is crucial to mention that β-elimination of serine can impact peptide structure (60), and oxidation can occur due to photosensitization processes or the catalytic activity of transition metals (52, 61). Moreover, protein therapeutics' oxidation, such as in methionine residues, can lead to adverse effects like diminished biological activity (62), reduced folding stability (61), and higher aggregation propensity (63). Therefore, RM-8 demonstrates chemical stability, a crucial factor for effective storage and development as a transduction enhancer for *ex vivo* gene transfer.

Notably, RM-8 PNFs demonstrated a superior ability to enhance VSV-G-LV transduction rates compared to Vectofusin-1. In fact, Vectofusin-1 showed no enhancement for VSV-G-LVs, aligning with prior research that suggested Vectofusin-1 doesn't improve VSV-G-LV delivery into T and B cells (64, 65). This differential behavior can likely be traced back to the distinct entry mechanisms adopted by various vector systems. For instance, γ-retroviral vectors like GALV-RV employ a pH-independent approach for binding and fusion at the host cell membrane (66). In contrast, VSV-G-LV operates differently, undergoing endocytosis after binding to the host cell. This is followed by fusion with endosomal vesicles in acidic conditions, leading to the release of its payload into the cell's cytoplasm (67). Therefore, it is suspected that Vectofusin-1 could potentially decrease the rate of endocytosis for vector particles that are attached to the cell surface (65). RM-8 PNFs achieved comparable γ-retroviral transduction rates of T cells as Vectofusin-1 and RetroNectin, without exhibiting any cytotoxic effects.

During the T-cell transduction procedure, we observed the emergence of large μm-sized fibrillar aggregates of RM8. Such aggregates could potentially induce unwanted effects if reintroduced into a patient during CAR T-cell therapy. Peptide aggregation is a common occurrence, culminating in either amorphous or amyloid-like fibrils (68, 69). This aggregation is dynamic, with amyloid-like fibrils capable of morphing into amorphous aggregates and *vice versa* (70). The exact influence of a peptide's amino acid sequence on its propensity to form aggregates remains not fully elucidated (71). Yet, attributes like hydrophobicity, charge, β-sheet propensity, among others, are recognized to play a role in this process (68, 72–74). Our recent studies, employing a data-mining approach, revealed that high β-sheet content and hydrophobicity in amyloidal peptides are pivotal. They not only facilitate interactions with viral particles and cells but also promote the assembly of fibrils into larger μm-sized aggregates (47). In an effort to prevent the formation of large aggregates by RM-8, we developed the D4 peptide. D4 assembles into smaller fibrils, avoiding the formation of large aggregates during T-cell transduction. We speculate that D4's heightened positive net charge, stemming from a threonine-to-arginine substitution, deters the creation of larger aggregates, possibly due to electrostatic repulsion (50). Interestingly, the chemically stable D4 PNFs displayed superior transduction rates in primary T and NK cells compared to both RM-8 and Vectofusin-1. We posit that the smaller aggregates, by offering a more expansive surface area, foster better interactions with viral particles and, subsequently, with cellular protrusions. This hypothesis aligns with our previous findings, where PNFs with numerous smaller μm-sized aggregates typically amplified transduction more effectively than their larger-aggregate-forming counterparts (47).

Immunogenicity refers to the ability of a molecule, typically foreign, to provoke either a humoral or cellular immune reaction from the patient (75). Considering the above, greater identity with endogenous molecules implies a lower risk of immunogenicity (76). An immune response against protein therapeutics often initiates with the activation of innate receptors, such as pattern recognition receptor (PRRs). This activation subsequently triggers the stimulation of antigen presenting cells (APC) (77–79). A notable link has been identified between aggregates in protein and peptide therapeutics and their immunogenic potential (58, 59). Additionally, chemical modifications, such as oxidation, can also trigger an immune response (80). When various PNFs were incubated with the THP1-Dual monocyte cell line, no activation of the NF-κB and IRF pathways was detected. In contrast, lipopolysaccharides (LPS), used as a positive control, activated both pathways through the toll-like receptor 4 (TLR4) (81). Moreover, the PNFs did not trigger any inflammatory response in CD4+ T cells, wheras consistent with literature, LPS stimulated the production of IL-1β, TNF-α and IL-6 (82). While our findings suggest that D4 PNFs are non-immunogenic, it's imperative to conduct further studies to ascertain if they undergo cellular degradation during the CAR-T/NK cell process, ensuring no residual fibrils in the final therapeutic product.

In conclusion, D4 PNF stand out as an innovative and potent transduction enhancer, outperforming Vectofusin-1 in facilitating γ-retroviral gene delivery into T cells and lentiviral gene delivery into both T and NK cells. Its cost-effectiveness, attributed to its small size, combined with its user-friendly application that eliminates the need for additional centrifugation, positions it favorably for incorporation into automated GMP processes tailored for *ex vivo* viral transduction of primary cells. Consequently, D4 PNFs present a promising nanotechnological solution to augment viral transduction efficiencies in laboratory research and the production of CAR-T and CAR-NK cell therapies.

Data availability statement

The original contributions presented in the study are included in the article/Supplementary Material. Further inquiries can be directed to the corresponding author.

Ethics statement

The studies involving humans were approved by NK cells from healthy donors were isolated from buffy coats acquired from the blood bank of the University Hospital Leipzig; ethic vote number 327/22-ek. T cells from healthy donors were isolated from buffy coats acquired from the Blutspendezentrale Ulm; ethic vote number 151/22 FSt/bal. The studies were conducted in accordance with the

local legislation and institutional requirements. The participants provided their written informed consent to participate in this study.

Author contributions

LR-W: Conceptualization, Formal Analysis, Investigation, Project administration, Validation, Visualization, Writing – original draft. AR: Conceptualization, Formal Analysis, Investigation, Writing – review & editing. KK: Formal Analysis, Investigation, Writing – review & editing. TtW: Investigation, Writing – review & editing. LZ: Investigation, Writing – review & editing. AR: Formal Analysis, Investigation, Writing – review & editing. DS: Conceptualization, Writing – review & editing. SW: Supervision, Writing – review & editing, Funding acquisition. LS: Supervision, Writing – review & editing, Funding acquisition. TnW: Supervision, Writing – review & editing, Funding acquisition. DoS: Conceptualization, Funding acquisition, Supervision, Writing – review & editing. JM: Conceptualization, Funding acquisition, Project administration, Supervision, Visualization, Writing – original draft.

Funding

The author(s) declare financial support was received for the research, authorship, and/or publication of this article. JM, TW and KK are supported by the German Research Foundation (DFG) through the CRC1279.

Acknowledgments

The authors acknowledge Merve Karacan and Nico Preising (Core Facility Functional Peptidomics, Ulm University Medical Center) for their technical assistance in peptide synthesis. Furthermore, we would like to thank Tim Berger, Clarissa Read and Paul Walther (Central Facility for Electron Microscopy, Ulm University) for their support in TEM analysis. Part of this work was presented as a poster presentation (P415) at the 32nd Annual Meeting of the Society for Virology. The manuscript's readability was improved with the assistance of ChatGPT (83).

Conflict of interest

JM is inventor on patents that claim to use peptide nanofibrils as transduction enhancer. JM, DS, LR-W, KK and TW filed additional patents to use peptides as transduction enhancer.

The remaining authors declare that the research was conducted in the absence of any commercial or financial relationships that could be construed as a potential conflict of interest.

Publisher's note

All claims expressed in this article are solely those of the authors and do not necessarily represent those of their affiliated organizations, or those of the publisher, the editors and the reviewers. Any product that may be evaluated in this article, or claim that may be made by its manufacturer, is not guaranteed or endorsed by the publisher.

Supplementary material

The Supplementary Material for this article can be found online at: https://www.frontiersin.org/articles/10.3389/fimmu.2023.1270243/full#supplementary-material

References

1. AlDallal SM. Yescarta: a new era for non-hodgkin lymphoma patients. *Cureus* (2020) 12:e11504. doi: 10.7759/cureus.11504

2. Wang M, Munoz J, Goy A, Locke FL, Jacobson CA, Hill BT, et al. KTE-X19 CAR T-cell therapy in relapsed or refractory mantle-cell lymphoma. *N Engl J Med* (2020) 382:1331–42. doi: 10.1056/NEJMoa1914347

3. Ali S, Kjeken R, Niederlaender C, Markey G, Saunders TS, Opsata M, et al. The european medicines agency review of kymriah (Tisagenlecleucel) for the treatment of acute lymphoblastic leukemia and diffuse large B-cell lymphoma. *Oncologist* (2020) 25: e321–7. doi: 10.1634/theoncologist.2019-0233

4. Sharma P, Kanapuru B, George B, Lin X, Xu Z, Bryan WW, et al. FDA approval summary: idecabtagene vicleucel for relapsed or refractory multiple myeloma. *Clin Cancer Res* (2022) 28:1759–64. doi: 10.1158/1078-0432.CCR-21-3803

5. Cappell KM, Kochenderfer JN. Long-term outcomes following CAR T cell therapy: what we know so far. *Nat Rev Clin Oncol* (2023) 20:359–71. doi: 10.1038/s41571-023-00754-1

6. Sadelain M. CD19 CAR T cells. *Cell* (2017) 171:1471. doi: 10.1016/j.cell.2017.12.002

7. Kochenderfer JN, Dudley ME, Feldman SA, Wilson WH, Spaner DE, Maric I, et al. B-cell depletion and remissions of Malignancy along with cytokine-associated toxicity in a clinical trial of anti-CD19 chimeric-antigen-receptor-transduced T cells. *Blood* (2012) 119:2709–20. doi: 10.1182/blood-2011-10-384388

8. June CH, Sadelain M. Chimeric antigen receptor therapy. *New Engl J Med* (2018) 379:64–73. doi: 10.1056/NEJMra1706169

9. Abramson JS, Palomba ML, Gordon LI, Lunning MA, Wang M, Arnason J, et al. Lisocabtagene maraleucel for patients with relapsed or refractory large B-cell lymphomas (TRANSCEND NHL 001): a multicentre seamless design study. *Lancet* (2020) 396:839–52. doi: 10.1016/S0140-6736(20)31366-0

10. Kamdar M, Solomon SR, Arnason J, Johnston PB, Glass B, Bachanova V, et al. Lisocabtagene maraleucel versus standard of care with salvage chemotherapy followed by autologous stem cell transplantation as second-line treatment in patients with relapsed or refractory large B-cell lymphoma (TRANSFORM): results from an interim analysis of an open-label, randomised, phase 3 trial. *Lancet* (2022) 399:2294–308. doi: 10.1016/S0140-6736(22)00662-6

11. Munshi NC, Anderson LD, Shah N, Madduri D, Berdeja J, Lonial S, et al. Idecabtagene vicleucel in relapsed and refractory multiple myeloma. *N Engl J Med* (2021) 384:705–16. doi: 10.1056/NEJMoa2024850

12. Martin T, Usmani SZ, Berdeja JG, Agha M, Cohen AD, Hari P, et al. Ciltacabtagene autoleucel, an anti-B-cell maturation antigen chimeric antigen receptor T-cell therapy, for relapsed/refractory multiple myeloma: CARTITUDE-1 2-year follow-up. *J Clin Oncol* (2023) 41:1265–74. doi: 10.1200/JCO.22.00842

13. Irving M, Lanitis E, Migliorini D, Ivics Z, Guedan S. Choosing the right tool for genetic engineering: clinical lessons from chimeric antigen receptor-T cells. *Hum Gene Ther* (2021) 32:1044–58. doi: 10.1089/hum.2021.173

14. Liu E, Marin D, Banerjee P, Macapinlac HA, Thompson P, Basar R, et al. Use of CAR-transduced natural killer cells in CD19-positive lymphoid tumors. *N Engl J Med* (2020) 382:545–53. doi: 10.1056/NEJMoa1910607

15. Wu J, Mishra HK, Walcheck B. Role of ADAM17 as a regulatory checkpoint of CD16A in NK cells and as a potential target for cancer immunotherapy. *J Leukoc Biol* (2019) 105:1297–303. doi: 10.1002/JLB.2MR1218-501R

16. Oei VYS, Siernicka M, Graczyk-Jarzynka A, Hoel HJ, Yang W, Palacios D, et al. Intrinsic functional potential of NK-cell subsets constrains retargeting driven by chimeric antigen receptors. *Cancer Immunol Res* (2018) 6:467–80. doi: 10.1158/2326-6066.CIR-17-0207

17. Lupo KB, Matosevic S. Natural killer cells as allogeneic effectors in adoptive cancer immunotherapy. *Cancers (Basel)* (2019) 11:769. doi: 10.3390/cancers11060769

18. Ueda T, Kumagai A, Iriguchi S, Yasui Y, Miyasaka T, Nakagoshi K, et al. Non-clinical efficacy, safety and stable clinical cell processing of induced pluripotent stem cell-derived anti-glypican-3 chimeric antigen receptor-expressing natural killer/innate lymphoid cells. *Cancer Sci* (2020) 111:1478–90. doi: 10.1111/cas.14374

19. Carlsten M, Childs RW. Genetic manipulation of NK cells for cancer immunotherapy: techniques and clinical implications. *Front Immunol* (2015) 6:266. doi: 10.3389/fimmu.2015.00266

20. Ran T, Eichmüller SB, Schmidt P, Schlander M. Cost of decentralized CAR T-cell production in an academic nonprofit setting. *Int J Cancer* (2020) 147:3438–45. doi: 10.1002/ijc.33156

21. Radek C, Bernadin O, Drechsel K, Cordes N, Pfeifer R, Sträßer P, et al. Vectofusin-1 improves transduction of primary human cells with diverse retroviral and lentiviral pseudotypes, enabling robust, automated closed-system manufacturing. *Hum Gene Ther* (2019) 30:1477–93. doi: 10.1089/hum.2019.157

22. Rajabzadeh A, Hamidieh AA, Rahbarizadeh F. Spinoculation and retronectin highly enhance the gene transduction efficiency of Mucin-1-specific chimeric antigen receptor (CAR) in human primary T cells. *BMC Mol Cell Biol* (2021) 22:57. doi: 10.1186/s12860-021-00397-z

23. Davis HE, Morgan JR, Yarmush ML. Polybrene increases retrovirus gene transfer efficiency by enhancing receptor-independent virus adsorption on target cell membranes. *Biophys Chem* (2002) 97:159–72. doi: 10.1016/s0301-4622(02)00057-1

24. Porter CD, Lukacs KV, Box G, Takeuchi Y, Collins MKL. Cationic liposomes enhance the rate of transduction by a recombinant retroviral vector *in vitro* and *in vivo*. *J Virol* (1998) 72:4832–40. doi: 10.1128/jvi.72.6.4832-4840.1998

25. Yolamanova M, Meier C, Shaytan AK, Vas V, Bertoncini CW, Arnold F, et al. Peptide nanofibrils boost retroviral gene transfer and provide a rapid means for concentrating viruses. *Nat Nanotechnology* (2013) 8:130–6. doi: 10.1038/nnano.2012.248

26. Lee H-J, Lee Y-S, Kim H-S, Kim Y-K, Kim J-H, Jeon S-H, et al. Retronectin enhances lentivirus-mediated gene delivery into hematopoietic progenitor cells. *Biologicals* (2009) 37:203–9. doi: 10.1016/j.biologicals.2009.01.008

27. Müller S, Bexte T, Gebel V, Kalensee F, Stolzenberg E, Hartmann J, et al. High cytotoxic efficiency of lentivirally and alpharetrovirally engineered CD19-specific chimeric antigen receptor natural killer cells against acute lymphoblastic leukemia. *Front Immunol* (2020) 10:3123. doi: 10.3389/fimmu.2019.03123

28. Nasiri F, Muhammadnejad S, Rahbarizadeh F. Effects of polybrene and retronectin as transduction enhancers on the development and phenotypic characteristics of VHH-based CD19-redirected CAR T cells: a comparative investigation. *Clin Exp Med* (2022) 23:2535–49. doi: 10.1007/s10238-022-00928-8

29. Pollok KE, Hanenberg H, Noblitt TW, Schroeder WL, Kato I, Emanuel D, et al. High-efficiency gene transfer into normal and adenosine deaminase-deficient T lymphocytes is mediated by transduction on recombinant fibronectin fragments. *J Virol* (1998) 72:4882–92. doi: 10.1128/JVI.72.6.4882-4892.1998

30. Vermeer LS, Hamon L, Schirer A, Schoup M, Cosette J, Majdoul S, et al. Vectofusin-1, a potent peptidic enhancer of viral gene transfer forms pH-dependent α-helical nanofibrils, concentrating viral particles. *Acta Biomater* (2017) 64:259–68. doi: 10.1016/j.actbio.2017.10.009

31. Schütz D, Rode S, Read C, Müller JA, Glocker B, Sparrer KMJ, et al. Viral transduction enhancing effect of EF-C peptide nanofibrils is mediated by cellular protrusions. *Advanced Funct Materials* (2021) 31:2104814. doi: 10.1002/adfm.202104814

32. Schütz D. *Mechanistic studies on transduction enhancing EF-C peptide nanofibrils and optimization for gene therapeutic applications* (2021). Universität Ulm. Available at: https://oparu.uni-ulm.de/xmlui/handle/123456789/39005 (Accessed March 13, 2023).

33. Goldschmidt L, Teng PK, Riek R, Eisenberg D. Identifying the amylome, proteins capable of forming amyloid-like fibrils. *PNAS* (2010) 107:3487–92. doi: 10.1073/pnas.0915166107

34. Rousseau F, Schymkowitz J, Serrano L. Protein aggregation and amyloidosis: confusion of the kinds? *Curr Opin Struct Biol* (2006) 16:118–26. doi: 10.1016/j.sbi.2006.01.011

35. Fernandez-Escamilla A-M, Rousseau F, Schymkowitz J, Serrano L. Prediction of sequence-dependent and mutational effects on the aggregation of peptides and proteins. *Nat Biotechnol* (2004) 22:1302–6. doi: 10.1038/nbt1012

36. Linding R, Schymkowitz J, Rousseau F, Diella F, Serrano L. A comparative study of the relationship between protein structure and beta-aggregation in globular and intrinsically disordered proteins. *J Mol Biol* (2004) 342:345–53. doi: 10.1016/j.jmb.2004.06.088

37. Walsh I, Seno F, Tosatto SCE, Trovato A. PASTA 2.0: an improved server for protein aggregation prediction. *Nucleic Acids Res* (2014) 42:W301–307. doi: 10.1093/nar/gku399

38. Gasteiger E, Hoogland C, Gattiker A, Duvaud S, Wilkins MR, Appel RD, et al. "Protein identification and analysis tools on the exPASy server.,". In: Walker JM, editor. *The proteomics protocols handbook. Springer protocols handbooks*. Totowa, NJ: Humana Press (2005). p. 571–607. doi: 10.1385/1-59259-890-0:571

39. Sieste S, Mack T, Lump E, Hayn M, Schütz D, Röcker A, et al. Supramolecular peptide nanofibrils with optimized sequences and molecular structures for efficient retroviral transduction. *Advanced Funct Materials* (2021) 31:2009382. doi: 10.1002/adfm.202009382

40. Schilling C, Mack T, Lickfett S, Sieste S, Ruggeri FS, Sneideris T, et al. Sequence-optimized peptide nanofibers as growth stimulators for regeneration of peripheral neurons. *Advanced Funct Materials* (2019) 29:1809112. doi: 10.1002/adfm.201809112

41. Papkalla A, Münch J, Otto C, Kirchhoff F. Nef enhances human immunodeficiency virus type 1 infectivity and replication independently of viral coreceptor tropism. *J Virol* (2002) 76:8455–9. doi: 10.1128/JVI.76.16.8455-8459.2002

42. Dull T, Zufferey R, Kelly M, Mandel RJ, Nguyen M, Trono D, et al. A third-generation lentivirus vector with a conditional packaging system. *J Virol* (1998) 72:8463–71. doi: 10.1128/JVI.72.11.8463-8471.1998

43. Zhang X-Y, La Russa VF, Reiser J. Transduction of bone-marrow-derived mesenchymal stem cells by using lentivirus vectors pseudotyped with modified RD114 envelope glycoproteins. *J Virol* (2004) 78:1219–29. doi: 10.1128/jvi.78.3.1219-1229.2004

44. Girard-Gagnepain A, Amirache F, Costa C, Lévy C, Frecha C, Fusil F, et al. Baboon envelope pseudotyped LVs outperform VSV-G-LVs for gene transfer into early-cytokine-stimulated and resting HSCs. *Blood* (2014) 124:1221–31. doi: 10.1182/blood-2014-02-558163

45. Iwanaszko M, Kimmel M. NF-κB and IRF pathways: cross-regulation on target genes promoter level. *BMC Genomics* (2015) 16:307. doi: 10.1186/s12864-015-1511-7

46. Kaygisiz K, Dutta A, Rauch-Wirth L, Synatschke CV, Münch J, Bereau T, et al. Inverse design of viral infectivity-enhancing peptide fibrils from continuous protein-vector embeddings. *Biomater Sci* (2023) 11:5251–61. doi: 10.1039/D3BM00412K

47. Kaygisiz K, Rauch-Wirth L, Dutta A, Yu X, Nagata Y, Bereau T, et al. Data-mining unveils structure–property–activity correlation of viral infectivity enhancing self-assembling peptides. *Nat Commun* (2023) 14:5121. doi: 10.1038/s41467-023-40663-6

48. Zandomeneghi G, Krebs MRH, McCammon MG, Fändrich M. FTIR reveals structural differences between native β-sheet proteins and amyloid fibrils. *Protein Sci* (2004) 13:3314–21. doi: 10.1110/ps.041024904

49. Grassi L, Cabrele C. Susceptibility of protein therapeutics to spontaneous chemical modifications by oxidation, cyclization, and elimination reactions. *Amino Acids* (2019) 51:1409–31. doi: 10.1007/s00726-019-02787-2

50. Roberts CJ. Therapeutic protein aggregation: mechanisms, design, and control. *Trends Biotechnol* (2014) 32:372–80. doi: 10.1016/j.tibtech.2014.05.005

51. Filipe V, Hawe A, Jiskoot W. Critical evaluation of nanoparticle tracking analysis (NTA) by nanoSight for the measurement of nanoparticles and protein aggregates. *Pharm Res* (2010) 27:796–810. doi: 10.1007/s11095-010-0073-2

52. Davies MJ, Truscott RJW. Photo-oxidation of proteins and its role in cataractogenesis. *J Photochem Photobiol B: Biol* (2001) 63:114–25. doi: 10.1016/S1011-1344(01)00208-1

53. Torosantucci R, Schöneich C, Jiskoot W. Oxidation of therapeutic proteins and peptides: structural and biological consequences. *Pharm Res* (2014) 31:541–53. doi: 10.1007/s11095-013-1199-9

54. Bari R, Granzin M, Tsang KS, Roy A, Krueger W, Orentas R, et al. A distinct subset of highly proliferative and lentiviral vector (LV)-transducible NK cells define a readily engineered subset for adoptive cellular therapy. *Front Immunol* (2019) 10. doi: 10.3389/fimmu.2019.02001

55. Rasko JEJ, Battini J-L, Gottschalk RJ, Mazo I, Miller AD. The RD114/simian type D retrovirus receptor is a neutral amino acid transporter. *Proc Natl Acad Sci* (1999) 96:2129–34. doi: 10.1073/pnas.96.5.2129

56. Marin M, Lavillette D, Kelly SM, Kabat D. N-linked glycosylation and sequence changes in a critical negative control region of the ASCT1 and ASCT2 neutral amino acid transporters determine their retroviral receptor functions. *J Virol* (2003) 77:2936–45. doi: 10.1128/jvi.77.5.2936-2945.2003

57. Sandrin V, Boson B, Salmon P, Gay W, Nègre D, Le Grand R, et al. Lentiviral vectors pseudotyped with a modified RD114 envelope glycoprotein show increased stability in sera and augmented transduction of primary lymphocytes and CD34+ cells derived from human and nonhuman primates. *Blood* (2002) 100:823–32. doi: 10.1182/blood-2001-11-0042

58. Rosenberg AS. Effects of protein aggregates: An immunologic perspective. *AAPS J* (2006) 8:E501–7. doi: 10.1208/aapsj080359

59. Cleland JL, Powell MF, Shire SJ. The development of stable protein formulations: a close look at protein aggregation, deamidation, and oxidation. *Crit Rev Ther Drug Carrier Syst* (1993) 10:307–77.

60. Palmer DE, Pattaroni C, Nunami K, Chadha RK, Goodman M, Wakamiya T, et al. Effects of dehydroalanine on peptide conformations. *J Am Chem Soc* (1992) 114:5634–42. doi: 10.1021/ja00040a024

61. Li S, Schöneich C, Borchardt RT. Chemical instability of protein pharmaceuticals: Mechanisms of oxidation and strategies for stabilization. *Biotechnol Bioengineering* (1995) 48:490–500. doi: 10.1002/bit.260480511

62. Hsu Y-R, Narhi LO, Spahr C, Langley KE, Lu HS. *In vitro* methionine oxidation of escherichia coli-derived human stem cell factor: Effects on the molecular structure, biological activity, and dimerization. *Protein Sci* (1996) 5:1165–73. doi: 10.1002/pro.5560050619

63. Mulinacci F, Capelle MAH, Gurny R, Drake AF, Arvinte T. Stability of human growth hormone: influence of methionine oxidation on thermal folding. *J Pharm Sci* (2011) 100:451–63. doi: 10.1002/jps.22293

64. Majdoul S, Seye AK, Kichler A, Holic N, Galy A, Bechinger B, et al. Molecular determinants of vectofusin-1 and its derivatives for the enhancement of lentivirally mediated gene transfer into hematopoietic stem/progenitor cells. *J Biol Chem* (2016) 291:2161–9. doi: 10.1074/jbc.M115.675033

65. Jamali A, Kapitza L, Schaser T, Johnston ICD, Buchholz CJ, Hartmann J. Highly efficient and selective CAR-gene transfer using CD4- and CD8-targeted lentiviral vectors. *Mol Ther Methods Clin Dev* (2019) 13:371–9. doi: 10.1016/j.omtm.2019.03.003

66. Maetzig T, Galla M, Baum C, Schambach A. Gammaretroviral vectors: biology, technology and application. *Viruses* (2011) 3:677–713. doi: 10.3390/v3060677

67. Sun X, Roth SL, Bialecki MA, Whittaker GR. Internalization and fusion mechanism of vesicular stomatitis virus and related rhabdoviruses. *Future Virol* (2010) 5:85–96. doi: 10.2217/FVL.09.72

68. Trainor K, Broom A, Meiering EM. Exploring the relationships between protein sequence, structure and solubility. *Curr Opin Struct Biol* (2017) 42:136–46. doi: 10.1016/j.sbi.2017.01.004

69. Riek R, Eisenberg DS. The activities of amyloids from a structural perspective. *Nature* (2016) 539:227–35. doi: 10.1038/nature20416

70. Almeida Z L, Brito R. Structure MM. and aggregation mechanisms in amyloids. *Molecules* (2020) 25:1195. doi: 10.3390/molecules25051195

71. Zapadka KL, Becher FJ, Gomes dos Santos AL, Jackson SE. Factors affecting the physical stability (aggregation) of peptide therapeutics. *Interface Focus* (2017) 7:20170030. doi: 10.1098/rsfs.2017.0030

72. De Baets G, Schymkowitz J, Rousseau F. Predicting aggregation-prone sequences in proteins. *Essays Biochem* (2014) 56:41–52. doi: 10.1042/bse0560041

73. Bolognesi B, Tartaglia GG. "Chapter three - physicochemical principles of protein aggregation.,". In: Giraldo J, Ciruela F, editors. *Progress in molecular biology and translational science. Oligomerization in health and disease*. Oxford, UK: Academic Press (2013). p. 53–72. doi: 10.1016/B978-0-12-386931-9.00003-9

74. Chiti F, Stefani M, Taddei N, Ramponi G, Dobson CM. Rationalization of the effects of mutations on peptide andprotein aggregation rates. *Nature* (2003) 424:805–8. doi: 10.1038/nature01891

75. Carrascosa JM. Immunogenicity in biologic therapy: implications for dermatology. *Actas Dermosifiliogr* (2013) 104:471–9. doi: 10.1016/j.ad.2013.02.005

76. Fernandez L, Bustos RH, Zapata C, Garcia J, Jauregui E, Ashraf GM. Immunogenicity in protein and peptide based-therapeutics: an overview. *Curr Protein Pept Sci* (2018) 19:958–71. doi: 10.2174/1389203718666170828123449

77. Vos Q, Lees A, Wu ZQ, Snapper CM, Mond JJ. B-cell activation by T-cell-independent type 2 antigens as an integral part of the humoral immune response to pathogenic microorganisms. *Immunol Rev* (2000) 176:154–70. doi: 10.1034/j.1600-065x.2000.00607.x

78. Geijtenbeek TBH, van Vliet SJ, Engering A, 't Hart BA, van Kooyk Y. Self- and nonself-recognition by C-type lectins on dendritic cells. *Annu Rev Immunol* (2004) 22:33–54. doi: 10.1146/annurev.immunol.22.012703.104558

79. Diebold SS. Activation of dendritic cells by toll-like receptors and C-type lectins. *Handb Exp Pharmacol* (2009) 188:3–30. doi: 10.1007/978-3-540-71029-5_1

80. van Beers MMC, Bardor M. Minimizing immunogenicity of biopharmaceuticals by controlling critical quality attributes of proteins. *Biotechnol J* (2012) 7:1473–84. doi: 10.1002/biot.201200065

81. Kuzmich NN, Sivak KV, Chubarev VN, Porozov YB, Savateeva-Lyubimova TN, Peri F. TLR4 signaling pathway modulators as potential therapeutics in inflammation and sepsis. *Vaccines (Basel)* (2017) 5:34. doi: 10.3390/vaccines5040034

82. McAleer JP, Vella AT. Understanding how lipopolysaccharide impacts CD4 T cell immunity. *Crit Rev Immunol* (2008) 28:281–99. doi: 10.1615/critrevimmunol.v28.i4.20

83. OpenAI. (2023). *ChatGPT (May 3 version)* [Large language model]. Available at: https://chat.openai.com

5.3 Appendix 3

Rauch-Wirth, L.*, La Roche, J.*, Kaygisiz, K., Kuhn, A., Jeon, N., Stifel, U., Zech, F., Fischer-Posovszky, P., Weil, T., Read, C. & Münch, J. **Structural morphology of peptide nanofibrils dictates viral capture and cellular uptake in gene therapy applications**. *Nano Today* 69, 103015 (2026). https://doi.org/10.1016/j.nantod.2026.103015.
* These authors contributed equally.

Reference[3]

License: CC By 4.0 (https://creativecommons.org/licenses/by/4.0/)

Nano Today 69 (2026) 103015

Contents lists available at ScienceDirect

Nano Today

journal homepage: www.elsevier.com/locate/nanotoday

Structural morphology of peptide nanofibrils dictates viral capture and cellular uptake in gene therapy applications

Lena Rauch-Wirth [a,1], Julia La Roche [b,1], Kübra Kaygisiz [c], Annalena Kuhn [a], Nayeong Jeon [d], Ulrich Stifel [e], Fabian Zech [a], Pamela Fischer-Posovszky [e,f], Tanja Weil [d], Clarissa Read [b,2], Jan Münch [a,*,2]

[a] Institute of Molecular Virology, Ulm University Medical Center, Ulm 89081, Germany
[b] Central Facility for Electron Microscopy, Ulm University, Ulm 89081, Germany
[c] Department of Chemistry, Massachusetts Institute of Technology, Cambridge, MA 02139, United States
[d] Department Synthesis of Macromolecules, Max Planck Institute for Polymer Research, Ackermannweg 10, Mainz 55128, Germany
[e] Department of Pediatrics and Adolescent Medicine, Ulm University Medical Center, Ulm 89075, Germany
[f] German Center for Child and Adolescent Health (DZKJ), Partner Site Ulm 89075, Germany

ARTICLE INFO

Keywords:
Peptide nanofibrils
Transduction enhancer
Retroviral transduction
PNF aggregates
Macropinocytosis
Aggregate morphology
Endocytosis

ABSTRACT

Peptide nanofibrils (PNFs) are gaining attention as promising transduction enhancers to improve viral vector delivery in ex vivo gene therapy applications. However, the influence of PNF structural morphology on viral capture and cellular interaction remains poorly understood. Here, we systematically compare two clinically relevant PNFs, D4, a short β-sheet-forming peptide, and Vectofusin-1, an α-helical peptide, focusing on their fibrillar architecture, viral particle binding, and interaction with host cells. Secondary structure analysis, molecular dynamics simulations and electron microscopy revealed that D4 forms loosely packed, β-sheet-rich aggregates, while Vectofusin-1 assembles into compact, α-helical structures. Both superstructures have a positive and hydrophobic surface which are key determinants for interaction with viral and plasma membranes. Upon exposure to virus-like particles (VLPs), D4 aggregates grew in size and density, while Vectofusin-1 formed more numerous, smaller aggregates. D4 bound VLPs with markedly higher density, yielding a uniform virion coating, in contrast to the lower and heterogeneous VLP association observed for Vectofusin-1. Notably, only D4 aggregates were actively engulfed by filopodia leading to active uptake via endocytosis mainly by macropinocytosis and subsequent degradation by lysosomes. In contrast, Vectofusin-1 binding to plasma membrane appeared more passive with minimal internalization. These distinct behaviors were maintained under transduction-like conditions, with D4 facilitating direct VLP contact with the plasma membrane and Vectofusin-1 forming extracellular networks. Our results reveal that PNF aggregate morphology critically determines viral and cellular interactions and suggest that D4 may offer superior efficacy and safety profiles for use in ex vivo gene therapies.

Introduction

Chimeric antigen receptor (CAR)-T cell therapies provide a targeted treatment strategy for hematologic malignancies, including B cell lymphoma, B cell acute lymphoblastic leukemia, and multiple myeloma [1–4]. This approach involves isolating patient's T cells, which are then genetically modified ex vivo using viral vectors to express a CAR on their surface, enabling specific recognition of tumor-associated antigens such as cluster of differentiation 19 (CD19) and B cell maturation antigen [5]. Following transduction, CAR-T cells undergo ex vivo expansion, functional assessment, and safety testing. After the patient receives lymphodepleting chemotherapy, the CAR-T cells are reinfused, where they selectively recognize and eliminate malignant cells [5]. To date, the U.S. Food and Drug Administration (FDA) has approved seven CAR-T cell therapies, utilizing either lentiviral vectors (idecabtagene vicleucel [4], lisocabtagene maraleucel [6], ciltacabtagene autoleucel [7],

* Correspondence to: Institute of Molecular Virology, Ulm University Medical Center, Meyerhofstrasse 1, Ulm 89081, Germany.
E-mail address: jan.muench@uni-ulm.de (J. Münch).
[1] Shared first.
[2] Shared last.

https://doi.org/10.1016/j.nantod.2026.103015
Received 16 December 2025; Received in revised form 29 January 2026; Accepted 20 February 2026
Available online 3 March 2026
1748-0132/© 2026 The Authors. Published by Elsevier Ltd. This is an open access article under the CC BY license (http://creativecommons.org/licenses/by/4.0/).

tisagenlecleucel [8] and obecabtagene autoleucel [9]) or γ-retroviral vectors (axicabtagene ciloleucel [1] and brexucabtagene autoleucel [2]) for CAR gene delivery. Furthermore, 1580 CAR-T cell therapy clinical trials were registered at ClinicalTrials.gov on April 2024 [10]. However, low vector titers and electrostatic repulsion between negatively charged viral and cellular membranes often result in suboptimal transduction efficiency [11], potentially limiting therapeutic efficacy and increasing production costs. The use of transduction enhancers has emerged as a strategy to improve transduction efficiency, thereby reducing the required viral vector dose, lowering manufacturing costs, and generating a greater number of CAR-T cells - critical factors for the success of CAR-T cell therapy [12–15].

The transduction enhancer RetroNectin has been applied to produce CAR-T cells [14,16]. RetroNectin, a recombinant human fibronectin fragment, enhances lentiviral and γ-retroviral transduction by facilitating the interaction between viral particles and the plasma membrane [14]. This is mediated through its heparin-binding domain and its ability to bind cellular integrin receptors. However, its application requires pre-coating of cell culture flasks, along with additional washing and centrifugation steps, making the process time-intensive [17]. Another class of transduction enhancers are peptides [11,18]. Their defined composition, tunable physicochemical properties, and capacity to form higher-order assemblies enable interactions with viral particles through electrostatic, hydrophobic, or sequence-specific mechanisms [11, 19–22]. These interactions can either enhance transduction by increasing viral attachment to plasma membrane [11,15,18,23] or inhibit infection by trapping, neutralizing, or destabilizing virions [22, 24,25]. Especially, cationic peptides that self-assemble into peptide nanofibrils (PNFs) such as Vectofusin-1 and EF-C have been shown to efficiently enhance retroviral and lentiviral transduction rates in a wide range of cells. These positive PNFs capture negatively charged viral particles, facilitating their interaction with the plasma membrane and thereby enhancing viral transduction rates [11,13,15,18–20,23].

Vectofusin-1 is a cationic 26-mer peptide that self-assembles into α-helical PNFs [23]. Unlike RetroNectin, Vectofusin-1 does not require pre-coating of the culture flasks but instead needs to be pre-mixed with the viral vector prior to transduction of the target cells. Transduction efficiency can be further enhanced by an additional centrifugation step, and washing the cells 6–24 h post-transduction is recommended. The positive charge of Vectofusin-1 enables it to capture negatively charged viral particles and promote their binding and fusion with the negatively charged plasma membrane [23]. Vectofusin-1 has been shown to significantly enhance the transduction efficiency of γ-retroviral and lentiviral vectors and is integrated into the automated, closed-system CliniMACS Prodigy® platform for the GMP-compliant production of CAR-T cells [13]. However, it does not enhance the transduction efficiency of lentiviral vectors pseudotyped with the vesicular stomatitis virus glycoprotein (VSV-G) [13,15,26], which remains the most commonly used vector for CAR-T cell therapy manufacturing [27].

The most extensively studied PNF is formed by the 12-mer peptide EF-C (Protransduzin), which is derived from the human immunodeficiency virus 1 (HIV-1) glycoprotein gp120 [18,19,28,29]. EF-C PNFs are actively captured by cellular protrusions such as filopodia, microvilli, and lamellipodia, which facilitate their transport to the cell body [28]. Additionally, they induce plasma membrane invaginations, increasing the surface area available for viral particle attachment and reducing the distance the viral capsid must travel to reach the nucleus. Following their attachment to the plasma membrane, EF-C PNFs are internalized via macropinocytosis and subsequently degraded by lysosomes [29]. This degradation prevents their intracellular accumulation as amyloid deposits, thereby minimizing potential side effects and enhancing their suitability for clinical applications [29]. EF-C offers several advantages over Vectofusin-1 and RetroNectin, including its shorter peptide length, which facilitates straightforward synthesis, and its ability to enhance transduction efficiency without the need for additional procedures such as centrifugation or pre-coating of the flasks. This simplifies the workflow, making EF-C a more cost-effective and user-friendly alternative. However, its chemical instability, arising from the cyclization of its N-terminal glutamine to pyroglutamate, poses a challenge since it promotes significant aggregate formation in cell culture [30].

Therefore, we developed the 8-mer peptide D4 (RRIFIISM) using an in silico screening approach followed by a structure-activity relationship (SAR) study [15]. D4 forms chemically stable PNFs without generating large aggregates. Compared to Vectofusin-1 and EF-C, D4 PNFs exhibit superior transduction efficiency [15]. We further demonstrated that D4 outperforms Vectofusin-1 in supporting γ-retroviral gene transfer into T cells as well as lentiviral gene delivery into both T and NK cells, without compromising T or NK cell viability, inducing inflammatory responses in $CD4^+$ T cells, or activating NF-κB or interferon regulatory factor signaling in the THP1-Dual monocyte reporter line [15]. We hypothesize that D4's enhanced performance is due to its high positive net charge, which prevents the formation of excessively large aggregates, likely through electrostatic repulsion. The resulting smaller aggregates may provide a larger surface area for viral particle binding and subsequent engagement by cellular protrusions [15]. This hypothesis aligns with our previous findings, which challenge earlier assumptions that PNFs themselves mediate transduction enhancement. Instead, our data suggest that the assembly of PNFs into numerous small μm-sized aggregates with a hydrophobic and positive surface is essential for their transduction enhancing activity, outperforming larger aggregates [20]. However, it is still not completely understood how PNF morphology and aggregation behavior influence their interaction with viral and cellular membranes.

In this study, we compared the transduction enhancers D4 and Vectofusin-1 using secondary structure analysis, molecular dynamics simulations and a range of electron and fluorescence microscopy techniques to analyze their aggregation behavior and their interaction with virus-like particles (VLPs) and cells. D4 assembled into loosely packed β-sheet-rich PNF aggregates that exhibited high VLP binding capacity and triggered plasma membrane invaginations, leading to endocytosis mainly via macropinocytosis and lysosomal degradation. In contrast, Vectofusin-1 formed smaller, α-helical PNF aggregates that organized into large interconnected networks partially enclosing cells. These aggregates showed lower VLP binding and limited uptake by the cells, primarily entangling filopodia without inducing obvious membrane remodeling. Notably, we demonstrate for the first time that VLP interaction can directly modulate PNF formation and aggregation behavior. These findings underscore the important role of PNF aggregate morphology in governing viral interactions and cellular responses, emphasizing the need for detailed aggregate characterization to ensure their safe and effective application as transduction enhancers in ex vivo gene therapies.

Results

Structural characterization of D4 and Vectofusin-1

Previously, we identified the 8-mer peptide D4 (RRIFIISM), which self-assembles into β-sheet peptide PNFs and enhances lentiviral and retroviral transduction rates in primary T and NK cells with greater and broader efficiency than Vectofusin-1 [15], a 26-mer peptide (KKALLHAALAHLLALAHHLLALLKKA-NH_2) that forms α-helical PNFs [23]. To investigate their secondary structure in detail, both peptides were analyzed by circular dichroism (CD) spectroscopy and attenuated total reflection Fourier transform-infrared (ATR FT-IR) spectroscopy. The CD spectrum of Vectofusin-1 exhibited two negative minima at approximately 223 nm and 211 nm, along with a positive maximum at 199 nm (Fig. S1A), consistent with a predominantly α-helical conformation [31] and in agreement with previously reported spectra [23]. In contrast, D4 CD spectrum displayed bands at 200 and 220 nm which is consistent with typical β-sheets structures (Fig. S1B). ATR FT-IR spectroscopy of Vectofusin-1 showed a characteristic α-helical peak at 1656 cm^{-1}

consistent with previous measurements [23]. D4 revealed a dominant peak at 1627 cm^{-1}, consistent with β-sheet conformations, accompanied by a weaker band at 1688 cm^{-1} that reflects the presence of antiparallel β-sheet components (Fig. S1C) [32]. This is in agreement with our previously published analysis of D4 [15]. In addition, both D4 and Vectofusin-1 spectra contained a band at approximately 1670 cm^{-1}, corresponding to β-turn structures. Second-derivative analysis of the ATR FT-IR spectra revealed a β-sheet content of 48.6% for D4 and an α-helical content of 69.3% for Vectofusin-1 (Fig. S1D). Dynamic light scattering (DLS) analysis showed that both peptides assembled into positively charged PNFs, as indicated by their positive zeta potentials, and revealed a hydrodynamic radius of 185 nm for D4 (0.5 mg/mL) and 93 nm for Vectofusin-1 (1 mg/mL) (Fig. S1D). However, it is important to note that particles larger than approximately 1 μm cannot be detected by DLS. Therefore, additional analytical methods were employed later to characterize larger aggregates.

Model-based analysis of Vectofusin-1 assembly

Since D4 and Vectofusin-1 PNFs differ in their secondary structure, we next analyzed the assembly mechanisms by structural modeling. Structural modeling of Vectofusin-1 was performed using PEP-FOLD4.0 [33–36]. The resulting model revealed that Vectofusin-1 adopts a stable α-helical conformation, with two positively charged lysine residues located at the N- and C-termini, which may serve as potential binding sites for viral particles and plasma membrane (Fig. S2A). Furthermore, helical wheel projection analysis using HeliQuest [37] demonstrated the alignment of multiple leucine residues along one face of the α-helix (Fig. S2B). According to literature, it is proposed that they facilitate leucine-zipper-like interactions, promoting lateral association through coiled-coil formation [23,38], a structural motif in which two or more α-helical peptides are wrapped around each other [39]. Longitudinal self-association may be facilitated by hydrophobic residues that do not

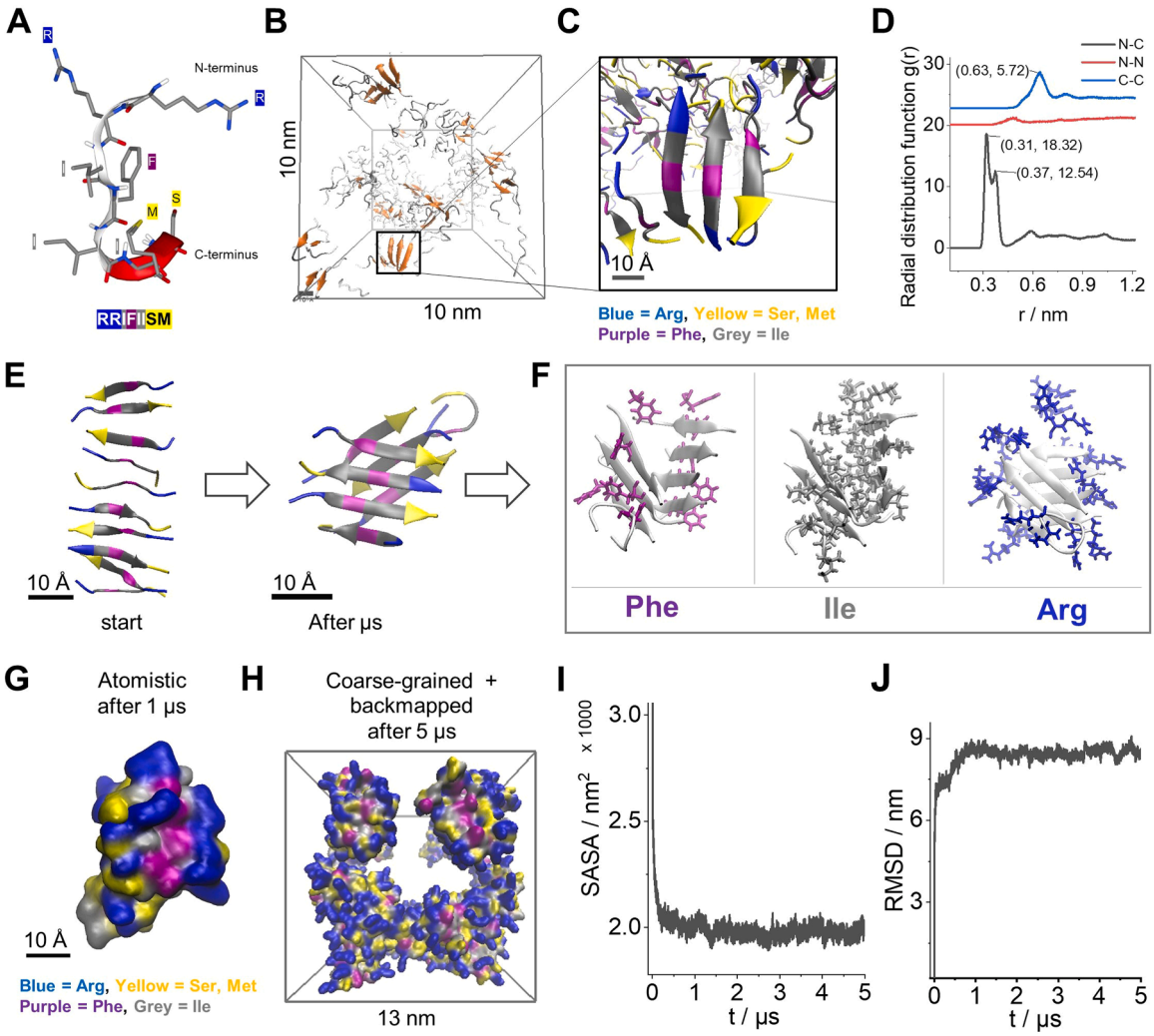

Fig. 1. Molecular dynamics simulations of the self-assembly of D4 peptide. (A) The highest-ranking 3D secondary structure of D4 analyzed by PEP-FOLD4.0. (B–D) All-atom simulations show initial formation of antiparallel β-sheets without extended ordering. All-atom simulations run with 150 molecules in a 10 nm × 10 nm × 10 nm box for 300 ns in explicit water at 278 K and 1 atm. Water and ions omitted for visualization. Replicate trajectory plots shown in Fig. S3. (B) Highlights β-sheet structures in orange color. (C) Detailed view of B highlighting the antiparallel β-sheet order. The color code represents amino acid residue position in cartoon representation (Blue = Arg, Yellow = Ser, Met, Purple = Phe, Gray = Ile), scale bar 10 Å. (D) Radial distribution function g(r) of intermolecular C- and N-terminal contacts (gray line), N- and N-terminal contacts (red line), and C- and C-terminal contacts (blue line). (E–G) Detailed views of a pre-assembled β-sheet structures before and after 1 μs atomistic simulation, scale bar 10 Å. Replicate trajectory plots shown in Fig. S6. (F) Cross-β assemblies with a hydrophobic core composed of Ile residues (gray) and Phe (purple) and Arg (blue) exposed to the solvent. (G) Surface view of seven antiparallel cross- β sheet oriented D4 peptides from pre-assembled atomistic simulation. Replicate trajectory plots shown in Fig. S9. (H–J) Coarse-grained simulations of 300 peptides in 13 nm × 13 nm × 13 nm over 5 μs show extended antiparallel β-sheet structures, that convergence within one microsecond as shown by I solvent accessible surface area (SASA) and J backbone root-mean-square deviation (RMSD) analysis. Replicate trajectory plots shown in Fig. S8.

directly participate in the zipper interface (Fig. S2C) [23]. Notably, histidine residues appear to be critical for fibril formation, as Vermeer et al. [23] demonstrated that substitution of the first two histidine residues in Vectofusin-1 with alanine prevents fibril assembly. To further elucidate the assembly mechanism of Vectofusin-1, coarse-grained simulations were performed. Vectofusin-1 formed elongated fibrils with a positively charged and hydrophobic surface, and its lysine residues were heterogeneously distributed across the exterior (Fig. S2D). Although Vectofusin-1 exhibited an aggregation propensity comparable to that of D4 (Fig. S2D, E), it formed smaller aggregates, consistent with our DLS measurements (Fig. S1D), and did not develop the β-sheet structures observed for D4, as discussed below.

Molecular dynamics simulations reveal antiparallel β-sheet formation in D4

As structural modeling with PEP-FOLD4.0 indicated that D4 does not adopt a well-defined secondary structure on its own (Fig. 1**A**), the

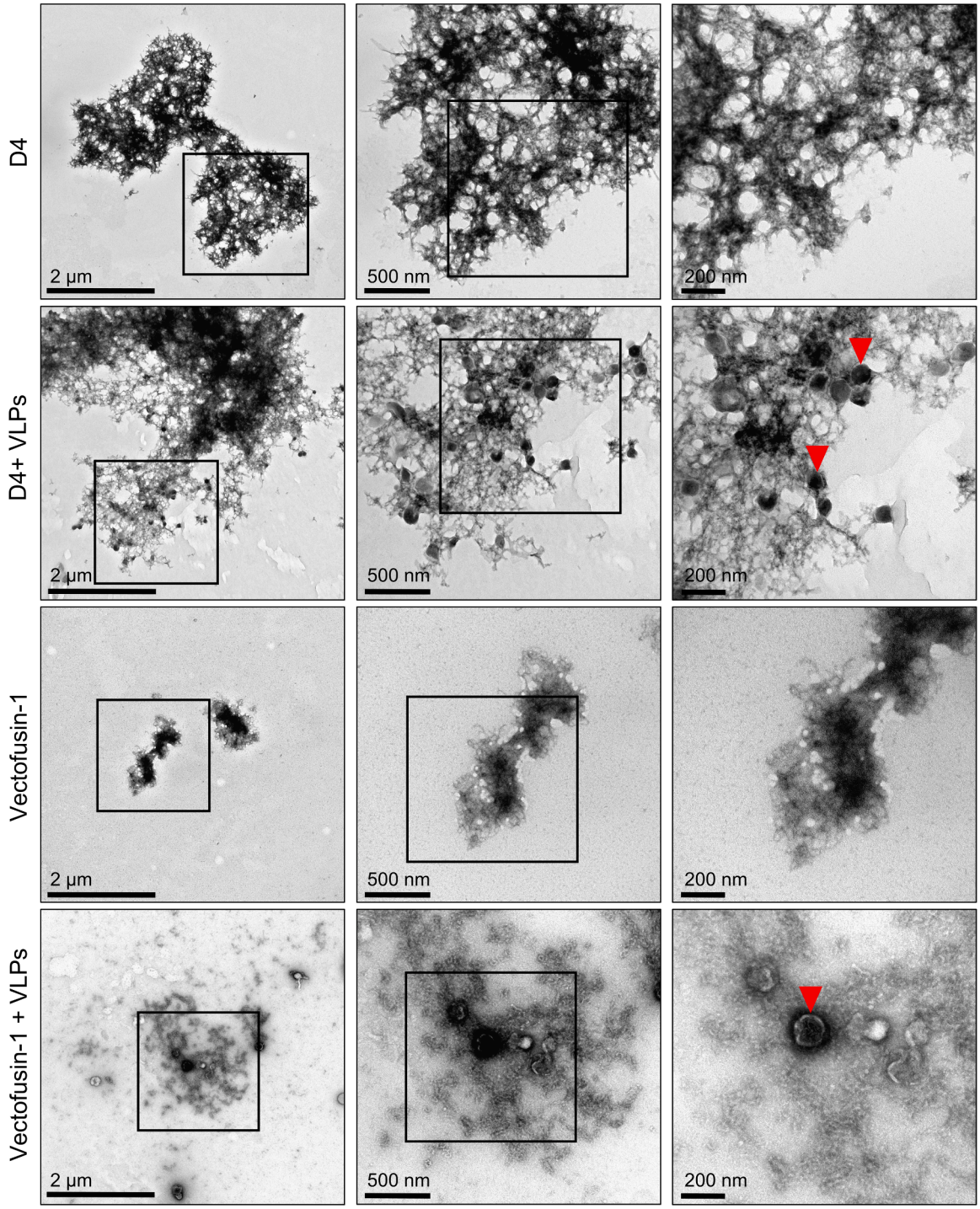

Fig. 2. Transmission electron microscopy (TEM) images of D4 and Vectofusin-1 PNFs after incubation with virus-like particles (VLPs). PNFs (250 µg/mL) were incubated with VLPs (MLV-gag YFP) for 10 min before TEM analysis was performed. VLPs are indicated by the red arrowheads. Representative images from 3 independent experiments.

assembly behavior of D4 peptides was further investigated using molecular dynamics simulations. The all-atom simulation showed that the D4 peptide self-assembles into short-range, antiparallel β-sheet structures typically consisting of 4–5 molecules. These assemblies are characterized by frequent kinks and turns, leading to a lack of long-range order, which are due to the limited simulation time (Fig. 1**B, C,** Fig. S3). The short intermolecular C-terminus to N-terminus distance observed via the radial distribution function and missing intermolecular N-terminal contacts (Fig. 1**D**) are in alignment with an antiparallel orientation. The found C-terminal contacts can be traced back to intersheet contacts between folded antiparallel β-sheets (Fig. S4). We conducted more detailed simulations focusing specifically on the antiparallel β-sheet assembly (Fig. 1**E–G**), starting from a pre-assembled elongated antiparallel β-sheet structure and all-atom simulation for 1000 ns. The

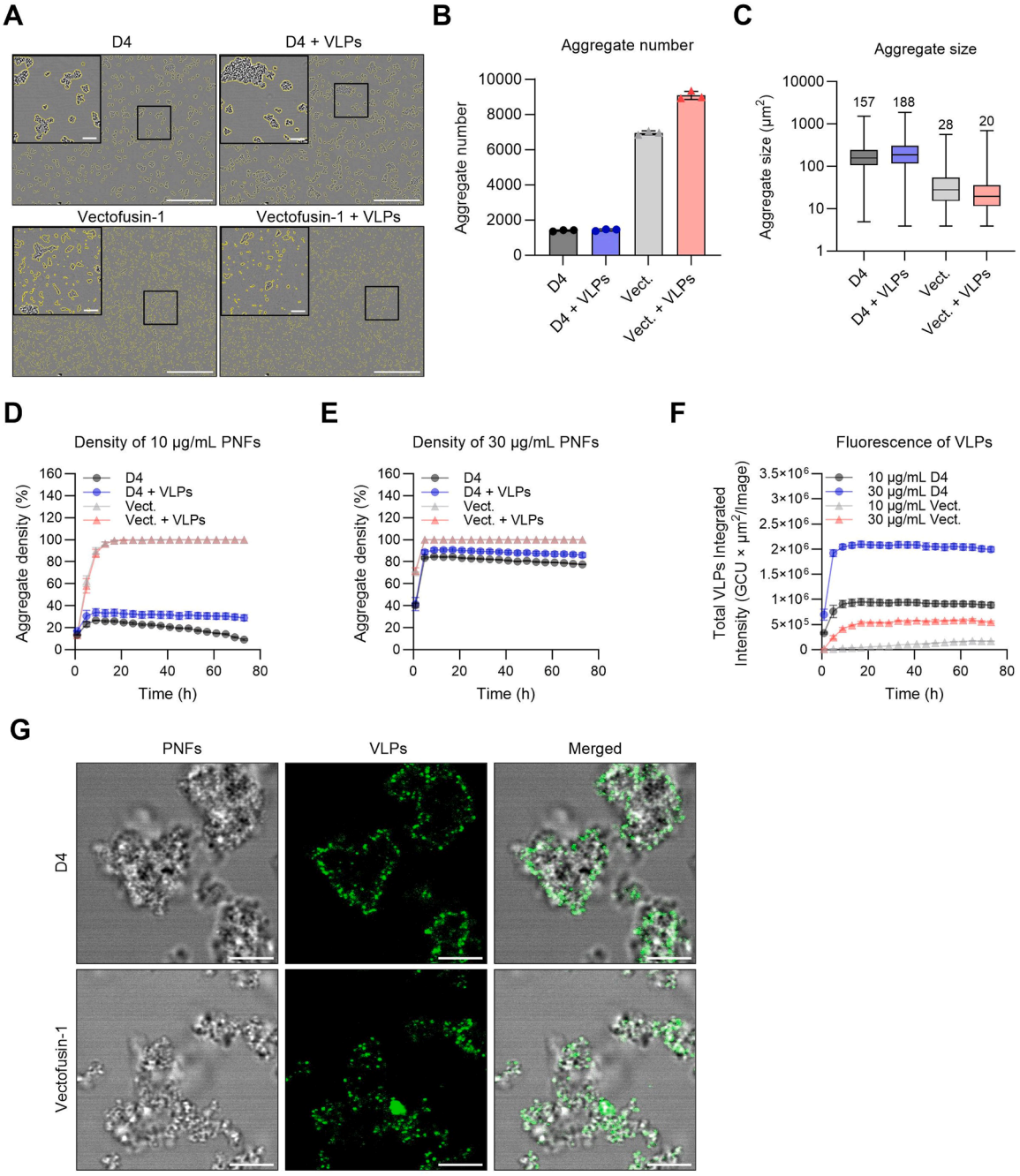

Fig. 3. Aggregate analysis of D4 and Vectofusin-1 PNFs using time-lapse imaging. (A) Representative images of D4 and Vectofusin-1 aggregates (10 µg/mL) in presence and absence of VLPs after 1 h of incubation. PNF aggregates are outlined yellow. Scale bars indicate 200 µm and for the insets 20 µm. Based on microscopic images aggregate number (B) and size (C) of D4 and Vectofusin-1 PNFs were determined using the 3D Counter of ImageJ. For B mean values (±SD) from triplicates are shown from one experiment. For each triplicate 4 images were analyzed (12 images in total per sample). The aggregate size is shown as median (number above the bar) ± maximal and minimal value. Density of 10 (D) and 30 µg/mL (E) D4 and Vectofusin-1 PNFs over 3 days. (F) Fluorescence of VLPs incubated with D4 and Vectofusin-1 PNFs. Background fluorescence of PNFs was subtracted. Shown are mean values (±SD) from triplicates for D-F. Images were taken every 4 h for 3 days and density and fluorescence were determined using the Incucyte Software. (G) Fluorescence microcopy using a 63× objective and 8× zoom. 20 µg/mL D4 and Vectofusin-1 PNFs were incubated for 1 h with VLPs before images were taken. Representative images of one experiment with 4 images per sample. Scale bar indicates 5 µm.

observed intermolecular distances (3–5 Å) and inter-sheet spacing (9–11 Å) are consistent with typical amyloid structures (Fig. S4). Antiparallel β-sheets are slightly more favored over parallel ones, as observed by comparative simulations (Fig. S5). The peptides transition from the pre-assembled elongated structure to cross-β structures (Fig. 1**E,** Fig. S6**)**. In these structures the hydrophobic isoleucine (Ile) residues are buried in the interior, while phenylalanine (Phe) and arginine (Arg) side chain residues are exposed to the exterior (Fig. 1 **F, G**). We additionally performed a longer coarse-grained simulation of 300 molecules in a 13 nm × 13 nm × 13 nm box over 5 μs, followed by backmapping into all-atom representation, to investigate the formation of folded, antiparallel cross-β structures over longer time periods (Fig. 1**H–J,** Fig. S7). We observed that β-sheet containing assemblies (Fig. S7–9) extend into larger aggregates (Fig. 1**H**), which stabilize within the first μs, as indicated by the solvent-accessible surface area (SASA, Fig. 1**I**) and backbone root-mean-square deviation (RMSD**,** Fig. 1**J**).

Overall, our analyses indicate that the D4 peptide self-assembles into twisted, antiparallel β-sheet–rich structures, whereas Vectofusin-1 forms smaller α-helical assemblies. Both peptides exhibit patchy surfaces composed of positively charged and hydrophobic regions, features known to facilitate interactions with viral and cellular membranes [20, 40]. This structural organization is consistent with our previous experimental observations for D4 (e.g., ATR FT-IR, zeta potential measurements, and transmission electron microscopy (TEM)) [15], as well as with findings for Vectofusin-1 reported by others [23,38].

Morphology of D4 and Vectofusin-1 peptide nanofibril aggregates

After gaining insights into the assembly mechanism, we next wanted to analyze the morphology of the assembled PNFs. Therefore, D4 and Vectofusin-1 PNFs were incubated for 10 min before being analyzed by TEM. D4 assembled into aggregates of short, nm-long fibrils (Fig. 2) that appear similar as the predicted structure determined by molecular simulation analysis (Fig. 1**H;** Fig. S5, A, B). In contrast, Vectofusin-1 assembled into shorter fibrils that appeared almost grainy and formed more compact and smaller aggregates (Fig. 2) similar to those predicted by molecular simulation analysis (Fig. S2D). Notably, a light grey background, probably Vectofusin-1 oligomers, covered the sample, suggesting that a fraction of the peptide did not assemble into fibrils. This may be attributed to the limited incubation time, consistent with previous reports indicating that the assembly of Vectofusin-1 into α-helical PNFs is highly dependent on both, elevated concentrations and prolonged incubation [23]. Given these morphological differences between Vectofusin-1 and D4 PNFs at the nm-scale, we also expected a different aggregation behavior at the μm-scale. To evaluate this, D4 and Vectofusin-1 PNFs were incubated for 1 h to allow aggregation and sedimentation before measuring their size and number by time-lapse imaging using a time-lapse imaging and analysis system. D4 PNFs formed fewer, but larger aggregates, with a median size of 157 μm^2, whereas Vectofusin-1 PNFs formed more but smaller aggregates, with a median size of 28 μm^2 (Fig. 3**A–C**). To investigate their aggregation kinetics, they were incubated for 1 h, followed by time-lapse imaging every 4 h over a 3-d period. The coverage of a defined area by aggregates (in %) was measured at a concentration of 10 μg/mL, which is typically used to enhance retroviral transduction in adherent cells. D4 PNFs aggregated until they reached a maximum coverage of 25% after 9 h, followed by a gradual dissociation leading to a decline in coverage (Fig. 3**D**, images of measurements in Fig. S10A) together with a reduction in aggregate size over time. Vectofusin-1 PNF aggregates covered a larger area, reaching even 100% after 17 h, which stayed constant over time (Fig. 3**D**). To assess the effect of higher peptide concentrations, the concentration was increased to 30 μg/mL, as used for retroviral transduction of primary cells such as T and NK cells [15]. At this concentration, both peptides reached a maximum coverage after 9 h, with D4 at approximately 85% and Vectofusin-1 again at 100% (Fig. 3**E;** Fig. S10B).

In summary, D4 self-assembles into PNFs that form loosely packed, μm-sized aggregates with rapid aggregation kinetics and a low number of aggregates. In contrast, Vectofusin-1 assembles into smaller PNFs that generate more, denser, but smaller aggregates with slower aggregation kinetics.

Virus-like particle-binding induce morphological changes of PNF aggregates

Both D4 and Vectofusin-1 PNFs enhance viral transduction by capturing viral particles through electrostatic interactions via their positively charged surfaces and facilitating viral contact with the plasma membrane [23,29]. Given their distinct secondary structures (β-sheet vs. α-helix) and differences in aggregate morphology, we investigated whether these structural differences influence their interaction with viral particles. For this, D4 and Vectofusin-1 PNFs were incubated with VLPs and analyzed by TEM. We used for this purpose murine leukemia virus (MLV)-gag yellow fluorescent protein (YFP) particles, which consist of a host cell-derived lipid bilayer envelope and MLV Gag proteins fused to YFP, labeling the viral capsid. As these VLPs lack envelope (Env) proteins and viral enzymes (Pol), they are non-infectious [41]. Due to the similar size and morphology of extracellular vesicles (EVs) and retroviral particles [42], supernatants from both transfected and non-transfected HEK293T cells were purified under identical conditions and analyzed in parallel. VLP preparations from transfected cells showed distinct yellow fluorescence and contained uniform particles measuring ~150 nm in diameter, as confirmed by TEM and nanoparticle tracking analysis (NTA, Fig. S11). In contrast, supernatants from non-transfected controls lacked fluorescent signal and particle structures.

To study PNF-VLP interactions, purified VLPs were incubated with D4 or Vectofusin-1 PNFs and analyzed by TEM. Upon VLP binding, both PNFs exhibited marked morphological changes in their aggregates (Fig. 2). D4 aggregates bound a high number of VLPs and appeared larger and less densely packed than their VLP-free counterparts. Vectofusin-1 aggregates also bound VLPs and displayed reduced packing density relative to untreated controls. To assess whether these interactions influence the size and number of aggregates, PNFs were incubated with VLPs for 1 h and analyzed using time-lapse imaging. Vectofusin-1 displayed a significant increase in the number of smaller aggregates upon VLP incubation, whereas D4 showed increased aggregate size but no change in aggregate number (Fig. 3**B, C**). Aggregation kinetics were further evaluated to quantify VLP-induced changes. Incubation with VLPs significantly accelerated the aggregation of D4 at both tested concentrations, resulting in increased aggregate density. In contrast, Vectofusin-1 aggregation kinetics remained largely unaffected by VLP binding (Fig. 3**D, E;** Fig. S10).

Taken together, TEM and time-lapse imaging analyses demonstrate that VLP binding induces distinct morphological responses in D4 and Vectofusin-1 PNFs. D4 forms larger, less densely packed aggregates, whereas Vectofusin-1 forms a greater number of smaller, loosely packed aggregates.

Virion binding induced distinct morphological and kinetic changes in PNFs

Following TEM observations suggesting more extensive VLP binding to D4 aggregates than to Vectofusin-1, we next quantified and compared the VLP binding capacity of both PNFs. To this end, VLP fluorescence was monitored in parallel with aggregation kinetics using time-lapse imaging. In the absence of PNFs, VLPs appeared as isolated fluorescent puncta (Fig. S12A). Upon incubation with D4 PNFs, a rapid and stable increase in VLP fluorescence intensity was observed, indicating efficient and sustained VLP binding (Fig. 3**F;** Fig. S12A). In contrast, Vectofusin-1 PNFs showed a slower fluorescence increase and overall lower signal intensity, indicative of a reduced and delayed VLP binding response (Fig. 3**F;** Fig. S12A). Nevertheless, quantitative comparisons at early time points and matched conditions indicate that D4 PNFs exhibit

approximately fourfold greater VLP binding capacity than Vectofusin-1 PNFs, independent of peptide concentration (Fig. 3**F**). This reduced binding capacity for Vectofusin-1 is consistent with qualitative impressions from TEM (Fig. 2).

To further examine the spatial organization of PNF-VLP interactions, D4 and Vectofusin-1 PNFs were incubated with VLPs for 1 h and analyzed by fluorescence microscopy. In line with previous findings, D4 formed larger aggregates than Vectofusin-1 and exhibited significantly more VLP binding (Fig. 3**G;** Fig. S12B). Notably, VLPs primarily localized around the periphery of D4 aggregates, suggesting surface-based binding. This was confirmed by z-stack imaging and 3D reconstruction, which revealed VLPs exclusively surrounding the outer surfaces of D4 aggregates, with no internalized particles detectable (**Video 1**, supplementary). In contrast, VLPs associated with Vectofusin-1 appeared to be randomly distributed throughout the smaller aggregates (Fig. 3**G;** Fig. S12B), consistent with previous observations by Vermeer et al. [23]. Due to their smaller size leading to higher diffusion rates, Vectofusin-1 aggregates exhibited rapid movement. Therefore, 3D visualization could not conclusively determine whether internal VLP binding occurred (**Video 2,** supplementary).

Supplementary material related to this article can be found online at doi:10.1016/j.nantod.2026.103015.

Impact of serum components on peptide–virus complex formation

Because serum components, particularly serum albumin as the most abundant protein, are known to markedly influence peptide aggregation and fibril formation [43–45], we sought to determine how varying concentrations of fetal bovine serum (FBS) affect the aggregation behavior of D4 and Vectofusin-1 and, consequently, their interaction with VLPs. In addition, we evaluated different concentrations of human serum, as it is commonly used alongside FBS in CAR T-cell manufacturing [46]. In our previous aggregation assays (Fig. 3**,** Fig. S10, Fig. S12), D4, Vectofusin-1, and VLPs were initially dissolved in serum-free Opti-MEM medium (as typically performed in published transduction enhancement protocols [13]) before being diluted into RPMI medium containing 10% FBS. In this experiment, both peptides and VLPs were directly prepared in RPMI medium supplemented with defined concentrations (0%, 2.5%, 5%, 10%, or 20%) of either FBS or human serum. After 1 h incubation, aggregation kinetic and VLP fluorescence were determined by time-lapse imaging every 4 h over a 3-day period.

D4 exhibited its lowest aggregation density in medium containing 0% FBS, while Vectofusin-1 did not form detectable aggregates under serum-free conditions (Fig. S13A). Both peptides showed maximal aggregation at 2.5% FBS, followed by a progressive decrease in aggregation density with increasing serum concentrations (Fig. S13A). Upon incubation with VLPs, D4 displayed a pronounced increase in aggregation density, consistent with previous observations, with 2.5% FBS again yielding the highest levels (Fig. S13B). In contrast, Vectofusin-1 showed its highest aggregation density after VLP exposure in the absence of FBS, which declined with increasing serum concentrations (Fig. S13B). Fluorescence-based VLP binding measurements revealed the strongest VLP association for both peptides under serum-free conditions, with binding efficiency decreasing as FBS levels increased. Notably, the VLP fluorescence difference between 0% and higher FBS concentrations was substantially greater for Vectofusin-1 than for D4 (Fig. S13C).

When incubated with human serum, 2.5% again yielded the highest aggregation density for D4 (Fig. S14A). However, across all human serum concentrations, D4 aggregates markedly decreased over time, and nearly no aggregates were detectable after 20 h (Fig. S14A). This effect was reversed upon incubation with VLPs, which restored D4 aggregation and resulted in increasing aggregate densities with higher human serum concentrations (Fig. S14B). Vectofusin-1 exhibited only low aggregation levels in human serum, which were only modestly enhanced in the presence of VLPs (Fig. S14A, B). Similar to the observations with FBS conditions, D4 showed the strongest VLP association under serum-free conditions, with binding efficiency progressively decreasing as human serum concentrations increased (Fig. S14C). In contrast, Vectofusin-1 demonstrated optimal VLP binding in serum-free medium, but unlike D4, increasing human serum concentrations resulted in enhanced VLP association (Fig. S14C).

In conclusion, D4 and Vectofusin-1 PNFs exhibit distinct VLP interaction profiles. D4 aggregates bind VLPs in a dense, uniform manner at their surface, while Vectofusin-1 aggregates display more heterogeneous and less efficient VLP association. These differences correlate with the distinct surface distributions of positively charged amino acids, arginine in D4 and lysine in Vectofusin-1, observed in our molecular dynamics simulations, and support the notion that structural and morphological features of PNFs critically influence viral particle interaction dynamics. Furthermore, D4 and Vectofusin-1 showed distinct serum-dependent aggregation behaviors, with both peptides aggregating most strongly at 2.5% serum but Vectofusin-1 failing to form detectable aggregates under serum-free conditions. Additionally, VLP binding was strongest for both peptides without serum, but increasing FBS concentrations reduced VLP binding, indicating that serum components interfere with peptide–VLP association.

D4 and Vectofusin-1 PNF aggregates differentially modulate plasma membrane dynamics

In a previous study, we demonstrated that, beyond their positive charge, EF-C PNFs form μm-sized aggregates that are actively captured by cellular protrusions, guiding them to the plasma membrane and thereby enhancing viral transduction [28]. These aggregates induce plasma membrane invaginations, increasing surface area for viral binding and entry, while also reducing the distance between the plasma membrane and the nucleus, facilitating nuclear delivery of viral vectors [29].

Based on these findings and our current observations, we hypothesized that the distinct morphologies and aggregation behaviors of D4 and Vectofusin-1 PNFs differentially affect their interactions with the cell surface. To test this, HeLa cells were incubated with D4 or Vectofusin-1 PNFs (2 μg/mL) for 1 h and analyzed by TEM and scanning electron microscopy (SEM). A lower PNF concentration was used for imaging to prevent excessive surface coverage that would hinder visualization. Both TEM and SEM confirmed morphological differences between D4 and Vectofusin-1 aggregates (Fig. S15). D4 PNFs presented in two distinct forms: predominantly as aggregates of short fibrils, similar to those observed in negative-stain TEM (Fig. 2), and predicted by molecular dynamics simulations (Fig. 1), and, in some cases, as longer, more extended fibrils located near the main aggregates (Fig. S15A**;** Fig. 4**B**, dark blue arrowhead), suggesting that fibril elongation may require extended incubation. In contrast, Vectofusin-1 formed smaller, denser, and more amorphous aggregates, without evidence of elongated fibrils (Fig. S15A).

SEM analysis of untreated HeLa cells revealed a uniform distribution of filopodia across the cell surface (Fig. S16). Upon exposure to either PNFs, elongated filopodia were observed clustering around PNF aggregates, suggesting active cellular engagement. Filopodia farther from the aggregates appeared shorter and less frequent (Fig. S15B). To further resolve PNF-cell interactions, scanning transmission electron microscopy (STEM) tomography was performed. This method combines TEM resolution with 3D architecture visualization and revealed numerous filopodia in close proximity to PNF aggregates. Notably, filopodia from D4-treated cells typically did not penetrate the aggregates but rather surrounded and engulfed them as whole aggregates (**Video 3, supplementary;** Fig. S17A). In contrast, Vectofusin-1-treated cells displayed filopodia that became entwined within the smaller Vectofusin-1 aggregates (**Video 4, supplementary;** Fig. S17B), suggesting a more passive binding behavior.

Since EF-C PNFs are known to be internalized via macropinocytosis

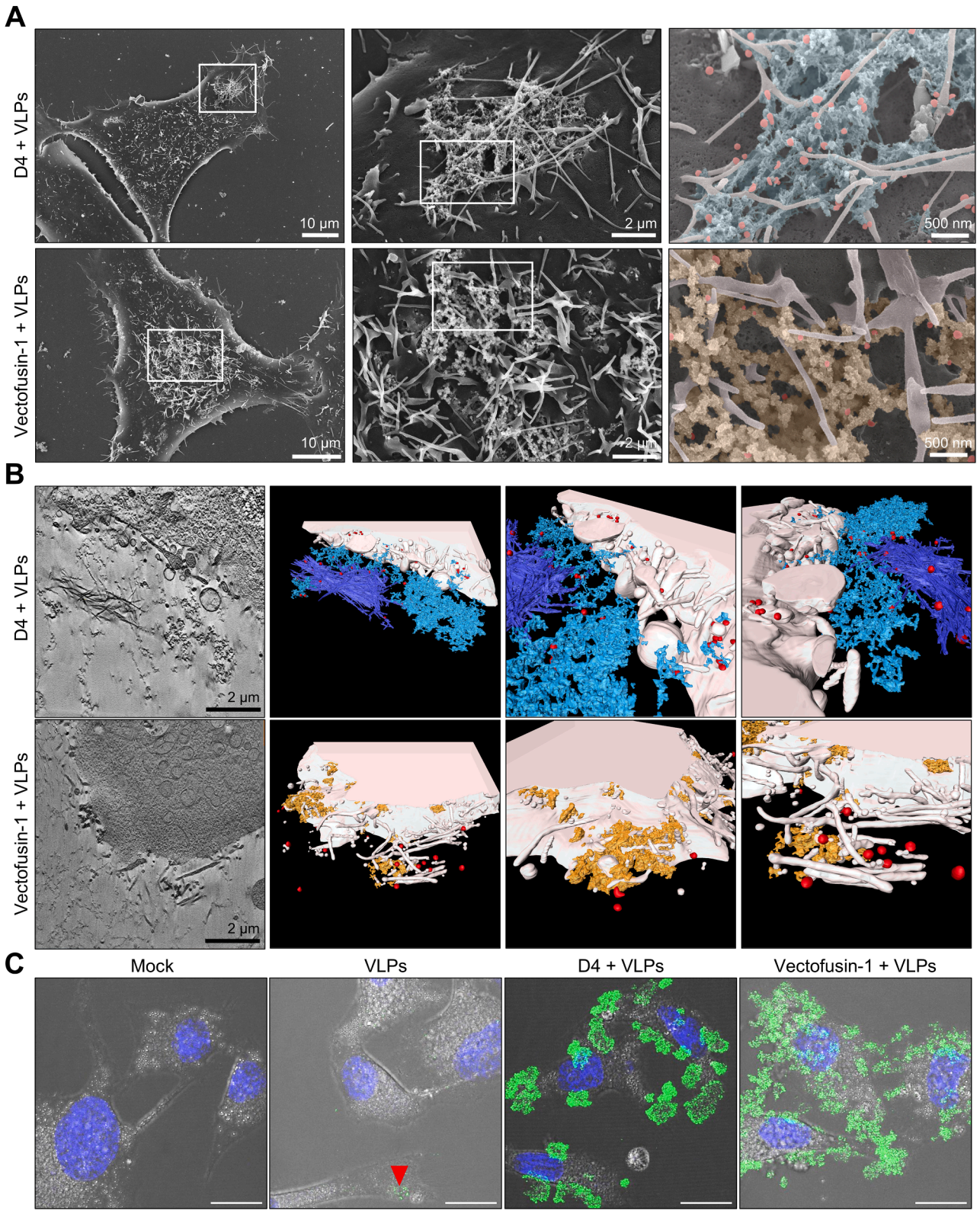

Fig. 4. Interaction of D4 and Vectofusin-1 PNFs with VLPs and HeLa cells. PNFs (2 µg/mL) were incubated with VLPs for 10 min before being added to HeLa cells for 1 h and analyzed by scanning electron microscopy (SEM) (A) and scanning transmission electron microscopy (STEM) tomography (B). Cells are colored in beige, VLPs in red, long D4 PNFs in blue, short D4 PNFs in cyan and Vectofusin-1 PNFs in orange. Tomograms and segmentations in Videos 5 (D4) and 6 (Vectofusin-1). Representative SEM images (A) from one experiment, at least 30 cells were analyzed per sample. Representative tomograms (B) from at least 10 tomograms per sample. (C) PNFs (10 µg/mL) were incubated with VLPs for 10 min before being added to HeLa cells for 1 h and analyzed by fluorescence microscopy using a 63× objective and 2× zoom. The cell nucleus is shown in blue and VLPs are shown in green (red arrowhead). Representative images of one experiment with 4 images per sample. Scale bar indicates 20 µm.

[29], a process which starts with membrane ruffling and the formation of macropinocytic cups [47], we examined whether similar plasma membrane remodeling occurs in response to D4 and Vectofusin-1. SEM analysis of untreated cells showed no membrane invaginations (Fig. S16). Cells exposed to Vectofusin-1 for 1 h displayed minimal membrane rearrangement (Fig. S15B), consistent with the observed passive binding pattern. Notably, when Vectofusin-1 was present as small isolated aggregates, we observed plasma membrane invaginations (**Video 4, supplementary**; Fig. S15B). In contrast, D4-treated cells showed extensive plasma membrane remodeling, including pronounced invaginations and filipodia clustering around D4 PNFs (Fig. S15A), indicating that macropinocytosis may be initiated within 1 h of incubation, similar to EF-C PNFs [29].

Supplementary material related to this article can be found online at doi:10.1016/j.nantod.2026.103015.

In summary, D4 and Vectofusin-1 PNFs induce distinct cell interaction patterns. Vectofusin-1 aggregates associate with filopodia without substantial membrane remodeling, whereas D4 aggregates trigger significant membrane restructuring, including large invaginations, suggestive of uptake via macropinocytosis. These differences likely contribute to the higher transduction-enhancing potential of D4.

VLP binding pattern of PNF aggregates influences interaction of VLPs with plasma membrane

To enhance viral transduction efficiency in ex vivo gene therapies such as CAR-T cell therapy, PNFs have been developed to simultaneously bind viral particles and target cells, thereby facilitating viral entry [15,18–21]. Our previous results demonstrated that D4 and Vectofusin-1 PNF aggregates exhibit distinct VLP binding patterns and differ in their interactions with HeLa cells. Since both viral and cellular binding are crucial for successful transduction, we investigated the combined effects of these interactions under co-incubation conditions.

D4 and Vectofusin-1 PNFs (2 μg/mL) were pre-incubated with MLV-Gag YFP VLPs for 10 min before being added to HeLa cells. After 1 h, cells were analyzed by electron microscopy as described previously. TEM analysis indicated that D4 PNFs formed more frequent and prominent aggregates consisting of μm-long fibrils when VLPs were present. These fibrils were often indirectly connected to the plasma membrane via nm-scale D4 fibrils (Fig. S18B**;** Fig. 4**B; Video 5**) and resembled structures previously observed in the absence of VLPs (Fig. S15A). This suggests that elongation of D4 PNFs into longer fibrils may require interaction with both VLPs and the plasma membrane. Consistent with earlier findings, D4 PNF-VLP aggregates appeared larger and more loosely packed upon VLP binding (Fig. 4**A** vs. Fig. S15B). In contrast, Vectofusin-1 PNFs formed smaller, less densely packed aggregates in the presence of VLPs, which were more numerous per cell compared to PNF-only conditions (Fig. 4**A** vs. Fig. S15B). This was confirmed by TEM and STEM tomography (Fig. 4**B;** Fig. S18B**; Video 6**) and supports our earlier observations that Vectofusin-1 morphology changes upon VLP binding. Moreover, these analyses revealed that the Vectofusin-1 aggregates consisted of smaller, disorganized structures upon VLP interaction.

Supplementary material related to this article can be found online at doi:10.1016/j.nantod.2026.103015.

When assessing the interaction between PNF-VLP complexes and cells, HeLa cells responded similarly to PNF-only conditions. Vectofusin-1 aggregates were passively bound by filopodia, while D4 aggregates induced active membrane ruffling and engulfment, indicating macropinocytosis initiation (Fig. S18B**;** Fig. 4**A**). STEM tomography confirmed these patterns and showed that, despite changes in PNF morphology upon VLP binding, the mode of cell interaction remained unaffected (Fig. 4**B; Video 5; Video 6**). These results reinforce the conclusion that D4 and Vectofusin-1 PNFs elicit distinct cellular responses independent of their VLP interactions.

We previously showed that D4 aggregates bind numerous VLPs on their surface. Here, electron microscopy confirmed that some of these VLPs were also in direct contact with filopodia or the plasma membrane (Fig. 4**A, B; Video 5**). This surface-binding pattern may facilitate VLP detachment from the fibrils and promote their direct engagement with the plasma membrane [48]. In contrast, control experiments with VLPs alone revealed minimal membrane association after 1 h (Fig. S16; Fig. S18A), highlighting the role of D4 PNFs in enhancing VLP-cell interaction, consistent with prior transduction studies [15]. For Vectofusin-1, fewer VLPs were bound to the aggregates, and they were more randomly distributed within the aggregates. Direct VLP-plasma membrane contact was not observed (Fig. 4**A, B; Video 6**), which may explain the lower transduction enhancement seen with Vectofusin-1. Nevertheless, STEM tomography revealed that many VLPs were associated with filopodia entwined by Vectofusin-1 PNFs, even though only a minority was directly bound to the fibrils (Fig. 4**B**). This suggests that Vectofusin-1 may still promote VLP-cell contact by positioning VLPs near filopodia, albeit less efficiently than D4.

To better mimic transduction-like conditions, D4 and Vectofusin-1 PNFs (10 μg/mL) were pre-incubated with VLPs for 10 min and added to HeLa cells. After 1 h, unbound material was removed and nuclei stained with Hoechst. Fluorescence microscopy showed that, in the absence of PNFs, only a few VLPs bound to cells (Fig. 4**C**), corroborating EM data. D4 PNFs formed individual aggregates that captured VLPs on their surface and adhered to the plasma membrane (Fig. 4**C**). In contrast, Vectofusin-1 formed smaller aggregates that spread across and between adjacent cells, creating a mesh-like network (Fig. 4**C**).

In summary, D4 and Vectofusin-1 PNFs not only differ in VLP binding capacity and morphology but also in how they mediate VLP interaction with the plasma membrane. D4 promotes surface-localized VLP binding and active engagement with the plasma membrane, likely supporting efficient transduction. Vectofusin-1, although less potent, may still facilitate viral entry by concentrating VLPs near filopodia, albeit via a more passive mechanism.

Cellular uptake of D4 and Vectofusin-1 PNFs

Minimizing side effects is crucial for clinical application of PNFs as transduction enhancers in ex vivo gene therapies (e.g., CAR-T cell therapy). In particular, PNFs should be internalized and degraded by target cells before infusion, as persistent aggregates may trigger immune responses or contribute to vascular occlusion [49]. Our previous findings demonstrated that D4 PNFs induce extensive membrane remodeling and filopodial engagement, morphological features frequently associated with early macropinocytosis. These observations suggested that D4 may undergo faster and more efficient uptake than Vectofusin-1, but did not exclude the involvement of additional endocytic pathways.

To directly compare uptake and intracellular processing, HeLa cells were incubated with 2 μg/mL of either D4 or Vectofusin-1 PNFs for 24 h and analyzed by TEM (Fig. 5**A**). D4-treated cells exhibited large intracellular vesicles (>2 μm), within the size range reported for macropinosomes (0.2–5 μm) [50], whereas such vesicles were absent in untreated controls (Fig. 5A). Two morphologically distinct forms of internalized D4 fibrils were detected: dark grey, thick aggregates representing intact PNFs (blue arrowhead), and lighter grey, thin structures consistent with disassembled PNFs (grey arrowhead). This pattern resembles our earlier observations with EF-C PNFs [29]. The presence of enclosed filopodial remnants inside these vesicles (purple arrowheads) supports recent uptake, because filopodial retraction is required for macropinosome closure [51]. Intraluminal vesicles (white arrowheads), characteristic of late endosomes, further indicate progression toward lysosomal degradation. Some D4 aggregates remained at the cell surface after 24 h (Fig. S19), but the plasma membrane at these sites appeared ruffled, suggesting that these remaining aggregates were in the process of being internalized.

In contrast, although some intracellular vesicles containing Vectofusin-1 PNFs were observed after 24 h, their morphology closely resembled that of surface-bound aggregates, with no evidence of

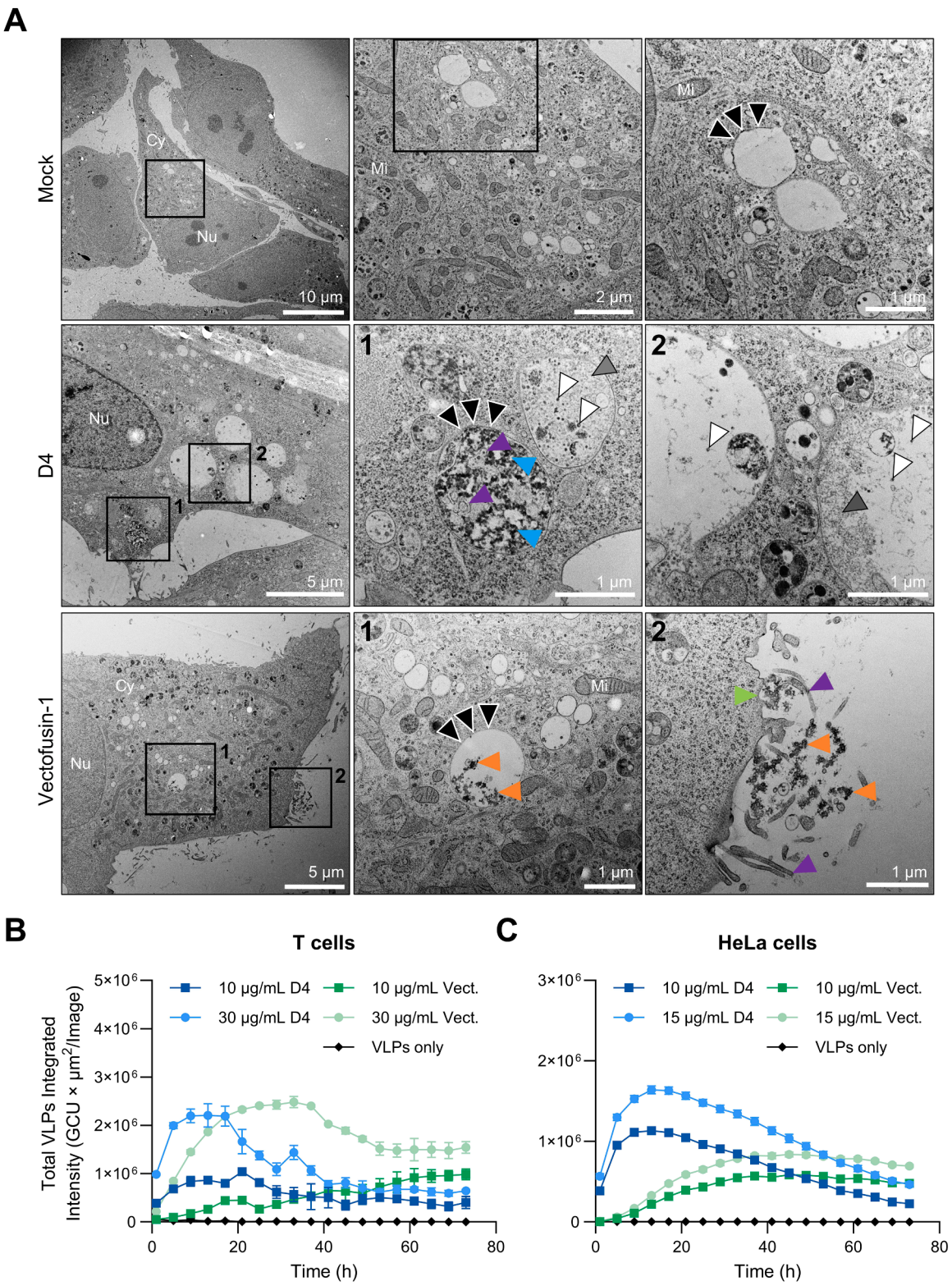

Fig. 5. Cellular uptake of D4 and Vectofusin-1 PNFs. (A) PNFs (2 µg/mL) were incubated with HeLa cells for 24 h and analyzed by TEM. Assembled D4 PNFs appear as dark structures (cyan arrowheads), Vectofusin-1 PNFs with a similar morphology (orange arrowheads). D4 PNFs in the process of disassembly appear as lighter structures (grey arrowheads). Vesicles are highlighted by black arrowheads that point at their enclosing membrane and intraluminal vesicles are indicated by white arrowheads. Cellular protrusions on the cell surface or protrusions taken up in vesicles, respectively, are indicated by purple arrowheads. Cy, cytoplasm; Mi, mitochondrium; Nu, nucleus. Representative images from one experiment, with at least 20 cells analyzed per sample. (B and C) VLPs were incubated with D4 and Vectofusin-1 PNFs for 10 min before they were added to HeLa (B) or T cells (C) for 3 days. After 1 h of incubation fluorescence of VLPs was measured every 4 h using time-lapse imaging. Background fluorescence of cells and PNFs were subtracted. Shown are mean values (±SD) from triplicates. For each triplicate 4 images were analyzed.

intraluminal vesicles or transitions from darker to lighter fibril appearance (Fig. 5**A**). This indicates that degradation had not yet begun. Fewer Vectofusin-1 aggregates were internalized overall. Nonetheless, occasional membrane invaginations and filopodial enclosures were detected, suggesting that Vectofusin-1 can also enter cells through macropinocytosis, albeit less efficiently and less extensively than D4.

To assess uptake dynamics, 10 μg/mL and 15 μg/mL of PNFs were pre-incubated with VLPs for 10 min before addition to HeLa cells. VLP fluorescence was monitored via time-lapse imaging over 72 h. In D4-treated samples, VLP fluorescence increased until 13 h and then declined (Fig. 5**B**), consistent with internalization, and mirroring observations in cell-free assays (Fig. 3**F**). Fluorescence microscopy corroborated a reduction in VLP/D4 aggregates at 49 h and 73 h (Fig. S20). In contrast, Vectofusin-1 fluorescence continued rising until ~47 h and then plateaued (Fig. 5**B**), indicating limited uptake and prolonged extracellular persistence. Microscopy showed that the number of VLP/Vectofusin-1 aggregates was greater at 73 h than at 1 h (Fig. S20). Three-day treatment of HeLa cells demonstrated that the PNF concentrations used above did not affect viability. A modest reduction was observed only at the highest concentration (80 μg/mL), lowering viability to ~80% for D4 and ~75% for Vectofusin-1 (Fig. S21A).

To examine uptake in a clinically relevant system, 10 and 30 μg/mL of PNFs were pre-incubated with VLPs and applied to activated $CD4^+$ T cells. Time-lapse imaging revealed that VLP/D4 fluorescence peaked at 13 h and declined thereafter, independent of concentration (Fig. 5**C**). For Vectofusin-1, fluorescence continued to rise over 72 h at 10 μg/mL, while at 30 μg/mL it plateaued at ~33 h and declined slightly after 57 h (Fig. 5**C**). Light microscopy showed that both PNFs increased T-cell clustering, consistent with activation and proliferation [52], and that these clusters were associated with PNF/VLP aggregates (Fig. S22). In D4-treated samples, cluster numbers declined over time, while Vectofusin-1 treatment led to the formation of an extensive fibrillar network that enclosed and connected cells (Fig. S22; Fig. S23). This aligns with previous findings showing that Vectofusin-1 forms a dense PNF network between cells, whereas D4 forms isolated aggregates that bind individually to cells (Fig. 4**C**). The absence of network-like structure in D4-treated samples likely facilitates eventual cluster disassembly over time. As prolonged or excessive T-cell clustering can impair cell expansion and viability [52], we assessed T-cell viability and proliferation. Only the highest concentration of Vectofusin-1 (30 μg/mL) significantly reduced viability after three days (Fig. S21B), while neither PNF impaired cell proliferation (Fig. S21C).

Intracellular trafficking and degradation of D4 PNFs

To directly track D4 degradation, D4-PNFs (1 mg/mL) were labeled with the amyloid-binding dye pFTAA, which binds filamentous β-sheet aggregates such as amyloid-β and tau fibrils [53,54], and has been used previously for EF-C PNFs [26]. TEM confirmed that pFTAA-labeling did not alter D4 morphology (Fig. S24A), and time-lapse imaging showed comparable aggregate size, number, and assembly kinetics between labeled and unlabeled D4 (Fig. S24B–D). pFTAA fluorescence intensity declined to ~50% in absence of cells over three days (Fig. S24E), likely reflecting gradual aggregate disassembly, as previously demonstrated by density measurements (Fig. 3**D**). Loss of dye during fibril remodeling explains the fluorescence reduction, although sufficient dye remained to allow detection of aggregate numbers, which remained constant (Fig. S24F). Importantly, pFTAA-labeled D4 enhanced HIV-1 infection to the same extent as unlabeled D4 demonstrating that pFTAA staining does not interfere with the transduction-enhancing activity of D4 (Fig. S24G). However, it should be noted that pFTAA-labeling detects D4 only when it forms β-sheet-rich structures, particularly PNFs, and therefore cannot be used to directly assess peptide degradation.

To investigate the uptake mechanisms in detail, we employed five endocytosis inhibitors targeting macropinocytosis (Wortmannin, EIPA, Dynasore), clathrin-mediated endocytosis (Dynasore, Chlorpromazine (CPZ)), and caveolin-mediated endocytosis (Nystatin). Prior to the uptake assay, viability testing confirmed that these inhibitor concentrations did not impair HeLa cell viability (Fig. S25A). HeLa cells were pre-incubated with each inhibitor for 30 min and then exposed to 10 μg/mL pFTAA-labeled D4 for 4 h. Extracellular fluorescence was quenched with trypan blue, and intracellular D4 was quantified by flow cytometry. Wortmannin caused a dose-dependent reduction in D4 uptake of up to ~60%, and all other inhibitors also partially reduced internalization (Fig. S25B). These results demonstrate that D4 does not rely exclusively on macropinocytosis, but rather enters cells via multiple endocytic pathways, including clathrin- and caveolin-mediated mechanisms.

Next, we assessed whether internalized D4 PNFs undergo lysosomal degradation. HeLa cells were incubated with pFTAA-labeled D4 for 24 h, after which lysosomes were stained with LysoTracker Blue DND-22. Fluorescence microscopy revealed clear colocalization of pFTAA-D4 with lysosomes (white arrowheads), appearing as enlarged vesicular structures (Fig. S26). Together with our TEM analysis demonstrating disassembly following cellular uptake, these findings suggest that D4 fibrils are degraded via the lysosomal pathway. In addition, large intracellular vesicles (>1 μm) containing only pFTAA-D4 (blue arrowhead) were detected; based on their size, these structures correspond to macropinosomes harboring recently internalized D4 PNFs (Fig. S26), consistent with our previous TEM observations (Fig. 5**A**).

We next assessed D4 degradation kinetics. HeLa cells were incubated with 10 μg/mL pFTAA-D4 PNFs for three days and monitored by time-lapse imaging. The number of pFTAA-D4 aggregates detected in the green channel increased up to 13 h, declined until approximately 61 h, and then plateaued. In cell-free controls, aggregate numbers increased until 13 h and subsequently remained stable (Fig. S27A). Normalization revealed a reduction of pFTAA-D4 aggregates to ~60% (Fig. S27B). The plateau after 61 h likely reflects near-confluent cell density, limiting further uptake and degradation of remaining aggregates (Fig. S27C).

Finally, to evaluate uptake under CAR-T-cell-like conditions, activated $CD8^+$/$CD4^+$ T cells were incubated with 30 μg/mL pFTAA-labeled D4 PNFs for 7 days. Fluorescence was quantified at 1 h, 24 h, 72 h, and 168 h (Fig. 6**A**). Because pFTAA fluorescence decays over time, input controls were prepared in which pFTAA-D4 PNFs were pre-incubated for the same durations before being added to cells for 1 h (medium exchanges and scaling steps matched identically). pFTAA-D4 fluorescence in T cells declined more rapidly than in the corresponding input controls, and after 7 days it was no longer detectable (Fig. 6**B**). Normalization to the input controls showed a reduction to ~2% after three days (Fig. 6**C**). These findings demonstrate that pFTAA-labeled D4 PNFs are progressively taken up by T cells. Given that CAR-T manufacturing typically spans 9–11 days [55], D4 is likely fully internalized and degraded during the production process. After 7 days, viable cell counts and viability measurements showed that pFTAA-D4 had no adverse effects on T-cell proliferation or viability (Fig. 6**D, E**).

In summary, D4 and Vectofusin-1 PNFs exhibit distinct cellular interaction and uptake profiles. D4 PNFs show high VLP binding capacity and a surface-binding pattern that promotes direct contact with filopodia and the plasma membrane. D4 induces membrane ruffling and bulk uptake consistent with macropinocytosis, while inhibitor experiments confirm that D4 additionally enters cells via clathrin- and caveolin-mediated endocytosis. Importantly, D4 aggregates are internalized by both, HeLa and T cells within 24–72 h, supporting their suitability for ex vivo gene-therapy workflows. In contrast, Vectofusin-1 forms smaller, more numerous aggregates with lower VLP binding efficiency, slower uptake, and less efficient degradation. Under transduction-like conditions, Vectofusin-1 forms a dense, interconnected aggregate network between cells, while D4 aggregates interact with cells individually. These mechanistic differences likely underlie their divergent efficiencies as transduction enhancers.

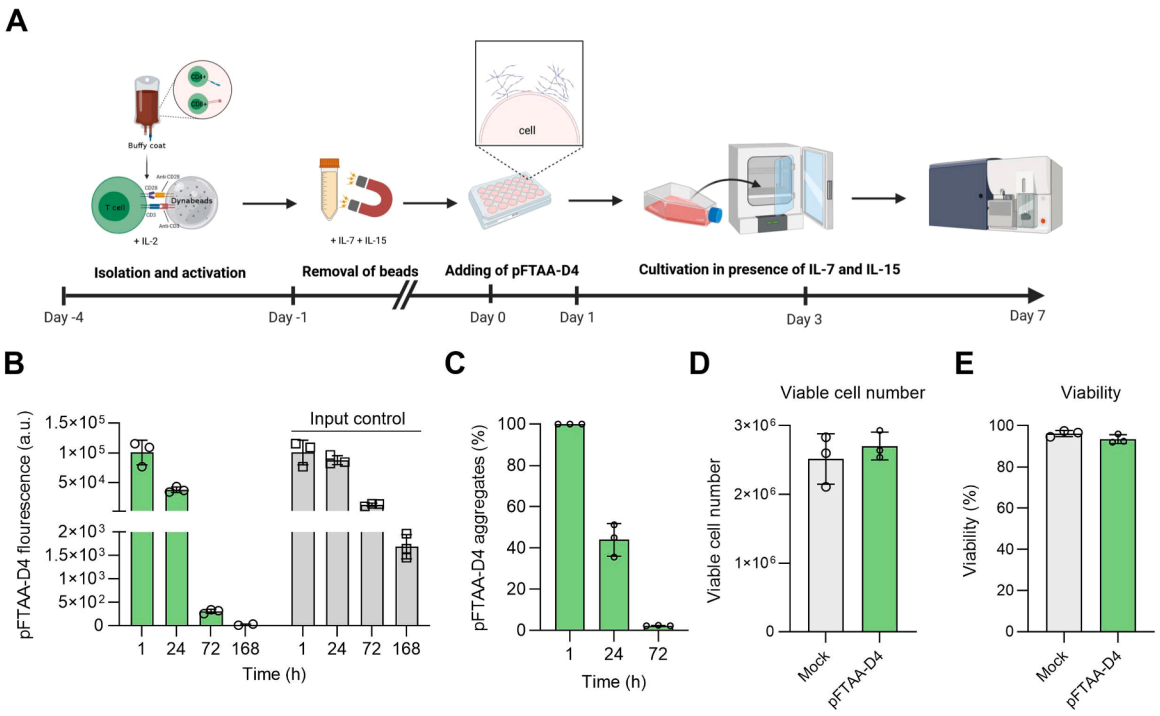

Fig. 6. pFTAA-D4 PNF aggregates decrease in presence of T cells over time. (A) Workflow of T cell cultivation under CAR-T cell like settings. CD4+/CD8+ T-cells were isolated from Buffy coats of 3 healthy donors and activated using Dynabeads™ Human T-Activator CD3/CD28 in presence of IL-2 over three days. Afterwards, the beads were removed and medium was exchanged to medium supplemented with IL-7 and IL-15. The next day (day 0), 30 µg/mL pFTAA-D4 PNFs were added to 50,000 CD4+/CD8+ T-cells. After 1, 24, 48, 73 and 168 h fluorescence of pFTAA-D4 PNFs was analyzed by flow cytometry. After 24 and 72 h a medium change was performed. Additionally, the cell concentration was adjusted to 1 million cells/mL after 72 h. Created in BioRender. Rauch, L. (2026) https://BioRender.com/aate9gs. (B) Fluorescence of pFTAA-D4 PNFs at indicated time points. Background fluorescence of untreated cells was subtracted. Shown are mean values (±SD) of three donors measured in triplicates. As an input control pFTAA-D4 PNFs were incubated for 1, 24, 72 and 168 h and added to the cells at indicated time points for 1 h before flow cytometry analysis. Similar to the other samples, medium exchanges were performed for the input control after 24 and 72 h. (C) Fluorescence of pFTAA-D4 aggregates (green bars in B) was normalized to the input control (grey bars in B). Viable cell number (D) and viability (E) of T cells was determined after 7 days. For mock treated cells mean values (±SD) of three donors measured in singlicates are shown. For pFTAA-D4 PNFs treated cells mean values (±SD) of three donors measured in triplicates are shown.

Discussion

In this study, we investigated how the structural and morphological properties of two relevant transduction enhancers, D4 and Vectofusin-1, dictate their interactions with viral particles and target cells. Although previous work using the model β-sheet peptide EF-C revealed that cationic PNFs can enhance viral transduction by capturing virions, promoting plasma-membrane engagement, and undergoing uptake via macropinocytosis followed by lysosomal degradation [18,28,29], these findings did not clarify how different PNF architectures (β-sheet vs α-helix), aggregate morphologies, or surface charge distributions shape viral binding and cellular responses. Importantly, our earlier work demonstrated that D4 outperforms Vectofusin-1 in γ-retroviral and lentiviral gene delivery to primary T and NK cells, without inducing inflammatory signaling or impairing cell viability [15]. However, the mechanistic basis for these functional differences, particularly how D4 and Vectofusin-1 aggregates differ in size, packing, VLP binding, membrane engagement, and cellular uptake, remained unclear. The present study addresses this gap by systematically comparing their structural organization, aggregation behavior, virion binding capacity, and cellular internalization pathways.

We performed a comparative analysis of D4 and Vectofusin-1, to understand how their sequence-encoded structures modulate assembly and function. In silico secondary structure predictions and molecular modeling provided initial clues to their self-assembly mechanisms. Vectofusin-1 (26-residues, KKALLHAALAHLLALAHHLLALLKKA-NH_2) was predicted to adopt an α-helical conformation, which we confirmed by CD and ATR FT-IR-analysis, with positively charged lysine residues at both the N- and C-termini, features that could serve as binding sites for negatively charged viral envelopes and plasma membranes. Helical wheel analysis indicated that multiple leucine residues line up along one face of the helix, a motif conducive to lateral self-association via coiled-coil interactions [23,38]. Additionally, hydrophobic residues (notably histidine residues positioned along the helix) were predicted to promote fibril formation [23]. Molecular dynamics simulations and zeta potential measurements revealed a positively charged and hydrophobic surface for Vectofusin-1, mainly driven by lysine and leucine residues, which are known to be essential for interaction of PNFs with viral and cellular membranes [20]. In contrast, the short D4 peptide (8 residues, RRIFISM) cannot stably fold into a defined secondary structure on its own. Instead, all-atom molecular dynamics simulations revealed that D4 monomers self-assemble into small antiparallel β-sheet oligomers containing approximately 4–5 peptides, which can further cluster into larger fibrillar aggregates. Within these assemblies, hydrophobic isoleucine residues pack inward to form a core, while the phenylalanine and arginine side chains remain exposed on the surface. This configuration is consistent with our experimental observations that D4 PNFs are rich in β-sheet content and present a cationic surface [15]. The combination of a hydrophobic core and positively charged surface is a known hallmark of effective transduction-enhancing fibrils, as it facilitates robust interactions with both viral particles and plasma membranes [20].

These inherent structural differences translated into distinct aggregate morphologies, as confirmed by our microscopy and kinetic analyses. TEM showed that D4 peptides assemble into loosely packed aggregates composed of short, nm-scale fibrils, closely resembling the

oligomeric β-sheet structures predicted by our all-atom molecular dynamic simulations. In contrast, Vectofusin-1 formed much shorter fibrils that clustered into smaller, more compact aggregates. We also observed nascent granular structures (potential fibril precursors) in Vectofusin-1 samples, suggesting that complete fibrillation might require longer incubation or higher peptide concentrations, consistent with prior reports for this peptide [23]. Quantitative live imaging of the aggregation process further supported these observations: D4 exhibited rapid aggregation kinetics, yielding a few large (μm-sized), loosely connected aggregates. Conversely, Vectofusin-1 polymerized more slowly and produced a greater number of small, tightly packed aggregates. These findings indicate that D4 and Vectofusin-1 differ not only in molecular secondary structure but also in the size, packing, and abundance of the PNF aggregates they form.

We next examined how these PNF aggregates interact with retroviral particles by introducing VLPs to preformed fibrils. Strikingly, virion binding induced pronounced changes in the morphology of both D4 and Vectofusin-1 aggregates. D4 aggregates became significantly larger and less densely packed upon VLP exposure, and the aggregation kinetics accelerated, suggesting that the association with virions promotes or stabilizes further PNF assembly. STEM tomography confirmed an increase in the prevalence of μm-length D4 fibrils after incubation with VLPs. One plausible explanation is that binding of negatively charged VLPs partially neutralizes the positively charged surface of D4 fibrils, thereby reducing electrostatic repulsion between PNF strands and enabling the extension of longer fibrils. This interpretation aligns with previous observations that EF-C fibrils can dramatically reduce the net surface charge of viral particles [29]. Our results imply a reciprocal effect whereby the virus can in turn modulate the charge state (and hence assembly behavior) of the fibril. By contrast, VLP binding to Vectofusin-1 had the opposite outcome. Instead of forming longer fibrils, Vectofusin-1 tended to break into a larger number of smaller, loosely packed aggregates upon exposure to virions, and no well-defined fibrillar structures were evident by TEM. This suggests that the attachment of VLPs actually disrupts or impairs the normal fibrillization pathway of Vectofusin-1. Structural modeling provides a potential rationale: the key lysine residues of Vectofusin-1 (critical for binding virions) lie in close proximity to its histidine residues (critical for peptide-peptide interactions during fibril growth) [23]. Thus, when VLPs bind to these lysine-rich regions, they may sterically or electrostatically hinder the histidine-mediated contacts required for fibril elongation, leading to incomplete, stunted assemblies. In summary, D4's interaction with virions appears to promote fibril growth (yielding larger, more open aggregates), whereas Vectofusin-1's interaction with virions tends to inhibit its fibril maturation (yielding a profusion of small aggregates).

In addition to altering aggregate size and structure, the presence of VLPs revealed distinct binding patterns on the two types of PNFs. D4 fibrillar aggregates were capable of capturing a high number of VLPs, which were observed to coat the PNF surface in a relatively uniform manner. This even distribution is consistent with our all-atom molecular dynamic simulation findings that D4 exposes multiple phenylalanine and arginine residues on its surface, thereby offering numerous hydrophobic and electrostatic contacts for the viral membrane. Our results here are similar to a previous study on designed peptide amphiphiles with a similar block architecture (hydrophobic moieties at one end and cationic residues at the other): such amphiphiles self-assemble into fibrils with an internal hydrophobic core and an outward-facing positively charged surface, and they showed the strongest plasma membrane binding and transduction enhancement among tested analogues [56]. In line with this, D4's ability to uniformly present both hydrophobic and cationic groups on its aggregates likely underpins its higher VLP binding capacity and, by extension, its potent transduction-enhancing effect [15]. By contrast, Vectofusin-1 aggregates bound far fewer VLPs, and the attached virions appeared in a more sporadic, scattered pattern rather than a continuous coating, which matches the heterogenous distribution of lysine residues across the surface of Vectofusin-1 PNFs predicted by our molecular dynamic simulations. Additionally, this observation agrees with earlier reports by Vermeer et al. [23], and suggests that Vectofusin-1's symmetric peptide design (positively charged lysine residues at both ends of the molecule) may lead to an assembled structure that presents fewer accessible viral binding sites on its surface.

It is worth noting that our assays utilized VLPs lacking viral envelope glycoproteins, which could influence the generality of these findings. Prior work with semen-derived amyloid fibrils (SEVI) demonstrated that a high density of glycosylated envelope glycoproteins on virions can sterically hinder fibril-virus interactions, resulting in lower enhancement of infection [57]. In our case, using glycoprotein-deficient VLPs allowed us to specifically probe the interactions between PNFs and the viral membrane itself, which is the principal determinant of binding in these systems. Moreover, D4's superior VLP binding ability correlates with its higher transduction enhancement compared to Vectofusin-1 under real viral transduction conditions [15]. Thus, we consider the VLP model appropriate for dissecting PNF-virus interactions, while acknowledging that envelope glycoprotein content is an additional factor in natural infections.

Furthermore, D4 and Vectofusin-1 exhibited distinct serum-dependent aggregation behaviors. Both peptides showed maximal aggregation at 2.5% serum, followed by a progressive decline in aggregation with increasing serum concentrations. This trend is consistent with the known chaperone-like activity of serum albumin, which can inhibit peptide aggregation and fibril formation [43,58], suggesting that higher serum levels impede PNF assembly. In addition, serum proteins are known to co-localize with amyloid fibrils [45], and may sterically hinder further fibril growth of D4 and Vectofusin-1. Interestingly, both PNFs displayed the lowest aggregation density under serum-free conditions, indicating that specific serum components may support PNF aggregation in a concentration-dependent manner. Serum contains charged molecules, including proteins, lipids, and salt ions [59], that alter the electrostatic environment and may promote fibril nucleation at low concentrations. For instance, lysozyme, BSA, and polysaccharides have been shown to facilitate α-synuclein fibril formation [60]. Both PNFs aggregated more rapidly in FBS than in human serum, which may reflect the presence of proteolytic enzymes in human serum capable of degrading the peptides. However, the complex and batch-variable composition of serum needs further investigation to elucidate the precise mechanisms underlying the reduced aggregation observed in presence of human serum. Incubation with VLPs accelerated the aggregation of both PNFs, consistent with reports that endogenous retroviral particles can promote protein aggregation in neurological disorders, although the underlying mechanisms remain incompletely understood [61]. We propose that VLP interaction may reduce electrostatic repulsion between the positively charged D4 and Vectofusin-1 fibrils, thereby facilitating assembly. Additionally, VLPs may serve as nanoscale scaffolds that concentrate fibrils at their surfaces and lower energetic barriers for nucleation and cross-linking. VLP binding was strongest for both peptides in the absence of serum and decreased progressively with increasing serum concentrations, suggesting that serum components interfere with peptide–VLP interactions. Given that serum contains extracellular vesicles with morphological similarity to VLPs [62], these vesicles may compete with VLPs for binding to D4 and Vectofusin-1.

We next investigated how the distinct aggregate structures and virus-binding profiles of D4 and Vectofusin-1 influence their interactions with cellular membranes. For these experiments, each peptide fibril preparation was incubated with HeLa cells and examined by TEM, SEM, and STEM tomography. D4 predominantly appeared on the cell surface as clusters of short fibrillar aggregates, consistent with its tendency to form short fibrils. Occasionally, longer individual fibrils were seen protruding from these aggregates, suggesting that D4 can also elongate into μm-sized fibrils. In contrast, Vectofusin-1 associated with cells mainly as small, dense amorphous aggregates, with virtually no linear fibrils visible. Intriguingly, we observed that many of the cell-bound

Vectofusin-1 aggregates contained vesicle-like structures roughly 50–80 nm in diameter. We propose that these vesicles are self-assembled nanostructures of Vectofusin-1 itself, reflecting the peptide's amphiphilic character. Amphiphilic peptides are well known to form not only fibrils but also sheet and vesicle morphologies under certain conditions [63,64]. For example, a designed amphiphilic oligopeptide (Ac-AAVVLLLW-$E_2/_7$-COOH) has been shown to self-assemble into ~60 nm vesicles [64], comparable in size to the structures we observed with Vectofusin-1. This propensity to form membrane-like vesicles might compete with or divert Vectofusin-1 away from fibrillar assembly when the peptide is in proximity to cellular membranes.

These ultrastructural differences translated into markedly different effects on plasma membrane dynamics. D4's interaction with cells appears to be an active, energy-dependent process, similar to what was previously described for EF-C fibrils [28]. Numerous D4 aggregates were found ensnared by filopodial tentacles on the cell surface, which often converged to draw the aggregates toward the cell body. At sites of D4 attachment, we frequently observed pronounced membrane ruffles and the formation of cup-like invaginations, indicative of uptake via macropinocytosis. Such membrane remodeling not only increases the surface area available for viral particle attachment but also facilitates more rapid internalization. By effectively bringing the plasma membrane deeper into the cytoplasm, these invaginations shorten the distance that viral capsid must travel to reach the nucleus, thereby potentially boosting the rate of successful transduction [29]. The idea that arginine-rich D4 PNFs trigger macropinocytosis is further supported by the wealth of literature on cell-penetrating peptides: poly-arginine sequences (e.g., octaarginine peptides, the HIV-1 Tat peptide, and branched arginine-rich peptides) are known to bind cell-surface heparan sulfate proteoglycans and initiate actin-driven membrane ruffling and macropinocytosis [65–67]. Indeed, arginine-rich peptides comprise a major class of cell-penetrating vectors for delivering macromolecules into cells [68]. Additionally, the uniform coating of VLPs on D4 aggregates likely facilitates direct engagement of virions with cellular filopodia and the plasma membrane. This supports our earlier hypothesis that filopodial bridges not only actively capture PNF-virus complexes but can also serve as conduits to deliver virions to entry sites on the cell surface [29]. It is noteworthy that pathogenic retroviruses such as HIV-1 and murine leukemia virus (MLV) have evolved to hijack filopodial networks: they attach to receptors on the tips of filopodia and then "surf" along these actin-rich cables toward the cell body to initiate infection [69]. A similar mechanism has been described for extracellular vesicles, which share size and membrane characteristics with our VLPs [62]. By coating VLPs along D4 fibrils, the cell's filopodial machinery might be co-opted to transport these VLP-loaded fibrils inward, thereby streamlining viral delivery to the cell.

Vectofusin-1's mode of cell interaction, by contrast, appears largely passive. Vectofusin-1 aggregates often entangled filopodia without inducing appreciable membrane ruffles or invaginations. In many cases, the peptide formed an extensive, net-like matrix enveloping the cell and bridging to neighboring cells, which could physically hinder the filopodia from reeling the aggregates into the cell body. We therefore surmise that Vectofusin-1 predominantly associates with the plasma membrane through non-specific electrostatic and hydrophobic interactions, whereas D4 not only engages in these interactions but, owing to its high arginine content, may additionally promote active endocytosis via cellular protrusions. While Vectofusin-1's network did capture some VLPs and hold them at the tips of filopodia, we did not observe instances of those virions being delivered to the plasma membrane or internalized. In summary, D4 actively engages the plasma membrane and cytoskeletal machinery to promote its uptake (and in doing so, also ferries bound virions into the cell), whereas Vectofusin-1 tends to remain extracellular, forming a static adhesive matrix that can trap virions on filopodia but does not efficiently bring them into contact with the plasma membrane for entry.

Consistent with these structural differences, we observed that the cellular uptake pathways of D4 and Vectofusin-1 diverge markedly. D4 PNF aggregates were efficiently internalized via macropinocytosis, as demonstrated by TEM and fluorescence microscopy, and further supported by the reduction in uptake upon treatment with macropinocytosis inhibitors. Inhibition of clathrin- or caveolin-mediated endocytosis also diminished D4 internalization, suggesting that D4 can enter cells through multiple endocytic routes. This is likely explained by the strong size-dependence of endocytic mechanisms [70,71] and, therefore, by the aggregation state of D4. Similar observations have been made for other fibril-forming peptides: α-synuclein fibrils are internalized predominantly via macropinocytosis [72], whereas monomers and oligomers enter cells mainly through clathrin-mediated endocytosis [73,74]. Moreover, arginine-rich cell-penetrating peptides have been shown to engage different uptake pathways depending on peptide concentration, cell type and cargo, further supporting the concept that structurally dynamic peptides can utilize multiple internalization mechanisms [75]. However, given the formation of μm-sized aggregates and the high conversion rate of D4 monomers self-assembling into PNFs (98%), as determined in our previous study [15], we propose that D4 is predominantly internalized via macropinocytosis. Colocalization of intracellular D4 with lysosomes and a time-dependent decrease of D4 aggregates in cell culture indicate lysosomal degradation after uptake by endocytosis and mirrors prior reports for other β-sheet–forming amyloid fibrils, including EF-C and even pathological fibrils like α-synuclein, which are known to undergo uptake via macropinocytosis and subsequent lysosomal degradation [29,72].

In stark contrast, Vectofusin-1 aggregates exhibited very limited internalization under the same conditions. We attribute this poor uptake to the physical barrier imposed by the dense Vectofusin-1 peptide network encasing the cells, which likely blocks the aggregates from accessing the endocytic machinery. Notably, when Vectofusin-1 was present not as a continuous network but as isolated aggregates on the cell surface, we did observe some uptake events via macropinocytosis (for instance, rare Vectofusin-1 aggregates were found inside macropinosomes by TEM after 24 h). This suggests that the network architecture, rather than an intrinsic incapacity for uptake, underlies Vectofusin-1's limited internalization. In practical terms, if the peptide remains dispersed (or if the network can be disrupted), Vectofusin-1 may still enter cells to some extent through similar pathways as D4. An additional factor contributing to the different uptake kinetics of D4 and Vectofusin-1 is their amino acid composition. Arginine-rich peptides are generally internalized by cells much more efficiently than those rich in lysine, ornithine, or histidine residues [76,77]. D4 contains multiple arginine residues, whereas Vectofusin-1's cationic content originates largely from lysine residues (along with histidine residues which are partly hydrophobic). This difference in composition might underlie a greater inherent propensity for D4 to be taken up by cells compared to Vectofusin-1, complementing the structural and morphological reasons discussed above.

The divergent uptake behaviors of D4 and Vectofusin-1 provide a mechanistic explanation for their differential effects on certain viral vectors. For example, Vectofusin-1 is known to fail in enhancing transduction of lentiviral vectors pseudotyped with the VSV-G glycoprotein (VSV-G LVs) [15,26,38]. VSV-G mediates viral entry via clathrin-mediated endocytosis through low-density lipoprotein (LDL) receptors on the cell surface [78,79]. We propose that the sheath-like PNF network formed by Vectofusin-1 on cells acts as a barrier that prevents VSV-G-bearing virions being efficiently endocytosed after receptor binding, thereby nullifying Vectofusin-1's benefit for that system. This is further supported by the observation that D4 PNFs efficiently enhance the transduction of VSV-G-pseudotyped lentiviral vectors in T cells, whereas Vectofusin-1 PNFs show no such enhancing effect [15]. In contrast, many other retroviral pseudotypes (such as those bearing the gibbon ape leukemia virus envelope) infect cells by direct fusion at the plasma membrane after receptor binding [80]. These viruses do not rely on uptake via endocytosis, and accordingly the presence of an

extracellular peptide network is less obstructive. Consistently, transduction by such fusogenic vectors remains strongly enhanced by Vectofusin-1, as demonstrated in multiple studies [13,15,81,82].

From a translational perspective, our findings carry important implications for using PNFs as transduction enhancers in ex vivo gene therapy (e.g., CAR-T cell manufacturing). It is crucial that any enhancer added to T cell cultures be effectively eliminated before the modified T cells are reinfused into patients, since residual peptide aggregates could trigger immune reactions or cause microemboli [49]. We therefore assessed the fate of D4 and Vectofusin-1 in primary human T cells. Consistent with the cell line data, D4 PNF aggregates were readily internalized by CD4+ T cells, whereas Vectofusin-1 aggregates mostly remained attached to the cell surface or extracellular matrix. However, we did not observe complete uptake of D4 fibrils within a 72 h period, indicating that clearance of these peptides may require more time. Therefore, we analyzed the uptake of D4 under CAR-T cell–like conditions including medium exchanges and scale-up over a 7-day period. Under these conditions, the majority of D4 aggregates had disappeared by day 3. In addition to cellular uptake and lysosomal degradation, the gradual disassembly of D4 PNF aggregates likely contributes to this loss, as smaller fragments may be removed during routine medium exchanges. In the context of a typical CAR-T cell production process lasting 9–11 days [55], it is conceivable that most D4 material would be internalized and degraded. Both types of PNFs were found to localize within T cell clusters (cell-cell aggregates) in culture. Interestingly, the two peptides had opposite effects on the evolution of these clusters: D4-induced cell clusters tended to break apart over time (consistent with the eventual uptake and clearance of D4), whereas Vectofusin-1 led to the formation of extensive peptide networks that increasingly interconnected cells into large clusters. Prolonged or excessive T cell clustering is known to impair cell expansion and viability [83], a phenomenon that we observed only at the highest Vectofusin-1 concentration (30 μg/mL), which led to a measurable reduction in cell viability. However, in a clinical context, Vectofusin-1 is applied at substantially lower concentrations (10–12 μg/mL), which did not affect T-cell viability or proliferation in our experiments, and is followed by a medium exchange or washing step after transduction, as recommended in the manufacturer's protocol. Under these conditions, we propose that peptide aggregates are dissolved and thereby disperse T cell clusters to restore normal cell expansion.

In summary, D4 and Vectofusin-1 illustrate how the nano-assembly of peptides can dictate their biological activity as transduction enhancers. D4 assembles into loosely packed, β-sheet-rich fibrillar aggregates that provide a high density of viral binding sites, actively remodel the plasma membrane, and undergo productive uptake via endocytosis followed by lysosomal degradation. In contrast, Vectofusin-1 forms α-helical fibrils that bundle into dense, web-like networks, characterized by lower viral binding capacity and predominantly surface-bound interactions with cells, with minimal internalization. Notably, our study is the first to demonstrate that interactions with VLPs can feed back to influence the assembly and morphology of PNF aggregates themselves, revealing a dynamic interplay between viral particles and enhancer nanostructures. Together, these findings highlight the critical role of PNF aggregate morphology in modulating viral capture and cellular uptake. A deeper understanding of these structure-function relationships will be vital for optimizing the design and use of PNF-based transduction enhancers, ensuring they maximize gene delivery efficiency while maintaining safety in the context of ex vivo gene therapies.

Material and methods

Cells

HeLa cells (ATCC, CRM-CCL-2) were cultured in Dulbecco's Modified Eagle Medium (DMEM, Gibco, 11965092) supplemented with 100 U/mL penicillin, 100 μg/mL streptomycin (PAN-Biotech, P06–07050), 2 mM L-glutamine (PAN-Biotech, P04-80050), and 10% inactivated fetal bovine serum (FBS, Gibco, 10437028). Human CD4+ T and CD8 + T cells were isolated from Buffy coats of healthy donors and activated as described in Rauch-Wirth et al. [15]. Activated T cells were cultured in supplemented RPMI (Gibco, 11875093, 100 U/mL penicillin, 100 μg/mL streptomycin, 2 mM L-glutamine, 10% FBS) in presence of 450 IU/mL IL-7 (Miltenyi Biotec, 130-095-362) and 50 IU/mL IL-15 (Miltenyi Biotec, 130-095-764).

Preparation of peptide nanofibrils (PNFs)

D4 (RRIFIISM) was synthesized by GaloreTx Pharmaceuticals (Udupi, India). D4 was dissolved in DMSO (Merck, Cat: 67-68-5) to 10 mg/mL and stored at 4 °C. For each experiment, D4 was freshly dissolved in PBS to 2 mg/mL and incubated for 10 min at room temperature to generate PNFs. For fluorescence labeling of D4 PNFs, 49 μl D4 (1 mg/mL) was stained with 0.7 μl pFTAA (1 mM, BioTracker Tau filaments pFTAA Live Cell Dye, Sigma-Aldrich, SCT066) for 30 min at 37 °C. Vectofusin-1 (Miltenyi Biotec, 130-111-163) was solved in sterile water to 1 mg/mL, stored at −80 °C and was further solved for each experiment according to manufacturing protocol.

Circular dichroism (CD) spectroscopy

CD spectra were obtained using a J-1500 CD spectrometer (Jasco, Japan) with a cell path length of 0.1 cm quartz cuvette at room temperature. Lyophilized peptides were directly dissolved or dispersed in DPBS (without $CaCl_2$ and $MgCl_2$; 137 mM NaCl, 2.7 mM KCl, 8.1 mM Na_2HPO_4, 1.5 mM KH_2PO_4, pH 7.4) to a final concentration of 0.1 mg/mL and incubated for 10 min prior to measurement. Unlike the original sample preparation method, DMSO was not used here because its strong absorption in the far-UV region interferes with CD measurements [84]. Spectra were collected at a scanning speed of 200 nm/min with a 1 nm data interval, and baseline correction was applied by subtracting the corresponding buffer spectrum. Each final spectrum represents the average of three consecutive scans.

Attenuated total reflection Fourier transform-infrared (ATR FT-IR) spectroscopy

Secondary structures of the assembled peptides were analyzed using ATR FT-IR spectroscopy. Peptide assemblies (1 mg/mL) were lyophilized, and the resulting powders were used for measurement. All spectra were recorded on a Bruker Tensor 27 spectrometer equipped with a diamond crystal as ATR element (PIKE MiracleTM) at a spectral resolution of 2 cm^{-1}. Each spectrum was collected by averaging 64 scans. Data were processed with OriginLab software, and each secondary structure content was quantified by deconvolution of the amide I region [19].

Dynamic light scattering (DLS) spectroscopy

The hydrodynamic diameter and surface charge of the peptide assemblies were determined using a Zetasizer Nano ZS (Malvern Instruments, United Kingdom). For hydrodynamic size determination, D4 was dissolved from DMSO stock solutions (10 mg/mL) into DPBS to a final concentration of 0.05 mg/mL, while Vectofusin-1 was directly dissolved in DPBS (1 mg/mL), and incubated for 10 min at room temperature. Measurements were conducted in 6 × 50 mm borosilicate glass disposable culture tubes (Kimble, United States), and each measurement consisted of at least three independent runs with 20 acquisitions each. Subsequently, zeta-potential measurements were conducted by diluting 60 μL of the peptide solution (1 mg/mL in DPBS) into 600 μL of filtered (0.45 μm pore size) 1 mM KCl solution. The measurements were carried out in disposable folded capillary cells (DTS–1070, Malvern). The zeta-potential values were calculated from the

electrophoretic mobility using the Smoluchowski formula implemented in the Zetasizer Nano ZS Software (V7.12). All reported values represent the mean value from at least three independent measurements with 20 runs each.

Helical wheel projection using HeliQuest

Vectofusin-1 was analyzed by HeliQuest [37] using following settings: Helix Type: α; windows size: FULL; one-letter size proportional to amino acids: yes; Rotation of the helix to align vertically the < μH> vector: yes.

3D structure analysis using PEP-FOLD4.0

Vectofusin-1 and D4 was analyzed at pH 7 by PEP-FOLD4.0 [33–36].

Molecular dynamics simulation

All atom and coarse-grained simulations were performed with GROMACS 2024 software [85–87] in triplicates. For all atom simulations we randomly placed 150 molecules in a 10 nm × 10 nm × 10 nm box (0.15 molecules/nm^3) using GROMACS inbuilt insert-molecules command, solvated in TIP3P water [88] and charge neutralized using 300 chloride ions using CHARMM36 force field [89]. We first performed energy minimization for 50,000 steps using 0.01 step size and steepest descent method. We used Verlet cutoff-scheme [90] and PME for long range electrostatic interactions with 1.0 for both, short-range electrostatic and Van der Waals cut-off. The LINear Constraint Solver (LINCS) algorithm was used for bond constraints [91]. Each simulation was performed with periodic boundary conditions in all 3 dimensions (xyz). Then, we ran a constant volume (NVT) simulation for 100 ps using a 2 fs time step at 310 K followed by a constant pressure (NPT) simulation with a 100 ps using 2 fs time step at 310 K and 1 bar with Parrinello-Rahman pressure coupling [92]. After the equilibration a production run using the NPT ensemble was conducted for 300 ns with 2 fs step size, v-rescale coupling method [93] and Parrinello–Rahman barostat at 298 K. The isothermal compressibility was 4.5×10^{-5} bar^{-1}.

Since we know from experiments and simulation that D4 peptides self-assemble into β-sheet rich fibers we designed a perfectly aligned fiber and performed atomistic simulations of these preformed fibers to investigate parallel vs. antiparallel intermolecular hydrogen bonding between peptides and behavior of the self-assembled fiber when stacking ten peptides along fiber axis. For the pre-assembled all atom simulations a D4 peptide fiber was prepared in Pymol software by placing 10 D4 peptides parallel or antiparallel in 4.8 Å distance to each other. A cubic simulation box measuring 7 nm × 7 nm × 7 nm (0.03 molecules/nm^3) was constructed with a minimum distance of 1.0 nm between the peptide molecules and the box edges followed by solvation in TIP3P water and charge neutralized using chloride ions using CHARMM36 force field. Energy minimization, NVT and NPT equilibration were performed as shown above for all atom simulations. After the equilibration a production run using the NPT ensemble was conducted for 1 μs with 2 fs step size using the same settings as shown for all atom simulations shown above.

Given the computational constraints of atomistic simulations at large scales, we used the coarse-grained simulations to investigate peptide self-assembly at longer time-scales. For coarse-grained simulations of D4 peptide we randomly placed 300 molecules in a 13 nm x 13 nm x 13 nm box (0.14 molecules/nm^3), for Vectorfusin-1 we randomly placed 60 molecules in a 13 nm × 13 nm × 13 nm box (0.03 molecules/nm^3) using the GROMACS inbuilt insert-molecules command. The peptides were modeled as coarse-grained representation using Martini 2.0 force field [94] and the charge was neutralized with 600 (D4) and 240 (Vectofusin-1) chloride ions and the box was solvated using the polarizable MARTINI water model [95]. Position restraints were applied during the energy minimization step, using a force constant of 1000 kJ·mol^{-1}·nm^{-2} along the x, y, and z directions for each atom. For the energy minimization we used 50,000 steps using 0.01 step size and steepest descent method. We used Verlet cutoff-scheme [90] and reaction-field for long range electrostatic interactions with 1.1 for both, short-range electrostatic and Van der Waals cut-off. The simulation was performed with periodic boundary conditions in all 3 dimensions (xyz). Then, we ran a constant volume (NVT) simulation for 20 ns using a 20 fs time step at 303 K followed by a constant pressure (NPT) simulation with a 20 ns using 20 fs time step at 303 K and 1 bar with Berendsen pressure coupling [96]. After the equilibration a production run using the NPT ensemble was conducted for 5 μs with 20 fs step size, v-rescale coupling method [93] and Parrinello–Rahman barostat at 298 K. The isothermal compressibility was 3×10^{-4} bar^{-1}.

By translating the coarse-grained simulations into atomistic resolution, we aim to examine the structural integrity and self-assembly organization after longer simulation times. For backmapping of the coarse-grained simulation to the all-atom representation model, we used the last frame of the coarse-grained simulation at 5 μs and converted into atomistic representation using *backward.py* script by Wassenaar et al. [97] and CHARMM36 force field as described here: The atomistic representation of the last frame is first minimized for 500 steps with steepest descent excluding non-bonded interactions and an additional energy minimization (500 steps) without exclusions, followed by position restrained NVT simulation (300 K), with time step 0.2 fs, position restrained NVT simulation (300 K), with time step 0.5 fs, position restrained NVT simulation (300 K), with time step 1.0 fs, and position restrained NVT simulation (300 K), with time step 2.0 fs. After the backmapping and energy minimization, we solvated in TIP3P and neutralized charges by adding 600 chloride ions. Energy minimization, NVT and NPT equilibration were performed as described for all atom simulations. After the equilibration a production run using the NPT ensemble was conducted for 300 ns with 2 fs step size using the same settings as shown for all atom simulations shown above.

A cutoff of 0.35 nm was used for the evaluation of hydrogen-bond interactions, and a probe cutoff of 0.14 nm was used for SASA calculations. The simulations were rendered using Visual Molecular Dynamics (VMD) software [98]. Secondary structure, e.g. β-sheets, were visualized using VMD's in-built STRIDE algorithm [99]. The aggregation propensity (AP) was determined by dividing the SASA at the start of the simulation by the SASA at the end.

Production of virus stocks

For generation of MLV Gag-YFP VLPs, 15×10^6 HEK293T cells were initially seeded in a T-175 flask in 20 mL supplemented DMEM, followed by adding 10 mL supplemented DMEM before transfection using 41.7 μg of the plasmid pMLV Gag-YFP (Addgene plasmid, #1813, a gift from Walther Mothes [100]) and TransIT-LT1 Transfection Reagent (Mirus Bio, Mir 2305) according to the manufacturer's protocol was performed on the next day. The resulting VLPs are non-infectious and emit a yellow fluorescence.

For electron microscopy experiments virus-containing supernatant and cell supernatant of non-transfected cells as control was sterile filtered (0.45 μm) and purified by ultracentrifugation (28,000 rpm, 2 h, 4 °C) using 20% Sucrose two days after transfection. Supernatant was removed and the pellet was resuspended in 100 μL PBS. After incubation for 30 min at 4 °C the resuspended virus was layered on Sucrose gradient (20–60%) and was purified by ultracentrifugation (38,000 rpm, 2 h, 4 °C). The now visible virus-containing band was harvested and stored at −80 °C. For Incucyte experiments virus-containing supernatant was centrifuged (4,000 rpm, 5 min, 4 °C) two days after transfection. 5 volumes of viral supernatant were layered on top of 1 vol 20% Sucrose followed by centrifugation (14,000 rpm, 3 h, 4 °C). The supernatant was removed and viral pellet was resuspended in 80 μL PBS and stored at −80 °C.

HIV-1 infection assay

To assess the impact of PNFs on HIV-1 infection, 10,000 TZM-bl cells—harbouring a β-galactosidase reporter gene under control of the HIV-1 LTR—were seeded into 96-well plates in 180 µL supplemented DMEM 24 h prior to infection. CCR5 tropic HIV-1 was generated by transfection of HEK293T cells as described previously [15]. Virus stocks were mixed 1:1 (v/v) with PNF solutions and incubated for 10 min to allow virion–PNF association before 20 µL of the mixture (corresponding to a 1:320 virus dilution on cells) was added to each well. Three days post-infection, β-galactosidase activity in cell lysates was measured using Gal-Screen system (Applied Biosystems) supplemented with 0.16% Triton-X (Sigma #T9284) as relative light units (RLU) with an Orion II Microplate Luminometer (Berthold).

Nanoparticle tracking analysis (NTA)

To analyze if VLP purification was successful, number of viral particles, diameter and fluorescence was determined by NTA using Zeta-View TWIN. To distinguish between viral particles and extracellular vesicles the purified cell supernatant was also measured. Videos of the light-refracting particles were recorded with the following settings: 25 °C fixed temperature, 11 positions, 1 cycle, sensitivity 90, shutter 100, 15 fps, 2 s videos/position, 3 measurements. Videos of the fluorescence using the 500 nm filter were recorded with the following settings: 25 °C fixed temperature, 11 positions, 1 cycle, sensitivity 96, shutter 32, 15 fps, 2 s videos/position, 3 measurements. The chamber was rinsed between the samples with particle-free PBS.

Analysis of PNFs by time-lapse imaging

To analyze aggregates of D4 (2 mg/mL) and Vectofusin-1 (1 mg/mL), PNFs were solved in Opti-Mem Medium (Gibco, 31985070) to 0.5 mg/mL before they were further diluted in supplemented RPMI to 10 µg/mL or 30 µg/mL in absence or presence of VLPs (1:12 diluted in Opti-MEM Medium). To analyze aggregates of pFTAA D4 and D4 they were incubated at 37 °C for 30 min before they were further diluted in supplemented RPMI to 10 µg/mL in absence or presence of VLPs (1:8 diluted). After 1 h incubation images were taken every 4 h for 72 h and green fluorescence was measured with the time-lapse imaging and analysis instrument Incucyte S3 (Sartorius AG) using following conditions: Phase and Green. Aggregate density was quantified by measurement of confluence using Incucyte 2024B software (Sartorius AG). Furthermore, aggregates (10 µg/mL, 1 h incubation) were marked via the confluence mask in the Incucyte software and subsequently their size and number of aggregates was evaluated using 3D objects counter function of ImageJ 1.54 g for triplicate measurements (4 images per measurement) similar as described in Kaygisiz et al. [56]. To analyze D4 and Vectofusin-1 aggregates in presence of cells, 50,000 CD4+ T cells or 20,000 HeLa cells were treated with 10 µg/mL or 30 µg/mL PNFs in presence and absence of VLPs and images were taken every 4 h for 72 h as described before. To analyze pFTAA-D4 aggregates in presence of cells, 20,000 HeLa cells were treated with 10 µg/mL PNFs in presence and absence of VLPs and images were taken every 12 h for 72 h as described above. Number of pFTAA-D4 aggregates were determined using Incucyte 2024B software.

To analyze the influence of FBS and human serum on aggregation behavior and both PNFs, D4 (2 mg/mL) and Vectofusin-1 (1 mg/mL) were directly solved in absence or presence of VLPs (1:8 diluted) in RPMI medium supplemented with defined concentrations (0, 2.5, 5, 10, or 20%) of either FBS or human serum (Type AB, Male; Capricorn Scientific, HUM-3B) to 10 µg/mL. After 1 h images were taken every 4 h for 72 h as described above.

Fluorescence microscopy

To visualize the interaction of VLPs with PNFs, 20 µg/mL of D4 and Vectofusin-1 PNFs were incubated with VLPs (1:12 diluted) for 1 h before microscopic images were taken with DMi8 Inverted Microscope (Leica Microsystems) using 63x objective and 8x zoom. Based on z-stack images a 3D visualization of PNFs and VLPs were generated using the software LAS X (Leica Microsystems). The interaction of VLPs/PNFs with HeLa cells was analyzed by incubating 10 µg/mL D4 or Vectofusin-1 PNFs for 10 min before the mix was added to HeLa cells for 1 h. The cell nucleus was stained by removing cell supernatant and adding of Hoechst 33342 (Invitrogen, 1:2000 dilution in medium) for 10 min according to manufacturer's protocol. After two washing steps to remove Hoechst staining and unbound PNFs, samples were analyzed by fluorescence microscopy using 63x objective and 2x zoom. Based on z-stack images a 3D visualization of HeLa cells with VLPs and PNFs were generated. For colocalization of D4 and lysosomes, 10,000 HeLa cells were seeded and on the next day 10 µg/mL pFTAA labeled D4 PNFs were added. After 24 h lysosomes were stained using 1 µM Lysotracker Blue DND-22 (Invitrogen, L7525) for 1 h. After washing with PBS cells were analyzed by fluorescence microscopy using 63x objective and 2.5x zoom

Transmission electron microscopy (TEM)

Negative staining was performed to visualize PNFs (10 µg/mL) and VLPs in comparison to cell supernatant (undiluted) and PNFs with VLPs (VLPs were diluted 1:10 in OptiMEM and then 5 µL of that dilution was added to 5 µL of PNF preparation (end concentration PNFs: 250 µg/mL)). 10 µL of each preparation was left to adhere on a glow-discharged, formvar coated and carbon enhanced 300-mesh copper grid (Plano GmbH) for 10 min. Then, three washing steps using 10 µL in three drops of aqua bidest were performed followed by staining with 10 µL 2% (w/v) uranyl acetate (Merck KGaK) in aqua bidest for 5 s. Most of the remaining uranyl acetate solution was removed by Whatman™ filter paper (Avantor, Inc.), the grids were air dried and samples were imaged with a JEM-1400 120 kV transmission electron microscope (JEOL GmbH) equipped with a CCD camera (Veleta, Olympus Soft Imaging Solutions GmbH) at 120 kV acceleration voltage.

For visualizing the interaction of PNFs with cells and VLPs, 50,000 HeLa cells were seeded on carbon-coated sapphire discs (3 mm diameter, 50 µm thickness, Wohlwend GmbH) in a 12 well plate and on the next day 2 µg/mL PNFs or PNFs mixed with VLPs (1:10 diluted) were incubated for 10 min and were added for 1 h to HeLa cells (1:10 diluted on cells). Samples were high pressure frozen (HPF Compact 01, Wohlwend GmbH), freeze substituted (EM AFS2, Leica), embedded in epoxy resin (EMbed-812 Embedding Kit, Science Services GmbH) and ultrathin sectioned (thickness of ~ 70 nm) as described previously [101]. Samples were imaged using a JEM-1400 electron microscope (JEOL GmbH) equipped with a CCD camera with an accelerating voltage of 120 kV.

Scanning electron microscopy (SEM)

50,000 HeLa cells were seeded on cover glasses in a 12 well plate. On the next day 2 µg/mL PNFs or PNFs mixed with VLPs (1:10 diluted) were pre-incubated for 10 min and then added for 1 h to HeLa cells (1:10 diluted on cells). Samples were fixed with 2.5% glutaraldehyde and 1% saccharose in 0.1 M phosphate buffer (pH 7.3) overnight at 4 °C. Then, samples were post-fixed in 2% osmium tetroxide on PBS at room temperature for 20 min, washed three times with PBS, dehydrated using increasing concentrations of propanol and critical point dried (CPD 030, BAL-TEC AG). Then samples were coated with ~5 nm platinum (BAF 300, BAL-TEC AG) and secondary electron images were recorded using a Hitachi S-5200 field emission scanning electron microscope (Hitachi, Tokyo, Japan) at an acceleration voltage of 5 kV as described previously [28].

Scanning transmission electron microscopy (STEM) tomography

To visualize interaction of PNF with cells and VLPs in 3D, epoxy resin embedded samples (see above) were cut into 800 nm-thick sections, mounted on a 200-mesh copper grid with parallel bars (Plano GmbH), and incubated with gold particles (25 nm, AURION Immuno Gold Reagents & Accessories) as fiducial markers aiding computational tomogram reconstruction. The detailed protocol was published previously [102]. Tomograms were recorded using a JEM-2100F field emission electron microscope (JEOL GmbH) with an acceleration voltage of 200 kV in STEM mode. Images from tilt angles ranging from −72° to + 72° with an increment of 1.5° were acquired, resulting in tilt series of 97 images. For aligning the images the IMOD software package [103] was used and structures were visualized by the Avizo 3D 2023.1.1 software (Thermo Fisher Scientific) as described previously [104].

Cell viability and proliferation

To determine the effect of PNFs on cell viability a CellTiter-Glo Luminescent Cell Viability Assay was performed. 10,000 HeLa or 50,000 CD4+ T cells were seeded and on the next day (HeLa cells) or on the same day (CD4+ T cells) were treated with the indicated PNFs concentrations for three days. Cell supernatant was removed and 100 µL CellTiter-Glo Reagent (Promega, Cat: G7571) 1:1 diluted in PBS (Gibco, 14200075) was added to HeLa cells or pelleted T cells for 10 min followed by transferring 50 µL of cell lysates to 96-well white flat-bottom plate, and luminescence was recorded by Orion microplate luminometer (Berthold) as described previously [15]. For proliferation analysis of T cells, 50,000 CD4+ T cells were incubated with indicated PNFs concentrations. After 1, 24, 48 and 72 h cell concentrations were determined using LUNA-II™ Automated Cell Counter (Logos Biosystems). The concentration of viable cells was determined by incubating cells 1:1 with trypan blue (0.4%, Invitrogen) before measurement.

Endocytosis inhibition

40,000 HeLa cells were seeded in 100 µL supplemented DMEM (10% FBS). After one day medium was replaced by 180 µL DMEM containing 1% FBS. 10 µL of endocytosis inhibitors Wortmannin (Sigma-Aldrich, TA9545855749–1MG), EIPA (MedChemExpress, HY-101840 5 mg), Dynasore, Chlorpromazine (Sigma-Aldrich, C8138-5G) and Nystatin (Sigma Aldrich, N6261–500KU) were added for 30 min before 10 µL pFTAA-labeled D4 (10 µg/mL) was added. For faster sedimentation of PNFs, cells were centrifuged (1300 rpm, 3 min). After 4 h incubation extracellular PNFs were quenched using trypan blue diluted 1:6 in PBS for 10 min. After two washing steps and detachment of cells using trypsin, cells were fixed with 4% PFA and pFTAA-positive cells were determined by flow cytometry using CytoFlex (Beckmann Coulter). Possible cytotoxic effects of endocytosis inhibitors were determined under same conditions using CellTiter-Glo Luminescent Cell Viability Assay as described above.

Analysis of pFTAA D4 under CAR-T cell like conditions

CD4+/CD8+ T cells were isolated from Buffy coats of 3 healthy donors and activated in presence of IL-2 over three days as described before [15]. Afterwards, the beads were removed and medium was exchanged, to medium supplemented with IL-7 and IL-15. The next day (day 0), 30 µg/mL pFTAA D4 PNFs were added to 50,000 CD4+/CD8+ T cells. After 1 h, 24 h, 48 h, 73 h and 168 h fluorescence of pFTAA D4 PNFs was analyzed by flow cytometry. After 24 h and 72 h a medium change was performed. Additionally, the cell concentration was adjusted to 1 million/mL after 72 h. After 7 days cell viability and cell concentration were determined after trypan blue staining using LUNA-II™ Automated Cell Counter.

Statistics

Statistical analysis were performed using GraphPad Prism version 10.1.0.

CRediT authorship contribution statement

Clarissa Read: Writing – review & editing, Supervision, Resources, Project administration, Funding acquisition. **Jan Münch:** Writing – review & editing, Supervision, Resources, Project administration, Funding acquisition. **Pamela Fischer-Posovszky:** Resources, Funding acquisition. **Tanja Weil:** Resources, Funding acquisition. **Ulrich Stifel:** Resources, Formal analysis. **Fabian Zech:** Investigation. **Annalena Kuhn:** Writing – review & editing, Visualization, Investigation, Formal analysis. **Nayeong Jeon:** Writing – review & editing, Visualization, Investigation, Formal analysis. **Kübra Kaygisiz:** Writing – original draft, Visualization, Validation, Investigation, Conceptualization. **Lena Rauch-Wirth:** Writing – original draft, Visualization, Validation, Investigation, Formal analysis, Conceptualization. **Julia La Roche:** Writing – original draft, Visualization, Validation, Formal analysis, Conceptualization.

Ethics statement

CD4+ and CD8+ T cells from healthy donors were isolated from buffy coats acquired from the Blutspendezentrale Ulm, ethic vote number 151/22 FSt/bal.

Declaration of Generative AI and AI-assisted technologies in the writing process

During the preparation of this work the author used ChatGPT (***G***PT-5.1, November 2025 version/OpenAI) in order to improve the readability and language of the manuscript. After using this tool/service, the authors reviewed and edited the content as needed and take full responsibility for the content of the publication.

Declaration of Competing Interest

The authors declare the following financial interests/personal relationships which may be considered as potential competing interests: Jan Muench has patent Viral Infection Enhancing Peptide licensed to assignee. Muench Jan has patent Fibril peptides pending to Assignee. Lena Rauch-Wirth has patent Fibril peptides pending to Assignee. If there are other authors, they declare that they have no known competing financial interests or personal relationships that could have appeared to influence the work reported in this paper.

Acknowledgements

This project has received funding through a Collaborative Research Centre grant of the German Research Foundation (316249678 – SFB 1279) to JM, CR, TW.

This project has received funding through the German Research Foundation (432000323).

The authors acknowledge the MIT Office of Research Computing and Data for providing high performance computing resources that have contributed to the research results reported within this paper.

Appendix A. Supporting information

Supplementary data associated with this article can be found in the online version at doi:10.1016/j.nantod.2026.103015.

Data availability

Data will be made available on request.

References

[1] S.M. AlDallal, Cureus 12 (2020) e11504, https://doi.org/10.7759/cureus.11504.
[2] M. Wang, J. Munoz, A. Goy, F.L. Locke, C.A. Jacobson, B.T. Hill, J. M. Timmerman, H. Holmes, S. Jaglowski, I.W. Flinn, P.A. McSweeney, D. B. Miklos, J.M. Pagel, M.-J. Kersten, N. Milpied, H. Fung, M.S. Topp, R. Houot, A. Beitinjaneh, W. Peng, L. Zheng, J.M. Rossi, R.K. Jain, A.V. Rao, P.M. Reagan, N. Engl. J. Med. 382 (2020) 1331–1342, https://doi.org/10.1056/NEJMoa1914347.
[3] S. Ali, R. Kjeken, C. Niederlaender, G. Markey, T.S. Saunders, M. Opsata, K. Moltu, B. Bremnes, E. Grønevik, M. Muusse, G.D. Håkonsen, V. Skibeli, M. E. Kalland, I. Wang, I. Buajordet, A. Urbaniak, J. Johnston, K. Rantell, E. Kerwash, M. Schuessler-Lenz, T. Salmonson, J. Bergh, C. Gisselbrecht, K. Tzogani, I. Papadouli, F. Pignatti, Oncologist 25 (2020) e321–e327, https://doi.org/10.1634/theoncologist.2019-0233.
[4] P. Sharma, B. Kanapuru, B. George, X. Lin, Z. Xu, W.W. Bryan, R. Pazdur, M. R. Theoret, Clin. Cancer Res. 28 (2022) 1759–1764, https://doi.org/10.1158/1078-0432.CCR-21-3803.
[5] M. Ayala Ceja, M. Khericha, C.M. Harris, C. Puig-Saus, Y.Y. Chen, J. Exp. Med. 221 (2024) e20230903, https://doi.org/10.1084/jem.20230903.
[6] J.S. Abramson, M.L. Palomba, L.I. Gordon, M.A. Lunning, M. Wang, J. Arnason, A. Mehta, E. Purev, D.G. Maloney, C. Andreadis, A. Sehgal, S.R. Solomon, N. Ghosh, T.M. Albertson, J. Garcia, A. Kostic, M. Mallaney, K. Ogasawara, K. Newhall, Y. Kim, D. Li, T. Siddiqi, Lancet 396 (2020) 839–852, https://doi.org/10.1016/S0140-6736(20)31366-0.
[7] T. Martin, S.Z. Usmani, J.G. Berdeja, M. Agha, A.D. Cohen, P. Hari, D. Avigan, A. Deol, M. Htut, A. Lesokhin, N.C. Munshi, E. O'Donnell, A.K. Stewart, J. M. Schecter, J.D. Goldberg, C.C. Jackson, T.-M. Yeh, A. Banerjee, A. Allred, E. Zudaire, W. Deraedt, Y. Olyslager, C. Zhou, L. Pacaud, D. Madduri, A. Jakubowiak, Y. Lin, S. Jagannath, J. Clin. Oncol. 41 (2023) 1265–1274, https://doi.org/10.1200/JCO.22.00842.
[8] M.C. O'Leary, X. Lu, Y. Huang, X. Lin, I. Mahmood, D. Przepiorka, D. Gavin, S. Lee, K. Liu, B. George, W. Bryan, M.R. Theoret, R. Pazdur, Clin. Cancer Res. 25 (2019) 1142–1146, https://doi.org/10.1158/1078-0432.CCR-18-2035.
[9] C. Roddie, K.S. Sandhu, E. Tholouli, A.C. Logan, P. Shaughnessy, P. Barba, A. Ghobadi, M. Guerreiro, D. Yallop, M. Abedi, J.M. Pantin, J.A. Yared, A. M. Beitinjaneh, S. Chaganti, K. Hodby, T. Menne, M.L. Arellano, R. Malladi, B. D. Shah, L. Mountjoy, K.M. O'Dwyer, K.S. Peggs, P. Lao-Sirieix, Y. Zhang, W. Brugger, E. Braendle, M. Pule, M.R. Bishop, D.J. DeAngelo, J.H. Park, E. Jabbour, N. Engl. J. Med. 391 (2024) 2219–2230, https://doi.org/10.1056/NEJMoa2406526.
[10] L.-Y. Cao, Y. Zhao, Y. Chen, P. Ma, J.-C. Xie, X.-M. Pan, X. Zhang, Y.-C. Chen, Q. Wang, L.-L. Xie, Front. Immunol. 16 (2025), https://doi.org/10.3389/fimmu.2025.1583116.
[11] C. Meier, T. Weil, F. Kirchhoff, J. Münch, WIREs Nanomed. Nanobiotechnol. 6 (2014) 438–451, https://doi.org/10.1002/wnan.1275.
[12] T. Ran, S.B. Eichmüller, P. Schmidt, M. Schlander, Int. J. Cancer 147 (2020) 3438–3445, https://doi.org/10.1002/ijc.33156.
[13] C. Radek, O. Bernadin, K. Drechsel, N. Cordes, R. Pfeifer, P. Sträßer, M. Mormin, A. Gutierrez-Guerrero, F. Cosset, A.D. Kaiser, T. Schaser, A. Galy, E. Verhoeyen, I. C.D. Johnston, Hum. Gene Ther. 30 (2019) 1477–1493, https://doi.org/10.1089/hum.2019.157.
[14] A. Rajabzadeh, A.A. Hamidieh, F. Rahbarizadeh, BMC Mol. Cell Biol. 22 (2021) 57, https://doi.org/10.1186/s12860-021-00397-z.
[15] L. Rauch-Wirth, A. Renner, K. Kaygisiz, T. Weil, L. Zimmermann, A.A. Rodriguez-Alfonso, D. Schütz, S. Wiese, L. Ständker, T. Weil, D. Schmiedel, J. Münch, Front. Immunol. 14 (2023) 1270243, https://doi.org/10.3389/fimmu.2023.1270243.
[16] F. Nasiri, S. Muhammadnejad, F. Rahbarizadeh, Clin. Exp. Med. 23 (2023) 2535–2549, https://doi.org/10.1007/s10238-022-00928-8.
[17] K.E. Pollok, H. Hanenberg, T.W. Noblitt, W.L. Schroeder, I. Kato, D. Emanuel, D. A. Williams, J. Virol. 72 (1998) 4882–4892, https://doi.org/10.1128/jvi.72.6.4882-4892.1998.
[18] M. Yolamanova, C. Meier, A.K. Shaytan, V. Vas, C.W. Bertoncini, F. Arnold, O. Zirafi, S.M. Usmani, J.A. Müller, D. Sauter, C. Goffinet, D. Palesch, P. Walther, N.R. Roan, H. Geiger, O. Lunov, T. Simmet, J. Bohne, H. Schrezenmeier, K. Schwarz, L. Ständker, W.-G. Forssmann, X. Salvatella, P.G. Khalatur, A. R. Khokhlov, T.P.J. Knowles, T. Weil, F. Kirchhoff, J. Münch, Nat. Nanotechnol. 8 (2013) 130–136, https://doi.org/10.1038/nnano.2012.248.
[19] S. Sieste, T. Mack, E. Lump, M. Hayn, D. Schütz, A. Röcker, C. Meier, K. Kaygisiz, F. Kirchhoff, T.P.J. Knowles, F.S. Ruggeri, C.V. Synatschke, J. Münch, T. Weil, Adv. Funct. Mater. 31 (2021) 2009382, https://doi.org/10.1002/adfm.202009382.
[20] K. Kaygisiz, L. Rauch-Wirth, A. Dutta, X. Yu, Y. Nagata, T. Bereau, J. Münch, C. V. Synatschke, T. Weil, Nat. Commun. 14 (2023) 5121, https://doi.org/10.1038/s41467-023-40663-6.
[21] K. Kaygisiz, A. Dutta, L. Rauch-Wirth, C.V. Synatschke, J. Münch, T. Bereau, T. Weil, Biomater. Sci. 11 (2023) 5251–5261, https://doi.org/10.1039/D3BM00412K.
[22] J. Dodd-o, A. Roy, Z. Siddiqui, R. Jafari, F. Coppola, S. Ramasamy, A. Kolloli, D. Kumar, S. Kaundal, B. Zhao, R. Kumar, A.S. Robang, J. Li, A.-R. Azizogli, V. Pai, A. Acevedo-Jake, C. Heffernan, A. Lucas, A.C. McShan, A.K. Paravastu, B. V.V. Prasad, S. Subbian, P. Král, V. Kumar, Nat. Commun. 15 (2024) 1142, https://doi.org/10.1038/s41467-024-45193-3.
[23] L.S. Vermeer, L. Hamon, A. Schirer, M. Schoup, J. Cosette, S. Majdoul, D. Pastré, D. Stockholm, N. Holic, P. Hellwig, A. Galy, D. Fenard, B. Bechinger, Acta Biomater. 64 (2017) 259–268, https://doi.org/10.1016/j.actbio.2017.10.009.
[24] J.A. Jackman, Biochim. et Biophys. Acta (BBA) - Biomembr. 1864 (2022) 183821, https://doi.org/10.1016/j.bbamem.2021.183821.
[25] X.-R. Zhou, Y. Liu, Z. Huang, Q. Yao, F. He, Y. Gao, Bioconjug. Chem. 32 (2021) 106–110, https://doi.org/10.1021/acs.bioconjchem.0c00706.
[26] A. Jamali, L. Kapitza, T. Schaser, I.C.D. Johnston, C.J. Buchholz, J. Hartmann, Mol. Ther. Methods Clin. Dev. 13 (2019) 371–379, https://doi.org/10.1016/j.omtm.2019.03.003.
[27] M. Irving, E. Lanitis, D. Migliorini, Z. Ivics, S. Guedan, Hum. Gene Ther. 32 (2021) 1044–1058, https://doi.org/10.1089/hum.2021.173.
[28] D. Schütz, S. Rode, C. Read, J.A. Müller, B. Glocker, K.M.J. Sparrer, O.T. Fackler, P. Walther, J. Münch, Adv. Funct. Mater. 31 (2021) 2104814, https://doi.org/10.1002/adfm.202104814.
[29] L. Rauch-Wirth, D. Schütz, R. Groß, S. Rode, B. Glocker, J.A. Müller, P. Walther, C. Read, J. Münch, Biomaterials 317 (2025) 123044, https://doi.org/10.1016/j.biomaterials.2024.123044.
[30] D. Schütz. Mechanistic Studies on Transduction Enhancing EF-C Peptide Nanofibrils and Optimization for Gene Therapeutic Applications (Dissertation), Ulm University, 2021.
[31] C. Toniolo, A. Polese, F. Formaggio, M. Crisma, J. Kamphuis, J. Am. Chem. Soc. 118 (1996) 2744–2745, https://doi.org/10.1021/ja9537383.
[32] G. Zandomeneghi, M.R.H. Krebs, M.G. McCammon, M. Fändrich, Protein Sci. 13 (2004) 3314–3321, https://doi.org/10.1110/ps.041024904.
[33] J. Rey, S. Murail, S. de Vries, P. Derreumaux, P. Tuffery, Nucleic Acids Res. 51 (2023) W432–W437, https://doi.org/10.1093/nar/gkad376.
[34] V. Binette, N. Mousseau, P. Tuffery, J. Chem. Theory Comput. 18 (2022) 2720–2736, https://doi.org/10.1021/acs.jctc.1c01293.
[35] A. Lamiable, P. Thévenet, J. Rey, M. Vavrusa, P. Derreumaux, P. Tufféry, Nucleic Acids Res. 44 (2016) W449–W454, https://doi.org/10.1093/nar/gkw329.
[36] P. Tufféry, P. Derreumaux, Front. Bioinform. 3 (2023) 1113928, https://doi.org/10.3389/fbinf.2023.1113928.
[37] R. Gautier, D. Douguet, B. Antonny, G. Drin, Bioinformatics 24 (2008) 2101–2102, https://doi.org/10.1093/bioinformatics/btn392.
[38] S. Majdoul, A.K. Seye, A. Kichler, N. Holic, A. Galy, B. Bechinger, D. Fenard, J. Biol. Chem. 291 (2016) 2161–2169, https://doi.org/10.1074/jbc.M115.675033.
[39] B. Apostolovic, M. Danial, H.-A. Klok, Chem. Soc. Rev. 39 (2010) 3541–3575, https://doi.org/10.1039/B914339B.
[40] D. Schütz, C. Read, R. Groß, A. Röcker, S. Rode, K. Annamalai, M. Fändrich, J. Münch, ACS Omega 6 (2021) 7731–7738, https://doi.org/10.1021/acsomega.1c00068.
[41] N.M. Sherer, M.J. Lehmann, L.F. Jimenez-Soto, A. Ingmundson, S.M. Horner, G. Cicchetti, P.G. Allen, M. Pypaert, J.M. Cunningham, W. Mothes, Traffic 4 (2003) 785–801, https://doi.org/10.1034/j.1600-0854.2003.00135.x.
[42] E. Nolte-'t Hoen, T. Cremer, R.C. Gallo, L.B. Margolis, Proc. Natl. Acad. Sci. 113 (2016) 9155–9161, https://doi.org/10.1073/pnas.1605146113.
[43] T.E. Finn, A.C. Nunez, M. Sunde, S.B. Easterbrook-Smith, J. Biol. Chem. 287 (2012) 21530–21540, https://doi.org/10.1074/jbc.M112.372961.
[44] A.A. Reyes Barcelo, F.J. Gonzalez-Velasquez, M.A. Moss, J. Biol. Eng. 3 (2009) 5, https://doi.org/10.1186/1754-1611-3-5.
[45] Y. Misumi, Y. Tabata, M. Tasaki, K. Obayashi, S. Yamakawa, T. Nomura, M. Ueda, Amyloid 30 (2023) 67–73, https://doi.org/10.1080/13506129.2022.2120800.
[46] F. Eberhardt, A. Hückelhoven-Krauss, A. Kunz, G. Jiang, T. Sauer, A. Reichman, B. Neuber, K. Böpple, A. Schmitt, C. Müller-Tidow, M. Schmitt, A. Keib, Int. J. Mol. Med. 52 (2023) 58, https://doi.org/10.3892/ijmm.2023.5261.
[47] R.R. Kay, Cells Dev. 168 (2021) 203713, https://doi.org/10.1016/j.cdev.2021.203713.
[48] J. La Roche, L. Rauch-Wirth, L. Zimmerman, F. Zech, J. Münch, C. Read, K. Kaygisiz, J. Pept. Sci. 31 (2025) e70051, https://doi.org/10.1002/psc.70051.
[49] M.L.E. Lundahl, S. Fogli, P.E. Colavita, E.M. Scanlan, RSC Chem. Biol. 2 (2021) 1004–1020, https://doi.org/10.1039/d1cb00067e.
[50] J.A. Swanson, Nat. Rev. Mol. Cell Biol. 9 (2008) 639–649, https://doi.org/10.1038/nrm2447.
[51] W.S. Garrett, I. Mellman, in: M.T. Lotze, A.W. Thomson (Eds.), Dendritic Cells, Second Edition, Academic Press, London, 2001, https://doi.org/10.1016/B978-012455851-9/50055-9.
[52] M. Li, L.-Y. Chin, S. Shukor, A.G. Tamayo, M.V. Maus, B. Parekkadan, Autoimmunity 52 (2019) 102–107, https://doi.org/10.1080/08916934.2019.1630064.
[53] J. Brelstaff, B. Ossola, J.J. Neher, T. Klingstedt, K.P.R. Nilsson, M. Goedert, M. G. Spillantini, A.M. Tolkovsky, Front. Neurosci. 9 (2015) 184, https://doi.org/10.3389/fnins.2015.00184.
[54] J. Brelstaff, M.G. Spillantini, A.M. Tolkovsky, Neural Regen. Res. 10 (2015) 1746–1747, https://doi.org/10.4103/1673-5374.165298.
[55] G. Agliardi, J. Dias, A. Rampotas, J. Garcia, C. Roddie, Lancet Haematol. 12 (2025) e57–e67, https://doi.org/10.1016/S2352-3026(24)00273-4.
[56] K. Kaygisiz, L. Rauch-Wirth, A. Iscen, J. Hartenfels, K. Kremer, J. Münch, C. V. Synatschke, T. Weil, Adv. Healthc. Mater. 13 (2024) 2301364, https://doi.org/10.1002/adhm.202301364.
[57] J.-A. Müller. The Versatile Role of Semen and Seminal Amyloid in Virus Infection (Dissertation), Ulm University, 2016.

[58] H.F. Stanyon, J.H. Viles, J. Biol. Chem. 287 (2012) 28163–28168, https://doi.org/10.1074/jbc.C112.360800.
[59] J. Mathew, P. Sankar, M.A. Varacallo, in: Physiology, Blood Plasma, StatPearls Publishing, Treasure Island (FL), 2025.
[60] L.A. Munishkina, E.M. Cooper, V.N. Uversky, A.L. Fink, J. Mol. Recognit. 17 (2004) 456–464, https://doi.org/10.1002/jmr.699.
[61] S. Carra, B. Fabian, H. Taghavi, E. Milanetti, V. Giliberti, G. Ruocco, J. Shepherd, M. Vendruscolo, M. Fuxreiter, Mol. Asp. Med. 103 (2025) 101369, https://doi.org/10.1016/j.mam.2025.101369.
[62] A. Schneider, M. Simons, J. Cell Biol. 213 (2016) 143–145, https://doi.org/10.1083/jcb.201604024.
[63] T.B. Schuster, D. de Bruyn Ouboter, N. Bruns, W. Meier, Small 7 (2011) 2158–2162, https://doi.org/10.1002/smll.201100701.
[64] A.J. van Hell, C.I.C.A. Costa, F.M. Flesch, M. Sutter, W. Jiskoot, D.J. A. Crommelin, W.E. Hennink, E. Mastrobattista, Biomacromolecules 8 (2007) 2753–2761, https://doi.org/10.1021/bm0704267.
[65] I. Nakase, A. Tadokoro, N. Kawabata, T. Takeuchi, H. Katoh, K. Hiramoto, M. Negishi, M. Nomizu, Y. Sugiura, S. Futaki, Biochemistry 46 (2007) 492–501, https://doi.org/10.1021/bi0612824.
[66] I. Nakase, M. Niwa, T. Takeuchi, K. Sonomura, N. Kawabata, Y. Koike, M. Takehashi, S. Tanaka, K. Ueda, J.C. Simpson, A.T. Jones, Y. Sugiura, S. Futaki, Mol. Ther. 10 (2004) 1011–1022, https://doi.org/10.1016/j.ymthe.2004.08.010.
[67] K. Morimoto, J. Ishitobi, K. Noguchi, R. Kira, Y. Kitayama, Y. Goto, D. Fujiwara, M. Michigami, A. Harada, T. Takatani-Nakase, I. Fujii, S. Futaki, M. Kanada, I. Nakase, ACS Appl. Mater. Interfaces 16 (2024) 17069–17079, https://doi.org/10.1021/acsami.3c14592.
[68] N. Schmidt, A. Mishra, G.H. Lai, G.C.L. Wong, FEBS Lett. 584 (2010) 1806–1813, https://doi.org/10.1016/j.febslet.2009.11.046.
[69] M.J. Lehmann, N.M. Sherer, C.B. Marks, M. Pypaert, W. Mothes, J. Cell Biol. 170 (2005) 317–325, https://doi.org/10.1083/jcb.200503059.
[70] X.-Y. Sun, Q.-Z. Gan, J.-M. Ouyang, Sci. Rep. 7 (2017) 41949, https://doi.org/10.1038/srep41949.
[71] J. Rejman, V. Oberle, I.S. Zuhorn, D. Hoekstra, Biochem. J. 377 (2004) 159–169, https://doi.org/10.1042/BJ20031253.
[72] A. Bayati, E. Banks, C. Han, W. Luo, W.E. Reintsch, C.E. Zorca, I. Shlaifer, E. Del Cid Pellitero, B. Vanderperre, H.M. McBride, E.A. Fon, T.M. Durcan, P. S. McPherson, Cell Rep. 40 (2022) 111102, https://doi.org/10.1016/j.celrep.2022.111102.
[73] A.T. Medeiros, L. Bubacco, J.R. Morgan, Neural Regen. Res. 13 (2018) 647–648, https://doi.org/10.4103/1673-5374.230289.
[74] L.J. Shearer, N.O. Petersen, M.T. Woodside, Biophys. J. 120 (2021) 877–885, https://doi.org/10.1016/j.bpj.2020.12.031.
[75] I. Ruseska, A. Zimmer, Beilstein J. Nanotechnol. 11 (2020) 101–123, https://doi.org/10.3762/bjnano.11.10.
[76] P.A. Wender, D.J. Mitchell, K. Pattabiraman, E.T. Pelkey, L. Steinman, J. B. Rothbard, Proc. Natl. Acad. Sci. 97 (2000) 13003–13008, https://doi.org/10.1073/pnas.97.24.13003.
[77] D. j Mitchell, L. Steinman, D. t Kim, C. g Fathman, J. b Rothbard, J. Pept. Res. 56 (2000) 318–325, https://doi.org/10.1034/j.1399-3011.2000.00723.x.
[78] X. Sun, V.K. Yau, B.J. Briggs, G.R. Whittaker, Virology 338 (2005) 53–60, https://doi.org/10.1016/j.virol.2005.05.006.
[79] D. Finkelshtein, A. Werman, D. Novick, S. Barak, M. Rubinstein, Proc. Natl. Acad. Sci. 110 (2013) 7306–7311, https://doi.org/10.1073/pnas.1214441110.
[80] T. Maetzig, M. Galla, C. Baum, A. Schambach, Viruses 3 (2011) 677–713, https://doi.org/10.3390/v3060677.
[81] C. Piovan, V. Marin, C. Scavullo, S. Corna, E. Giuliani, S. Bossi, A. Galy, D. Fenard, C. Bordignon, G.P. Rizzardi, C. Bovolenta, Mol. Ther. Methods Clin. Dev. 5 (2017) 22–30, https://doi.org/10.1016/j.omtm.2017.02.003.
[82] S. Majdoul, A.K. Seye, A. Kichler, N. Holic, A. Galy, B. Bechinger, D. Fenard, J. Biol. Chem. 291 (2016) 2161–2169, https://doi.org/10.1074/jbc.M115.675033.
[83] M. Li, L.-Y. Chin, S. Shukor, A.G. Tamayo, M.V. Maus, B. Parekkadan, Autoimmunity 52 (2019) 102–107, https://doi.org/10.1080/08916934.2019.1630064.
[84] N.J. Greenfield, Nat. Protoc. 1 (2006) 2876–2890, https://doi.org/10.1038/nprot.2006.202.
[85] M.J. Abraham, T. Murtola, R. Schulz, S. Páll, J.C. Smith, B. Hess, E. Lindahl, SoftwareX 1–2 (2015) 19–25, https://doi.org/10.1016/j.softx.2015.06.001.
[86] M. Abraham, A. Alekseenko, V. Basov, C. Bergh, E. Briand, A. Brown, M. Doijade, G. Fiorin, S. Fleischmann, S. Gorelov, G. Gouaillardet, A. Gray, M.E. Irrgang, F. Jalalypour, J. Jordan, C. Kutzner, J.A. Lemkul, M. Lundborg, P. Merz, V. Miletic, D. Morozov, J. Nabet, S. Pall, A. Pasquadibisceglie, M. Pellegrino, H. Santuz, R. Schulz, T. Shugaeva, A. Shvetsov, A. Villa, S. Wingbermuehle, B. Hess, E. Lindahl, Software X (2024) 19–25, https://doi.org/10.5281/zenodo.10589643.
[87] D. Van Der Spoel, E. Lindahl, B. Hess, G. Groenhof, A.E. Mark, H.J.C. Berendsen, J. Comput. Chem. 26 (2005) 1701–1718, https://doi.org/10.1002/jcc.20291.
[88] W.L. Jorgensen, J. Chandrasekhar, J.D. Madura, R.W. Impey, M.L. Klein, J. Chem. Phys. 79 (1983) 926–935, https://doi.org/10.1063/1.445869.
[89] R.B. Best, X. Zhu, J. Shim, P.E.M. Lopes, J. Mittal, M. Feig, A.D. MacKerell, J. Chem. Theory Comput. 8 (2012) 3257–3273, https://doi.org/10.1021/ct300400x.
[90] H. Grubmüller, H. Heller, A. Windemuth, K. Schulten, Mol. Simul. 6 (1991) 121–142, https://doi.org/10.1080/08927029108022142.
[91] B. Hess, H. Bekker, H.J.C. Berendsen, J.G.E.M. Fraaije, J. Comput. Chem. 18 (1997) 1463–1472, https://doi.org/10.1002/(SICI)1096-987X(199709)18:12%253C1463::AID-JCC4%253E3.0.CO;2-H.
[92] M. Parrinello, A. Rahman, J. Appl. Phys. 52 (1981) 7182–7190, https://doi.org/10.1063/1.328693.
[93] G. Bussi, D. Donadio, M. Parrinello, J. Chem. Phys. 126 (2007), https://doi.org/10.1063/1.2408420.
[94] D.H. de Jong, G. Singh, W.F.D. Bennett, C. Arnarez, T.A. Wassenaar, L.V. Schäfer, X. Periole, D.P. Tieleman, S.J. Marrink, J. Chem. Theory Comput. 9 (2013) 687–697, https://doi.org/10.1021/ct300646g.
[95] S.O. Yesylevskyy, L.V. Schäfer, D. Sengupta, S.J. Marrink, PLoS Comput. Biol. 6 (2010) e1000810, https://doi.org/10.1371/journal.pcbi.1000810.
[96] H.J.C. Berendsen, J.P.M. Postma, W.F. van Gunsteren, A. DiNola, J.R. Haak, J. Chem. Phys. 81 (1984) 3684–3690, https://doi.org/10.1063/1.448118.
[97] T.A. Wassenaar, K. Pluhackova, R.A. Böckmann, S.J. Marrink, D.P. Tieleman, J. Chem. Theory Comput. 10 (2014) 676–690, https://doi.org/10.1021/ct400617g.
[98] W. Humphrey, A. Dalke, K. Schulten, J. Mol. Graph. 14 (1996) 33–38, https://doi.org/10.1016/0263-7855(96)00018-5.
[99] D. Frishman, P. Argos, Proteins: Struct. Funct. Bioinform. 23 (1995) 566–579, https://doi.org/10.1002/prot.340230412.
[100] N.M. Sherer, M.J. Lehmann, L.F. Jimenez-Soto, A. Ingmundson, S.M. Horner, G. Cicchetti, P.G. Allen, M. Pypaert, J.M. Cunningham, W. Mothes, Traffic 4 (2003) 785–801, https://doi.org/10.1034/j.1600-0854.2003.00135.x.
[101] P. Walther, A. Ziegler, J. Microsc. 208 (2002) 3–10, https://doi.org/10.1046/j.1365-2818.2002.01064.x.
[102] C. Read, P. Walther, J. von Einem, in: A.D. Yurochko (Ed.), Human Cytomegaloviruses: Methods and Protocols, Springer US, New York, NY, 2021, pp. 265–289, https://doi.org/10.1007/978-1-0716-1111-1_14.
[103] J.R. Kremer, D.N. Mastronarde, J.R. McIntosh, J. Struct. Biol. 116 (1996) 71–76, https://doi.org/10.1006/jsbi.1996.0013.
[104] B. Beitzinger, F. Gerbl, T. Vomhof, R. Schmid, R. Noschka, A. Rodriguez, S. Wiese, G. Weidinger, L. Ständker, P. Walther, J. Michaelis, M. Lindén, S. Stenger, Adv. Healthc. Mater. 10 (2021) e2100453, https://doi.org/10.1002/adhm.202100453.

6 List of publications

Chronological order.

1. Conzelmann, C., Weil, T., Olari, L.-R., Gilg, A., Rauch, L., Albers, D. P. J., Groß, R., Müller, J. A. & Münch, J. **Virucidal activity of SARS-CoV-2 rapid antigen extraction buffers.** *J. Clin. Virol.* **147**, 105062 (2022).
2. Groß, R., Dias Loiola, L. M., Issmail, L., Uhlig, N., Eberlein, V., Conzelmann, C., Olari, L.-R., Rauch, L., Lawrenz, J., Weil, T., Müller, J. A., Cardoso, M. B., Gilg, A., Larsson, O., Höglund, U., Pålsson, S. A., Tvilum, A. S., Løvschall, K. B., Kristensen, M. M., Spetz, A.-L., Hontonnou, F., Galloux, M., Grunwald, T., Zelikin, A. N. & Münch, J. **Macromolecular Viral Entry Inhibitors as Broad-Spectrum First-Line Antivirals with Activity against SARS-CoV-2.** *Adv. Sci.* **9**, 2201378 (2022).
3. Weil, T., Kirupakaran, A., Le, M.-H., Rebmann, P., Mieres-Perez, J., Issmail, L., Conzelmann, C., Müller, J. A., Rauch, L., Gilg, A., Wettstein, L., Groß, R., Read, C., Bergner, T., Pålsson, S. A., Uhlig, N., Eberlein, V., Wöll, H., Klärner, F.-G., Stenger, S., Kümmerer, B. M., Streeck, H., Fois, G., Frick, M., Braubach, P., Spetz, A.-L., Grunwald, T., Shorter, J., Sanchez-Garcia, E., Schrader, T. & Münch, J. **Advanced Molecular Tweezers with Lipid Anchors against SARS-CoV-2 and Other Respiratory Viruses.** *JACS Au* **2**, 2187–2202 (2022).
4. Kaygisiz, K., Dutta, A., Rauch-Wirth, L., Synatschke, C. V., Münch, J., Bereau, T. & Weil, T. **Inverse design of viral infectivity-enhancing peptide fibrils from continuous protein-vector embeddings.** *Biomater. Sci.* **11**, 5251–5261 (2023).
5. Kaygisiz, K., Rauch-Wirth, L., Dutta, A., Yu, X., Nagata, Y., Bereau, T., Münch, J., Synatschke, C. V. & Weil, T. **Data-mining unveils structure–property–activity correlation of viral infectivity enhancing self-assembling peptides.** *Nat. Commun.* **14**, 5121 (2023).
6. Olari, L.-R., Bauer, R., Gil Miró, M., Vogel, V., Cortez Rayas, L., Groß, R., Gilg, A., Klevesath, R., Rodríguez Alfonso, A. A., Kaygisiz, K., Rupp, U., Pant, P., Mieres-Pérez, J., Steppe, L., Schäffer, R., Rauch-Wirth, L., Conzelmann, C., Müller, J. A., Zech, F., Gerbl, F., Bleher, J., Preising, N., Ständker, L., Wiese, S., Thal, D. R., Haupt, C., Jonker, H. R. A., Wagner, M., Sanchez-Garcia, E., Weil, T., Stenger, S., Fändrich, M., von Einem, J., Read, C., Walther, P., Kirchhoff, F., Spellerberg, B. & Münch, J. **The C-terminal 32-mer fragment of hemoglobin alpha is an amyloidogenic peptide with antimicrobial properties.** *Cell. Mol. Life Sci.* **80**, 151 (2023).
7. Rauch-Wirth, L., Renner, A., Kaygisiz, K., Weil, T., Zimmermann, L., Rodriguez-Alfonso, A. A., Schütz, D., Wiese, S., Ständker, L., Weil, T., Schmiedel, D. & Münch, J. **Optimized peptide nanofibrils as efficient transduction enhancers for in vitro and ex vivo gene transfer.** *Front. Immunol.* **14**, 1270243 (2023).
8. Hayn, M., John, T., Bandak, J., Rauch-Wirth, L., Abel, B. & Münch, J. H**ybrid Materials From Peptide Nanofibrils and Magnetic Beads to Concentrate and Isolate Virus Particles.** *Adv. Funct. Mater.* **34**, 2316260 (2024).
9. Kaygisiz, K., Rauch-Wirth, L., Iscen, A., Hartenfels, J., Kremer, K., Münch, J., Synatschke, C. V. & Weil, T. **Peptide Amphiphiles as Biodegradable Adjuvants for Efficient Retroviral Gene Delivery.** *Adv. Healthc. Mater.* **13**, 2301364 (2024).
10. Dolles, S., Leukel, S., Gensberger-Reigl, S., Rohrhofer, A., Rauch-Wirth, L., Kaygisiz, K., Synatschke, C. V., Münch, J., Schmidt, B., Pischetsrieder, M. & Eichler, J. V**ersatile Features of an Antibody Mimetic Peptide and Its Variants.** *J. Pept. Sci.* **31**, e70005 (2025).

11. Rauch-Wirth, L.*, Schütz, D.*, Groß, R., Rode, S., Glocker, B., Müller, J. A., Walther, P., Read, C. & Münch, J. **Transduction enhancing EF-C peptide nanofibrils are endocytosed by macropinocytosis and subsequently degraded.** *Biomaterials* **317**, 123044 (2025). * These authors contributed equally.
12. La Roche, J., Rauch-Wirth, L., Zimmerman, L., Zech, F., Münch, J., Read, C. & Kaygisiz, K. **Interactions of Peptide Amphiphiles With Viruses and Cells Are Enabled by Amorphous Nanostructures.** *J. Pept. Sci.* **31**, e70051 (2025).
13. Rauch-Wirth, L. & Münch, J. Peptidnanofibrillen als Transduktionsverstärker für die Gentherapie. *Biospektrum* **31**, 284–287 (2025).
14. Rauch-Wirth, L.*, La Roche, J.*, Kaygisiz, K., Kuhn, A., Jeon, N., Stifel, U., Zech, F., Fischer-Posovszky, P., Weil, T., Read, C. & Münch, J. **Structural morphology of peptide nanofibrils dictates viral capture and cellular uptake in gene therapy applications.** *Nano Today* **69**, 103015 (2026). * These authors contributed equally.
15. J. Münch, D. Schütz & L. Rauch. **Fibril peptides.** Patent (EP4314030). EPO. https://register.epo.org/application?lng=en&number=EP22713684. (Patent status: examination is in progress)

7 Acknowledgments

I would like to thank Jan Münch for giving me the opportunity to pursue my Master's thesis and PhD at the Institute for Molecular Virology. I am especially grateful for your trust and support, particularly during my parental leave, as well as insightful discussions and enthusiasm for the projects. I would also like to thank Desiree Schütz for her excellent supervision, continuous support, and positive energy throughout my master's thesis and beyond, which laid the foundation for my PhD project. Furthermore, I thank Frank Kirchhoff and Konstantin Sparrer for their constructive scientific input during presentations. I am also grateful to the members of my thesis advisory committee, Barbara Spellerberg and Tanja Weil, for their valuable feedback during my evaluations and for taking the time to assess my thesis. I would like to express my sincere thanks to all collaborators who contributed to the success of my projects. In particular I thank Kübra Kaygisiz for fruitful discussions, as well as her continuous help and support. I thank Clarissa Read and Julia La Roche for their valuable input and support during experiments and paper preparation. I am grateful to Annalena for her reliable, excellent support with experiments and to Laura for her helpful assistance. I also thank Rüdiger for always taking the time to answer my scientific questions, which helped me a lot. My further thanks go to Dominik Schmiedel and Alexander Renner for doing NK cell experiments, to Armando A. Rodriguez-Alfonso and Nico Preising for peptide characterization and synthesis, and to Nicola Schrott and Daniela Krnavek for lab organization and experimental support. I also thank Dré van der Merwe for his technical support.

I would like to thank Tati and Lukas for always being there for me, for listening, and for offering me a place to stay overnight. I thank Janis for his positive energy, support and the refreshing bouncy and spike ball breaks. I am very thankful for all my wonderful colleagues – Jan (Flipp), Marta, Lia, Dan, Mirja, Alina, Annalena, Hanna, Sofya, Rüdiger, Pascal, Carina, Shreyans, Sichen and Ariel – for creating such a supportive and enjoyable working environment. It was truly a joy not only to work with you but also to share so many great moments outside the lab. My thanks extend to all members of the Institute of Molecular Virology. Finally, and most importantly, I would like to thank my husband, my wonderful daughter, and my family for their endless love and support and always believing in me. A special thank you goes to my dad for being such an inspiring role model. I am also deeply grateful to my mum and mother-in-law for taking such loving care of my daughter – without your help, this journey would not have been possible.

8 Statutory declaration

I hereby declare that I wrote the present dissertation with the topic:

"Novel peptide nanofibrils as efficient transduction enhancers for *ex vivo* viral gene transfer"

independently and used no other aids than those cited. In each individual case, I have clearly identified the source of the passages that are taken word for word or paraphrased from other works. During the preparation of this work, I used AI only in order to improve language and readability. After using AI, I reviewed and edited the content as needed and take full responsibility for the content of this thesis.
I also hereby declare that I have carried out my scientific work according to the principles of good scientific practice in accordance with the current „Satzung der Universität Ulm zur Sicherung guter wissenschaftlicher Praxis" [Rules of the University of Ulm for Assuring Good Scientific Practice].

Ulm, _____

_____

Lena Rauch-Wirth